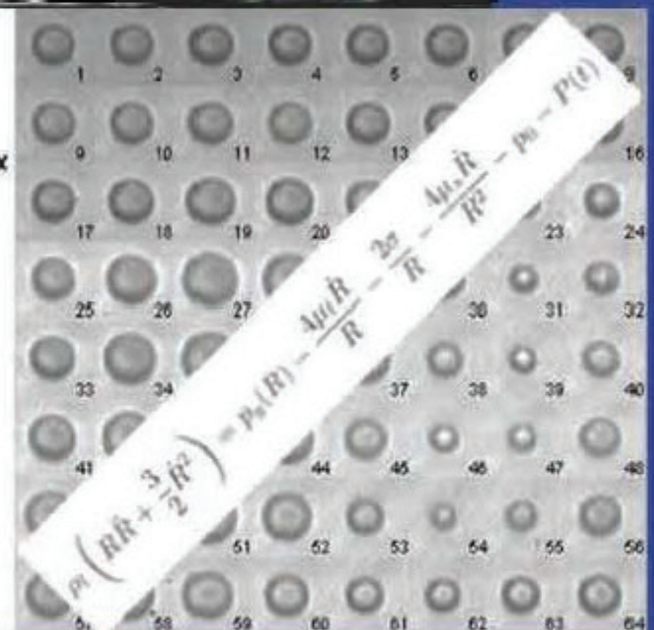
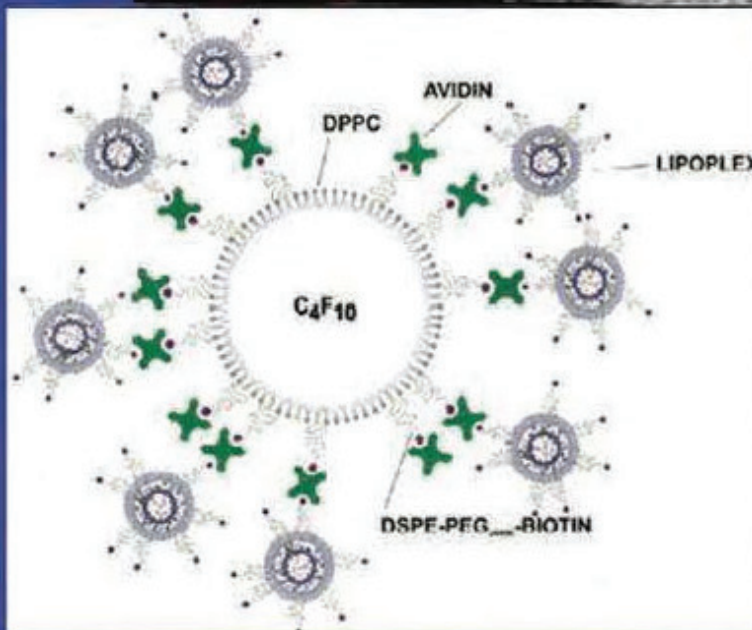
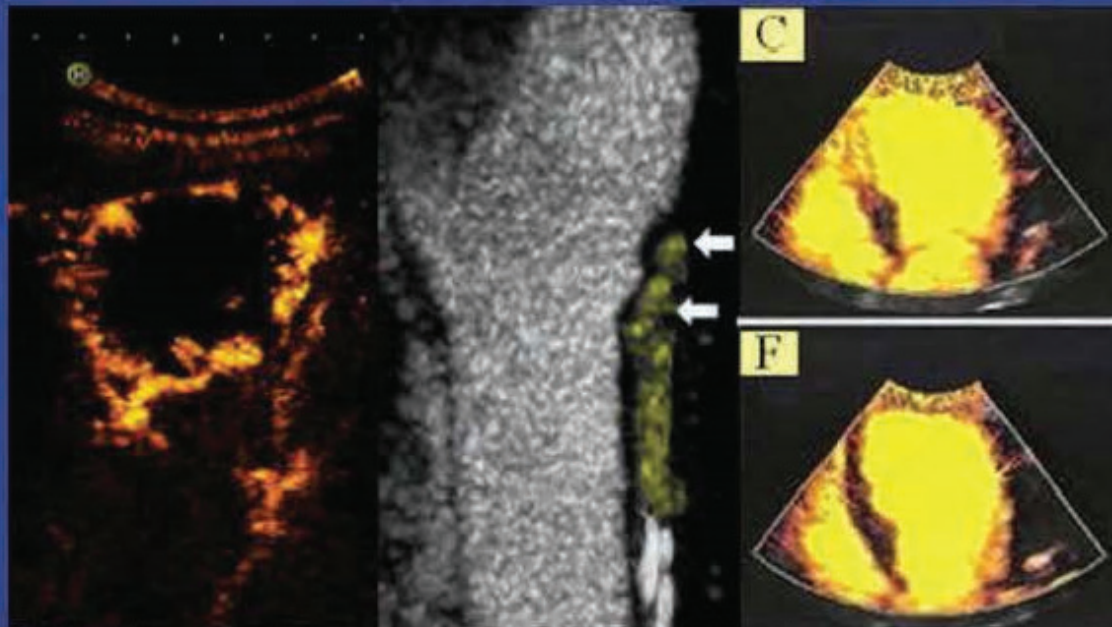


The 24th European Symposium on Ultrasound Contrast Imaging - An ICUS Conference -



Abstract book

17-18 January 2019, Rotterdam, the Netherlands

Organised by Nico de Jong, Folkert ten Cate, Rik Vos, Klazina Kooiman,
Annemien van den Bosch, and Arend Schinkel

Erasmus MC Rotterdam



Thursday, 17 January 2019

Evening Dinner

Diergaarde Blijdorp, Entry Oceanium

Blijdorplan 8, 3041 JG Rotterdam

Dinner Buffet: around 19:00

Coaches will be leaving from Hilton at 18:30 and will be back at Hilton around 22:30

24th EUROPEAN SYMPOSIUM ON ULTRASOUND CONTRAST IMAGING
17-18 JANUARY 2019, Rotterdam, The Netherlands

WEDNESDAY, 16 January 2019

18.00 – 20.00 Registration - Welcome Drinks [1st floor, Hilton hotel Rotterdam]

THURSDAY, 17 January 2019

Oral program

08.00 – 09.00	Registration	
09.00 – 09.10	Introduction and opening	Peter Burns
09.10 – 10.20	(PRE)CLINICAL THERAPY	<i>Chairpersons: Steve Feinstein and Ayache Bouakaz</i>
Kullervo Hynynen	Review of the clinical experience with enhancing blood-brain barrier permeability using focused ultrasound	1
	and microbubbles	
John Eisenbrey	Augmenting radiotherapy with ultrasound-sensitive microbubbles	3
Paul Sheeran	Peripheral flow augmentation mediated by microbubble cavitation from a programmable clinical matrix array transducer	5
Richard Benninger	Detecting pancreatic islet immune infiltration in pre-symptomatic type1 diabetes using sub-micron scale ultrasound.....	7
	contrast agents	
10.20 – 10.55	Postersessions C and D	
10.55 – 11.10	Coffee	
11.10 – 12.40	THERAPY: Towards clinical use	<i>Chairpersons: Beat Kaufmann and Folkert ten Cate</i>
Pintong Huang	A Novel Therapeutic Strategy using Ultrasound Mediated Microbubbles Destruction to Treat Colon Cancer in	10
	A Mouse Model	
Constantin Coussios	Passively Mapped Cavitation-Enhanced Oncological Drug Delivery using Sub-Micron Gas-Stabilizing Solid Particles	11
Jean-Michel Escoffre	Nab-paclitaxel delivery with microbubble-assisted ultrasound in human pancreatic cancer mouse model	13
Twan Lammers	Visualizing and Quantifying Sonoporation-induced Nanocarrier Translocation across the Blood-Brain Barrier	16
John Pacella	Ultrasound-targeted microbubble cavitation with sodium nitrite synergistically enhances nitric oxide production	18
	and microvascular perfusion	
12.40 – 13.40	LUNCH	
13.40 – 14.10	DUTCH HEART FOUNDATION LECTURE	<i>Chairperson: Annemien van den Bosch</i>
Wilson Mathias	Clinical Outcome of Patients Treated With Diagnostic Ultrasound Guided High Mechanical Index Impulses	21
	To Restore Microvascular Flow in ST segment Elevation Acute Myocardial Infarction.....	
14.10 – 15.40	THERAPY: The Basics	<i>Chairpersons: Olivier Couture and Klazina Kooiman</i>
Eleanor Stride	A Multi-Bubble Sonoluminescence in Sonodynamic Therapy	22
Christy Holland	Lipid-shelled microbubbles for ultrasound-triggered release of Xenon for neuroprotection	24
Brandon Helfield	Transendothelial perforations and the sphere of influence of single site sonoporation	26
Inés Beekers	Cellular calcium during microbubble-mediated drug delivery revealed with combined confocal microscopy and	27
	Brandaris 128 imaging	
Silke Roovers	Liposome-loaded microbubbles and ultrasound enhance drug delivery in a 3D tumor spheroid	29
15.40 – 16.10	Intermission	
16.10 – 17.40	HIGH FRAME RATE IMAGING	<i>Chairpersons: Dan Adam and Mike Averkiou</i>
Olivier Couture	Brain ultrasonography, with and without contrast agents	32
Jason Voorneveld	High-volume-rate 4D echoPIV, in vitro results in a dynamic left ventricular phantom	35
Baptiste Heiles	Volumetric ultrafast Ultrasound Localisation Microscopy in vivo	37
Mengxing Tang	Towards Real-Time Super-Resolution Imaging: Fast Acoustic Wave Sparsely Activated Localization Microscopy.....	39
	(fast-AWSALM) using Octafluoropropane Nanodroplet	
Annemien van den Bosch	Left ventricular flow patterns: A new aspect elucidated by high-frame rate echocardiography	42
18.30 – 22.30	EVENING PROGRAM (Incl. Dinner buffet)	

24th EUROPEAN SYMPOSIUM ON ULTRASOUND CONTRAST IMAGING
17-18 JANUARY 2019, Rotterdam, The Netherlands

FRIDAY, 18 January 2019

07.30 – 08.00 Registration

07.30 – 09.00 MODERATED POSTER SESSIONS A and B

Oral program

09.00 – 10.10	BUBBLE TECHNOLOGY <i>Chairpersons: Michel Versluis and Rik Vos</i>	
Mark Borden	A study of radiation force effects in plane-wave transmission mode	45
Steven Wrenn	Influence of Electric Field on Acoustic Spectra of Nested Contrast Agents	46
Tim Segers	Tunable shell stiffness of phospholipid coated monodisperse microbubbles for non-invasive blood pressure measurement ...	48
David Maresca	Nonlinear X-Wave Ultrasound Imaging of Acoustic Biomolecules.....	51
10.10 – 10.45	Postersessions E and F	
10.45 – 11.00	Coffee	
11.00 – 12.30	CLINICAL CONTRAST IMAGING <i>Chairpersons: Pintong Huang and Arend Schinkel</i>	
Steven Feinstein	Vascular imaging: Biomarker of systemic atherosclerosis/inflammation	52
Misun Hwang	Quantitative CEUS Parameters for Detection of Neonatal Hypoxic Ischemic Injury	55
Norbert Lorenz	Intravenous CEUS in a pediatric setting - common and rare applications.....	56
Rogier Wildeboer	Prostate cancer localization based on multiparametric quantification of three-dimensional transrectal	58
	contrast-enhanced ultrasound.....	
Reinhard Kubale	Quantification of Endoleaks in EVAR.....	62
12.30 – 13.30	LUNCH	
13.30 – 15.15	COMPETITION: IMAGE GUIDED THERAPY <i>Chairpersons: Eleanor Stride and Nico de Jong</i>	
Ryan Jones	Ultrafast Three-Dimensional Microbubble Imaging Predicts Tissue Damage Following Nonthermal Brain Ablation.....	65
Sophie Morse	Single-cycle ultrasound drug delivery and passive acoustic mapping in the brain in vivo.....	67
Christophoros Mannaris	Predictive Real-Time Monitoring of Cavitation-Enhanced Immunotherapies by Passive Acoustic Mapping	69
Aditi Bellary	Perfusion-Guided Monitoring of Tumor Response to Sonoporation and Prediction of Liposomal Doxorubicin Uptake.....	71
	Using Microbubble Contrast Agents.....	
Dingjie Suo	Image-guided bubble-enhanced thermal ablation.....	73
Alexander Klibanov	Image-guided therapy with ultrasound and microbubbles: a tool to monitor in vivo events in real time.....	76
15.15 – 15.45	COEUR LECTURE <i>Chairperson: Peter Burns</i>	
Fabian Kiessling	The magnificent bubble: More than just air	78
16.00 – 16.10	DISCUSSION AND CONCLUSIONS	
16.00 – 16.10	CLOSING REMARKS <i>Nico de Jong</i>	
16.10	FAREWELL DRINKS	
	ANNOUNCEMENT OF THE WINNERS OF THE COMPETITION AND POSTER PRIZES	

Organised by: Nico de Jong, Folkert ten Cate, Rik Vos, Klazina Kooiman, Annemien van den Bosch, Arend Schinkel

Scientific board: Mike Averkiou, Mark Borden, Paolo Colonna, Olivier Couture, Beat Kaufmann, Eleanor Stride.

Poster sessions Thursday

Thursday 10.25-11.10		POSTER SESSION C: NEW DIRECTIONS TECHNOLOGY I Election by the audience	
C1)	Hongjian Chen	Sequence design for ultrasound imaging of polyvinyl alcohol microbubbles	80
C2)	Isabel Newsome	Assessment of the Superharmonic Response of Microbubble Contrast Agents for Acoustic Angiography	84
		As A Function of Microbubble Parameter	
C3)	Hugo Robert	Longitudinal Follow-up Analyses for Quantification of Contrast-Enhanced Ultrasound Imaging.....	86
C4)	Gonzalo Collado	Measuring the effect of Radiotherapeutic Radiation on Commercially Available Microbubbles	88
C5)	Ryan Hammond	Segmentation of stationary microbubbles: the foundation for targeted molecular imaging	90
C6)	John Hossack	Catheter-based, instrumented, flow focusing microfluidics device for production, counting and sizing of monodisperse	92
		microbubbles optimized for sonothrombolysis	
C7)	Jason Voorneveld	High frame rate echoPIV reveals the transient flow patterns in heart failure patients	94
C8)	Laura Peralta Pereira / Kirsten Christensen	Microbubble Contrast Agents for Coherent Multi-Transducer Ultrasound Imaging	96
C9)	Stefan Engelhard	Contrast-Enhanced Ultrasound for velocimetry in the diseased aorto-iliac tract	98
 Thursday 10.25-11.10		 POSTER SESSION D: NEW DIRECTIONS BIOLOGY/CLINICAL Election by the audience	
D1)	Christophe Mannaerts	Detection of significant prostate cancer: Contrast-enhanced ultrasound and multiparametric MRI-targeted	99
		biopsy in comparison with standard systematic biopsy	
D2)	Noboru Sasaki	Ultrasound-mediated intravesical chemotherapy: ex vivo evaluation	103
D3)	Roel Deckers	Ultrasound-sensitive liposomes for macromolecular drug delivery	105
D4)	Mindaugas Tamošiūnas	Cytotoxicity evaluation of sonodynamic therapy combined with microbubble contrast agent in vitro.....	107
D5)	Josanne de Maar	Bleomycin plus ultrasound and microbubbles to treat feline oral squamous cell carcinoma, as a model for human	108
		head and neck cancer, study design of the BUBBLEFISH Trial.....	
D6)	Matthew Copping	Drug delivery across the blood-brain barrier using short 300-kHz pulses of ultrasound and microbubbles.....	110
D7)	Rahul Misra	3D tumor spheroid model for in-vivo therapeutic predictions of Sonochemotherapy	112
D8)	Xucaï Chen	STAT3 Decoy Oligonucleotide-carrying Microbubbles with Pulsed Ultrasound for Enhanced Therapeutic Effect	114
		in Head and Neck Tumors	
D9)	Joop Kouijzer	Targeted microbubbles as a novel therapy for Staphylococcus aureus biofilms on cardiac devices	116
D10)	Charis Rousou	Therapeutic applications of ultrasound for retinal drug delivery using <i>in vitro</i> and <i>ex vivo</i> models	119

24th EUROPEAN SYMPOSIUM ON ULTRASOUND CONTRAST IMAGING
17-18 JANUARY 2019, Rotterdam, The Netherlands

FRIDAY, 18 January 2019

07.30 – 08.00 Registration

Poster sessions Friday

07.30 – 09.00

MODERATED POSTER SESSION A: BIOLOGY/CLINICAL *Moderator: Klazina Kooiman*

A1) Anne Rix	Contrast enhanced ultrasound treatment enhances tumor perfusion in breast cancer patients – first results	122
A2) Yue Song	Ultrasonic Induction of Apoptosis of Pancreatic Cancer through Activation of the Mechanosensitive Channel Piezo	123
A3) Ragnhild Haugse	Sonoporation efficacy and intracellular mechanisms: Cancer cells vs. healthy cells	124
A4) Gareth LuTheryn	Ultrasound Responsive Bioactive Microbubbles for the Eradication of Biofilms	126
A5) Tiffany Chan	Ultrasound-mediated delivery of DNA-coated gold nanoparticles across the blood-brain barrier	128
A6) Oliver Vince	The role of microbubble composition in sonoporation	130
A7) Filip Istvanic	Clinical Translation of Sonoreperfusion Therapy for Treatment of Microvascular Obstruction	132
A8) Liza Villanueva	Ultrasound-mediated antitumor efficacy of liposomal doxorubicin conjugated polymer microbubbles with reduced	135
	cardiotoxicity in a mouse model of soft tissue sarcoma	

07.30 – 09.00

MODERATED POSTER SESSION B: TECHNOLOGY *Moderator: Rik Vos*

B1) Kenneth Bader	Classification of histotripsy liquefaction in vitro with passive cavitation imaging	137
B2) Pauline Muleki-Seya	Ultrafast radial modulation imaging.....	140
B3) Emmanuel Gaud	The Bubble Counter: a unique device for the precise control of microfluidically formed monodisperse microbubbles.....	142
B4) Peiran Chen	Blood flow patterns analysis in the left ventricle by dynamic contrast-enhanced ultrasound at low frame rates.....	144
B5) Jemma Brown	High Dynamic Range Non-linear Ultrasound Imaging	148
B6) Jorinde Kortenbout	Repeatability of contrast enhanced ultrasound to measure cerebral blood flow using the middle cerebral artery	150
	as a reference	
B7) Luzhen Nie	Motion Compensation for High Frame-rate Contrast-enhanced Echocardiography using Diverging Waves.....	152
B8) Kirsten Christensen / Mengxing Tang	3D Super-Resolution Ultrasound Imaging In Vitro using a 2D Sparse Array.....	155

Friday 10.15-11.00

POSTER SESSION E: NEW DIRECTIONS UCA.....*Election by the audience*

E1) Ryo Suzuki	Development of a long-circulating ultrasound contrast agent	157
E2) Sophie Heymans	Investigation of PCDA-PFB nanodroplets for multimodal imaging and <i>in vivo</i> dosimetry of radiation therapy	158
E3) Amanda Pessoa	Microfluidic production of fibrin-targeted polymerized shell microbubbles.....	162
E4) Yosra Toumia	Graphene Hybrid Contrast Agents for Ultrasound and Multiplexed Photoacoustic Imaging	166
E5) Andrea Ancona	Removed from Document	169
E6) Fabio Domenici	Development of a polymeric contrast platforms.....	171
E7) Alexandra Kosareva	Targeting of vascular cell adhesion molecule 1 with an ultrasound contrast agent bearing Designed Ankyrin Repeat	175
	Proteins as targeting ligands.....	
E8) Shashank Sirsi	Formulation and Stability of Chemically-Crosslinked Microbubble Clusters: Novel Applications in Imaging and Therapy	177
E9) Simone Langeveld	Lipid coating structure and acoustic response of ultrasound contrast agents containing cholesterol	179
E10) Sara Ferri	Acoustically-stimulated nanodroplets for bone fracture repair	181

Friday 10.15-11.00

POSTER SESSION F: NEW DIRECTIONS TECHNOLOGY II*Election by the audience*

F1) Gihun Son	Level-set based numerical simulation of acoustic droplet vaporization	184
F2) Elliott Teston	Ultrasound precise vaporization threshold microdroplets	185
F3) Simona Turco	Pharmacokinetic analysis of targeted nanobubbles for quantitative assessment of PSMA expression in prostate cancer	188
F4) Catherine Paverd	Multi-Source Passive Acoustic Source Localisation for Diagnostic and Therapeutic Applications	192
F5) Cameron Smith	Spatiotemporal assessment of the cellular safety of cavitation-based therapies by passive acoustic mapping	194
F6) Roger Domingo-Roca	Microbubble – microvessel interactions and their influence on UmTDD: Simulation study.....	196
F7) Sara Keller	Real-time Cavitation Therapy Monitoring with a Clinical Scanner	199
F8) James Bezer	Single-bubble-induced elastic deformation of capillary-mimicking hydrogel channels	202
F9) Michael Calvisi	A novel model for an encapsulated microbubble based on transient network theory	204

Review of the clinical experience with enhancing blood-brain barrier permeability using focused ultrasound and microbubbles

Kullervo Hynynen

¹*Physical Sciences Platform, Sunnybrook Research Institute, Toronto, Ontario, Canada*

²*Department of Medical Biophysics, University of Toronto, Toronto, Ontario, Canada*

Corresponding author: khynynen@sri.utoronto.ca

Introduction

A large body of pre-clinical research has shown that an exposure of brain to focused ultrasound with ultrasound contrast agents has been found to be an effective tool for increasing the permeability of the blood-brain barrier to therapeutic and diagnostic molecules, particles and even cells^{1,2}. After approximately 15 years of research this method is now in an early phase of clinical testing. This talk will review the studies conducted at the Sunnybrook Research Institute and discusses the future potential based on the findings so far. The studies have been published in^{3,4}.

Methods

In our studies the patients head was shaved prior to fixing a stereotactic frame on the head. The patient was placed on the MRI table with a hemispherical ultrasound array with 1024 individually driven transmit elements operating at the frequency of 230 kHz (InSightec). The head was placed in the array and sealed with a flexible rubber membrane placed tightly around the head and fixed to the open end of the transducer array. The array was positioned such that the geometric focus of the hemisphere was in the middle of the targeted area. The space between the array and the head was filled with degassed water. The patient with the array was placed in the MRI scanner (3T,750, General Electric,) and targeting imaging was performed. The sonications were targeted based on the images. Approximately 30 s prior each sonication a bolus of ultrasound contrast agent with preformed microbubbles was injected IV (4µl per kg, Definity). The sonications consisted of either 3x3 or 2x2 sonications in a grid pattern with the spacing of 2.5 or 3mm. For each location a 300ms burst sonication (2 ms on, 28 ms off) were delivered before moving the next spot. After 2.7 s the sonication was repeated in each spot. This was continued for 50 s in the first patients and for 90 s in the later patients⁵. The applied power for each grid was determined by ramping the power during the first bolus injection while sonicating one of the grid points. The pressure level that showed a sudden increase on the sub-harmonic signal measured by hydrophones during the sonications was used as a calibration point and then the grid sonications conducted either at half-power or half-pressure value as described by O'Reilly et al.,⁶. After the sonications contrast enhanced MRI was used to evaluate the increase in the BBB permeability and T2- and T2*-weighted imaging to evaluate tissue damage. These images were repeated 24h later. Two studies have been conducted so far, one with tumour patients the other with patients with Alzheimer's disease. For further detail see^{3,4}.

Results

For all of the studies showed safe BBB permeability increase without any adverse events. The sonications were well tolerated without pain or discomfort except caused by the insertion of the metal pins into the skull to secure the frame and the discomfort caused by lying on the MRI table.

Conclusions

Focused ultrasound and microbubbles can be used to induce image-guided local BBB permeability increase for targeted drug delivery. We are currently conducting further studies with larger number of patients to establish potential therapeutic gains that may be induced by the method.

References

- [1]. Hynynen K, McDannold N, Vykhodtseva N, Jolesz FA. Noninvasive MRI-guided focal opening of blood brain barrier. 2001;320.
- [2]. Park J-W, Jung S, Junt T-Y, Lee M-C. Focused Ultrasound Surgery for the Treatment of Recurrent Anaplastic Astrocytoma: A Preliminary Report. In: Clement GT, McDannold NJ, Hynynen K, eds. New York: American Institute of Physics; 2006:238-240.
- [3]. Lipsman N, Meng Y, Bethune AJ et al. Blood-brain barrier opening in Alzheimer's disease using MR-guided focused ultrasound. Nat.Commun. 2018;9:2336-04529.
- [4]. Mainprize TG, Lipsman N, Huan Y, et al. Blood-Brain Barrier Opening in Primary Brain Tumors with Non-invasive MR-Guided Focused Ultrasound: A Clinical Safety and Feasibility Study. Scientific Reports 2018;(in print):
- [5]. Huang Y, Alkins R, Schwartz ML, Hynynen K. Opening the Blood-Brain Barrier with MR Imaging-guided Focused Ultrasound: Preclinical Testing on a Trans-Human Skull Porcine Model. Radiology. 2016;152:154.
- [6]. O'Reilly MA, Hynynen K. Blood-brain barrier: real-time feedback-controlled focused ultrasound disruption by using an acoustic emissions-based controller. Radiology. 2012;263(1):96-106.

Augmenting radiotherapy with ultrasound-sensitive microbubbles

John R. Eisenbrey,¹ Lauren J. Delaney,¹ Sriharsha Gummadi,^{1,2} Corinne E. Wessner,¹ Priscilla Machado,¹ Andrej Lyshchik,¹ Patrick O’Kane,¹ Jesse Civan,³ Allison Tan,¹ Flemming Forsberg,¹ Colette M. Shaw¹

¹*Department of Radiology, Thomas Jefferson University, Philadelphia, USA*

²*Department of Surgery, Lankenau Medical Center, Wynnewood, USA*

³*Department of Medicine, Division of Gastroenterology and Hepatology, Thomas Jefferson University, Philadelphia, USA*

Corresponding author: john.eisenbrey@jefferson.edu

Introduction

The use of radioembolization has been shown to be successful for the treatment and downstaging of hepatocellular carcinoma as well as liver metastases. When performing radioembolization, glass beads filled with radioactive isotope yttrium-90 (Y-90) are locally distributed within the tumor arterial blood supply via a transarterial catheter. The local beta emissions from Y-90 have been shown to provide a therapeutic benefit of a 25-60% increased response on modified response evaluation criteria in solid tumors (mRECIST) and a 13 month disease progression free survival.

Ultrasound-triggered microbubble destruction (UTMD) has been demonstrated to temporarily alter both cellular and vascular permeability, making it a potential tool for improving localized drug delivery. Importantly, localized microbubble destruction has recently been shown to sensitize tissue to radiotherapy by inducing vascular endothelial-cell apoptosis [1-3]. In an orthotopic HCC model in nude rats, our group has demonstrated significant tumor radio-sensitization of HCC using UTMD without further compromising liver function [4]. We hypothesize that localized UTMD within the tumor vasculature will sensitize tissue to radiation after the placement of Y-90 beads, thereby improving patient outcomes. This work will present recent data from an ongoing pilot clinical trial using localized UTMD to improve HCC response to radioembolization.

Methods

As part of an Institutional Review Board and Food and Drug Administration approved study, patients scheduled for radioembolization of HCC provided informed consents before being randomized to receive Y-90 radioembolization alone (control group) or radioembolization combined with UTMD exams 2-6 hours, 7 days, and 14 days post radioembolization to sensitize malignant tissue to localized Y-90. For patients in the experimental group, a flash destruction-replenishment technique was used to induce microbubble cavitation within the tumour vasculature. Five millilitres of activated Optison (GE Healthcare, Princeton NJ, USA) was suspended in 50 ml of saline and infused through an 18 to 20 gauge angiocatheter placed in a peripheral arm vein at a rate of 120 ml/hour. Imaging was performed using an S3000 HELX scanner with a C6-1 probe (Siemens Healthineers, MountView CA, USA). After confirmation of contrast-enhancement within the mass, a series of flash-replenishment sequences was generated to destroy microbubbles within the imaging plane. With the patient temporarily halting respiration, 4 second UTMD pulses were initiated (MI = 1.13 at 1.5 MHz, transmitting 2.3 μ s pulses at a pulse repetition frequency of 100 Hz), followed by nonlinear imaging of contrast replenishment at lower intensity using Cadence Pulse Sequencing (MI = 0.06) for 10 seconds. Following patient respiration, this sequence was repeated at multiple imaging planes throughout the tumour and then repeated throughout the entire tumour volume for the duration of the infusion (UTMD performed in 20-30 sequences).

The safety of UTMD was evaluated by monitoring patient physiological data (temperature, heart rate, and blood pressure) immediately before and after UTMD and by changes in liver function 1 month post treatment. Treatment response was determined using time to required next treatment (TTNT) and

mRECIST criteria at 3-4 month follow up (evaluated by two radiologists in consensus blinded to the group allocation).

Results

To date, 16 patients have been enrolled in this ongoing study. One month blood work has been collected on 13 patients and follow up imaging completed in 12 patients. In total, one adverse event has been repeated in the UTMD + radioembolization group (fatigue) and one in the radioembolization alone group (fatigue). In patients receiving UTMD, no statistically significant differences in heart rate, body temperature, or systolic and diastolic pressures were observed over the course of bubble therapy ($p > 0.18$). When comparing blood work at 1 month, no significant differences in changes in bilirubin, white blood cell count, creatinine, aspartate transaminase or alanine aminotransferase were observed between the two groups ($p > 0.17$) indicating UTMD does not contribute to additional damage to the healthy liver.

Using mRECIST to evaluate tumoral response, 75% of patients in the control group (Y-90 radioembolization alone) have shown stable disease, while 25% have demonstrated partial response on cross-sectional imaging follow up. Within the experimental group (UTMD + radioembolization), 14% of patients have shown stable disease, 57% have shown partial response and 29% of patients have shown complete response on imaging follow up. These improvements in tumour control also appear to translate to improved patient outcomes. While longer term follow up continues, patients receiving UTMD + radioembolization have also demonstrated longer TTNT (Hazard Ratio = 4.6, $p=0.13$). Similarly, patient survival also appears to improve with 86% of patients receiving UTMD + radioembolization living at least 3 months post treatment, but only 50% of patients receiving radioembolization alone survived this long.

Conclusions

Ultrasound-triggered microbubble destruction appears safe in patients with HCC being treated with radioembolization. In addition, early results indicate UTMD successfully sensitizes the tumor to radiation, thereby improving both tumoral response and longer term patient outcomes.

References

- [1]. Al-Mahrouki AA, Iradji S, Tyan TT, Czarnota GJ. Cellular characterization of ultrasound-stimulated microbubble radiation enhancement in a prostate cancer xenograft model. *Dis Model Mech* 7:363-7, 2014.
- [2]. Czarnota GJ, Karshafian R, Burns, PN, et al. Tumor radiation response enhancement by acoustical stimulation of the vasculature. *Proc Natl Acad Sci USA* 109:E2033-41, 2012.
- [3]. Tran WT, Iradji S, Sofroni E, et al. Microbubble and ultrasound radioenhancement of bladder cancer. *Br J Cancer* 107:469-76, 2012.
- [4]. Daecher A, Stanczak M, Liu JB, Zhang J, Du S, Forsberg F, Leeper DB, Eisenbrey JR. Localized microbubble cavitation-based antivasular therapy for improving HCC treatment response to radiotherapy. *Cancer Letters* 411:100-5, 2017.

Peripheral flow augmentation mediated by microbubble cavitation from a programmable clinical matrix array transducer

O'Neil Mason¹, Paul S. Sheeran^{1,2}, Jeffry Powers², Brian P. Davidson³, J. Todd Belcik³,
Matthew Muller³, Jonathan R. Lindner^{1,3}

¹*Knight Cardiovascular Institute, Oregon Health & Science University, Portland, OR, USA*

²*Philips Healthcare, Bothell, WA, USA*

³*Oregon National Primate Research Center, Oregon Health & Science University, Portland, OR, USA*

Corresponding author: lindnerj@ohsu.edu

Introduction

The role of ultrasound (US) in therapeutic applications that leverage controlled cavitation of microbubbles (MB) has expanded substantially. In previous studies, the high shear environments produced by oscillating microbubbles has been shown to augment tissue blood flow in a highly localized response that is mediated by cellular release of ATP [1,2] and downstream release of vasodilators (NO, prostanoids). This academic/industry translational collaboration focused on optimizing acoustic transmit design for cavitation-mediated augmentation in perfusion with the clinical goal of using contrast-enhanced ultrasound (CEU) to treat ischemic peripheral artery disease. Biologic readouts for the study included both low-power CEU perfusion imaging and ATP release by optical imaging.

Methods

A commercial clinical imaging system (EPIQ, Philips Healthcare) was custom-programmed to deliver therapy pulses from a cardiac matrix array transducer (X5-1) at 1.3 MHz with a mechanical index (MI) of 1.3. Pulse duration was set to either 5 cycles, 40 cycles, or a sequence of eight 5 cycle pulses. The beam density was programmed over a total arc of 64 degrees in the lateral/axial plane and symmetrically centered at the transducer face. The therapy plane was programmed to have either 1, 2, or 4 degrees between each neighboring beam (line density of 65, 33 or 17); thereby producing a 3x3 matrix of line density and pulse duration. Transmit design was validated in 3D by hydrophone measurements paired with FieldII ultrasound simulations.

Wild-type C57B1/6 mice between 10-20 weeks of age were studied. A subset of these mice had undergone unilateral inflow arterial ligation to create a model of chronic limb ischemia (approximately 20% reduction in resting flow and 30% reduction in flux rate). A jugular vein was cannulated for administration of MBs and materials for ATP optical imaging. The mid-portion of the muscle on the proximal left hindlimb was placed at a 4cm focal depth relative to the X5-1 transducer face. An intravenous bolus of 2x10⁸ lipid-shelled decafluorobutane MBs was administered over a period of 1 minute and therapeutic ultrasound pulses applied over a total of 10 minutes with 5 s intervals between each "frame" of lines.

CEU perfusion imaging of the proximal hindlimb exposed to high-power CEU and the contralateral control limb was performed immediately after therapy with a 15L8 linear array on a Siemens Sequoia 512 according to previously established protocols. The resulting data were analyzed offline using custom software and fit to a mono-exponential curve describing intensity as a function of microvascular blood volume and rate constant. In vivo optical imaging was performed within 10 min after the completion of therapy using a luminescent assay for ATP release using luciferase (I.V.) and d-luciferin (I.P.).

Results

The custom-programmed clinical imaging system was capable of delivering a highly focused spatially-patterned sequence of therapeutic pulses with a mechanical index between 0.03 and 3.44. In non-ischemic mice, after 10 minute exposure to cavitation at an MI of 1.3 and line densities of either 33 or 65 lines,

microvascular perfusion was approximately 4-fold higher in the ultrasound-exposed versus contralateral limb irrespective of the pulse duration (5-cycles, 8×5cycles, 40 cycles). At a lower line density (17 lines), perfusion in the limb undergoing cavitation increased incrementally from 5-cycles to 8×5cycles to 40 cycles, and again was 4-fold higher at 40-cycles compared to the contralateral limb. On optical imaging, ATP was several hundred to several thousand times higher in the ultrasound-exposed versus control limb. Greater degrees of ATP release were found for longer pulse duration, even at higher line density, indicating a saturation effect where once ATP release reaches a certain level, further flow augmentation does not occur. In mice with limb ischemia, ten minutes of cavitation exposure using a 65-line density and a 8×5cycle pulse scheme rescued tissue ischemia; an effect that persisted at 24 hrs.

Conclusions

The results demonstrate that flow augmentation via ultrasound-mediated microbubble cavitation are influenced by basic transmit design functions including line density and pulse type/duration on a clinical imaging platform. At diagnostic ultrasound pressures, the use of high line density and long-pulse duration, whether segmented or continuous, results in the greatest ATP release and represents an optimal pulse design strategy for human translation. These parameters are able to resolve tissue ischemia for 24 hrs in pre-clinical models of peripheral artery disease.

References

- [1]. Belcik JT, Mott BH, Xie A, Zhao Y, Kim S, Lindner NJ, Ammi A, Linden JM, Lindner JR, Augmentation of limb perfusion and reversal of tissue ischemia produced by ultrasound-mediated microbubble cavitation, *Circ Cardiovasc Imaging*, 8(4): 1-9, 2015.
- [2]. Belcik JT, Davidson BP, Xie A, Wu MD, Yadava M, Liang S, Chon CR, Ammi A, Field J, Harmann L, Chilian WM, Linden JM, Lindner JR, Augmentation of muscle blood flow by ultrasound cavitation is mediated by ATP and purinergic signaling, *Circulation*, 135(13): 1-13, 2017.

Detecting pancreatic islet immune infiltration in pre-symptomatic type1 diabetes using sub-micron scale ultrasound contrast agents

Richard K.P. Benninger¹, David Ramirez¹, Agata Exner², Mark Borden³

¹Department of Bioengineering, University of Colorado Anschutz Medical campus, Aurora CO. USA.

²Department of Radiology, Case Western Reserve University, Cleveland, OH. USA

³Department of Mechanical Engineering, University of Colorado Boulder, Boulder CO. USA.

Corresponding author: richard.benninger@ucdenver.edu

Introduction

Type1 diabetes is a chronic disease in which immune cells infiltrate and destroy the clusters of insulin producing cells within the pancreas (insulinitis) , which leads to loss of glucose homeostasis and requirement for lifelong exogenous insulin therapy. Detecting this ongoing insulinitis and decline in insulin producing cells, particularly during the pre-symptomatic stage prior to diabetes onset, would allow therapeutic intervention to prevent diabetes. One promising approach has been measuring the uptake of magnetic nanoparticles, as measured using MRI. However ultrasound modalities provide much greater cost-effectiveness and wide-spread deployment, with high spatial and temporal resolution. We have previously utilized ablation-reperfusion measurements with microbubbles to detect signatures of local inflammation within the pancreas [1]. Here we describe the application of sub-micron sized bubbles or phase change agents for detecting immune infiltration within the islet, for diagnosis of pre-symptomatic type1 diabetes.

Methods

Sub-micron sized ‘nanobubbles’ were synthesized by the Exner lab, as published in [2], and included formulations with rhodamine fluorophore incorporation. Sub-micron sized ‘nanodrops’ were synthesized as published in [3]: Size-isolated perfluorobutane microbubbles (3-5 μ m) were formed from a suspension of DPPC and DPSE-PEG2000, and then condensed into nanodrops under high pressure and low temperature (~2degC). Size distributions were measured using a multi-sizer (Beckman coulter). An open source ULA-OP system was used for acoustic characterization of nanodrops. A VEVO2100 (Visual Sonics) small animal ultrasound machine using a linear array transducer at 12MHz or 18MHz, was used in contrast mode for imaging bubble sub-harmonic signal kinetics in mouse models of type1 diabetes. Bubble formulations were infused IV. For nanobubble imaging, images in contrast mode were acquired over 3 minutes prior to infusion and continuously after infusion for up to 35 minutes. For nanodrop vaporization and imaging, images in contrast mode were acquired over 3 minutes prior to infusion, then upon infusion imaging was halted for 25minutes to avoid droplet vaporization while localization of nanodrops occurred. After this delay imaging and droplet vaporization resumed for 10minutes followed by flash-destruction. Histological analysis of bubble-fluorophore distribution within the pancreas was achieved by imaging rhodamine and autofluorescence within frozen tissue sections from the pancreas dissected 1h after bubble infusion.

Results

Following nanobubble infusion, sub-harmonic ‘contrast’ signal showed an initial increase followed by a slower additional increase within the pancreas of 10w NOD mice, which show significant insulinitis and develop diabetes within a few weeks of this time point. This slow increase in contrast signal plateaued at 25minutes after infusion and was specific to the pancreas, where there was no significant slow increase in contrast signal at 25minutes within the kidney (Fig.1). No such contrast signal increase at 25minutes post infusion was observed in the pancreas of immunodeficient NOD-Rag1ko mice which do not show insulinitis and do not develop diabetes. A small micron-sized component (~0.01% by number) was discovered

through microscopy based analysis. However infusing solely a micron sized component from the activated formulation, separated through centrifugation, led to no significant increase in contrast signal at 25minutes. Furthermore 3-4um or 1-2um size isolated microbubbles also did not show any contrast signal remaining at 25minutes post infusion.

Histological analysis following infusion of rhodamine-labelled nanobubbles showed significant accumulation of rhodamine fluorophore within the insulin producing cells of NOD mice that show significant immune infiltration. No significant rhodamine fluorophore was observed within the exocrine tissue compartment of the pancreas where there is no immune infiltration, nor was any rhodamine mice (Fig.2).

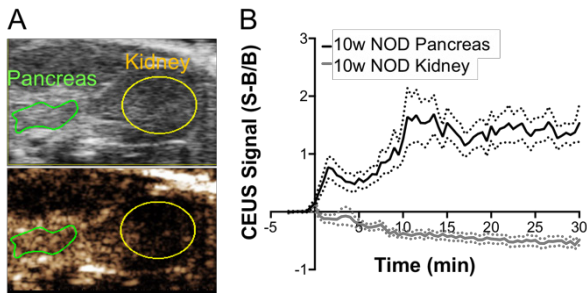


Figure 1. Nanobubble (NB) signal marking pancreas in NOD mice. A) B-mode and contrast mode images 20min following NB infusion. B) contrast signal over time in pancreas and kidney following NB infusion at t=0.

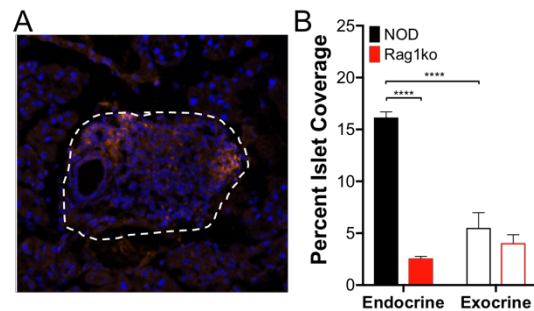


Figure 2. Nanobubble (NB) targeting of insulin producing cells. A) NB-fluorophore labelling of insulin producing cells (dashed line). B) proportion of insulin-producing cells (endocrine) and exocrine compartment labelled by NBs, in NOD mice and NOD-Rag1ko mice.

Following nanodrop infusion and 25minute delay, a significant contrast signal elevated within the pancreas after ~30seconds of imaging. This contrast signal remained elevated over ~10minutes consistent with residency within the tissue. No such contrast signal increased within the kidney, consistent with a lack of nanodrop accumulation and retention within the tissue. The subharmonic signal within the tissue indicated that nanodrops were spontaneously vaporizing during imaging. The signal increase within the pancreas was significantly reversed following flash destruction, consistent microbubbles destruction. In contrast, with continual imaging during infusion an increase in signal was observed within the pancreas and kidney, although this was again higher within the pancreas.

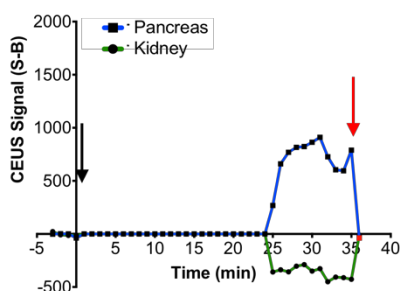


Figure 3. Contrast signal following nanodrop infusion (black arrow, t=0) and vaporization following imaging (t=25) within the pancreas (blue and kidney (green). Flash destruction (red arrow, t=35min) removes contrast signal in pancreas

Conclusions

Accumulation of sub-micron sized droplets or bubbles specifically within the islets within the pancreas provides a means to diagnose ongoing insulinitis and the pre-symptomatic stage of type1 diabetes. This can allow for early therapeutic intervention to prevent diabetes emergence. Furthermore these agents may provide vehicles for image guided drug delivery specifically to the islet for targeted therapeutic treatment.

References

- [1]. St Clair JR, Ramirez D, Passman S, Benninger RKP, Contrast-enhanced ultrasound measurement of pancreatic blood flow dynamics predicts type 1 diabetes progression in preclinical models. *Nature Communications*. 9:1742. 2018
- [2]. Hernandez C, Nieves L, de Leon AC, Advincula R, Exner AA. Role of Surface Tension in Gas Nanobubble Stability Under Ultrasound. *ACS Applied Material Interfaces*. 10:9949-9956. 2018
- [3]. Mountford PA, Sirsi SR, Borden MA. Condensation phase diagrams for lipid-coated perfluorobutane microbubbles. *Langmuir*. 30:6209-18 2014

A Novel Therapeutic Strategy using Ultrasound Mediated Microbubbles Destruction to Treat Colon Cancer in A Mouse Model

Yang Sun¹, Hang Zhou¹, Yue Song¹, Tongcun Huang¹, Pintong Huang^{1*}
¹ Department of Ultrasonography, the 2nd Affiliated Hospital of Zhejiang University
College of Medicine, Hangzhou, 310009 China;
*Corresponding author: huangpintong@zju.edu.cn

Introduction

In recent decades, cavitation of ultrasonic microbubbles (MBs) has been proposed as an innovative method for low-invasive and tissue-specific delivery of genes and drugs to the cancer tissues of interest. Based on the understanding of the ultrasound (US) mechanisms and previous studies, cavitation energy created by the collapse of the MBs has been considered as a key mechanism in intracellular delivery, however, high MBs concentrations and high acoustic power exposure can lead to undesirable side effects of local tissue damage and hemorrhage. In this study, we focus on investigating whether or not the side effects of ultrasound mediated MBs destruction (UMMD) might mechanically destroy the tumor cells and vessels within the tumors.

Methods

Six-week-old balb/c female nude mice were subcutaneously inoculated with HT29-GFP cells (HT29 cells labeled with green fluorescent dye) in axilla to establish a xenograft mouse model of colon carcinoma, which were randomly divided into 5 groups (n=10 each): group A (blank group): no treatment; group B (saline only); group C (saline + ultrasound exposure); group D (intravenous microbubbles only); and group E (intravenous microbubbles +ultrasound exposure). Treatment of each group was performed on days 20, 21, and 22 after inoculation. Tumor growth and metastatic spread were monitored by the whole-body fluorescent imaging, tumor volume growth and body weight growth curve were obtained as well. The mice were euthanized 30 days after treatment. Specimens of the tumor tissues were evaluated pathologically using light microscopy and transmission electron microscopy. Necrosis percentages, microvascular density and tumor cells damage of each tumor were assessed histologically.

Results

1. Tumor growth in group E (intravenous microbubbles +ultrasound exposure) was significantly decreased after four weeks post inoculation, compared with other control treatments ($P<0.05$);
2. The tumor weight at sacrifice in group E was significantly lower than that in other groups;
3. The intravenous microbubbles combined with ultrasound exposure treated mice showed significantly decreased expression levels of CD31.
4. The pathological changes of absence of nucleus membrane, chromatin condensation, mitochondrial vacuolation and hemorrhagic damage of microvessel were observed in the tumors of group E only, whereas these changes occurred rarely in other groups;
5. No metastatic lesion was found in any group throughout this study using whole-body fluorescent imaging, and the skin of the mouse in group E was intact after UMMD treatment.

Conclusions

Our results suggest that UMMD can be used as a promising novel therapeutic strategy to treat colon cancer.

Passively Mapped Cavitation-Enhanced Oncological Drug Delivery using Sub-Micron Gas-Stabilizing Solid Particles

Constantin C. Coussios¹, Christophoros Mannaris¹, Prateek S. Katti^{1,2,3}, Catherine Paverd¹,
Alexander Martin¹, Claudia Hill¹, Jamie Wallis¹, Cameron A.B. Smith¹,
Cliff Rowe⁴, Michael Gray¹, Joanna Hester³, Christian Coviello⁴, Robert Carlisle¹

¹Biomedical Ultrasonics, Biotherapy & Biopharmaceuticals Laboratory (BUBBL)
Institute of Biomedical Engineering, University of Oxford, Oxford, UK

²Center for Interventional Oncology, National Institutes of Health, Bethesda, USA

³Nuffield Department of Surgical Science, University of Oxford, Oxford, UK

⁴OxSonics Ltd, Oxford, UK

Corresponding author: constantin.coussios@eng.ox.ac.uk

Introduction

Tumour physiology presents a formidable barrier to the delivery of current and emerging anticancer therapeutics, by virtue of the elevated intratumoural pressure, sparse vasculature and dense extracellular matrix. Several recent studies [1, 2] have demonstrated that ultrasound-mediated cavitation occurring simultaneously with the intratumoural or intravenous administration of unmodified therapeutic agents can significantly enhance their delivery, penetration, and distribution throughout the tumour.

With microstreaming hypothesized to be the dominant transport mechanism for drug delivery, the likely benefit of using sub-micron cavitation nucleation agents capable of extravasating alongside the therapeutic through the leaky tumour vasculature, rather than microbubbles confined to the blood pool, warrants investigation. The recent development of more sophisticated techniques for spatiotemporal characterization of cavitation activity also now makes it possible to modulate, monitor and control cavitation activity within tumours during drug delivery. Building on these recent advances, we investigate the impact that the nature, intensity, persistence, and spatial distribution of cavitation activity mediated either by microbubbles or by sub-micron gas-stabilizing solid particles has on the safety, delivery, and efficacy enhancement achieved across emerging therapeutic classes, including oncolytic viruses, antibodies and antibody-drug conjugates.

Methods

A new type of sub-micron cavitation nucleation agent was designed, developed, and produced by seed polymerization [3] to produce a hemispherical cup-shaped particle of mean diameter 480 nm and polydispersity index 0.1, stabilizing a single gas nanobubble of characteristic size 200 nm. Modelling, high-speed imaging (Brandaris, Univ. of Twente, the Netherlands) and passive cavitation detection techniques [4, 5] were first used *in vitro* to characterize and compare the type and persistence of cavitation activity and the cavitation thresholds produced by these agents relative to commercially available microbubble formulations (SonoVue[®], Bracco) over a range of therapeutic ultrasound frequencies (0.5-3.3 MHz) and pressure amplitudes (0-3 MPa). The effect of sustained cavitation on the functional and structural patency of four different agents, doxorubicin, cetuximab, adenovirus and vaccinia virus were also assessed *in vitro*.

For *in vivo* investigations, a dual-transducer setup was developed consisting of two orthogonal 0.5 MHz therapeutic ultrasound transducers (Sonic Concepts, USA), each embedding a coaxial 128-element diagnostic array (L11-5v, Verasonics, USA). Real-time implementation of Passive Acoustic Mapping (PAM) using the Robust Capon Beamformer [6] made it possible to map the nature, intensity, location and extent of cavitation activity within tumours in real time with a spatial resolution of 400 microns axially and transversely, well below the 3mm x 3mm spot size of the the therapeutic ultrasound focus.

A variety of both xenograft (ZR-75-1, SKOV3, HEPG2) and syngeneic (CT26, EMT6) subcutaneous tumour models were used to investigate cavitation-enhanced delivery and subsequent therapeutic efficacy

of uncapped and capped oncolytic viruses, therapeutic antibodies, antibody-drug conjugates as well as free and encapsulated mRNAs. Delivery quantification was performed both *in vivo* using an IVIS Spectrum Imaging system (Perkin Elmer, Waltham, MA, USA) and following tumour excision using appropriate analytical methods including qPCR and ELISA. Both H&E and immunohistochemistry staining were used to ascertain the safety of the ultrasound intervention and drug distribution relative to blood vessels.

Results

In vitro passive cavitation detection demonstrated that, above a frequency-dependent cavitation threshold, the polymeric cups exclusively produced broadband acoustic emissions associated with inertial cavitation, in contrast to microbubbles which also exhibited narrowband emissions indicative of non-inertial cavitation. For comparable initial gas volume fractions and ultrasound exposure parameters chosen to induce broadband emissions (0.5 MHz, 1.5 MPa, 5% duty cycle), polymeric cups were able to produce sustained inertial cavitation for at least 10 minutes, whilst cavitation activity from microbubbles subsided after 2 minutes. No measurable change in the structural integrity and activity of small molecules, antibodies, and viruses could be detected even after 10 minutes of sustained inertial cavitation activity [7].

In vivo, co-administration of an oncolytic virus with microbubbles driven either in a non-inertial or inertial cavitation regime at constant input acoustic energy demonstrated limited enhancement of delivery and penetration unless sustained inertial cavitation occurred. Under identical ultrasound exposure conditions designed to cause inertial cavitation, use of microbubbles resulted in a 5-fold enhancement of transgene expression, whilst polymeric cups delivered a 50-fold enhancement relative to passive delivery [8]. This enhanced delivery was associated with significantly improved distribution and persistence of cavitation activity throughout the tumour, as monitored by PAM, resulting in a 1000-10000-fold increase in transgene expression due to the virus by day 5 following administration. Histological and immunohistochemical examination of excised tumours demonstrated extensive extravasation of the polymeric cups throughout the tumour, and an absence of direct cellular damage within the tumour mass. Subsequent studies identified comparable enhancements in the delivery and distribution of therapeutic antibodies and antibody-drug conjugates, associated with a significantly enhanced survival in groups treated with sustained and well-spatially-distributed inertial cavitation.

Conclusions

The combination of sub-micron cavitation nucleation agents capable of crossing leaky tumour vasculature with improved Passive Acoustic Mapping and control of cavitation activity during treatment enables safe, sustained and spatially distributed microstreaming throughout the tumour mass for enhanced convective transport and efficacy of unmodified next-generation anticancer therapeutics.

References

- [1]. Bazan-Peregrino, M., et al., Cavitation-enhanced delivery of a replicating oncolytic adenovirus to tumors using focused ultrasound. *J Control Release*, 2013. 169(1-2): p. 40-7.
- [2]. Carlisle, R., et al., Enhanced Tumor Uptake and Penetration of Virotherapy Using Polymer Stealthing and Focused Ultrasound. *Jnci-Journal of the National Cancer Institute*, 2013. 105(22): p. 1701-1710.
- [3]. Kwan, J.J., et al., Ultrasound-Propelled Nanocups for Drug Delivery. *Small*, 2015. 11(39): p. 5305-5314.
- [4]. Kwan, J., et al., Ultrahigh-Speed Dynamics of Micrometer-Scale Inertial Cavitation from Nanoparticles. *Physical Review Applied*, 2016. 6(4): p. 044004.
- [5]. Kwan, J., et al., Ultrasound-induced inertial cavitation from gas-stabilizing nanoparticles. *Physical Review E*, 2015. 92(2): p. 023019.
- [6]. Coviello, C., et al., Passive acoustic mapping utilizing optimal beamforming in ultrasound therapy monitoring. *The Journal of the Acoustical Society of America*, 2015. 137(5): p. 2573-2585.
- [7]. Myers, R., et al., Ultrasound-mediated cavitation does not decrease the activity of small molecule, antibody or viral-based medicines. *International Journal of Nanomedicine*, 2018. 13: p. 337-349.
- [8]. Myers, R., et al., Polymeric Cups for Cavitation-mediated Delivery of Oncolytic Vaccinia Virus. *Mol Ther*, 2016. 24(9): p. 1627-33.

Nab-paclitaxel delivery with microbubble-assisted ultrasound in human pancreatic cancer mouse model

Jean-Michel Escoffre¹, Diane Bressand², Anthony Novell², Alban Girault³, William Raoul³, Gaëlle Fromont^{4,5}, Thierry Lecomte^{2,3}, Ayache Bouakaz¹

¹iBrain UMR 1253, Université de Tours, Inserm, Tours, France; ²Departement of Gastro-enterology and Digestive Cancerology, University Hospital CHU, Tours, France; ³Université de Tours, EA7501 GICC, Team PATCH, Tours, France; ⁴Department of Pathological Anatomy and Cytology, University Hospital CHU, Tours, France; ⁵UMR 1069, Nutrition, Croissance, Cancer, Université de Tours, Inserm, Tours, France

Corresponding author: jean-michel.escoffre@univ-tours.fr

Introduction

The combination of microbubbles (MBs) and ultrasound is an emerging method for non-invasive and targeted enhancement of anticancer drugs uptake. This method showed to increase local drug extravasation in tumor tissue while reducing the systemic adverse side effects in various tumor models. The present study aims into evaluating the therapeutic efficacy of 2 types of microbubbles both *in-vitro* and *in-vivo* for Nab-paclitaxel delivery in a pancreatic tumor model.

Methods

In-vitro, a suspension of human pancreatic cancer BxPC3 cells was exposed to ultrasound (1 MHz, 100 μ s PRP, 40% DC, 400 kPa, 30s) in presence of QA3216 microbubbles or BR38[®] with a ratio of 5:1 MBs/cell. Nab-paclitaxel was injected at a concentration of 2.5 ng/mL. Seventy-two hours later, MTT assay was performed to assess cell viability.

In-vivo, BxPC3 tumors were induced by a subcutaneous injection of 5×10^6 cells in both flanks of male nude mouse. When the tumor was significantly perfused, the treatment was initiated as follows: an i.v. administration of Nab-paclitaxel (5 or 20 mg/kg) followed by an i.v. administration of MBs (70 μ L). Ultrasound insonation as applied using a single-element transducer at 1 MHz (100 μ s PRP, 40% DC, 400 kPa, 3 mins). The therapeutic efficacy was determined by monitoring the tumor growth using ultrasound imaging. Quality of life of the animals was also assessed.

Results

In-vitro Nab-paclitaxel delivery - The exposure of BxPC-3 cells to ultrasound at 400 kPa in presence of BR38[®] and QA3216 MBs did not modify the cell viability in comparison to the control condition. As shown in **Figure 1**, when the BxPC-3 cells were treated with 2.5 ng/mL of Nab-paclitaxel only, the cell viability significantly decreased compared to the control condition without Nab-paclitaxel ($61 \pm 2\%$ vs $100 \pm 0.1\%$; $p < 0.001$). BxPC-3 cells treated with Nab-paclitaxel at 2.5 ng/mL and exposed to ultrasound in the presence of BR38[®] MBs showed a slight but non-significant decrease in their viability in comparison to the treatment with Nab-paclitaxel alone. However, the combination of ultrasound with QA3216 MBs and 2.5 ng/mL of Nab-paclitaxel induced a significant decrease in the cell viability compared to the Nab-paclitaxel treatment alone ($50 \pm 2\%$ vs $61 \pm 2\%$; $p < 0.01$). All together, these results clearly show that QA3216 MBs in combination with ultrasound and Nab-paclitaxel induced a higher cell mortality compared to Nab-paclitaxel treatment alone.

In-vivo Nab-paclitaxel delivery - Subcutaneous pancreatic cancer tumors were treated with either QA3216 MB-assisted ultrasound on its own, or i.v. administration of Nab-paclitaxel at 5 or 20 mg/kg on its own, or by i.v. injection of Nab-paclitaxel at 5 or 20 mg/kg in combination with MB-assisted ultrasound and a co-administration of either QA3216 or BR38[®] MBs. The therapeutic effectiveness of Nab-paclitaxel delivery with or without MBs and ultrasound was monitored using anatomical ultrasound imaging every day before starting the treatment session.

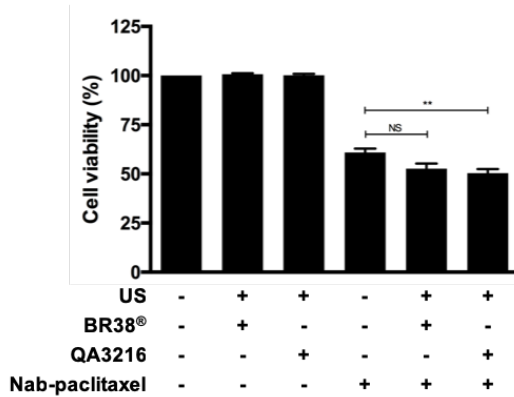


Figure 1. *In-vitro* Nab-paclitaxel delivery using MB-assisted ultrasound. Data expressed as mean \pm SEM were calculated from five independent experiments. Significance was defined as $p < 0.05$ (* $p < 0.05$; ** $p < 0.01$; Mann-Whitney test).

As shown in **Figure 2A**, QA3216 MBs in combination with ultrasound application did not affect the tumor growth compared to the control group. In addition, the repeated i.v. administration of one Nab-paclitaxel dose at 5 mg/kg on its own led to a significant decrease in the tumor volume compared to control group (**Figures 2A and 2B**; $p < 0.05$). Furthermore, the combination of Nab-paclitaxel at 5 mg/kg with QA3216 MBs and ultrasound induced a significant and additional decrease in tumor volume after three treatments in comparison to Nab-paclitaxel treatment alone (**Figure 2B**; $p < 0.05$). As shown in **Figure 2C**, the repeated i.v. injection of one Nab-paclitaxel dose at 20 mg/kg on its own resulted in a significant decrease in tumor volume compared to the repeated delivery of a Nab-paclitaxel dose at 5 mg/kg on its own or in combination with QA3216 MB-assisted ultrasound ($p < 0.01$). The repeated delivery of one Nab-paclitaxel dose at 20 mg/kg in combination with QA3216 MB-assisted ultrasound led to an additional and statistically significant decrease in tumor volume compared to the 20 mg/kg Nab-paclitaxel treatment alone (**Figure 2C**; * $p < 0.05$).

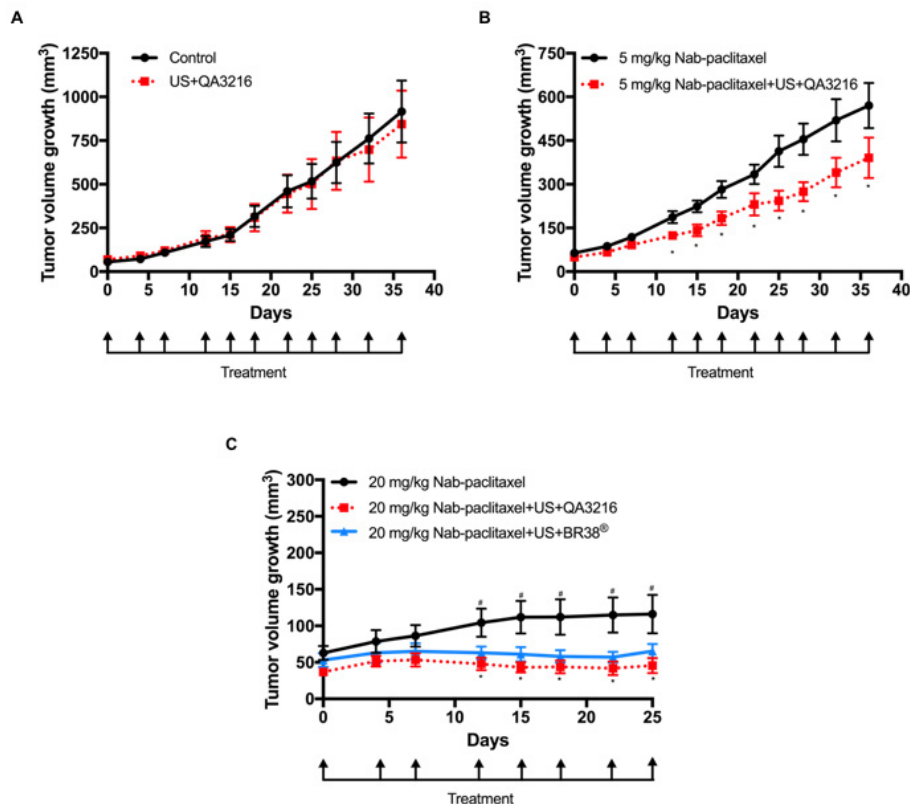


Figure 2. *In-vivo* Nab-paclitaxel delivery using microbubble-assisted ultrasound. Data expressed as mean \pm SEM were calculated from 8-10 tumors. Significance was defined as $p < 0.05$ (* $p < 0.05$; # $p < 0.05$; Mann-Whitney test).

However, the combination of this chemotherapy with BR38[®] MB-assisted ultrasound resulted in a significant reduction in tumor volume until the 8th treatment in comparison to the 20 mg/kg Nab-paclitaxel treatment alone (**Figure 2C**; [#] $p < 0.05$). No significant difference in the therapeutic effectiveness was observed between both types of MBs for the repeated delivery of one Nab-paclitaxel dose at 20 mg/kg (**Figure 2C**). These results suggest that MB-assisted ultrasound potentiate the therapeutic effectiveness of one Nab-paclitaxel dose at 5 mg/kg as well as at 20 mg/kg in subcutaneous pancreatic cancer mouse model.

Conclusions

The present study showed that Nab-paclitaxel delivery using MB-assisted ultrasound enhanced the *in-vitro* and *in-vivo* therapeutic effectiveness of paclitaxel in comparison with Nab-paclitaxel treatment on its own.

Acknowledgement

We acknowledge Bracco Research Geneva for supplying the microbubbles, Prof. Caroli-Bosc (CHRU d'Angers, France) and Dr. Tournamille (CHRU de Tours, France). This work was supported by the CANCECEN (DB), FARE-SNFGE and Cancéropôle Grand-Ouest (TL), Ligue Contre le Cancer and Inserm (AB) grants.

Visualizing and Quantifying Sonoporation-induced Nanocarrier Translocation across the Blood-Brain Barrier

Twan Lammers^{1,2,3}, Jan-Niklas May¹, Susanne Golombek¹, Fabian Kiessling¹

¹*Dept. of Nanomedicine and Theranostics, Institute for Experimental Molecular Imaging, RWTH Aachen University Clinic, Aachen, Germany*

²*Dept. of Targeted Therapeutics, University of Twente, Enschede, The Netherlands*

³*Dept. of Pharmaceutics, Utrecht University, Utrecht, The Netherlands*

Corresponding author: tlammers@ukaachen.de

Introduction

Efficient and safe drug delivery across the blood-brain barrier (BBB) remains to be one of the major challenges of biomedical and (nano-) pharmaceutical research. The combination of ultrasound (US) and microbubbles (MB) can be employed to induce a temporarily and spatially controlled opening of the BBB, allowing for the extravasation of drugs and delivery systems out of the blood vessels into the central nervous system (CNS) [1]. This phenomenon, which is traditionally referred to as sonoporation, has also already been successfully employed to improve drug delivery to tumors [2], even in patients [3]. In the present study, we employed multimodal and multiscale optical imaging, and clinically relevant PHPMA polymers (10 nm) and PEGylated liposomes (100 nm), to systematically study the potential of sonoporation for shuttling nanocarriers of different sizes across the BBB (see Figure 1).

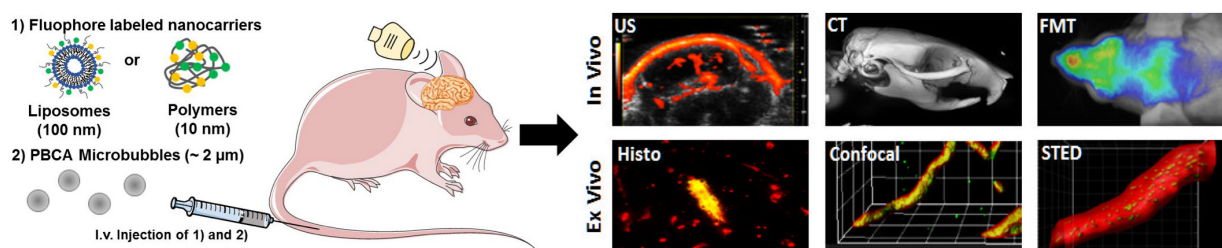


Figure 1: Study design. Fluorophore-labeled PHPMA polymers (10 nm) and PEGylated liposomes (100 nm) were intravenously co-injected together with PBCA-based polymeric microbubbles, and the BBB was subsequently opened via the application of transcranial ultrasound for 10 minutes. The accumulation and penetration of the two differently sized nanocarriers was visualized and quantified using multiple in vivo and ex vivo imaging techniques.

Methods

CD-1 nude mice were intravenously co-injected with MB and with pHPMA polymers (10 nm) or PEGylated liposomes (100 nm). Both nanocarriers were labeled with Alexa488 and Cy7. Upon US treatment (16 MHz, 50% power, mechanical index 0.45, continuously applied for 10 minutes), the accumulation of the two prototypic drug delivery systems was longitudinally monitored using hybrid computed tomography-fluorescence molecular tomography (CT-FMT [4]). Prior to sacrifice, rhodamine-labeled lectin was intravenously injected to counter-stain functional blood vessels in the brain. Ex vivo analysis included fluorescence reflectance imaging (FRI), fluorescence microscopy (FM), confocal microscopy (CM), multiphoton microscopy (MPM) and stimulated emission depletion (STED) nanoscopy. Possible side effects and the overall extent of BBB opening were also investigated, using H&E and immunofluorescence (with antibodies directed against extravasated endogenous IgG).

Results

In all experimental groups, the efficiency of sonoporation-induced BBB opening was confirmed via a significant increase in the number of blood vessels positive for IgG extravasation. H&E stainings showed that sonoporation, at the US times and settings employed, did not induce obvious brain damage. While the extravasation and penetration of the 10 nm-sized polymeric drug carriers upon sonoporation was clearly visible with all optical imaging modalities, clear-cut extravasation of 100 nm liposomes could only be observed using highly sensitive and high-resolution techniques, such as CM, MPM and STED nanoscopy. Using software tools to quantify the penetration depth of fluorescent drugs and drug delivery systems out of the blood vessels into the brain [5], we found that 10 nm polymers penetrated significantly more efficiently and much deeper into the CNS upon sonoporation than 100 nm liposomes.

Conclusions

Sonoporation can be employed to efficiently and safely open up the BBB, allowing 10 and 100 nm-sized drug delivery systems to translocate across the endothelium and penetrate into the brain. Multimodal and multiscale optical imaging shows that small nanocarrier materials accumulate more efficiently and penetrate deeper into the brain upon sonoporation than large nanocarriers. These findings contribute to development of novel therapeutic and theranostic approaches to improve the treatment of brain tumors and CNS disorders.

References

- [1]. Dasgupta A, Liu M, Ojha T, Storm G, Kiessling F, Lammers T. Ultrasound-mediated drug delivery to the brain: principles, progress and prospects. *Drug Discov Today* 20: 41-48 (2016)
- [2]. Theek B, Baues M, Ojha T, Möckel D, Steitz J, van Bloois L, Storm G, Kiessling F, Lammers T. Sonoporation enhances liposome accumulation and penetration in tumors with low EPR. *J Control Release* 231: 77-85 (2016)
- [3]. Dimceviski G, Kotopoulis S, Bjanec T, Hoem D, Schjott J, Gjertsen B, Biermann M, Molven A, Sorbye H, McCormack E, Postema M, Gilja O. A human clinical trial using ultrasound and microbubbles to enhance gemcitabine treatment of inoperable pancreatic cancer. *J Control Release* 243: 172-181 (2016)
- [4]. Kunjachan S, Gremse F, Theek B, Koczera P, Pola R, Pechar M, Etrych T, Ulbrich K, Storm G, Kiessling F, Lammers T. Non-invasive optical imaging of nanomedicine biodistribution. *ACS Nano* 7: 252-262 (2013)
- [5]. Lammers T, Koczera P, Fokong S, Gremse F, Storm G, Van Zandvoort M, Kiessling F. Theranostic USPIO-loaded microbubbles for mediating and monitoring blood-brain barrier permeation. *Adv Funct Mater* 25: 36-43

Acknowledgements

The authors gratefully acknowledge financial support by the European Research Council (ERC-StG 309495: NeoNaNo) and the European Commission (EU-ERANET-EuroNanoMed-III: NSC4DIPG).

Ultrasound-targeted microbubble cavitation with sodium nitrite synergistically enhances nitric oxide production and microvascular perfusion

Gary Yu¹, Filip Istvanic¹, Xucai Chen¹, Mehdi Nourai², John Pacella¹

¹Center for Ultrasound Molecular Imaging and Therapeutics, Department of Medicine, University of Pittsburgh, Pittsburgh, PA, USA

²Division of Pulmonary, Allergy, and Critical Care Medicine, Department of Medicine, University of Pittsburgh, Pittsburgh, PA, USA

Corresponding author: pacellajj@upmc.edu

Introduction

Contemporary therapy for acute myocardial infarction (AMI) is reperfusion through percutaneous coronary intervention (PCI). Despite the fact that reperfusion times have decreased over the past two decades, congestive heart failure (CHF) following AMI is on the rise. This is due to microvascular obstruction (MVO), which prevents complete reperfusion and limits myocardial salvage. MVO occurs due to mechanical obstruction of the microcirculation by atherothrombotic debris, inflammation, and a milieu of oxidative stress, accentuated by a lack of nitric oxide (NO) bioavailability. Replenishing NO would provide numerous therapeutic pathways for MVO, owing to its multilevel role in various signaling pathways which ultimately decrease tissue reactive oxygen species, platelet adhesion, inflammatory cell adhesion, and microvascular permeability. Therefore, specifically increasing NO bioavailability is attractive for mitigating both the occurrence and sequelae of MVO.

We have previously demonstrated that ultrasound-targeted microbubble cavitation (UTMC) can be used to relieve MVO through mechanical mechanisms. More recently, we have also discovered that UTMC increases endogenous NO bioavailability, and this contributes significantly to the efficacy of UTMC. Another means to increase NO bioavailability can be achieved through administration of exogenous NO in the form of nitrite (NO₂⁻), which can also be leveraged for therapeutic benefit. Accordingly, in the present study, we sought to determine whether co-administration of IV nitrite during UTMC would further enhance the important therapeutic bioeffects of UTMC for the treatment of MVO.

Methods

Lipid-encapsulated perfluorocarbon microbubbles (average radius of 3±1µm) were synthesized in-house. In rats weighing 275±20 g, synthesized microbubbles were delivered first-pass to the treatment hindlimb through the femoral artery for UTMC therapy (2×10⁸ microbubbles/mL at 1.5 mL/hr for 2 min) while Definity contrast microbubbles were infused through the internal jugular vein post-treatment for contrast perfusion imaging (2 mL/hr). In select groups, sodium nitrite (4 mg/kg) and/or N-Nitro-L-arginine methyl ester (LNAME), an endothelial nitric oxide synthase (eNOS) inhibitor (10 mg/kg), were given 5 minutes prior to UTMC therapy, where LNAME was used to determine whether changes in NO were attributable to eNOS.

Therapeutic ultrasound was delivered using a 1 MHz single-element transducer for 2 minutes (5 ms bursts every 3 seconds at a peak negative pressure of 1.5 MPa). Following UTMC, burst-replenishment perfusion imaging was performed in contrast pulse sequence mode (Siemens Sequoia, 7 MHz, framerate of 5 Hz and mechanical index of 0.2, with a burst of 5 frames at mechanical index of 1.9) at 3, 6, 10, and 30 minutes. Recorded cine-loops were analysed in MATLAB for microvascular blood volume. Additionally, an NO catheter probe was placed in the treated hindlimb musculature for real-time NO concentration measurements over the 30-minute observation period.

For microvascular blood volume, the effects of UTMC, nitrite, and LNAME were evaluated using a mixed effect model (with restricted maximum likelihood). Statistical significance was taken at $p < 0.0005$ for all comparisons accounting for multiple comparisons using a Bonferroni correction.

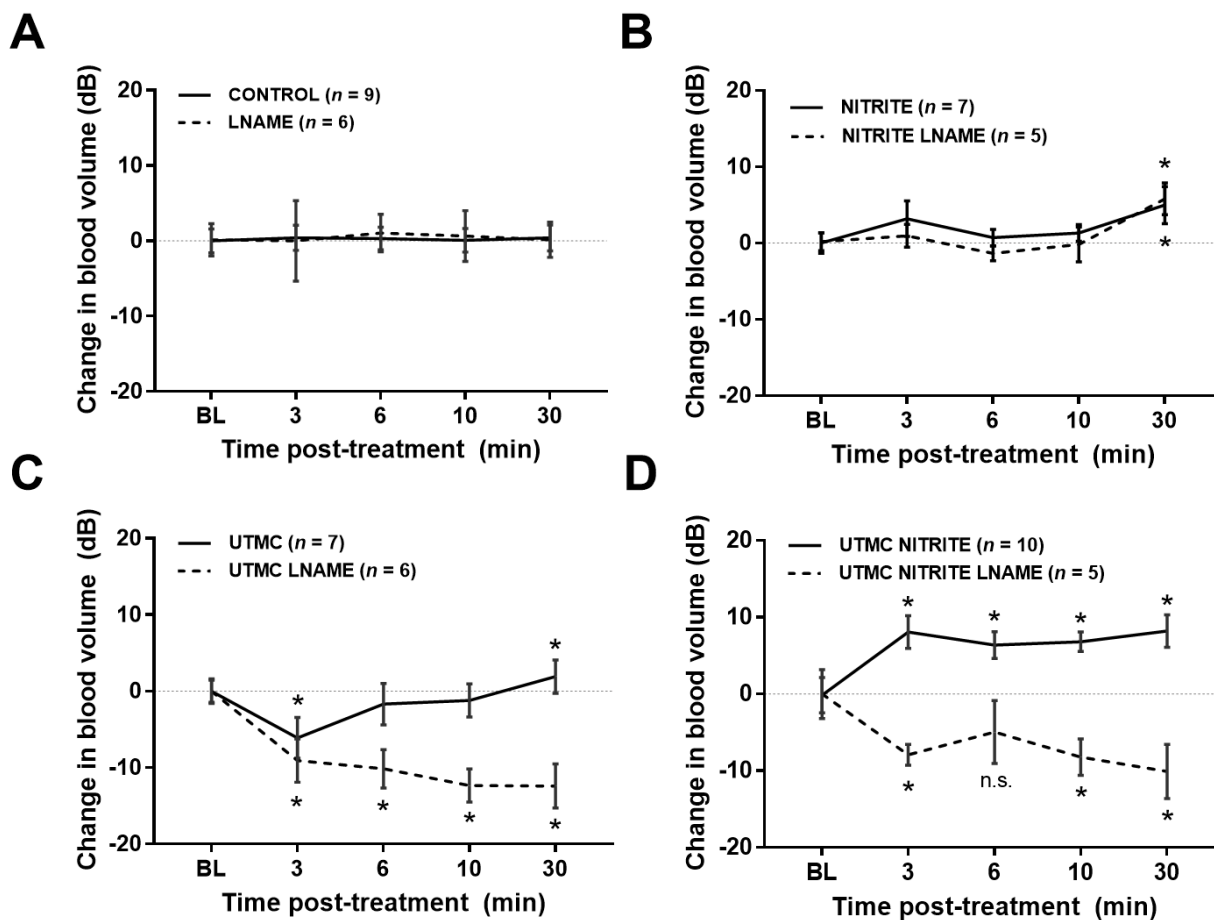


Figure 1: Change in microvascular blood volume from baseline (BL). Points and error bars indicate mean and standard deviation. All combinations of UTMC therapy, nitrite (4 mg/kg), and LNAME (10 mg/kg) are shown. Asterisk indicates statistical significance ($p < 0.0005$) from control group relative to baseline.

Results

The factors of UTMC, nitrite, and LNAME all had significant interaction effects. The LNAME only (no UTMC) condition compared to the control condition (no treatment) showed no significant changes in blood volume at any time point relative to baseline (Fig. 1A). Nitrite with and without LNAME significantly increased blood volume at 30 minutes (Fig. 1B). UTMC alone showed a transient decrease in blood volume at 3 minutes, which recovered at 6 minutes and increased above baseline at 30 minutes (Fig. 1C). Addition of LNAME to UTMC therapy ablated the return of blood volume to baseline, resulting in significantly decreased blood volume beyond UTMC alone at 6, 10, and 30 minutes. Combined UTMC and nitrite therapy resulted in significantly increased blood volume at all time points above no treatment, and above UTMC only therapy at 3, 6, and 10 minutes (Fig. 1D). Although UTMC with both nitrite and LNAME showed similarly decreased blood volumes as UTMC LNAME at 3, 10, and 30 minutes, blood volume temporarily returned to baseline levels at 6 minutes in the UTMC nitrite LNAME group.

UTMC and nitrite had a synergistic effect on increasing NO compared to either UTMC or nitrite alone (Fig. 2A). LNAME administration with UTMC and nitrite reversed this effect, resulting in decreasing NO concentration (Figure 2B). This suggests some eNOS dependency. However, when comparing UTMC and LNAME to UTMC with both nitrite and LNAME, the decrease in NO concentration in the latter is blunted, suggesting eNOS independent effects of nitrite as well.

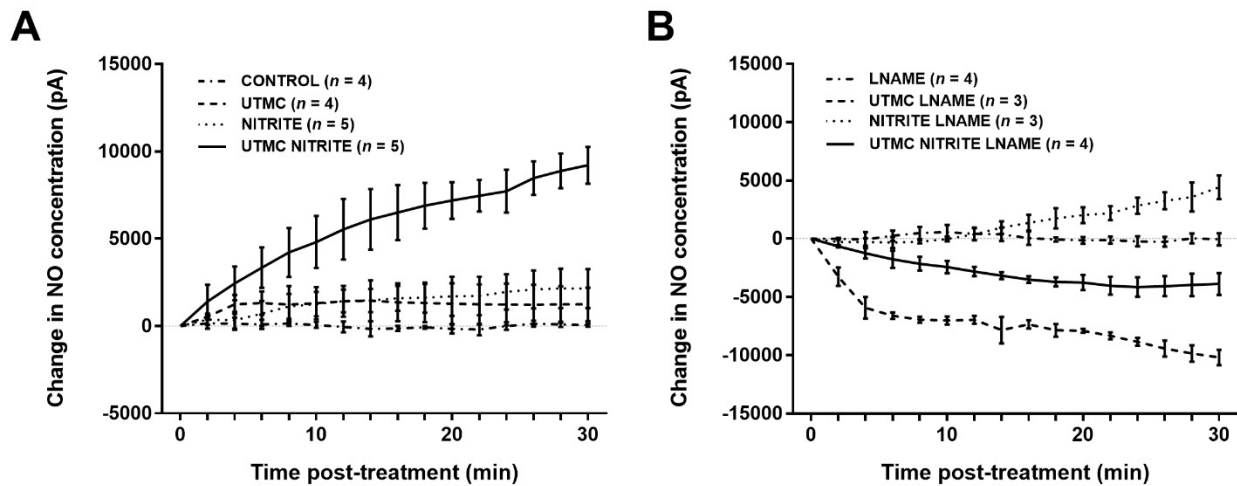


Figure 2: Change in NO concentration over the 30-minute observation interval measured by intramuscular catheter probe. Points and error bars indicate mean and standard deviation.

Conclusions

We have shown that the combination therapy of UTMC and nitrite results in synergistic improvement of microvascular blood volume and NO concentration in a healthy rat hindlimb model. We have also shown that nitrite alone has eNOS independent effects on increasing blood volume. However, the synergy with UTMC therapy is partially dependent on eNOS activity as evidenced by the blunting of this effect with LNAME administration. These findings provide mechanistic insight into UTMC therapy and provide another means to enhance its efficacy through increasing NO bioavailability.

Clinical Outcome of Patients Treated With Diagnostic Ultrasound Guided High Mechanical Index Impulses To Restore Microvascular Flow in ST segment Elevation Acute Myocardial Infarction

Wilson Mathias, Jr.¹, Jeane M. Tsutsui¹, Bruno G. Tavares¹, Agostina Fava², Miguel O. D. Aguiar¹, Bruno C. Borges¹, Mucio T. Oliveira Jr.¹, Alexandre Soeiro¹, Jose C. Nicolau¹, Henrique B. Ribeiro¹, Hsu Pochiang¹, João C. N. Sbrano¹, Abdul Morad², Andrew Goldsweig², Carlos E. Rochitte¹, Bernardo B.C. Lopes¹, José A. F. Ramirez, Roberto Kalil Filho¹, Thomas R. Porter².

*Heart Institute (InCor) - University of São Paulo, Medical School, São Paulo, Brazil¹
University of Nebraska Medical Center, Omaha, NE²*

Background

Preliminary clinical studies have confirmed that high mechanical index (MI) impulses from a diagnostic ultrasound transducer (DUS) during an intravenous microbubble infusion may be effective in restoring epicardial and microvascular flow in acute ST segment elevation myocardial infarction (STEMI).

Objective

The objective of this study was to prospectively test the effect of DUS high MI impulses in first-time STEMI patients.

Methods

From May 2014 through August 2018 patients arriving with their first STEMI were prospectively randomized to either DUS-guided high MI impulses during an intravenous Definity infusion prior to, and for 20 minutes following, emergent percutaneous coronary intervention (PCI, n=50), or control group that received low MI imaging only (n=50). Initial epicardial recanalization rates prior to emergent PCI, pre-discharge left ventricular (LV) infarct size (IS;% of LV mass) and microvascular obstruction (MVO) by cardiac magnetic resonance imaging (CMRI), as well as one and six month measurements of systolic function (LVEF) outcomes were compared.

Results

Median door to dilation times were 72 + 15 minutes in the high MI group versus 82 + 26 minutes in the low MI group. Angiographic recanalization prior to PCI was 48% with high MI versus 20% with low MI (p<0.001). %IS by CMRI was significantly lower (p=0.03) as was extent of MVO (p=0.02) in high MI treated patients. Mean MVO size in LAD infarctions was 5+6 grams in the high MI group (n=23) versus 12+13 grams in controls (n=25; p=0.02). LVEF was not different before treatment, but increased significantly post PCI only in the high MI group (p<0.0001) and remained significantly higher at one month although not at six months.

Conclusions

High MI DUS impulses during a microbubble infusion lead to early recanalization, reduced area of MVO, and improvement in systolic function at one month post STEMI.

Key Words: Ultrasound, acute myocardial infarction, microbubbles

Reference

[1]. Mathias W Jr., Tsutsui JM, Porter TR. Diagnostic ultrasound impulses improve microvascular flow in patients with STEMI receiving intravenous microbubbles. *J Am Coll Cardiol* 2016; 68:2031-32.

A Multi-Bubble Sonoluminescence in Sonodynamic Therapy

Estelle Beguin¹, Shamit Shrivastava¹, Nikolai V. Dezhkunov², Anthony P. McHale³, John F Callan³ and Eleanor Stride¹

¹ *Department of Engineering Science, Institute of Biomedical Engineering, University of Oxford, Oxford OX3 7DQ, United Kingdom*

² *BSUIR, P. Brovka St. 6, 220013 Minsk, Belarus*

³ *Biomedical Sciences Research Institute, University of Ulster, Coleraine, Northern Ireland, UK.
Corresponding author: eleanor.stride@eng.ox.ac.uk*

Introduction

Multi-bubble sonoluminescence is a process whereby bubbles oscillating under ultrasound excitation emit light.¹ In previous studies, the exposure conditions associated with sonoluminescence have been very different from those used in biomedical applications of ultrasound. However, with the increasing use of microbubbles in both ultrasound imaging and therapy, and studies showing sonoluminescence at ultrasound frequencies in the MHz range²⁻⁸, there is a need to understand whether these extreme events can in fact occur in tissue.

Methods

Three different formulations of microbubbles containing either oxygen or Sulphur hexafluoride were insonated using a 1 MHz US transducer at an intensity of 3.5 W/cm², 30% duty cycle, and 100 Hz pulse repetition frequency for 2 minutes. Sonoluminescence events were recorded via photomultiplier tubes (PMTs). One PMT and a passive cavitation detector (PCD) were used simultaneously to correlate the overall light and acoustic emissions. When the sonoluminescence was investigated at specific wavelengths, a second PMT was used as a reference to normalise the filtered PMT signal. Phospholipid-coated microbubbles of 2.1 ± 1.6 μm in size were used, corresponding to the agents used in ultrasound imaging and therapy. These were also diluted to 5×10^5 microbubble/mL in deionised water to reflect the concentrations that would be present in the human blood stream following injection.

Results

The results provide direct evidence that phospholipid-coated microbubbles produce broadband sonoluminescence when exposed to low-intensity 1 MHz ultrasound at 37°C (Figure 1). Furthermore, upon the addition of a photosensitiser, a reduction in the optical emissions at the absorption wavelength of the drug was observed.

Conclusions

These findings provide an explanation for the mechanism underlying sonodynamic therapy (SDT), wherein photosensitisers can be locally activated by exposure to ultrasound.⁴ As sound can be focused at greater tissue depths than light, this offers an opportunity for utilising photosensitive drugs to treat a wider range of lesions than is currently possible.

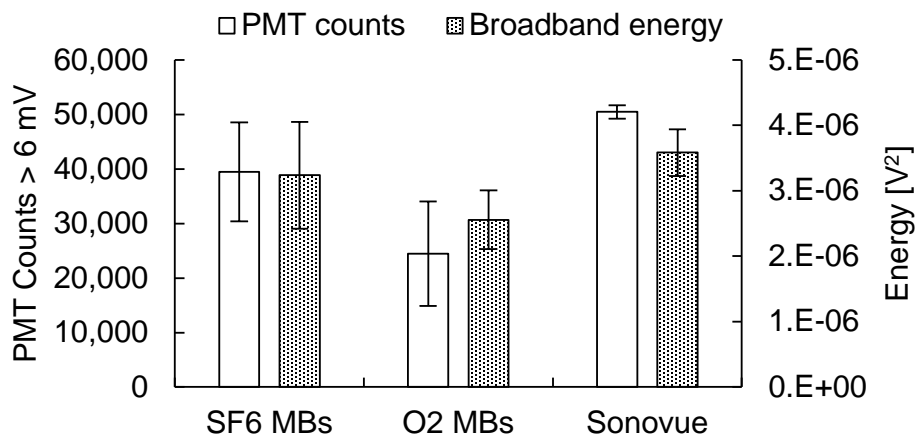


Figure 1 Measurements of sonoluminescence and acoustic emissions of three lipid-coated microbubble formulations excited at 1 MHz, of 3.5 W/cm², 30% duty cycle, and 100 Hz pulse repetition frequency for 2 minutes (n=3 runs of 1000 acquisitions each, error bars indicate standard deviations). Total photomultiplier tube (PMT) counts above 6 mV in amplitude and integrated broadband energy are displayed.

References

- [1]. Suslick, K. S., Doktycz, S. J. & Flint, E. B. On the origin of sonoluminescence and sonochemistry. *Ultrasonics* 28, 280–290 (1990).
- [2]. Srinivasan, D. & Holroyd, L. V. Optical spectrum of the sonoluminescence emitted by cavitated water. *J. Appl. Phys.* 32, 449–453 (1961).
- [3]. Pickworth, M. J. W., Dendy, P. P., Leighton, T. G. & Walton, A. J. Studies of the cavitation effects of clinical ultrasound by sonoluminescence: 2. Thresholds for sonoluminescence from a therapeutic ultrasound beam and the effect of temperature and duty cycle. *Phys. Med. Biol.* 33, 1249–1260 (1988).
- [4]. Umemura, S., Yumita, N., Nishigaki, R. & Umemura, K. Mechanism of Cell Damage by Ultrasound in Combination with Hematoporphyrin. *Japanese J. Cancer Res.* 81, 962–966 (1990).
- [5]. Ciuti, P., Dezhkunov, N. V., Iernetti, G. & Kulak, A. I. Cavitation phenomena in pulse modulated ultrasound fields. *Ultrasonics* 36, 569–574 (1998).
- [6]. Beckett, M. A. & Hua, I. Impact of ultrasonic frequency on aqueous sonoluminescence and sonochemistry. *J. Phys. Chem. A* 105, 3796–3802 (2001).
- [7]. Weninger, K. R., Camara, C. G. & Putterman, S. J. Observation of bubble dynamics within luminescent cavitation clouds: Sonoluminescence at the nano-scale. *Phys. Rev. E - Stat. Physics, Plasmas, Fluids, Relat. Interdiscip. Top.* 63, 1–7 (2001).
- [8]. Giuntini, F. et al. Insight into ultrasound-mediated reactive oxygen species generation by various metal-porphyrin complexes. *Free Radic. Biol. Med.* 121, 190–201 (2018).

Lipid-shelled microbubbles for ultrasound-triggered release of Xenon for neuroprotection

Christy K. Holland¹, Himanshu Shekhar¹, Arunkumar Palaniappan¹, Tao Peng², Melanie R. Moody², Kevin J. Haworth¹, Shaoling Huang², David D. McPherson²

¹Department of Internal Medicine, Division of Cardiovascular Health and Disease, University of Cincinnati, Cincinnati, OH, USA

²Department of Internal Medicine, Division of Cardiovascular Medicine, University of Texas Health Science Center-Houston, Houston, TX, USA

Corresponding author: Christy.Holland@uc.edu

Introduction

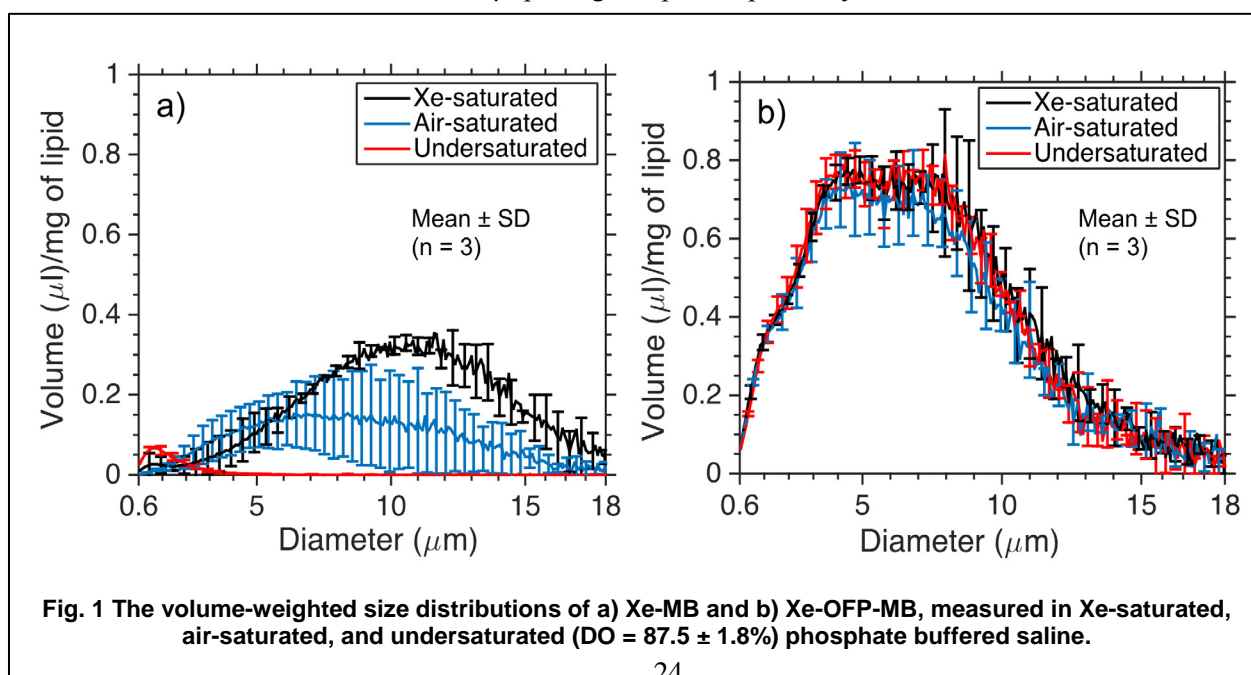
Ischemia-reperfusion-induced neurological injury is a primary cause of stroke disability. Xenon (Xe), a bioactive gas, has potential as an effective and nontoxic neuroprotectant for the treatment of ischemic stroke [1]. When Xe is delivered by inhalation, high concentrations (50–70% v/v) are necessary to obtain a therapeutic effect, but limit the fraction of inspired oxygen. The goal of this work was to develop Xe-loaded lipid-shelled microbubbles for site-specific release of Xe upon pulsed ultrasound exposure in the neurovasculature. By encapsulating Xe into micron-sized lipid-shelled microbubbles, the therapeutic gas can be shuttled through the vasculature until delivery is triggered by ultrasound exposure.

Methods

Xenon-loaded microbubbles (Xe-MBs) were synthesized by high-shear mixing of 1 ml lipid dispersion (9:1 molar ratio of DSPC and 18:0 PEG2000 PE) in a vial that contained 1 ml Xe, or a combination of Xe and octofluoropropane (OFP) (90/10% v/v), in the headspace. The size distribution and acoustic attenuation spectrum of XeMB were measured using a Coulter counter and broadband attenuation spectroscopy (over 2 – 25 MHz), respectively [2]. Gas chromatography–mass spectrometry was employed to measure Xe dose.[3, 4].

Results

Co-encapsulation of OFP increased the total volume, attenuation coefficient, and stability of microbubbles, shown in Figures 1 and 2. Triggered release of the Xenon gas payload was demonstrated with 6-MHz duplex Doppler and 220-kHz pulsed ultrasound. The total Xe dose in Xe-MB and Xe-OFP-MB were 111.8 ± 16.1 and 127.0 ± 29.1 μl per mg of lipid, respectively, shown in Table 1.



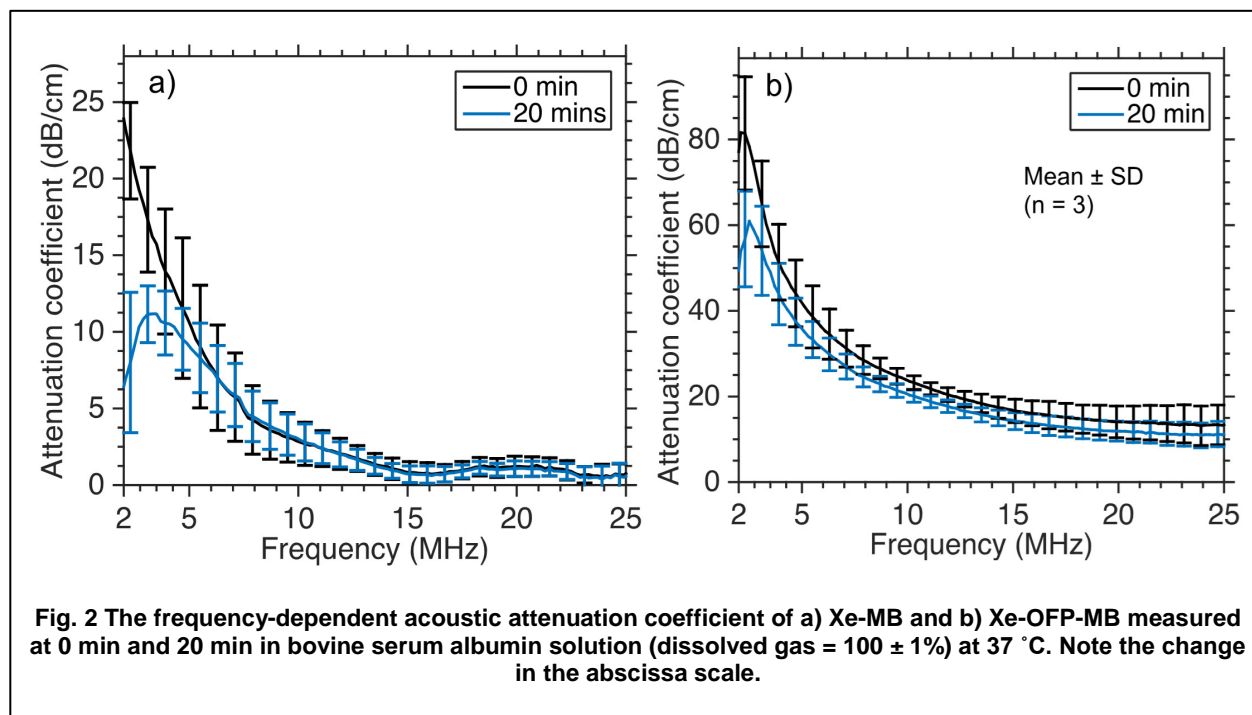


Table 1. Xenon concentration measured using gas chromatography/mass spectrometry. Four vials were tested for Xe-MB and Xe-OFP-MB, and 3 vials for Xe-saturated and Xe-OFP-saturated solution.

Agent	[Xe] (ml/ml of solution)*
Xe-MB	111.8 ± 16.1
Xe-OFP-MB	127.0 ± 29.1
Xe-saturated solution	34.1 ± 2.7 (with sonication)
	57.6 ± 4.2 (8 hr equilibration)
Xe-OFP-saturated solution	39.1 ± 2.1 (with sonication)
	51.0 ± 3.3 (8 hr equilibration)

* The Xenon dose per ml of solution is equivalent to the Xe dose per mg of lipid.

Conclusions

These results motivate the continued investigation of lipid-shelled microbubbles for ultrasound-triggered Xe delivery. Intravenous administration of microbubbles carrying a neuroprotective gas in combination with ultrasound exposure has potential as a novel noninvasive strategy for local therapeutic delivery to modulate the effects of cerebral ischemia.

References

- [1]. Britton GL, Kim H, Kee PH, Aronowski J, Holland CK, McPherson DD, Huang S-L, In vivo therapeutic gas delivery for neuroprotection with echogenic liposomes, *Circulation* 122:1578-1587, 2010.
- [2]. Raymond JL, Haworth KJ, Bader KB, et al. Broadband attenuation measurements of phospholipid-shelled ultrasound contrast agents. *Ultrasound Med Biol* 40:410-421, 2014.
- [3]. Holland CK, Palaniappan A, Shekhar H, Lipid-shelled microbubbles for ultrasound-triggered release of Xenon to treat stroke, *Neurotherapeutics* 15:823, 2018.
- [4]. Shekhar H, Palaniappan A, Peng T, Moody MR, Huang S, Haworth KJ, McPherson DD, Holland CK, Lipid-shelled microbubbles for ultrasound-triggered release of Xenon, *J Acoust Soc Am* 144:1851, 2018.

Transendothelial perforations and the sphere of influence of single-site sonoporation

Brandon L. Helfield^{1,2}, Xucai Chen², Simon Watkins³, Flordeliza Villanueva²

¹Physical Sciences Platform, Sunnybrook Research Institute, Toronto, Canada

²Centre for Ultrasound Molecular Imaging and Therapeutics, University of Pittsburgh, Pittsburgh, USA

³Department of Cell Biology, University of Pittsburgh, Pittsburgh, USA

Introduction

Ultrasound-stimulated microbubbles are emerging as targeted drug/gene delivery vehicles for the treatment of cancer and cardiovascular disease. The microbubble-cell interactions that facilitate therapeutic payload delivery across cell membranes and into cells outside the vasculature, and hence strategies to optimize this platform, remain poorly understood. The objective of this work is therefore to elucidate the biophysical context of reversible sonoporation by investigating the biophysics on a single-cell level; from plasma membrane perforation and repair to its association with cytoskeletal reorganization – mechanistic insight from which will help propel this platform towards the clinical area.

Methods

We examined the cellular biophysics resulting from ultrasound-triggered microbubble cavitation by employing acoustically-coupled live-cell 3D confocal microscopy during real-time sonoporation. Live-cell microscopy was performed within an environmentally controlled incubation chamber at 37°C with a Nikon A1 spectral confocal microscope ($\Delta z=1\ \mu\text{m}$, volume frame rate~0.13 fps). As microbubbles are confined to the vasculature, we first set out to examine endothelial plasma membrane perforation dynamics resulting from sonoporation ($n=12$). Individual phospholipid-encapsulated microbubbles laying adjacent to a cultured human umbilical vein endothelial cell (HUVEC) monolayer were insonicated with a single, 8-cycle pulse at 1 MHz, ranging in peak-negative pressures from 0.1-0.9 MPa ($MI = 0.1-0.9$). The endothelial cell membrane was fluorescently labeled with a novel fluorogen-activating protein and cell impermeant propidium iodide (PI) was diluted in the culture medium as a surrogate drug and sonoporation marker. As membrane dynamics are powered by cytoskeletal activity, a subset of experiments consisted of HUVECs co-labeled to visualize F-actin ($n=12$).

Results

We show for the first time that sonoporation generates transendothelial perforations (TEPs) that confer intracellular permeability only during their opening phase. The opening phase of TEPs (and thus membrane permeability) is an order of magnitude faster than its resealing phase ($p<0.001$), suggesting distinct biophysical origins between enhanced cellular versus vascular permeability. The extent of actin breaching and re-organization at the TEP site increases with TEP area and PI uptake ($p<0.001$). The perforation resealing phase is led by actin recruitment along the TEP perimeter and results in an actin-poor plasma membrane protrusion, suggesting membrane budding and shedding as a potential sonoporation healing mechanism.

Conclusions

While the opening of TEPs is largely a passive process, actin recruitment plays a significant role in the TEP resealing mechanism and occurs over much longer timescales (10-20 min), revealing the range of timescales associated with sonoporation for enhanced cellular and vascular permeability; for example applications aimed at site-specific endothelial gene delivery versus those focused on opening of the blood-brain barrier for drug delivery. This work contributes towards understanding the biophysical context of reversible sonoporation as a targeted drug/gene delivery platform, necessary for its clinical translation.

Cellular calcium during microbubble-mediated drug delivery revealed with combined confocal microscopy and Brandaris 128 imaging

Inés Beekers¹, Phoei Ying Tang¹, Merel Vegter¹, Frits Mastik¹, Robert Beurskens¹, Antonius F. W. van der Steen^{1,2}, Martin D. Verweij^{1,2}, Nico de Jong^{1,2}, Klazina Kooiman¹

¹Department of Biomedical Engineering, Erasmus MC, Rotterdam, the Netherlands

²Acoustical Wavefield Imaging, Delft University of Technology, Delft, the Netherlands

Corresponding author: d.beekers@erasmusmc.nl

Introduction

The vasculature is an important barrier hindering efficient drug delivery to diseased tissue. However, using lipid-coated microbubbles drug delivery can be locally enhanced. These microbubbles oscillate upon ultrasound insonification and thereby can permeabilize cell membranes (sonoporation), open cell-cell junctions, and stimulate endocytosis [1]. Nevertheless, if we want to control and optimize these drug delivery pathways we need to understand their underlying biological mechanisms. To achieve the nanometer and nanosecond resolution necessary to visualize the cellular effects and resolve microbubble oscillation, a unique optical imaging system was used consisting of the Brandaris 128 ultra-high speed camera [2] coupled to a custom build Nikon A1R confocal microscope. To unravel the underlying biological mechanisms, we monitored intracellular calcium (Ca_i^{2+}) fluctuations since Ca_i^{2+} plays a crucial role in membrane resealing, intercellular signaling, and opening of cell-cell junctions [3].

Methods

Human umbilical endothelial cells (HUVEC) were cultured to full confluency in a CLINICell [4] and lipid-coated microbubbles were targeted to the $\alpha_v\beta_3$ receptor expressed during angiogenesis. To unravel the underlying biological mechanisms, we monitored the cellular effect of single microbubbles ($n=138$) up to 4 min after ultrasound insonification (2 MHz, 100-250-400 kPa, 10 cycles). Drug delivery was assessed by evaluating sonoporation with Propidium Iodide (PI) and opening of cell-cell junctions with Cell Mask. Fluctuations of Ca_i^{2+} were simultaneously monitored with Fluo-4.

Results

The Ca_i^{2+} level remained stable when no pore formation was achieved. Sonoporated cells showed simultaneous PI uptake and increased Ca_i^{2+} levels. When the amount of PI uptake was low, the chance was higher for Ca_i^{2+} to return to its basal level, suggesting membrane resealing after sonoporation. When PI uptake was high, Ca_i^{2+} remained either elevated for >3 min or clustered into intracellular vesicles. A typical example of Ca_i^{2+} clustering and the corresponding microbubble oscillation is shown in Fig. 1A. Cells adjacent to a sonoporated cell showed a delayed Ca_i^{2+} increase, always returning to basal levels within 3 min. The microbubble excursion amplitude was significantly smaller when either Ca_i^{2+} remained stable or was elevated <3 min before returning to basal level ($p<0.01$, Fig. 1B). In addition, cell-cell junctions opened more often when Ca_i^{2+} remained elevated >3 min (35%) or clustered (78%) than when Ca_i^{2+} returned to basal levels (23%), as shown in Fig. 1C.

Conclusions

Using the state-of-the-art imaging system we can now unravel the missing link between microbubble oscillation and cellular response. Larger microbubble oscillation resulted in higher Ca_i^{2+} levels and eventually to irreversible Ca_i^{2+} uptake. We found a correlation between sonoporation, Ca_i^{2+} influx, and cell-cell opening. This suggests a clear relationship between the drug delivery pathways and cell recovery. Further understanding of these underlying mechanisms will aid the development of safe and efficient ultrasound-mediated drug delivery.

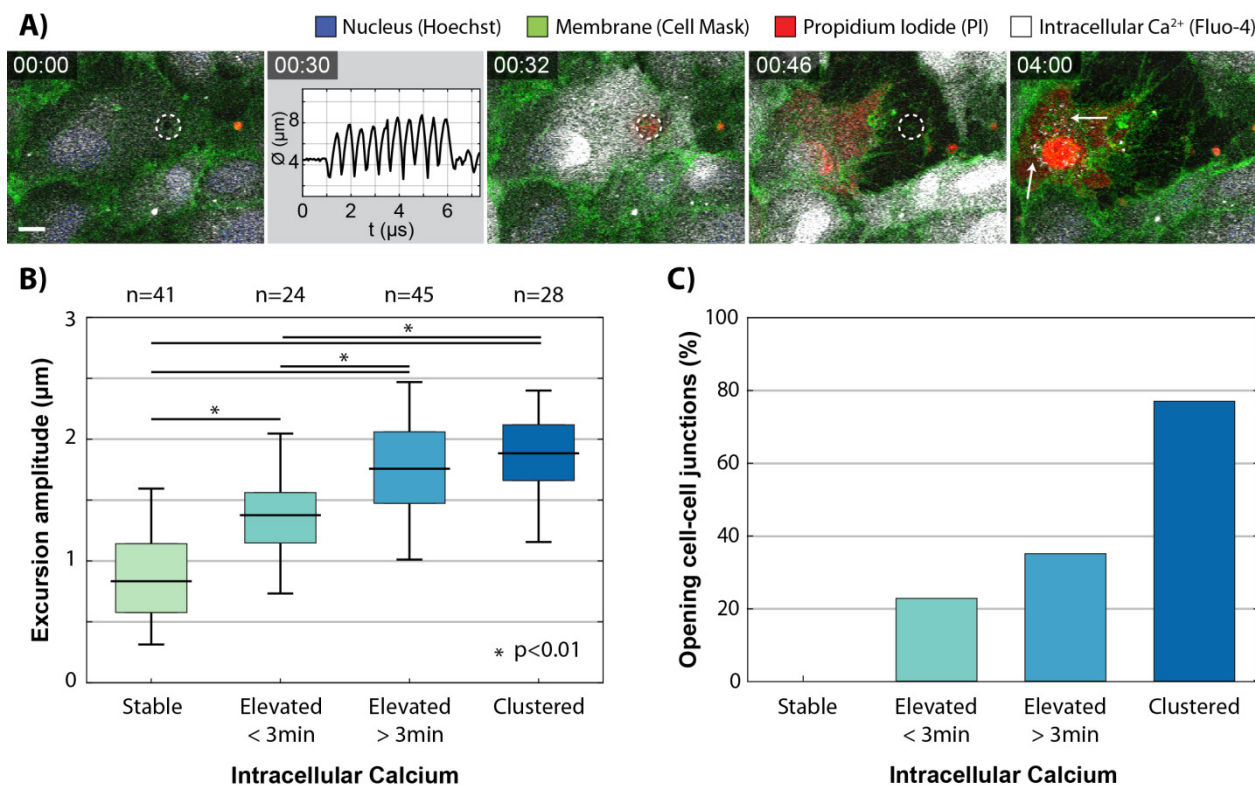


Fig. 1: A) Imaging time sequence with confocal microscopy before ultrasound, microbubble diameter (\varnothing) as recorded with the Brandaris 128, and confocal microscopy of the cellular response showing Ca_i²⁺ clustering into intracellular vesicles (arrows). Scale bar 10 μm . B) Microbubble excursion amplitude for each classification based on Ca_i²⁺ uptake. C) Occurrence of cell-cell junctions opening for each Ca_i²⁺ class.

Acknowledgements

The authors thank Michiel Manten and Geert Springeling from the Department of Biomedical Engineering, Thoraxcenter, Erasmus MC, the Netherlands and Nikon Instruments Europe for technical assistance.

References

- [1]. Kooiman K, Vos HJ, Versluis M, de Jong N, Acoustic behavior of microbubbles and implications for drug delivery, *Adv Drug Deliv Rev*, vol 72, pp 28-48, 2014.
- [2]. Chin CT, Lancée C, Brosboom J, Mastik F, Frijlink ME, de Jong N, Versluis M, Lohse D, Brandaris 128: A digital 25 million frames per second camera with 128 highly sensitive frames, *Rev Sci Instrum*, vol 74, no 12, pp 5026-5034, 2003.
- [3]. Qin P, Han T, Yu ACH, Xu L, Mechanistic understanding the bioeffects of ultrasound-driven microbubbles to enhance macromolecule delivery, *J Control Release*, vol 272, pp 169-181, 2018.
- [4]. Beekers I, van Rooij T, van der Steen AFW, de Jong N, Verweij MD, Kooiman K, Acoustic Characterization of the CLINICell for Ultrasound Contrast Agent Studies, *IEEE Trans Ultrason Ferroelectr Freq Control*, 2018, DOI:10.1109/TUFFC.2018.2881724

Liposome-loaded microbubbles and ultrasound enhance drug delivery in a 3D tumor spheroid

S. Roovers¹, De Cock I.¹, Lajoinie G.², Prakash J.², Versluis M.², De Smedt S.C.¹, Lentacker I.¹

¹*Ghent Research Group on Nanomedicines, Ghent University, Ghent, Belgium*

²*MIRA institute, University of Twente, Enschede, The Netherlands*

Corresponding author: Silke.Roovers@Ugent.be

Introduction

Drug-loaded microbubbles have proven very promising for drug delivery purposes since they not only allow localized drug release but can also enhance the delivery of the drugs into the tissue [1]. Recently, we have proposed “sonoprinting” as a third possible mechanism, next to sonoporation and enhanced endocytosis, that may be responsible for the improved drug delivery when using drug-loaded microbubbles and ultrasound [2-4]. Sonoprinting is defined as the direct deposition of elongated patches of nanoparticles along with parts of the bubble shell upon applying ultrasound to nanoparticle-loaded microbubbles [2]. However, earlier studies have shown that the presence of a stiff membrane on which the cells are cultured *in vitro*, can cause asymmetrical oscillations of microbubbles [5,6] and as such influence microbubble-cell interactions. In this study, we investigated the delivery of model drugs from liposome-loaded microbubbles to three-dimensional tumor cultures under ultrasound exposure and the role of sonoprinting therein.

Methods

4T1 murine breast cancer cells and 3T3 fibroblasts were used to form mono- and co-spheroids by self-aggregation in ultra-low adhesion agar microwells [7]. The 3D micro-environment of these multicellular spheroids resembles the *in vivo* situation, as an extracellular matrix can be formed that acts as a major physical barrier for drug penetration [8,9]. Liposome-loaded microbubbles were prepared by attaching biotinylated (thermosensitive and regular) liposomes containing doxorubicin (DOX) and/or DiD as a fluorescent marker, to the shell of biotinylated lipid microbubbles with the aid of an avidin linker. The spheroids were incubated with liposome-loaded microbubbles in an ultrasound transparent chamber, after which ultrasound of 1 MHz center frequency, 10% duty cycle, 2 W/cm² was applied for 10 seconds. The spheroids were subsequently studied using confocal microscopy, flow cytometry and toxicity assays. Cryosections of 10 μm were made to investigate the DOX and liposome penetration into the spheroids in further detail.

Results and discussion

When treating the multicellular spheroids with liposome-loaded microbubbles and ultrasound, the mean liposomal fluorescence that was found on the spheroid cells using flow cytometry was 90x higher compared to incubation with liposomes alone and 74x higher than when the liposomes and microbubbles were co-administered before ultrasound radiation. The results show that sonoprinting can also occur in soft tissue environments and that it is therefore not an artefact caused by the formation of asymmetrical bubble jets directed towards a stiff membrane.

When studying intact spheroids under confocal microscopy, it became clear that this increase in liposome delivery was caused by a large deposition of liposomes on the outer cell layers of the tumor spheroid. This could be a promising delivery strategy for chemotherapeutics such as doxorubicin, as it can provide a depot system in close proximity of the tumor tissue from which the drug can leak out and exert its function locally. Adding a heating step ensured a local DOX release from the thermosensitive liposomes attached to the spheroid surface, from where the drug was able to penetrate through the spheroid (Fig 1A). However, the regular liposomes did not allow leakage of the drug 24h, and the drug molecule remained present on the outside of the spheroid (Fig. 1B).

Toxicological assays show that the tumor cell killing is improved after 72h when the tumor spheroids were treated with both the regular and the thermosensitive DOX liposome-loaded microbubbles and

ultrasound compared to each type of liposomes alone and to the liposomes co-administered with microbubbles and ultrasound (Fig. 2). This indicates that even without the immediate release of the chemotherapeutic drug from the liposomal patches, the treatment remained effective.

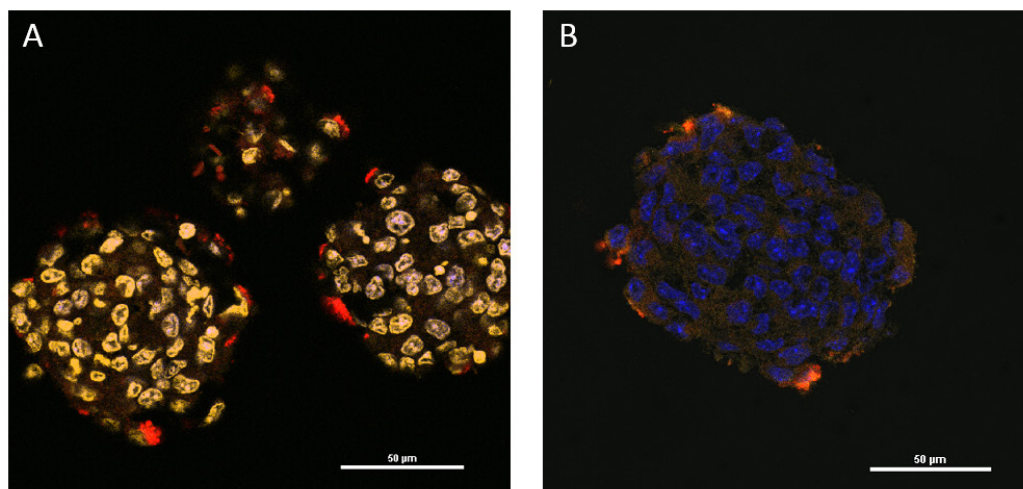


Figure 1: Confocal images of 10 μm cryosections from monospheroids treated with (A) thermosensitive liposomes or (B) regular liposomes coupled onto microbubbles and exposed to ultrasound. In both cases, patches of liposomal material (red) can be observed on the outer layers of the spheroids, while the doxorubicin (yellow) was only able to leak out of the thermosensitive liposomes and penetrate through the entire spheroid to reach the nuclei (blue) after 24h.

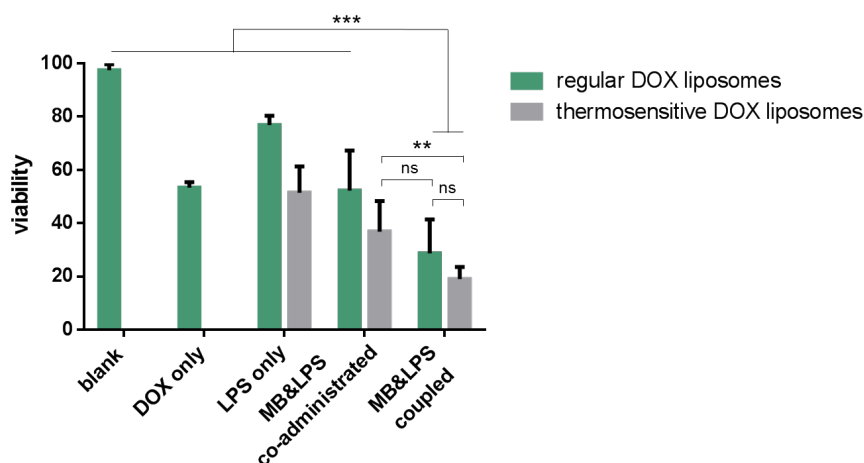


Figure 2: viability as estimated using CellTiter Glo 3D[®] after 72h indicating that both regular and thermosensitive liposomes (LPS) coupled onto microbubbles (MB) significantly improve the tumor killing.

Conclusions

Microbubble and ultrasound guided-delivery of doxorubicin-containing liposomes can provide a local delivery of the liposome material on a 3D tumor culture surface, followed by a drug release into the deeper layers of the tissue. This study shows that sonoprinting can also occur in a soft tissue environment and that it can be an interesting method to form a local drug reservoir in close proximity to target sites.

References

- [1]. Hernot S. and Klivanov A.L., Microbubbles in ultrasound-triggered drug and gene delivery. ADDR, 2008.
- [2]. De Cock I. et al, Sonoprinting and the importance of microbubble loading for the ultrasound mediated cellular delivery of nanoparticles, Biomaterials, 2016.
- [3]. Meijering B.D. et al, Ultrasound and microbubble-targeted delivery of macromolecules is regulated by induction of endocytosis and pore formation. Circ. Res. 104 (5), 2009.

- [4]. De Cock I. et al, Ultrasound and microbubble mediated drug delivery: Acoustic pressure as a determinant for uptake via membrane pores or endocytosis, JCR 197, 2015.
- [5]. Doinikov A.A. et al, Acoustic scattering from a contrast agent microbubble near an elastic wall of finite thickness, Phys Med Biol, 2011.
- [6]. Zhang A.M. et al, The dynamic behavior of a gas bubble near a wall, Ocean Eng. 36, 2009.
- [7]. Vrij E. et al, Directed assembly and development of material-free tissues with complex Architectures, Advanced Materials, 2016.
- [8]. Leong D.T. et al, Probing the relevance of 3D cancer models in nanomedicine research, ADDR, 2014.
- [9]. Alemany-Ribes M. et al, Bioengineering 3D environments for cancer models, ADDR, 2014.
- [10]. Barenholz Y. et al, Doxil®--the first FDA-approved nano-drug: lessons learned. JCR, 2012

Brain ultrasonography, with and without contrast agents

Olivier Couture

¹*CNRS, INSERM, ESPCI, PSL-University, 17 rue Moreau, 75012, Paris, olivier.couture@espci.fr*

The brain remains insufficiently explored by ultrasound, with respect to other imaging modalities such as MRI, CT or PET. This is mainly due to the fact that the skull protects the brain against most mechanical perturbations, including acoustic waves. Nevertheless, there is a strong incentive in pursuing brain ultrasonography, as it could benefit the diagnosis of tumours, stroke, aneurysm, but also help us understand the mechanism of thought. We should therefore seek anatomical, physiological and functional imaging of the brain with ultrasound, both in humans but also in animal models.

Currently, human brain can be imaged with transcranial Doppler, which exploits windows of natural thinning of the skull, to observe the larger vessels of the brain. This technique is particularly interesting for the assessment of vascular defect, rupture or blockage, especially in the emergency setting.

Beyond conventional Doppler, several recent advances based on ultrafast ultrasound [Tanter and Fink 2014], such as ultrasensitive Doppler, functional ultrasound (fUS) and ultrasound localization microscopy have impacted the imaging of the animal brain and are starting to modify our vision of the human brain. For instance, fUS exploits the increase in cerebral blood flow induced by the neuro-vascular coupling to map brain activity [Deffieux et al. 2018]. Current implementations exploits ultrafast Doppler, which increased the sensitivity of Doppler to blood flow by more than an order of magnitude [Bercoff et al. 2011, Demene et al. 2015].

In animals, fUS can highlight the activity of the brain linked to an external stimulation, such as an electrical [van Raaij et al. 2011], whisker [Macé et al. 2011], olfactory [Osmanski et al 2014] or a visual stimulation [Gesnik et al. 2017]. It has also been used to describe the abnormal brain activity linked to epilepsy [Macé et al. 2011]. Most demonstrations were performed in anesthetized animals, but several experiments on awake animals were shown [Urban et al. 2015, Sieu et al. 2015], which highlights a strong advantage of fUS with respect to other modalities. Moreover, fUS is sufficiently sensitive to map the functional connectivity of the brain [Osmanski et al. 2014]. Functional ultrasound is often performed with a craniotomy or a thinned skull, even though it is not necessary for mice [Tiran et al. 2017]. fUS could even be performed through an intact rat skull with the use of contrast agents [Errico et al. 2016].

Beyond the rat, mice, primate [Dizeux et al. 2018] and even pigeon [Rau et al. 2018], fUS was also demonstrated in humans. In the surgery room, through a craniotomy performed for tumor resection, fUS has described the selective activation of brain regions in human patients [Imbault et al. 2017]. In the neonates, fUS has also been performed through the fontanelles and was able to highlight abnormal brain activity [Demene et al. 2017]. Surgical and neonatal imaging are applications where other brain imaging modalities show some deficits and where fUS could make the difference.

Microbubbles have shown that they could allow super-resolution imaging using ultrasound localization microscopy [ULM, Couture et al. 2018]. In the rat brain, we demonstrated that 8 microns resolution could be obtained in-depth by tracking the movement of individual microbubbles detected through spatio-temporal filtering [Errico et al. 2015]. This technique not only highlight microvessels, but also describe the velocity of each microbubbles and can thus help describe the dynamics of the flow in vessels smaller than a human hair. The highly vascularized rat brain was used to describe the resolution limits of ULM with respect to acquisition time [Hingot et al. 2018]. In our view, the future of ultrasound localization microscopy is three-dimensional. A super-resolved 3D volume of the rat brain microvasculature was recently displayed and showed that an entire organ can be characterized within one acquisition [Heiles et al. 2018].

Quite recently, ULM was also demonstrated in the clinical setting in the brain [Demene et al. 2018]. As in transcranial Doppler, the temporal window was used to localize and track the passage of microbubbles within the middle cerebral artery, part of the circle of Willis and their surrounding microvessels. Aberration correction and motion correction was performed to improve the image quality. Ultrasound localization microscopy was able to describe the complex flow pattern within an aneurysm.

These new approaches for brain ultrasonography parallel the rapid development of ultrasound therapy of the brain, which show promises for treating mental illnesses and dementias [Meng et al. 2018]. In the future, ultrasound could thus become the ideal tool for brain theranostics.

References

- [1]. Bercoff, J., Montaldo, G., Loupas, T., Savery, D., Mézière, F., Fink, M. and Tanter, M., 2011. Ultrafast compound Doppler imaging: Providing full blood flow characterization. *IEEE Transactions on Ultrasonics, Ferroelectrics and Frequency Control*, 58(1), pp.134-147.
- [2]. Couture, O., Hingot, V., Heiles, B., Muleki-Seya, P. and Tanter, M., 2018. Ultrasound localization microscopy and super-resolution: A state of the art. *IEEE transactions on ultrasonics, ferroelectrics, and frequency control*, 65(8), pp.1304-1320.
- [3]. Deffieux, T., Demene, C., Pernot, M. and Tanter, M., 2018. Functional ultrasound neuroimaging: a review of the preclinical and clinical state of the art. *Current opinion in neurobiology*, 50, pp.128-135.
- [4]. Demené, C., Deffieux, T., Pernot, M., Osmanski, B.F., Biran, V., Gennisson, J.L., Sieu, L.A., Bergel, A., Franqui, S., Correas, J.M. and Cohen, I., 2015. Spatiotemporal clutter filtering of ultrafast ultrasound data highly increases Doppler and fUltrasound sensitivity. *IEEE transactions on medical imaging*, 34(11), pp.2271-2285.
- [5]. Demene, C., Baranger, J., Bernal, M., Delanoe, C., Auvin, S., Biran, V., Alison, M., Mairesse, J., Harribaud, E., Pernot, M. and Tanter, M., 2017. Functional ultrasound imaging of brain activity in human newborns. *Science translational medicine*, 9(411), p.6756.
- [6]. Demene C, Puke L, Robin J, Heiles B, Hingot V, Couture O, Pernot M, Perren-Landis F, Tanter M., 2018 Deep Transcranial Ultrasound Localization Microscopy of the adult human brain vascularization. *IEEE Ultrasonics Kobe 2018*.
- [7]. Dizeux, A., Gesnik, M., Ahnine, H., Blaize, K., Arcizet, F., Picaud, S., Sahel, J.A., Deffieux, T., Pouget, P. and Tanter, M., 2018. Ultrasound functional neuroimaging reveals propagation of task-related brain activity in behaving primates. *bioRxiv*, p.464487.
- [8]. Errico, C., Pierre, J., Pezet, S., Desailly, Y., Lenkei, Z., Couture, O. and Tanter, M., 2015. Ultrafast ultrasound localization microscopy for deep super-resolution vascular imaging. *Nature*, 527(7579), p.499.
- [9]. Errico, C., Osmanski, B.F., Pezet, S., Couture, O., Lenkei, Z. and Tanter, M., 2016. Transcranial functional ultrasound imaging of the brain using microbubble-enhanced ultrasensitive Doppler. *NeuroImage*, 124, pp.752-761.
- [10]. Heiles B, Rabut C, Hingot V, Rahal L, Lopez P, Pernot M, Tanter M, Couture O. Ultrafast Volumetric Ultrasound Localization Microscopy in vivo. *IEEE Ultrasonics Kobe 2018*.
- [11]. Hingot V, Errico C, Heiles B, Rahal L, Tanter M, Couture O. Microvascular flow dictates the compromise between spatial resolution and acquisition time in ultrasound localization microscopy, in *Review*, 2018.
- [12]. Imbault, M., Chauvet, D., Gennisson, J.L., Capelle, L. and Tanter, M., 2017. Intraoperative functional ultrasound imaging of human brain activity. *Scientific reports*, 7(1), p.7304.
- [13]. Macé, E., Montaldo, G., Cohen, I., Baulac, M., Fink, M. and Tanter, M., 2011. Functional ultrasound imaging of the brain. *Nature methods*, 8(8), p.662.
- [14]. Meng, Y., Volpini, M., Black, S., Lozano, A.M., Hynynen, K. and Lipsman, N., 2017. Focused ultrasound as a novel strategy for Alzheimer disease therapeutics. *Annals of neurology*, 81(5), pp.611-617.
- [15]. Osmanski, B.F., Pezet, S., Ricobaraza, A., Lenkei, Z. and Tanter, M., 2014. Functional ultrasound imaging of intrinsic connectivity in the living rat brain with high spatiotemporal resolution. *Nature communications*, 5, p.5023.
- [16]. Osmanski, B.F., Martin, C., Montaldo, G., Lanièce, P., Pain, F., Tanter, M. and Gurden, H., 2014. Functional ultrasound imaging reveals different odor-evoked patterns of vascular activity in the main olfactory bulb and the anterior piriform cortex. *Neuroimage*, 95, pp.176-184.
- [17]. Rau, R., Kruijzinga, P., Mastik, F., Belau, M., de Jong, N., Bosch, J.G., Scheffer, W. and Maret, G., 2018. 3D Functional Ultrasound Imaging of Pigeons. *bioRxiv*, p.302323.
- [18]. Sieu, L.A., Bergel, A., Tiran, E., Deffieux, T., Pernot, M., Gennisson, J.L., Tanter, M. and Cohen, I., 2015. EEG and functional ultrasound imaging in mobile rats. *Nature methods*, 12(9), p.831.

- [19]. Tanter, M. and Fink, M., 2014. Ultrafast imaging in biomedical ultrasound. *IEEE transactions on ultrasonics, ferroelectrics, and frequency control*, 61(1), pp.102-119.
- [20]. Tiran, E., Ferrier, J., Deffieux, T., Gennisson, J.L., Pezet, S., Lenkei, Z. and Tanter, M., 2017. Transcranial functional ultrasound imaging in freely moving awake mice and anesthetized young rats without contrast agent. *Ultrasound in medicine & biology*, 43(8), pp.1679-1689.
- [21]. Urban, A., Dussaux, C., Martel, G., Brunner, C., Mace, E. and Montaldo, G., 2015. Real-time imaging of brain activity in freely moving rats using functional ultrasound. *nature methods*, 12(9), p.873.
- [22]. van Raaij, M.E., Lindvere, L., Dorr, A., He, J., Sahota, B., Foster, F.S. and Stefanovic, B., 2011. Functional micro-ultrasound imaging of rodent cerebral hemodynamics. *Neuroimage*, 58(1), pp.100-108.

High-volume-rate 4D echoPIV, *in vitro* results in a dynamic left ventricular phantom

Jason Voorneveld¹, Hicham Saaid², Christiaan Schinkel³, Antonius F.W. van der Steen¹, Frank J.H. Gijzen¹, Nico de Jong¹, Tom Claessens⁴, Hendrik J. Vos¹, Sasa Kenjeres³, Johan G. Bosch¹

¹Department of Biomedical Engineering, Thorax Center, Erasmus MC, Rotterdam, Netherlands

²Institute of Biomedical Technology, Ghent University, Ghent, Belgium

³Department of Chemical Engineering, Faculty of Applied Sciences, Delft University of Technology, Delft, Netherlands

⁴Department of Materials, Textiles and Chemical Engineering, Ghent University, Ghent, Belgium

Corresponding author: j.vorneveld@erasmusmc.nl

Introduction

Left ventricular (LV) blood flow is a promising early stage biomarker of ventricular dysfunction [1]. However, blood flow in the LV is a 3D phenomenon and current clinical measurement techniques are limited to 1D /2D. Echo-particle image velocimetry (echo-PIV) can be used to measure 3D blood flow patterns but requires high frame rates to effectively track the fast flows expected in the LV. In this study, we use a prototype transesophageal (TEE) matrix probe, capable of 3D high volume rate (4 kHz) imaging to test the capabilities of 4D echo-PIV in a realistic and dynamic LV phantom.

Methods

A compliant, optically and acoustically transparent silicone LV chamber, encased in an acrylic box, was fitted with bio-prosthetic mitral and aortic valves (Edwards), connecting to atrial and compliance chambers (Figure 1.a). The system uses a piston pump (ViVitro) to impose volume changes in the acrylic box, causing similar flow patterns to those observed *in vivo* (Figure 1.b). The ‘ground truth’ flow patterns in the LV are captured using tomographic PIV (tomoPIV), a 3D optical velocimetry technique with high spatial (0.963 mm³) and temporal (2000 fps) resolution (Figure 1.c).

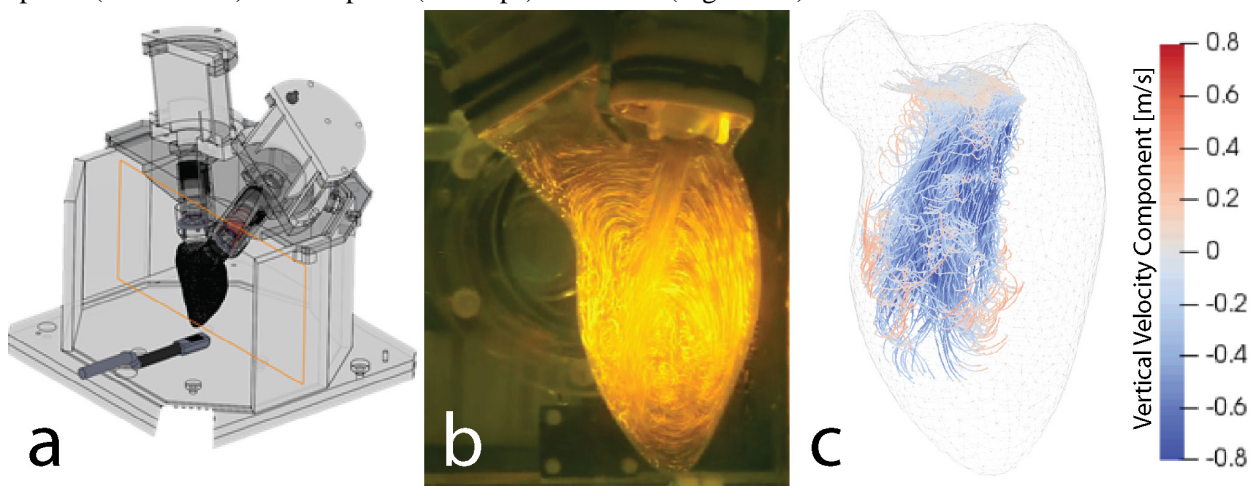


Figure 1: a) Schematic of LV phantom. b) Phone-camera photograph of LV phantom illuminated during tomoPIV recording. c) Streamline visualisation of tomoPIV result.

Using the TEE matrix probe (Oldelft, 5 MHz), connected to a Verasonics Vantage 256, single diverging waves were transmitted to insonify a field of view of 24° x 24° up to a depth of 10 cm (Figure 2.a). Nine overlapping beams were acquired in a gated sequence, synchronized with the pump cycle, to obtain the full field of view of the LV without reducing frame rate. Ultrasound contrast agent (SonoVue,

20 μ l/l) was added for visualizing LV flow. Echo-PIV was then performed in the spherical domain using normalized cross correlation with a kernel size of 5.7mm x 12 $^{\circ}$ x 12 $^{\circ}$ and an overlap of 50% x 75% x 75%, resulting in a vector map resolution of 2.5mm x 3 $^{\circ}$ x 3 $^{\circ}$.

Results

The vector maps obtained with echo-PIV (Figure 2.b) were qualitatively compared to the tomographic PIV results (after conversion to cartesian domain). The high velocity trans-mitral jet velocities of \sim 1 m/s could be captured by 4D-echo-PIV although there was still some underestimation present, especially in the lateral directions, likely due to the anisotropic point-spread-function (PSF). This phantom is a useful tool for further optimization of echo-PIV.

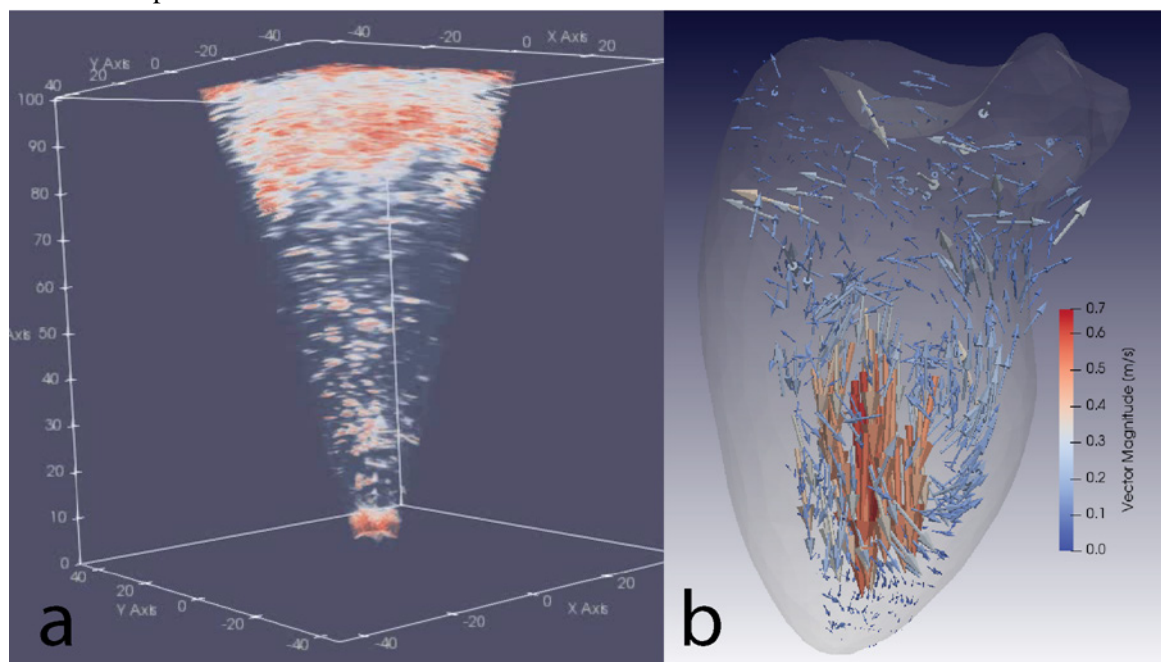


Figure 2: a) Volume rendering of single 24 $^{\circ}$ x24 $^{\circ}$ beam with air-bubbles (SonoVue too dense for visualisation). b) echo-PIV vector rendering during diastolic phase.

Conclusions

4D echo-PIV was performed with the prototype TEE probe in a dynamic LV phantom and was compared to tomographic PIV. A method to compensate for the anisotropic PSF may improve lateral tracking performance of 4D echo-PIV.

Reference

- [1] Sengupta, P. P. et al. Emerging trends in CV flow visualization. *JACC Cardiovasc. Imaging*, 5, 305–316, 2012.

Volumetric ultrafast Ultrasound Localisation Microscopy in vivo

Baptiste Heiles¹, Vincent Hingot¹, Line Rahal¹, Pauline Lopez^{1,2}, Claire Rabut¹, Antoine Bergel¹, Mathieu Pernot¹, Mickael Tanter^{1,*}, Olivier Couture^{1,*}

¹Institut Langevin, CNRS, INSERM, ESPCI Paris, PSL Research University, 17 rue Moreau, 75012, Paris

²Institut Cochin INSERM U1016, France

*These authors contributed equally

Introduction

Inspired by FPALM in optics and exploiting ultrafast ultrasound imaging, ultrafast Ultrasound Localization Microscopy (ULM) allows the reconstruction of a full velocity map of the rat brain vasculature with a micrometric resolution (8 μm) [1] [2]. Despite additional successes for tumour imaging [3] this plane-by-plane technique suffers from minute-long acquisitions, out-of-plane microbubbles and tissue motion which cannot be corrected for [4] and the loss of information due to the projection of a 3D vascular structure into a 2D image. We previously proposed the use of an isotropic matrix array for 3D *in vitro* superresolution imaging at high frame rates. We present here the application of this process in the rat brain *in vivo*.

Methods

The 2D matrix array with 1024 elements arranged in a 32x32 isotropic plane was controlled by the customised programmable 1024-channel system presented in [5]. Sprague Dawley rats underwent craniectomy surgery under Ketamin-Xylazin anesthesia. The anesthesia was later switched to Ketamin-Domitor. The probe was driven at 9MHz to transmit plane waves at 12 different angles to achieve a compounded volume rate of up to 500Hz. It was decided to repeat 540 blocs of 185 volumes with a pause in between to allow for data transfer. A 3D ULM process previously described [5] was applied to determine the position of the bubbles, track them and perform velocimetry. An additional experiment was conducted where the rat was released from the stereotactic frame and thus added breathing motion on the images. Two different algorithms for motion correction were then applied to improve the quality of the images. The first one relied on correcting motion in between continuous blocs of volume while ignoring volume to volume motion. The second one corrected for motion each volume before applying ULM and then corrected the super-resolved images for bloc-to-bloc motion.

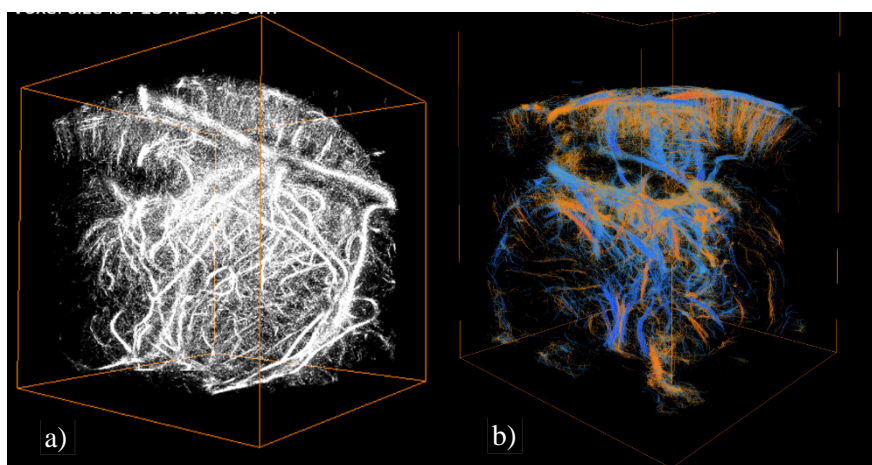


Figure 1. 3D rendering of rat brain after volumetric ULM
a) Density of microbubbles b) Velocimetry (blue towards bottom, red towards top)

Results

After implementation of this technique on 99900 volumes, a volumetric rendering of the rat's brain microvasculature was obtained (figure 1.). At 9MHz, the conventional resolution with this 2D array is around 250 μm . The maximum theoretical microbubble localization precision obtainable with volumetric ULM was calculated to be less than 1 μm in the axial direction and around 5 μm in the lateral and elevational directions. Velocimetry was performed to yield a large range of velocity fields in microvessels from a few tens micrometers to a few centimeters per second. The motion correction step allowed to correct for global and volume to volume motion to achieve greater quality images (figure 2.). There are notable differences between the two different schemes as one seems to increase contrast of the large vessels at the expense of sharpness while the other one increases contrast less but retains sharpness. This effect is further exacerbated on small vessels.

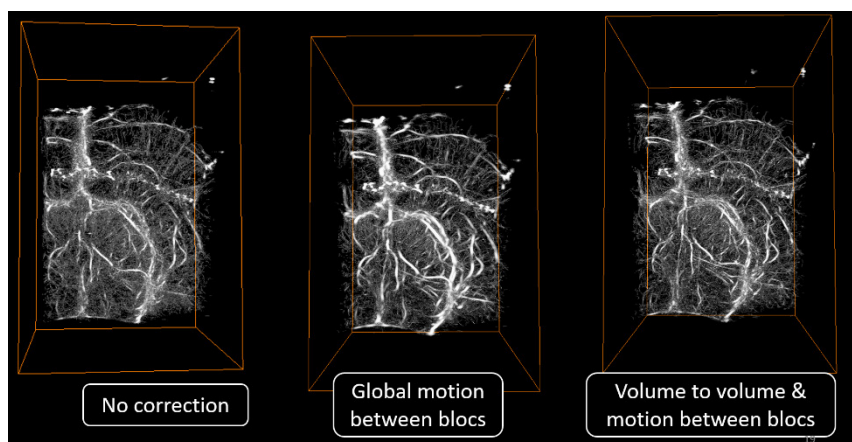


Figure 2. 3D renderings of moving rat brain after volumetric ULM with different techniques for motion correction

Conclusions

Volumetric ULM was successfully demonstrated *in vivo* on a rat brain and it was shown that classical 2D techniques developed for ULM were translatable to 3D. It was also demonstrated that velocimetry was possible in the three dimensions. Volumetric ULM allows to surpass the conventional resolution in 3 dimensions in a large volume with only 200s of acquisition time. However, the limited sensitivity of the 2D matrix arrays, the data size, computation and transfer times remain major challenges.

References

- [1]. C. Errico et al., « Ultrafast ultrasound localization microscopy for deep super-resolution vascular imaging », *Nature*, vol. 527, no 7579, p. 499-502, nov. 2015.
- [2]. O. Couture, V. Hingot, B. Heiles, P. Muleki-Seya, et M. Tanter, « Ultrasound localization microscopy and super-resolution: a state-of-the-art », *IEEE Trans. Ultrason. Ferroelectr. Freq. Control*, p. 1-1, 2018.
- [3]. F. Lin, S. E. Shelton, D. Espíndola, J. D. Rojas, G. Pinton, et P. A. Dayton, « 3-D Ultrasound Localization Microscopy for Identifying Microvascular Morphology Features of Tumor Angiogenesis at a Resolution Beyond the Diffraction Limit of Conventional Ultrasound », *Theranostics*, vol. 7, no 1, p. 196-204, 2017.
- [4]. V. Hingot, C. Errico, M. Tanter, et O. Couture, « Subwavelength motion-correction for ultrafast Ultrasound Localization Microscopy », 2017, p. 1-1.
- [5]. J. Provost et al., « 3D ultrafast ultrasound imaging *in vivo* », *Phys. Med. Biol.*, vol. 59, no 19, p. L1-L13, oct. 2014.

Towards Real-Time Super-Resolution Imaging: Fast Acoustic Wave Sparsely Activated Localization Microscopy (fast-AWSALM) using Octafluoropropane Nanodroplets

Ge Zhang¹, Sevan Harput¹, Hanyu Hu¹, Kirsten Christensen-Jeffries², Jiaqi Zhu¹, Jemma Brown², Chee Hau Leow¹, Chris Dunsby^{3}, Robert J. Eckersley^{2*}, Meng-Xing Tang^{1*}*

¹*Department of Bioengineering, Imperial College London, London, UK, SW7 2AZ, United Kingdom*

²*Biomedical Engineering Department, School of Biomedical Engineering and Imaging Sciences, Kings College London, London, SE1 7EH, UK*

³*Department of Physics and Centre for Pathology, Imperial College London, London, SW7 2AZ, UK*

** These authors contributed equally to this work*

Corresponding author: MengXing.Tang@Imperial.ac.uk

Introduction

Ultrasound super-resolution imaging techniques have shown the capability of breaking the diffraction limit in spatial resolution [1,2]. However, these current localization-based ultrasound super-resolution imaging techniques rely on a low concentration of active flowing microbubble signals. This means that, for slow flows associated with the micro-vasculature, a longer acquisition time is required for the microbubbles to replenish. During this long acquisition time, motion is very likely to be introduced to lower the imaging quality of super-resolution imaging. Therefore, there is a need to develop a super-resolution imaging technique to acquire images sufficiently rapidly in order to avoid motion artefacts. We have recently developed Acoustic Wave Sparsely Activation and Localisation Microscopy (AWLSALM) [3], which is able to achieve super resolution in no-flow condition using activation and deactivation of phase change nano-droplets. While this method has great potential to achieve fast super-resolution imaging, the relatively high boiling point droplets used mean that separate ultrasound transmissions are required for droplets activation and for imaging, leading to extra acquisition time. In this study, fast acoustic wave sparsely activated localization microscopy (fast-AWSALM) is developed to simultaneously image, activate and deactivate octafluoropropane nanodroplets during high-frame-rate plane-wave ultrasound imaging to achieve ultrasound super-resolution images on a sub-second timescale.

Methods

Octafluoropropane nanodroplets consist of octafluoropropane liquid cores encapsulated by lipid shells. A 200 μm cellulose tube (Hemophan®, Membrana) phantom was fixed and immersed in a water tank where the walls were covered with acoustic absorbers. A L11-4v transducer equipped with ultrasound research platform (Verasonics Vantage 128, Kirkland, USA) was held 20 mm above the center of the tube. The water temperature was maintained at 24 °C. A concentration of diluted nanodroplet solution ($\sim 1.35 \times 10^7$ PCCAs/mL) was prepared. A customised ‘Imaging/Activation’ sequence was implemented on an ultrasound research platform (Verasonics Vantage 128, Kirkland, USA) with a L11-4 38-mm linear array probe (ATL, USA). Briefly, a 1-cycle single-angle plane-wave pulse at 3.5 MHz with a peak-negative-pressure (PNP) of 1.42 MPa was transmitted in order to simultaneously image, activate, and deactivate the octafluoropropane nanodroplets. The frame rate was 5000 Hz and 1000 frames were acquired in 200ms. Singular value decomposition (SVD) processing was used to obtain the changing contrast signals. The SVD thresholds were automatically determined from the location of the largest gradient on the energy versus singular value order curve. After SVD processing, super-localization was performed to reject the noise and detect potential vaporized droplets [3]. The location of single isolated vaporized droplets was calculated by the “centroid” method. The resulting super-resolution map was created from all the localizations detected over all the imaging frames.

Results

Figure 1 shows three representative successive image frames after SVD filtering. It can be seen that the octafluoropropane nanodroplets were sparsely activated or deactivated by plane-wave pulses in the tube without any flow. Acoustic droplet vaporization has only been performed using focused single element transducers or linear-array probes with focus-wave transmissions in previous literature. The activation of nanodroplets via plane-waves without the need of using focus-wave enables a faster imaging and activation acquisition. Figure 2 shows the comparison between the summation of 1000 conventional B-mode image frames acquired in 200 ms and the corresponding super-resolution image which superimposes all the localization events in these 1000 frames. It can be seen that, in the super-resolution imaging, it not only has a better resolution but also help to remove some imaging artefacts appeared on the B-mode image. Figure 3 shows the resolution measurement of the B-mode and super-resolution image at the same lateral ROI from -8.6 to -8.4 mm. According to the measurement, the super-resolution image gives a FWHM of 190 μm whereas the B-mode image shows a FWHM value of 550 μm .

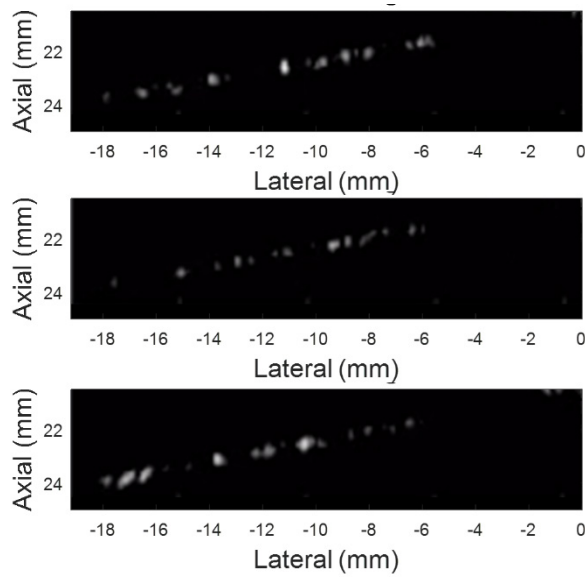


Figure 1. Three representative successive SVD-filtered image frames shows that octafluoropropane nanodroplets were sparsely activated or activated octafluoropropane nanodroplets were sparsely deactivated. Images were acquired with no flow in the tubes.

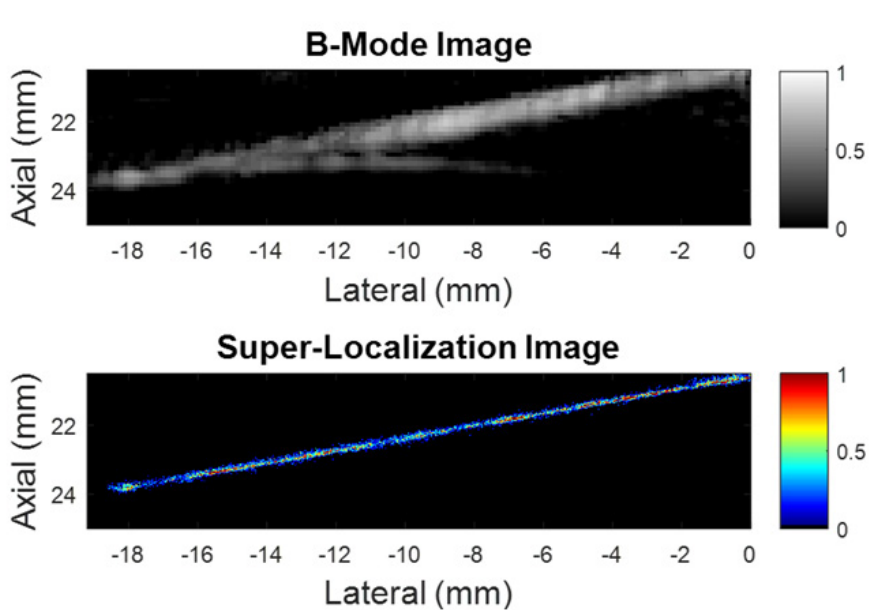


Figure 2. The summation of 1000 conventional B-mode image frames acquired in 200 ms (a) Super-resolution image superimposes all the localization events in 1000 frames acquired in 200 ms. Note that there is no flow in the tube.

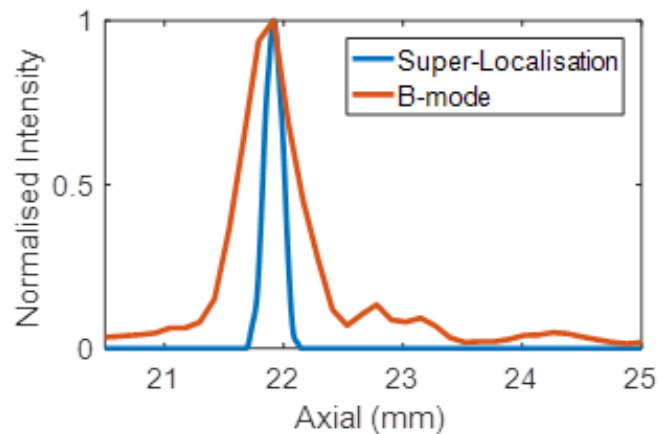


Figure 3. Full-width-half-maximum (FWHM) resolution measurement of the B-mode and super-resolution images at same lateral region of interest (ROI) from -8.6 to -8.4 mm.

Conclusions

In summary, this study demonstrates sub-second temporal resolution super-resolution can be achieved using the proposed fast-AWSALM – using high-frame-rate plane-wave transmit pulses to simultaneously image, activate and deactivate the octafluoropropane nanodroplets. The imaging frequency used in this study (3.5 MHz) indicates that this technique can be used for deep-tissue imaging. The acoustic pressure of the plane-wave pulses was well within the FDA-approved safety range. This study shows fast-AWSALM, a faster version of AWSALM, which is also flow independent and does not require a precise control on contrast agent concentration.

References

- [1] K. Christensen-Jeffries, R. J. Browning, M. Tang, C. Dunsby and R. J. Eckersley, In Vivo Acoustic Super-Resolution and Super-Resolved Velocity Mapping Using Microbubbles, *IEEE Transactions on Medical Imaging*, 34: 433-440, 2015.
- [2] C. Errico, J. Pierre, S. Pezet, Y. Desailly, Z. Lenkei, O. Couture and M. Tanter, Ultrafast ultrasound localization microscopy for deep super-resolution vascular imaging, *Nature*, 527: 499, 2015.
- [3] G. Zhang, S. Harput, S. Lin, K. Christensen-Jeffries, C. H. Leow, J. Brown, C. Dunsby, R. J. Eckersley and M. Tang, Acoustic wave sparsely activated localization microscopy (AWSALM): Super-resolution ultrasound imaging using acoustic activation and deactivation of nanodroplets, *Applied Physics Letter*, 113: 1, 2018.

Left ventricular flow patterns: A new aspect elucidated by high-frame rate echocardiography

Jeffrey Goei¹, Jason Voorneveld², Lana Keijzer², Mihai Strachinaru¹, Dan Bowen¹, Folkert ten Cate¹, Nico de Jong², Rik Vos², Hans Bosch², Annemien van den Bosch¹

¹Department of Cardiology, Thorax Center, Erasmus MC, Rotterdam, The Netherlands

²Department of Biomedical Engineering, Thorax Center, Erasmus MC, Rotterdam, The Netherlands

Corresponding author: j.goei@erasmusmc.nl

Introduction

Blood flow dynamics in the left ventricle (LV) show geometrical and anatomical characteristics that specify cardiac function. These parameters, obtained with echocardiography, are limited in temporal resolution, hampering the tracking of highly dynamic flow features (1). High-frame rate (HFR) contrast enhanced echocardiography, using diverging waves, is able to track higher velocities and gives insights into the blood flow dynamics of the LV (2). Blood flow patterns potentially are an early-stage diagnostic marker for cardiac dysfunction. Therefore, it is clinically relevant to assess these LV blood flow patterns. The aim of this study is to explore the feasibility of LV blood flow pattern analysis with HFR echocardiography in patients with systolic and diastolic heart failure (HF).

Methods

Five HF patients were included in this study. The patients were divided into two groups: HF with systolic dysfunction (systolic HF, n=3) and HF with preserved systolic function (diastolic HF, n=2). HFR echocardiography measurements were performed in a 3-chamber apical view at a frame rate of 1225 Hz (Pulse Inversion with 2 angled compounding at a PRF of 4900 Hz). Ultrasound contrast agent (SonoVue®, Bracco) was continuously infused at 1.2 ml/min. Movies were created offline and the flow patterns and vortices were assessed by eye (see Figure 1). Flow patterns were described based on the following parameters: velocity, direction and influence ability. The ability of the contraction to influence the flow dynamics was defined as influence ability. The vortex patterns were assessed with respect to rotation, velocity, position, size and duration (see Table 1). The cardiac cycle was subdivided in different phases (isovolumetric relaxation, rapid filling, diastasis, atrial ejection, isovolumetric contraction, systole) and the analysis was repeated for each phase.

Table 1. Differences in flow and vortices between systolic and diastolic HF patients averaged over all phases of cardiac cycle.

	Systolic HF (n=3)	Diastolic HF (n=2)
Flow		
1. Velocity	1. Slow	1. Medium/fast
2. Direction	2. Indetermined	2. Counterclockwise
3. Influence ability	3. Minimal	3. Normal
Vortex		
1. Rotation	1. Clockwise	1. Counterclockwise
2. Velocity	2. Fast	2. Fast
3. Position	3. Central	3. Apical
4. Size*	4. V: 33.60 mm (±3.76) H: 34,85 mm (±5.78)	4. V: 26.25 mm (±5.30) H: 25.00 mm (±3.54)
5. Duration	5. Through complete cycle	5. In RF and diastasis

*= Mean size of distinctive vortex (Systolic HF: central vortex. Diastolic HF: apical vortex). V = vertical axis. H = horizontal axis.

Results

In the three systolic HF patients a central clockwise vortex was observed. Diastolic HF patients showed smaller counterclockwise vortices. The central clockwise vortices in systolic HF patients remained to exist throughout all phases of the cardiac cycle. The counterclockwise vortices of diastolic HF patients, only existed in the rapid filling (RF) phase and diastasis. Two systolic HF patients showed an extra counterclockwise vortex in the apical region. In the other systolic HF patient with 100% pacing, this was not observed. In diastolic HF patients, the flow amongst the LV walls abruptly changed direction during systole. On the contrary, for systolic HF patients the influence of systolic contraction on the flow was found to be minimal, especially amongst the apical walls.

Conclusions

This study demonstrates that LV blood flow pattern analysis with HFR echocardiography is feasible in humans. We observed clear differences in blood flow patterns between systolic and diastolic HF. This technique may offer new insights into the mechanism of heart failure.

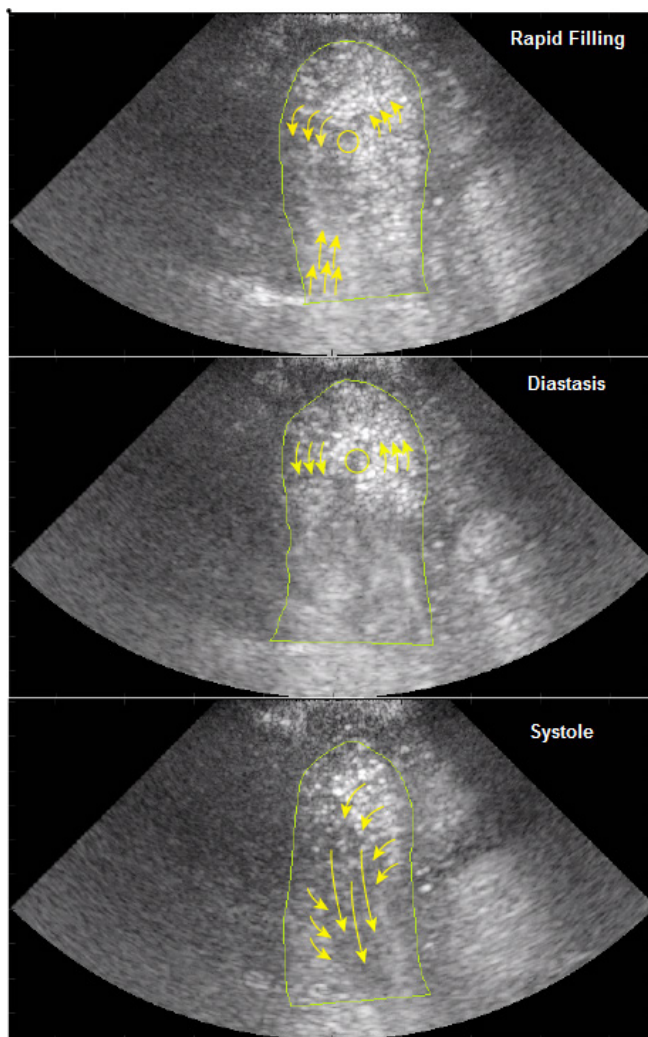


Figure 1. A 3-chamber apical contrast HFR echocardiography of a diastolic HF patient. Flow is represented in three cardiac phases: RF, diastasis and systole.

References

- [1]. Prinz C, Faludi R, Walker A, Amzulescu M, Gao H, Uejima T, et al. Can echocardiographic particle image velocimetry correctly detect motion patterns as they occur in blood inside heart chambers? A validation study using moving phantoms. *Cardiovasc Ultrasound*. 2012;10:24.
- [2]. Vorneveld J, Muralidharan A, Hope T, Vos HJ, Kruizinga P, van der Steen AFW, et al. High Frame Rate Ultrasound Particle Image Velocimetry for Estimating High Velocity Flow Patterns in the Left Ventricle. *IEEE Trans Ultrason Ferroelectr Freq Control*. 2017.

A study of radiation force effects in plane-wave transmission

Mark A. Borden¹, Francesco Guidi², Outi Supponen¹, Awaneesh Upadhyay¹, Lauchlin Blue¹, Rik Vos³, Piero Tortoli²

¹Mechanical Engineering, University of Colorado, Boulder, CO, USA

²Information Engineering, University of Florence, Florence, Italy

³Biomedical Engineering, Erasmus MC, Rotterdam, Netherlands

Corresponding author: mark.borden@colorado.edu

Introduction

Significant microbubble displacements due to the primary radiation force have been observed in the focal region of single-element and array probes [1]. This effect has been harnessed to increase contact between ligand-bearing microbubbles and targeted endothelium for applications in targeted drug delivery and ultrasound molecular imaging. In this study, microbubble displacements associated with plane-wave transmission are investigated and compared to displacements obtained in focussed-wave transmission at equivalent burst length, pulse repetition frequency, center frequency and peak negative pressure.

Methods

Size-isolated microbubbles of 1-2, 3-4, 4-5 and 5-8 μm diameter, as well as polydisperse microbubbles (AMB Labs, Boulder, CO) were diluted with purified water to 10^4 to 10^5 mL^{-1} in a 1 L beaker. The microbubbles were insonified at 4 kHz pulse repetition frequency (PRF) by the LA332 linear array probe (100% bandwidth around 4.6 MHz) connected to the 64-channel ULA-OP open scanner. For each microbubble size population, multiple experimental conditions were established by varying the transmit frequency (range: 3-7 MHz) and the burst length (1-10 μs), to transmit plane-wave or focused-wave beams with 100-330 kPa peak negative pressure (PNP). Whichever transmit modality was used, the echo-data beamformed along one or multiple lines were acquired for several seconds and processed using a multi-gate spectral Doppler (MGD) approach. This analysis allowed estimation of the microbubble displacements along the line(s) selected in the insonified region.

Results

In all plane-wave experiments, the transmission of 1- μs burst length pulses yielded peak displacements lower than 2 μm per transmission event. Displacement significantly increased for longer transmission pulses and higher PNP, especially at a frequency close to the microbubble resonance. For example, with pulses of 10 μs and 320 kPa peak negative pressure, peak displacements were measured up to 20 μm per transmission in a population with size range 3-4 μm . In particular, it was observed that in focused-wave mode the peak microbubble displacements were similar to, although typically slightly lower than, the values measured for plane wave.

Conclusions

The radiation force effects are equivalent in plane-wave and in focussed-wave transmission modes when similar transmission parameters are used. In both cases, microbubbles are displaced by an amount that increases with burst length, peak negative pressure and as the center frequency approaches microbubble resonance. However, for plane wave transmission, the microbubble displacements are nearly uniform over the field of view (rather than peaked at the focal region). The results of this study could be useful to facilitate uniform displacements over wide tissue volumes for applications in ultrasound molecular imaging and targeted drug delivery.

Reference

- [1]. H. J. Vos, F. Guidi, E. Boni, and P. Tortoli, "Method for microbubble characterization using primary radiation force," *IEEE Trans. Ultrason. Ferroelectr. Freq. Control*, vol. 54, no. 7, pp. 1333–1345, Jul. 2007.

Influence of Electric Field on Acoustic Spectra of Nested Contrast Agents

Steven P. Wrenn¹, Michael J. Cimorelli¹, Aaron T. Fafarman¹, Michael A. Flynn¹, Brett Angel², and Andrew R. Kohut³

¹Chemical & Biological Engineering, Drexel University, Philadelphia, USA

²College of Medicine, Drexel University, Philadelphia, USA

³Perelman School of Medicine, University of Pennsylvania, Philadelphia, USA

Corresponding author: spw22@drexel.edu

Introduction

We recently introduced a voltage-sensitive ultrasound contrast enhancing agent that shows promise for myocardial perfusion imaging [1]. The agent comprises coated liquid perfluorocarbon nanodroplet nested within the aqueous core of a phospholipid vesicle. In the absence of an electric field, the acoustic activity of the agent is relatively weak, and the agent transforms in the presence of an electric field to become acoustically active. In this talk we will present the details of the agent formulation and construction and quantify the acoustic scattering and attenuation that result from the agent in the absence and presence of an electric field.

Methods

For details of synthesis and characterization please see our 2018 *Applied Acoustics* article. Briefly, an emulsion of surfactant-coated perfluorocarbon droplets is nested within liposomes via a double emulsion process. The formulation is characterized in a variety of ways: in a home-built acoustic spectrometer that enables both scattering and attenuation measurements as a function speaking transducer intensity and frequency; in a tissue-mimicking phantom as imaged with a clinical imaging system; and in animals using the same imaging system used with the phantom. In all cases, the agent is tested both in the absence and presence of an electric field; in the case of animals, the electric field is that of the heart (where absence of field correlates with regions outside the myocardium). This talk will also describe and include results of recent infarct studies performed in swine.

Results

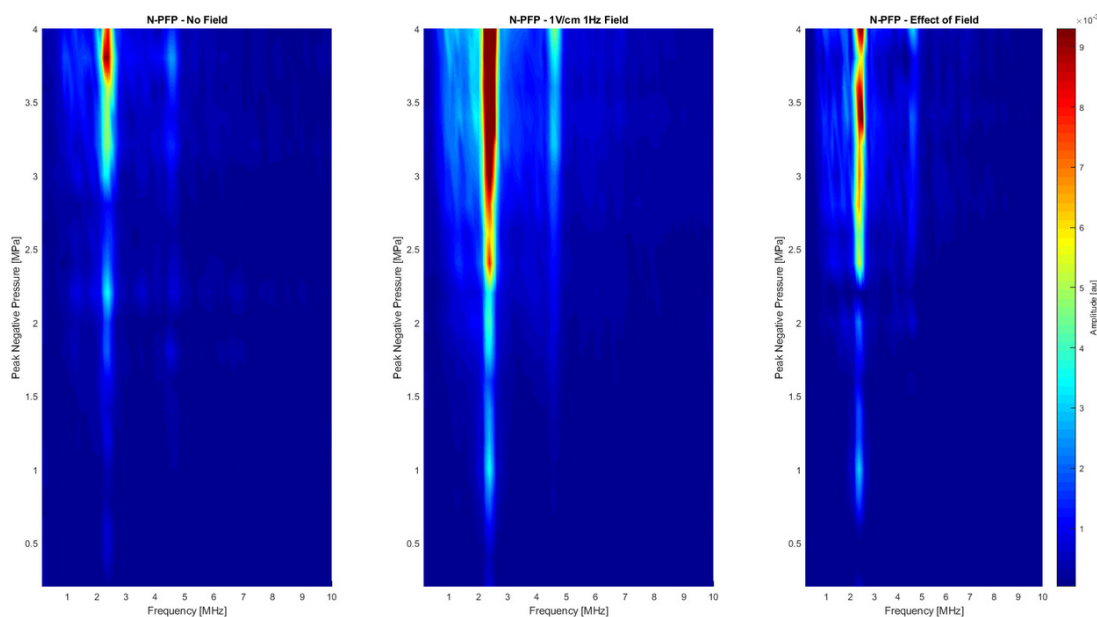


Figure 1 – Acoustic Spectra in the absence (left) and presence (middle) of an electric field and difference thereof (right)

Figure 1 shows results from a typical acoustic scattering measurement. Each panel is an acoustic spectrum that shows intensity (brightness scale at right of all panels) over a range of speaking peak negative pressures (vertical scale in MPa; speaking frequency was 2.25 MHz) and listening frequencies (horizontal scale, MHz). The left and middle panels give the spectra obtained in the absence and presence of an alternating electric field (1 V/cm at 1 Hz), respectively, and the right panel shows the net effect resulting from the electric field by subtracting the results of the left panel from those of the middle panel. Above a peak negative pressure of ~0.6 MPa (or MI ~0.4), the electric field enhances response at the driving frequency; at a peak negative pressure of ~2.0 (or MI ~1.3) the electric field enhances response at the 2nd harmonic; and at a peak negative pressure of ~2.3 (or MI ~1.5) the electric field enhances response at sub-harmonic frequency.

Figure 2 shows results from a closed-chest swine study. Shown are images of the left ventricle using a GE Vividi at baseline, which was prior to administering ELECTRAST and prior to ballooning (left panel), and during ballooning with administration of ELECTRAST (right panel). The myocardium (as well as the chamber somewhat) showed enhanced brightening in the presence of ELECTRAST but not the region of the myocardium believed to correspond to the region of balloon blockage; the latter region darkened relative to baseline.

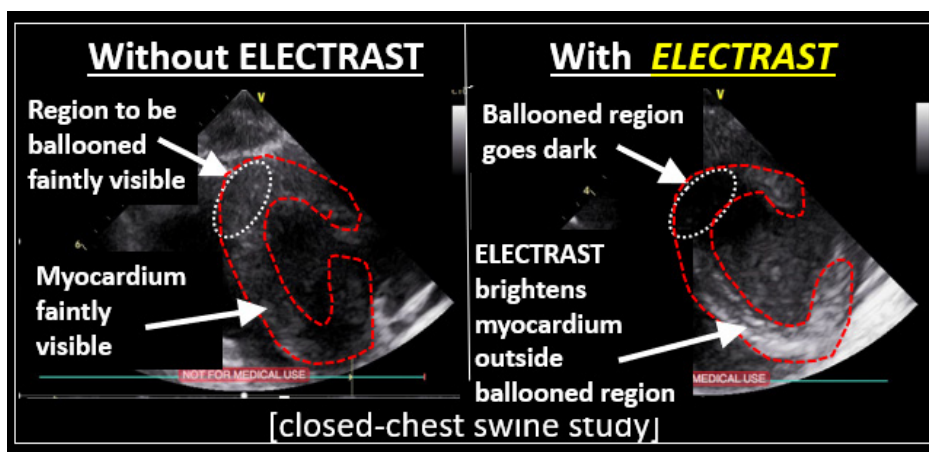


Figure 2 – Closed-chest swine study showing baseline (left) and infarct (right) as detected by ELECTRAST

Conclusions

ELECTRAST is a voltage-activated, nested phase change agent with an acoustic signal that depends on electric field. The agent shows promise both in the laboratory and in animals. Early tests suggests that ELECTRAST has potential for myocardial perfusion imaging, and other applications involving electric field could follow.

Reference

- [1]. Cimorelli MJ, Angel B, Fafarman A, Kohut AR, Andrien BM, Barrett KJ, and Wrenn SP, Introducing a nested phase change agent with an acoustic response that depends on electric field: A candidate for myocardial perfusion imaging and drug delivery, *Applied Acoustics*, 138: 9-17, 2018.

Tunable shell stiffness of phospholipid coated monodisperse microbubbles for non-invasive blood pressure measurement

Tim Segers, Benjamin van Elburg, Guillaume Lajoinie, Michel Versluis

Physics of Fluids group, University of Twente, Enschede, The Netherlands

Corresponding author: t.j.segers@utwente.nl

Introduction

To date, invasive catheter-based methods are the only routine solution for in-vivo pressure measurements, e.g., to diagnose portal hypertension [1]. Therefore, the use of phospholipid-coated microbubbles for non-invasive blood pressure measurement has received considerable attention over the last decade. Hydrostatic pressure measurements using lipid-coated microbubbles relies on the change in the microbubble resonance frequency with ambient pressure. Increased ambient pressure decreases the bubble size, which leads to an increased lipid packing density which in turn increases shell elasticity until the buckling radius is reached, see Fig. 1A [2]. When the microbubble shell buckles, it reaches a surface tensionless state with a lower resonance frequency. Thus, the effective shell elasticity, and the corresponding resonance frequency, decreases with increasing ambient pressure. However, the use of this unique non-linear feature for blood pressure measurements is limited by the acoustic inhomogeneity of commercially available UCAs resulting from their polydispersity in size and shell properties.

Recently, we fully characterized the parameter space for stable monodisperse microbubble synthesis by flow-focusing [3]. We showed that coalescence-free microbubble suspensions are more efficiently produced at temperatures above room temperature [4]. However, optimal microbubble design for non-invasive blood pressure measurements requires more than control over microbubble size and stability alone, as shell stiffness governs the resonance frequency shift upon bubble compression. Tuning the shell stiffness of microfluidically formed bubbles remains a major challenge. Here, we show, for the first time, that the shell stiffness of microbubbles formed by flow-focusing can be precisely tuned over one order of magnitude with values between 0.5 N/m to 4.5 N/m. We also show that the subharmonic response of these monodisperse microbubbles is strongly dependent on the ambient pressure. This work is therefore a route to the design of novel contrast microbubble tailored for non-invasive blood pressure measurements.

Methods

Monodisperse bubbles were produced using the in-house developed BubbleMaker. It consists of precise flow-control and a feedback loop to control the size and monodispersity of the freshly formed bubbles in a microfluidic flow-focusing device (Fig. 1B). Two routes for control over the shell elasticity were investigated. First, the molar ratio of DPPE-PEG5000 was varied in the employed lipid mixture. Second, palmitic acid was added at molar ratios up to 60%. For both routes, DPPC and DSPC were used as a primary lipid mixed with DPPE-PEG5000 and palmitic acid. The microbubble suspensions were characterized by narrowband scattering and attenuation measurements at transmit frequencies ranging from 1 to 5 MHz and at peak negative acoustic pressures ranging from 10 to 100 kPa in steps of 10 kPa (Fig. 1C). The viscoelastic shell parameters were obtained from a model fit [2] to the attenuation spectra. In a second experiment, subharmonic scattering power was measured as a function of the ambient pressure. The transmit frequency was set to twice the resonance frequency of the bubble suspension measured at 100 kPa.

Results

It was found that the shell elasticity of microfluidically formed bubbles cannot be tuned through PEG5000 molar ratio variations. The shell elasticity of microbubbles formed using 5 to 10 mol% of DPPE-PEG5000 was 0.6 N/m for all molar percentages. On the other hand, we found a dramatic increase of the shell stiffness for lipid mixtures to which palmitic acid was added. Figure 1D shows the attenuation

spectra of a microbubble suspension measured at peak negative pressures of 10 to 100 kPa in steps of 10 kPa. At a pressure of 100 kPa, the resonance frequency of the microbubbles is 20% lower than that at a pressure of 10 kPa. By contrast, for microbubbles formed with a lipid mixture containing 60 mol% of palmitic acid, the resonance frequency decreases by 65% when the acoustic pressure is increased from 10 to 100 kPa, see Fig. 1E. The results show that shell stiffness can be tuned over one order of magnitude, i.e. from 0.5 N/m at zero palmitic acid concentration up to 4.5 N/m at a molar palmitic acid percentage of 60%.

Figure 1F shows that the subharmonic scattering response of monodisperse phospholipid coated bubbles is strongly dependent on the ambient pressure, i.e. it increases exponentially with ambient pressure. Thus, ambient pressure variations as small as 1 to 2 kPa can be measured when the bubbles are used at overpressures ranging approximately from 5 to 10 kPa.

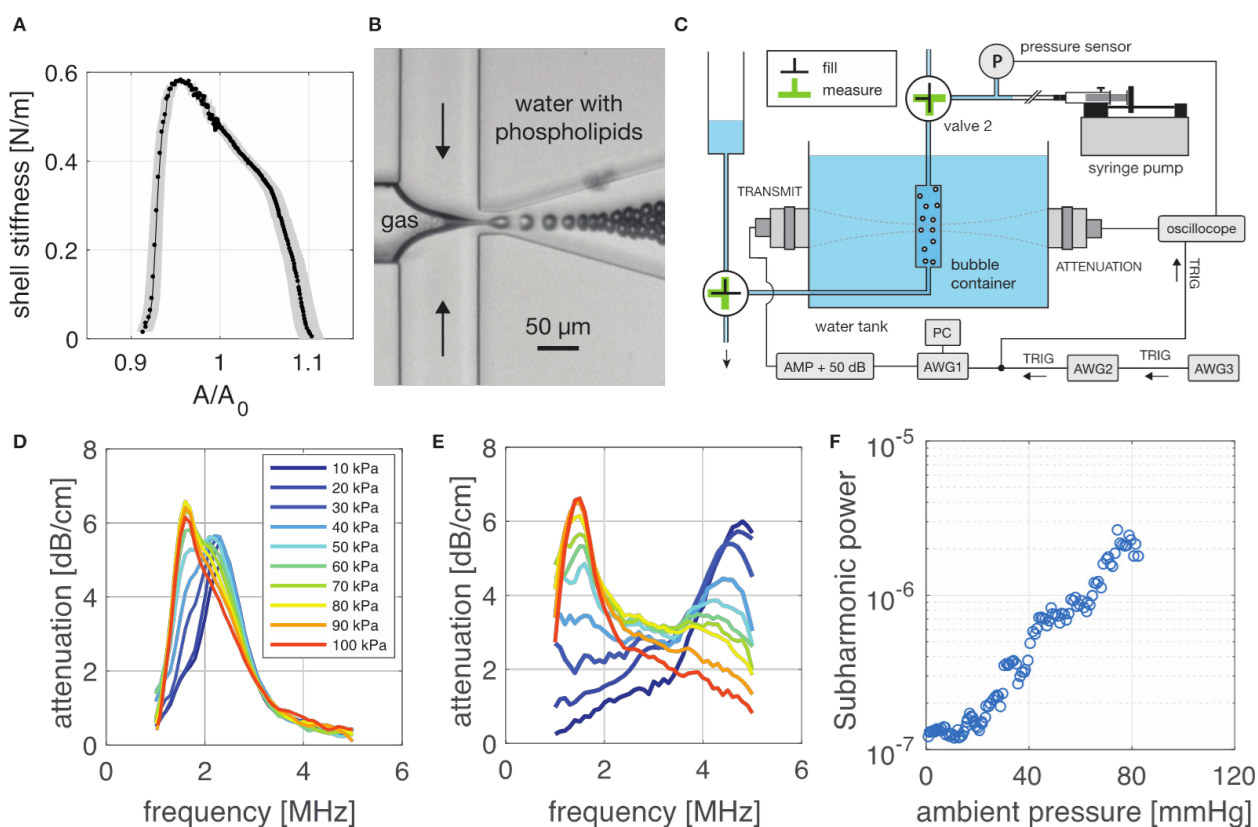


Fig. 1 (A) During bubble compression, the shell stiffness of lipid coated microbubbles first increases and then, at maximum compression, drops to zero as a result of a buckled monolayer. (B) Monodisperse bubbles were formed in a microfluidic flow-focusing device. (C) Acoustic characterization setup to measure the ambient pressure dependent resonance behavior and subharmonic response. (D) Attenuation spectra of microbubbles formed without palmitic acid. The shell elasticity was measured to be 0.5 N/m (E) Attenuation spectra of microbubbles formed with 60 mol% of palmitic acid. The shell stiffness was measured at 4.5 N/m. (F) Subharmonic scattered power as a function of the ambient pressure.

Conclusions

The shell stiffness of monodisperse phospholipid coated microbubbles can be tuned over one order of magnitude ranging from 0.5 N/m up to 4.5 N/m through the addition of palmitic acid to the lipid mixture. Furthermore, the subharmonic response of monodisperse microbubbles is strongly dependent on the ambient pressure. These new insights lay a foundation for the development of non-invasive blood pressure measurements using microbubbles and ultrasound.

References

- [1]. Tremblay-Darveau, Charles, Ross Williams, and Peter N. Burns. "Measuring absolute blood pressure using microbubbles." *Ultrasound in medicine & biology* 40.4 (2014): 775-787.
- [2]. Segers, T., Gaud, E., Versluis, M., & Frinking, P. (2018). High-precision acoustic measurements of the non-linear dilatational elasticity of phospholipid coated monodisperse microbubbles. *Soft Matter*.
- [3]. Segers, T., Lohse, D., Versluis, M., & Frinking, P. (2017). Universal Equations for the Coalescence Probability and Long-Term Size Stability of Phospholipid-Coated Monodisperse Microbubbles Formed by Flow Focusing. *Langmuir*, 33(39), 10329-10339.
- [4]. Segers, T., Lassus, A., Bussat, P., Guad, P., Frinking, P. (2018) Improved coalescence stability of monodisperse phospholipid-coated microbubbles formed by flow-focusing at elevated temperatures. *Lab on a Chip*, DOI: 10.1039/C8LC00886H

Nonlinear X-Wave Ultrasound Imaging of Acoustic Biomolecules

David Maresca¹, Daniel P. Sawyer², Guillaume Renaud³, Audrey Lee-Gosselin¹ and Mikhail G. Shapiro¹

¹Division of Chemistry and Chemical Engineering, California Institute of Technology, Pasadena, California 91125, USA

²Division of Biology and Biological Engineering, California Institute of Technology, Pasadena, California 91125, USA

Corresponding author: dmaresca@caltech.edu

The basic physics of sound waves enables ultrasound to visualize biological tissues with high spatial and temporal resolution. Recently, this capability was enhanced with the development of acoustic biomolecules—proteins with physical properties enabling them to scatter sound. The expression of these unique air-filled proteins, known as gas vesicles (GVs), in cells allows ultrasound to image cellular functions such as gene expression *in vivo*, providing ultrasound with its analog of optical fluorescent proteins. Acoustical methods for the *in vivo* detection of GVs are now required to maximize the impact of this technology in biology and medicine. We previously engineered GVs exhibiting a nonlinear scattering behavior in response to acoustic pressures above 300 kPa and showed that amplitude modulated (AM) ultrasound pulse sequences that excite both the linear and nonlinear GV scattering regimes were highly effective at distinguishing GVs from linear scatterers like soft biological tissues.

Unfortunately, the *in vivo* specificity of AM ultrasound imaging is systematically compromised by the nonlinearity added by the GVs to propagating waves, resulting in strong image artifacts from linear scatterers downstream of GV inclusions. To address this issue, we present an imaging paradigm, cross amplitude modulation (xAM), which relies on cross-propagating plane-wave transmissions of finite aperture X waves to achieve quasi-artifact-free *in vivo* imaging of GVs [1]. The xAM method derives from counterpropagating wave interaction theory, which predicts that, in media exhibiting quadratic elastic nonlinearity like biological tissue, the nonlinear interaction of counterpropagating acoustic waves is inefficient. By transmitting cross-propagating plane waves, we minimize cumulative nonlinear interaction effects due to collinear wave propagation while generating a transient wave-amplitude modulation at the two plane waves' intersection. In both simulations and experiments, we show that residual xAM nonlinearity due to wave propagation decreases as the plane-wave cross-propagation angle increases. We demonstrate in tissue-mimicking phantoms that imaging artifacts distal to GV inclusions decrease as the plane-wave cross-propagation angle opens, nearing complete extinction at angles above 16.5 degrees. Finally, we demonstrate that xAM enables highly specific *in vivo* imaging of GVs located in the gastrointestinal tract, a target of prime interest for future cellular imaging. These results advance the physical facet of the emerging field of biomolecular ultrasound and are also relevant to synthetic ultrasound contrast agents.

Reference

- [1]. Maresca D, Sawyer DP, Renaud G, Lee-Gosselin A, and Shapiro MG, Nonlinear X-Wave Ultrasound Imaging of Acoustic Biomolecules, *Physical Review X*, 8: 041002, 2018.

Vascular imaging: Biomarker of systemic atherosclerosis/inflammation

Steven Feinstein, MD, FACC, FESC
Professor of Medicine/Cardiology
Rush University Medical Center
Chicago, Illinois, USA

Introduction

Atherosclerotic cardiovascular disease (ASCVD) remains the leading cause of morbidity and mortality, globally. (Lloyd-Jones 2010) Historically, the use of ultrasound imaging of the carotid artery has served as a unique biomarker or “window” for identification of a patient’s underlying cardiovascular risk. (Tardif, Heinonen et al. 2006) Thus, the presence and degree of atherosclerosis noted in the carotid arterial system would serve to classify or reclassify individuals for treatment.

Historically, measurements of the carotid intima-media thickness (c-IMT) provided an easily accessible, biomarker for the classification of cardiovascular risk for individuals as well as population cohorts.

Recently, the presence of carotid artery plaque superseded c-IMT as a more accurate biomarker of underlying cardiovascular disease. (Nambi, Chambless et al. 2010)

Today, measurement of total plaque volumes using 2D and 3D ultrasound techniques has supplanted the earlier c-IMT measurements as a predictor of future CV events. Standard 2D imaging, while clinically useful, has certain limitations when used for carotid artery imaging including persistent operator dependence, variable image quality and out-of-plane registration errors. (Staub, Partovi et al. 2010) Recent technological developments permit 3D volumetric characterization of arterial wall anatomy and function including plaque characterization with enhanced spatial resolution. (Ainsworth, Blake et al. 2005; Spence 2017) (Spence 2017) (Sillesen, Sartori et al. 2017) (Sandholt, Collet-Billon et al. 2017)

Another substantial advance includes the use of contrast-enhanced ultrasound imaging (CEUS). Combined with carotid artery ultrasound imaging, CEUS, provides a safe and effective method for assessing carotid arterial luminal surfaces, vessel patency, plaque morphology, and intra-plaque neovascularization including proliferation of adventitial vasa vasorum; all which represent markers of plaque vulnerability. (Feinstein 2004; Feinstein 2006) (Staub, Schinkel et al. 2010)

Paradigm change: Anatomy versus physiology

It is increasingly recognized that the genesis of major cardiovascular clinical events is not solely based on the concept that anatomic, linear progression culminates in a acute luminal obstruction. Rather, acute events are often triggered by pathologic events within an unstable plaque characterized by increased intra-plaque neovascularization driven by local hypoxia, inflammation, etc. (Hellings, Peeters et al. 2010) (Michel, Virmani et al. 2011) (Matic, Jesus Iglesias et al. 2018) This re-assessment of the vulnerable plaque physiology has ignited interest in developing an *a priori* biomarker for the identification of the plaque features that confer higher risk for subsequent adverse events.

In a landmark study in 2010, Hellings, et al., (Hellings, Peeters et al. 2010) reported that the presence of intra-plaque vessel density and intra-plaque hemorrhage were the only significant histological findings associated with plaque vulnerability and subsequent clinical cardiovascular events in a prospective analysis of 818 patients who underwent carotid endarterectomy. The authors further noted, that the presence of macrophage infiltration, large lipid core, calcification, and smooth muscle cell infiltration within the plaques were not associated with cardiovascular outcomes. These recent observations are consistent with earlier histopathology studies and cross-sectional studies of patients who had undergone

carotid endarterectomy and were found to have increased intra-plaque neovascularity compared to patients with no history of ASCVD events. (Fleiner, Kummer et al. 2004)

Contrast-enhanced Ultrasound Imaging (CEUS)

CEUS is composed of intravenously injected acoustic microspheres ("microbubbles") with a mean size of ~2 microns. These unique, acoustic microspheres act as surrogate red blood cells traversing unhindered through the capillaries providing unparalleled, real-time, organ perfusion, including intraplaque neovascularization. No other imaging modality, CT, MR or PET, provide the spatial and temporal heterogeneity of microvascular perfusion afforded by CEUS. In 1994, Alunex, was the first commercial ultrasound contrast agent approved by the FDA. (Feinstein, Cheirif et al. 1990) CEUS is now widely used internationally for organ and tissue perfusion, thus providing benefits to patients by avoiding unnecessary ionizing radiation, iodinated dyes, nucleotides, and Gadolinium. (Feinstein, Coll et al. 2009) Exceedingly small volumes are required clinically, such that the standard intravenous dose is 0.5-1.0ml with ~5-8x10⁸ microspheres/cc. The clinical safety, efficacy and improved patient outcomes have been well established. (Feinstein, Cheirif et al. 1990; Darge, Papadopoulou et al. 2013; Main, Hibberd et al. 2013; Main, Hibberd et al. 2014)

The first reported use of CEUS to identify intraplaque carotid artery neovascularization was published in 2004. (Feinstein 2004) and has been validated at multiple centers using histopathology correlations. These data are summarized in a recent meta-analysis in 2016. (Huang, Abdelmoneim et al. 2016) From their report, the authors concluded that CEUS is a promising, novel method for defining microvascular perfusion although, requires standardization.

With regard to CEUS clinical outcomes studies, Staub et al., noted in a retrospective study in 2009, that 147 who patients underwent CEUS exhibited a carotid arterial plaque in 76% of the study sample and (Staub, Patel et al. 2009) and the prevalence of intra-plaque neovascularization was 54%. The presence of intra-plaque neovascularization using CEUS was the most significant covariate associated with a prior history of clinical ASCVD events, including stroke and myocardial infarction (multivariable-adjusted odds ratio 4.0, 95% CI 1.3-12.6). These data suggest a strong association between intra-plaque neovascularization and ASCVD events. (Staub, Patel et al. 2009)

As an extension of the localized impact of using CEUS to identify carotid plaque vulnerability, investigators in 2013 correlated the degree of carotid artery intra-plaque neovascularization with the severity of systemic atherosclerosis in patients undergoing coronary arteriography, thus providing a broader platform of diagnostic utility. (Deyama, Nakamura et al. 2013)

Today, 3D imaging and CEUS provides enhancement of the entire vascular system including, luminal characteristics, plaque volumes, luminal ulcers and, intraplaque/adventitial neovascularization. Cantisani et al., were the first to report 3D CEUS of the carotid artery employed using advanced ultrasound technologies. (Gourineni V 2014) (Di Leo, Venturini et al. 2018) The combination of CEUS and 3D technologies is designed to reduce or eliminate operator dependence leading to a standardized approach for image registration and analysis of the arterial vascular system. This powerful combination foreshadows a leadership role for ultrasound imaging of the carotid artery as a biomarker for the prediction and management and treatment of impending cardiovascular events in at risk individuals and populations.

References

- [1]. Ainsworth, C. D., C. C. Blake, et al. (2005). "3D ultrasound measurement of change in carotid plaque volume: a tool for rapid evaluation of new therapies." *Stroke* 36(9): 1904-9.
- [2]. Darge, K., F. Papadopoulou, et al. (2013). "Safety of contrast-enhanced ultrasound in children for non-cardiac applications: a review by the Society for Pediatric Radiology (SPR) and the International Contrast Ultrasound Society (ICUS)." *Pediatr Radiol* 43(9): 1063-73.
- [3]. Deyama, J., T. Nakamura, et al. (2013). "Contrast-enhanced ultrasound imaging of carotid plaque neovascularization is useful for identifying high-risk patients with coronary artery disease." *Circ J* 77(6): 1499-507.

- [4]. Di Leo, N., L. Venturini, et al. (2018). "Multiparametric ultrasound evaluation with CEUS and shear wave elastography for carotid plaque risk stratification." *J Ultrasound*.
- [5]. Feinstein, S. B. (2004). "The powerful microbubble: from bench to bedside, from intravascular indicator to therapeutic delivery system, and beyond." *Am J Physiol Heart Circ Physiol* 287(2): H450-7.
- [6]. Feinstein, S. B. (2006). "Contrast ultrasound imaging of the carotid artery vasa vasorum and atherosclerotic plaque neovascularization." *J Am Coll Cardiol* 48(2): 236-43.
- [7]. Feinstein, S. B., J. Cheirif, et al. (1990). "Safety and efficacy of a new transpulmonary ultrasound contrast agent: initial multicenter clinical results." *J Am Coll Cardiol* 16(2): 316-24.
- [8]. Feinstein, S. B., B. Coll, et al. (2009). "Contrast enhanced ultrasound imaging." *J Nucl Cardiol* 17(1): 106-15.
- [9]. Fleiner, M., M. Kummer, et al. (2004). "Arterial neovascularization and inflammation in vulnerable patients: early and late signs of symptomatic atherosclerosis." *Circulation* 110(18): 2843-50.
- [10]. Gourineni V, S. S., Cao K, Jin J, Dentinger A, Mills D, Padfield DR, Wallace KD, Reddy V, Shur B, Yamout F, McCarthy, W, March R, Jacobs J, Liuzzo A, Goldin M, Adam D, Feinstein SB (2014). "3D Contrast-enhanced Ultrasound (CEUS) Imaging of Carotid Artery Plaques and Intra-plaque Angiogenesis." *Circulation* 130: A17471.
- [11]. Hellings, W. E., W. Peeters, et al. (2010). "Composition of carotid atherosclerotic plaque is associated with cardiovascular outcome: a prognostic study." *Circulation* 121(17): 1941-50.
- [12]. Huang, R., S. S. Abdelmoneim, et al. (2016). "Detection of Carotid Atherosclerotic Plaque Neovascularization Using Contrast Enhanced Ultrasound: A Systematic Review and Meta-Analysis of Diagnostic Accuracy Studies." *J Am Soc Echocardiogr* 29(6): 491-502.
- [13]. Lloyd-Jones, D. M. (2010). "Cardiovascular risk prediction: basic concepts, current status, and future directions." *Circulation* 121(15): 1768-77.
- [14]. Main, M. L., M. G. Hibberd, et al. (2013). "Acute mortality in critically ill patients undergoing echocardiography with or without an ultrasound contrast agent." *JACC Cardiovasc Imaging* 7(1): 40-8.
- [15]. Main, M. L., M. G. Hibberd, et al. (2014). "Acute mortality in critically ill patients undergoing echocardiography with or without an ultrasound contrast agent." *JACC Cardiovasc Imaging* 7(1): 40-8.
- [16]. Matic, L. P., M. Jesus Iglesias, et al. (2018). "Novel Multiomics Profiling of Human Carotid Atherosclerotic Plaques and Plasma Reveals Biliverdin Reductase B as a Marker of Intraplaque Hemorrhage." *JACC Basic Transl Sci* 3(4): 464-480.
- [17]. Michel, J. B., R. Virmani, et al. (2011). "Intraplaque haemorrhages as the trigger of plaque vulnerability." *Eur Heart J* 32(16): 1977-85, 1985a, 1985b, 1985c.
- [18]. Nambi, V., L. Chambless, et al. (2010). "Carotid intima-media thickness and presence or absence of plaque improves prediction of coronary heart disease risk: the ARIC (Atherosclerosis Risk In Communities) study." *J Am Coll Cardiol* 55(15): 1600-7.
- [19]. Sandholt, B. V., A. Collet-Billon, et al. (2017). "Inter-Scan Reproducibility of Carotid Plaque Volume Measurements by 3-D Ultrasound." *Ultrasound Med Biol* 44(3): 670-676.
- [20]. Sillesen, H., S. Sartori, et al. (2017). "Carotid plaque thickness and carotid plaque burden predict future cardiovascular events in asymptomatic adult Americans." *Eur Heart J Cardiovasc Imaging*.
- [21]. Spence, J. D. (2017). "3D Ultrasound for Imaging and Quantifying Carotid Ulcers." *AJNR Am J Neuroradiol* 38(5): E34-E36.
- [22]. Spence, J. D. (2017). "Approaching Automated 3-Dimensional Measurement of Atherosclerotic Plaque Volume." *J Am Coll Cardiol* 70(3): 314-317.
- [23]. Staub, D., S. Partovi, et al. (2010). "Correlation of carotid artery atherosclerotic lesion echogenicity and severity at standard US with intraplaque neovascularization detected at contrast-enhanced US." *Radiology* 258(2): 618-26.
- [24]. Staub, D., M. B. Patel, et al. (2009). "Vasa vasorum and plaque neovascularization on contrast-enhanced carotid ultrasound imaging correlates with cardiovascular disease and past cardiovascular events." *Stroke* 41(1): 41-7.
- [25]. Staub, D., A. F. Schinkel, et al. (2010). "Contrast-enhanced ultrasound imaging of the vasa vasorum: from early atherosclerosis to the identification of unstable plaques." *JACC Cardiovasc Imaging* 3(7): 761-71.
- [26]. Tardif, J. C., T. Heinonen, et al. (2006). "Vascular biomarkers and surrogates in cardiovascular disease." *Circulation* 113(25): 2936-42.

Quantitative CEUS Parameters for Detection of Neonatal Hypoxic Ischemic Injury

Misun Hwang¹, Anush Sridharan², Kassa Darge¹

*¹Department of Radiology, Children's Hospital of Philadelphia
Philadelphia, PA*

Corresponding author: Hwangm@email.chop.edu

Introduction

CEUS offers practical advantages over brain MRI and may also prove to be superior in depicting perfusion changes occurring at the microvascular level in neonatal hypoxic ischemic injury¹. Given its potential to serve as a diagnostic tool to objectively identify infants at high risk for hypoxic brain injury, we undertook this prospective cohort study to establish feasibility of obtaining CEUS and comparing it to available cerebral MRI perfusion data in neonates and infants at risk for HII.

Methods

All infants and neonates with open fontanels at risk for HII were recruited from the Neonatal Intensive Care Unit (NICU) and Pediatric Intensive Care Unit (PICU) at Johns Hopkins Hospital during a 6-month period in 2017. Parental consent was obtained prior to enrollment into this Institutional Review Board approved prospective observational cohort study. CEUS studies were subsequently categorized as normal or abnormal based on the follow-up MRI and/or clinical assessment. Image analysis of CEUS clips was performed offline on a desktop computer using the MATLAB (The Mathworks Inc., Natick, MA, USA) Image Processing Toolbox. The CEUS cine clips were imported into the MATLAB workspace in their DICOM (Digital Imaging and Communications in Medicine) format to prevent any additional image quality degradation through compression to an image format such as JPEG. All CEUS clips were reviewed by an US researcher (A.S) in conjunction with a pediatric radiologist (M.H) to identify regions of interest (ROIs) corresponding to the central gray nuclei and cortex. Once these ROIs were established, the averaged image intensity within each ROI was evaluated for the duration of the cine clip. Subsequently, the temporal image intensity data was used to generate time-intensity curves (TICs) for each of the ROIs corresponding to the central gray nuclei and cortex. In order to compensate for any motion or image artifacts, a regression based fit was performed to remove any outliers along the TIC that caused transient noise. For each curve, standardized CEUS perfusion metrics including peak enhancement (PE), time to peak (TTP), rise time (RT), wash-in slope or perfusion (PER), wash-in area under the curve (WiAUC) during RT, perfusion index (PERi; i.e., WiAUC/RT), rate of early wash-out, average intensity during early-washout were evaluated.

Results

Our results demonstrate that during the wash-in phase, brain perfusion ratios rather than absolute perfusion intensities are more accurate in detecting the presence of hypoxic ischemic injury ($p=0.06$ for ratios vs $p=0.12-0.85$ for absolute intensities). During the wash-out phase, rate of early wash-out was a more sensitive marker for detection of hypoxic ischemic injury than average intensity during early wash-out ($p=0.02$).

Conclusions

The study demonstrates that with further validation in a larger prospectively cohort, brain CEUS can advance as a useful bedside tool for diagnosis of neonatal hypoxic ischemic injury. This is of significant clinical importance, as neonates during their critical illness are not easy candidates for MRI and are in much need of a highly sensitive bedside tool for early diagnosis, monitoring, and prognostication.

Reference

- [1]. Hwang M. Introduction to contrast-enhanced ultrasound of the brain in neonates and infants: current understanding and future potential. *Pediatric Radiology*. 2018

Intravenous CEUS in a pediatric setting - common and rare applications

N. Lorenz¹, Th. Haufe¹, G. Heubner¹, L. Steffgen²

¹Children's Hospital, General Hospital of Dresden, Teaching Hospital of the Technical University Dresden

²Trainings-Zentrum Ultraschall-Diagnostik LS GmbH, Mainleus, Germany

Corresponding author: Norbert.Lorenz@khdn.de

Introduction

The European Medicines Agency (EMA) did not authorize the use of any ultrasonography contrast agent for pediatric intravenous use so far. In contrast, Lumason[®] (marketed in Europe as Sonovue[®] (Bracco Imaging SpA)) got the approval by U.S. Food and Drug Administration (FDA) for Contrast Enhanced Ultrasonography (CEUS) of the liver in both adults and infants. The EFSUMB European Federation of Societies for Ultrasound in Medicine and Biology) position statement of 2016 is a very useful tool for establishing CEUS in the pediatric setting.

Methods

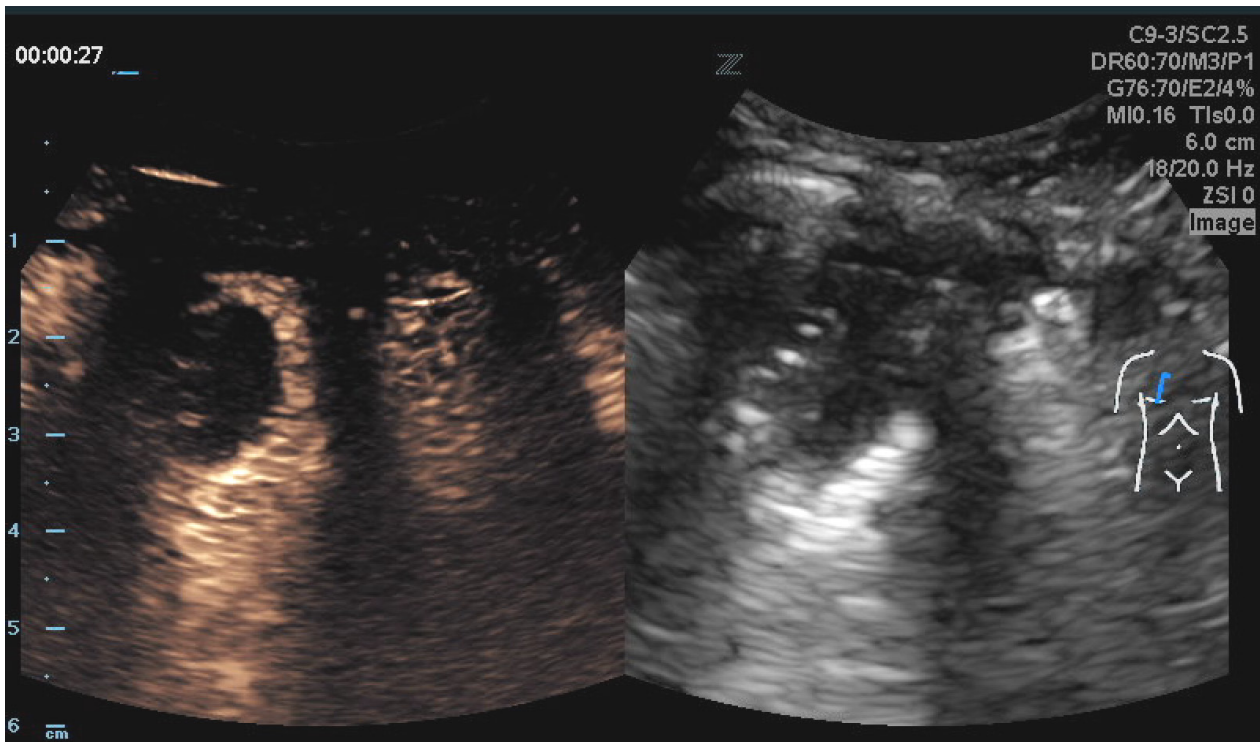
Report of all CEUS examinations performed at Children's Hospital at General Hospital of Dresden since the beginnings in 2016. CEUS exams were performed when indicated on the basis of the EFSUMB position statement. In every single case parents' and if applicable patients' informed consent was obtained by individual information on indication, off-label-use, safety and efficacy profile and alternatives of Sonovue[®] and its use as a CEUS agent. Written parental consent was given by use of a standardized form. All patients were followed up for one hour after CEUS and, if age appropriate, asked to describe any undesired effects.

Results

64 CEUS examinations were performed in 47 patients in a 3 years period using a ZS3 Zonare[®] ultrasound platform and Sonovue[®]. The patients' age range was 4 hours to 17 years. Common CEUS applications were in the liver (hemangioma, focal nodular hyperplasia, trauma) and kidneys (abscess, infarction, tubular interstitial nephritis, trauma). In selected rare cases patients were examined using CEUS in testis (testicular torsion, segmental infarction, post surgery perfusion), spleen (cysts, infarction, suspicious noduli), pulmonary abscess formation, parapharyngeal abscess formation and differentiation of a soft tissue tumor. Only one parent choose an other imaging modality than CEUS (intraabdominal abscess – MRI). No undesired effects of Sonovue[®] were observed.

Conclusions

Pediatric CEUS was a safe imaging tool in our setting and well accepted among patients, parents and colleagues. Pediatric CEUS is a fast and if needed bedside available method. The method is not only resource and time sparing but also not dependent on sedation in younger patients in comparison to MRI. A more widespread application of this method could be achieved by enhancing scientific discussion among colleagues.



Rare application: Lung abscess of 2 cm diameter in a consolidation of the right middle lobe in pneumonia caused by *Streptococcus pneumoniae* in an 11 month old infant

Prostate cancer localization based on multiparametric quantification of three-dimensional transrectal contrast-enhanced ultrasound

Rogier R. Wildeboer¹, Ruud J.G. van Sloun¹, P. Huang², H. Wijkstra^{1,3}, and M. Misch¹

¹Dept. of Electrical Engineering, Eindhoven University of Technology, The Netherlands

²Dept. of Ultrasonography, Second Affiliated Hospital of Zhejiang University, Hangzhou, China

³Dept. of Urology, Amsterdam University Medical Centers, University of Amsterdam, The Netherlands

Corresponding author: r.r.wildeboer@tue.nl

Introduction

Despite being a prominent field of biomedical research, imaging of prostate cancer (PCa) has not yet been demonstrated to enable replacing systematic biopsy (SBx) [1]. The latter procedure relies on a standard 10 to 12-core biopsy template to sample the prostate tissue for subsequent histopathological examination [2]. Reliable imaging does not only have the potential to reduce procedure time and patient discomfort, but it could potentially also reduce the incidence of SBx-related complications [3] and improve diagnostic accuracy by providing means for a targeted biopsy procedure.

Dynamic contrast-enhanced ultrasound (DCE-US) has been considered as one of the candidates for robust PCa diagnosis [4]. Especially three-dimensional (3D) DCE-US, alleviating the limitation of being bound to a 2D plane, might be used to characterize prostate tissue prior to biopsy [5]. The underlying principle is that the visualization of vascularity through the use of tiny microbubble contrast agents [6] could highlight changes in the microvascular network associated with cancer angiogenesis [7].

Over the years, several quantification algorithms have been developed to extract features from the dynamic DCE-US recordings that reflect those changes. For this, we analyse the contrast intensity over time (i.e., the time-intensity curve, TIC) as the contrast bolus spreads through the prostate vasculature. In 2D, TIC features ranging from the simple heuristic wash-in time to more sophisticated parameters representing contrast-agent velocity and dispersion were proven useful in the diagnosis of prostate cancer [8]–[10]. Especially in 3D, where the sizable volume videos are not readily interpreted, these parameters can considerably elevate the diagnostic potential [5], [11], [12].

The aim of this work is therefore to expand the former 2D-only analyses to three dimensions and investigate their joint potential for the localization of PCa. As shown in 2D, multiparametric combination by means of machine learning is capable of capturing complementary information of different parameters [13]. Therefore, we also compare the results of combined 3D quantification in volumetric regions of interest against the histopathological findings of SBx in those regions.

Methods

For this study, 43 patients with a suspicion of prostate cancer underwent a 12-core SBx procedure. Prior to the procedure, they received a 3D DCE-US recording using a 2.4-mL bolus injection of SonoVue® (Bracco, Milan, Italy), administered intravenously. The recording was carried out using GE's LOGIQ E9 ultrasound scanner equipped with a RIC5-9 probe at the Second Affiliated Hospital of Zhejiang University. The SBx cores were histopathologically examined [14], marking the corresponding tissue either benign (B), Gleason 3+3=6 insignificantly malignant (iPCa), or significantly malignant (sPCa).

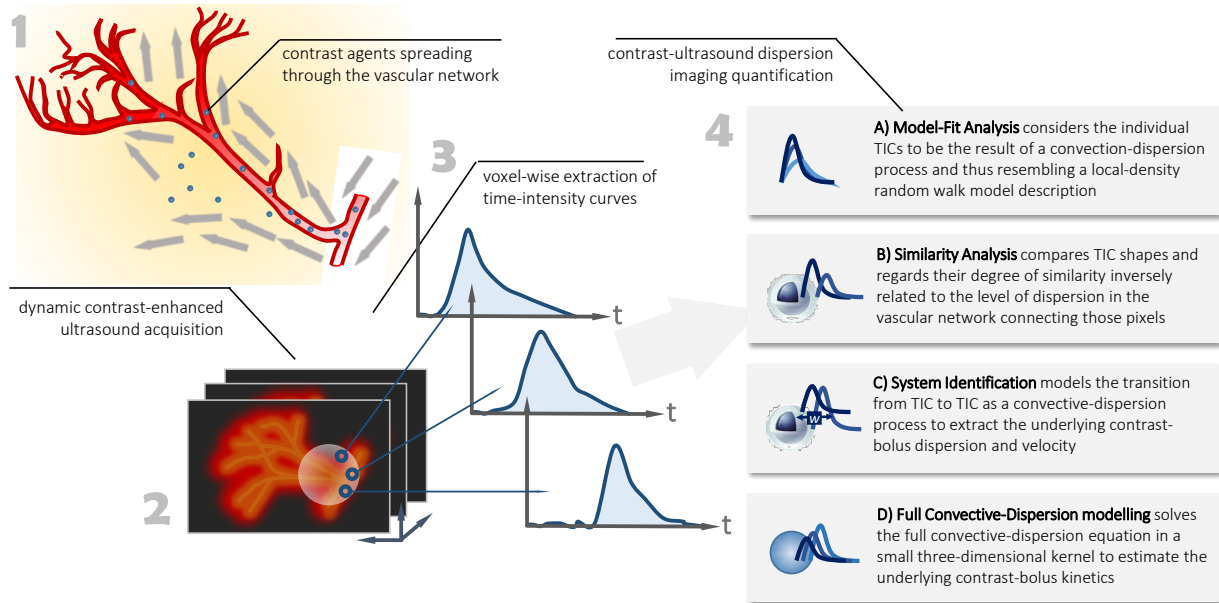


Fig. 1 Schematic representation of the CUDI framework, highlighting the (1) physiology, (2) imaging, (3) data extraction, and (4) CUDI analysis.

The volumetric contrast videos were subsequently extracted from the device and subjected to several quantification analyses. More specifically, all four Contrast Ultrasound Dispersion Imaging (CUDI) algorithms were expanded to 3D and used to generate parametric maps corresponding to the 3D DCE-US data (see Fig. 1). CUDI analysis is based on modelling of contrast bolus spreading through the prostate as a convective-dispersion process. Here, (1) **model-fit analysis** (i.e., fitting each voxel's TIC by a local-density random walk model) allows the estimation of several parameters related to dispersion and perfusion [8], whereas (2) **similarity analysis** compares the shape of the TICs in a small ring-shaped kernel to quantify the local degree of dispersion [9], [11]. In addition, the underlying convection and dispersion coefficients can be estimated by (3) **system identification** among voxels [10], or by solving the (4) **full convective-dispersion** equation in a small 3D kernel [12]. We refer to earlier publications for a more elaborate explanation of the individual quantification techniques.

The parametric maps resulting from the 3D CUDI analyses were appended with heuristic parameters and fractal dimension analysis [15] to create a dataset comprising 16 CEUS parameters that could be correlated to SBx-histopathology. To this end, we divided the volumetric maps into 12 regions of interest corresponding to the SBx locations [16], and computed the median parameter values per region. Their diagnostic potential was subsequently assessed using Receiver Operating Characteristics (ROC) analysis, more specifically, the area under the ROC curve. To combine the parameters, we employed machine learning through a Gaussian Mixture Model (GMM) which was trained in a leave-one-prostate-out cross-validation fashion. Features were selected within the training loop following the backward feature elimination scheme based on the ROC curve areas.

Results

The individual parameters had an appreciable classification performance for both PCa and sPCa versus the benign SBx-cores. The best-performing parameters in terms of PCa classification were convective-dispersion velocity (ROC = 0.71) and the wash-in time (ROC = 0.71). Best suited for classification of sPCa were the convective-dispersion velocity (ROC = 0.80) and the model-fitted mean transit time (ROC = 0.79).

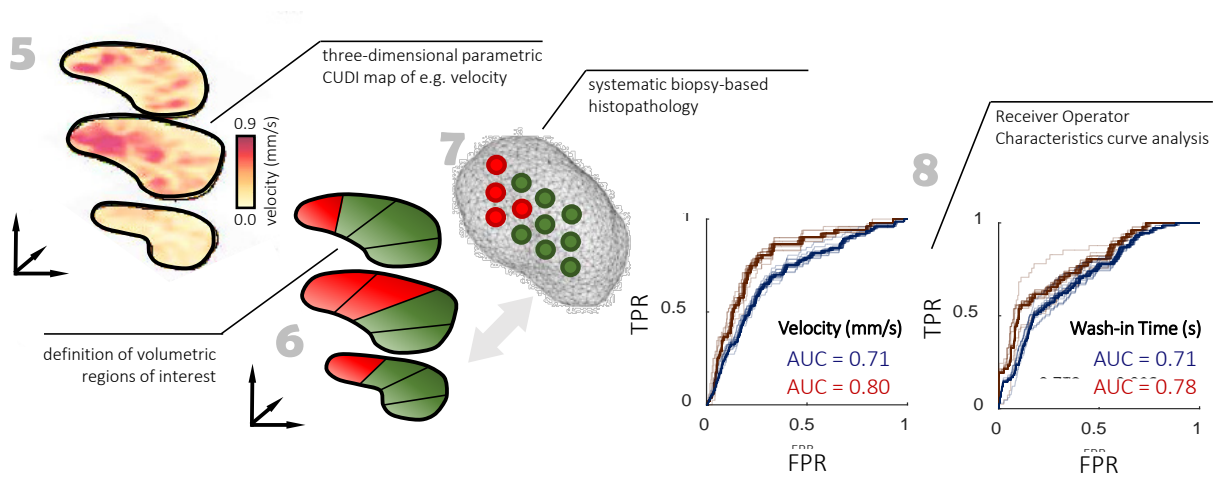


Fig. 2 (cont'd from Figure 1) Schematic representation of the validation framework, highlighting the (5) three-dimensional parametric maps, (6) region of interest allocation, (7) histopathology, and (8) ROC curves of both convective-dispersion velocity and the wash-in time.

The combined impact of quantification by means of multiparametric GMM improved the classification performance of the 3D DCE-US parameters to 0.76 and 0.81, respectively. A selection of the ROC curves is depicted as the final step in the schematic in Figure 2.

Conclusions

This work reports on the use of 3D DCE-US quantification for the localization of prostate cancer, showing appreciable results when correlating the median parameter values in volumetric regions of interest with the outcomes of SBx-histopathology. Moreover, we showed that a multiparametric 3D DCE-US approach could potentially add to the diagnostic accuracy of the technique.

We recognize that biopsy-core histopathology is limited by its tendency to undersample the tissue; therefore, tumour hotspots could have been missed or biopsy positions might have deviated from the centre of the corresponding region of interest. In future studies, this limitation will be alleviated through comparison of the parametric maps with whole-prostate pathology after radical prostatectomy, allowing us to assess the PCa localization performance on a smaller scale. Moreover, further assessment of the possible benign disease in false-positive regions of interest might elucidate on the relation between 3D DCE-US parameters and underlying physiology and spur the development of more specific imaging.

In the future, we hope to confirm the results of this preliminary study in an extended patient group, enabling also comparison with radical prostatectomy specimens. Extension of the dataset will also allow more extensive machine-learning strategies, which we deem a very promising approach given the feasibility shown in this work.

Acknowledgments

This research was conducted in the framework of the IMPULS2 program in collaboration with Philips. It also received funding from the Dutch Cancer Society (#UVA2013-5941), the European Research Council (#280209), and the National Natural Science Foundation of China (#81420108018 and #81527803).

References

- [1]. N. Mottet, J. Bellmunt, M. Bolla, E. Briers, M. G. Cumberbatch, M. De Santis, N. Fossati, T. Gross, A. M. Henry, S. Joniau, T. B. Lam, M. D. Mason, V. B. Matveev, P. C. Moldovan, R. C. N. van den Bergh, T. Van den Broeck, H. G. van der Poel, T. H. van der Kwast, O. Rouvière, I. G. Schoots, T. Wiegel, and P. Cornford, “EAU-ESTRO-SIOG Guidelines on Prostate Cancer. Part 1: Screening, Diagnosis, and Local Treatment with Curative Intent,” *Eur. Urol.*, vol. 71, no. 4, pp. 618–629, Jun. 2017.
- [2]. M. A. Bjurlin and S. S. Taneja, “Standards for prostate biopsy,” *Curr. Opin. Urol.*, vol. 24, no. 2, 2014.
- [3]. S. Loeb, A. Vellekoop, H. U. Ahmed, J. Catto, M. Emberton, R. Nam, D. J. Rosario, V. Scattoni, and Y. Lotan, “Systematic Review of Complications of Prostate Biopsy,” *Eur. Urol.*, vol. 64, no. 6, pp. 876–892, 2013.
- [4]. A. van Hove, P.-H. Savoie, C. Maurin, S. Brunelle, G. Gravis, N. Salem, and J. Walz, “Comparison of image-guided targeted biopsies versus systematic randomized biopsies in the detection of prostate cancer: a systematic literature review of well-designed studies,” *World J. Urol.*, vol. 32, no. 4, pp. 847–858, 2014.
- [5]. S. G. Schalk, L. Demi, M. Smeenge, D. M. Mills, K. D. Wallace, J. J. M. C. H. De Rosette, H. Wijkstra, M. Mischi, and S. Member, “4-D Spatiotemporal Analysis of Ultrasound Contrast Agent Dispersion for Prostate Cancer Localization : A Feasibility Study,” *IEEE Trans. Ultrason. Ferroelectr. Freq. Control*, vol. 62, no. 5, pp. 839–851, 2015.
- [6]. D. Cosgrove, “Ultrasound contrast agents: An overview,” *Eur. J. Radiol.*, vol. 60, no. 3, pp. 324–330, Dec. 2006.
- [7]. G. Russo, M. Mischi, W. Scheepens, J. J. De La Rosette, and H. Wijkstra, “Angiogenesis in prostate cancer: Onset, progression and imaging,” *BJU Int.*, vol. 110, no. 11 C, pp. 794–808, 2012.
- [8]. M. P. J. Kuenen, M. Mischi, and H. Wijkstra, “Contrast-ultrasound diffusion imaging for localization of prostate cancer,” *IEEE Trans. Med. Imaging*, vol. 30, no. 8, pp. 1493–1502, 2011.
- [9]. M. Mischi, M. P. J. Kuenen, and H. Wijkstra, “Angiogenesis imaging by spatiotemporal analysis of ultrasound contrast agent dispersion kinetics,” *IEEE Trans. Ultrason. Ferroelectr. Freq. Control*, vol. 59, no. 4, pp. 621–629, 2012.
- [10]. R. J. G. van Sloun, L. Demi, A. W. Postema, J. J. de la Rosette, H. Wijkstra, and M. Mischi, “Ultrasound-contrast-agent dispersion and velocity imaging for prostate cancer localization,” *Med. Image Anal.*, vol. 35, pp. 610–619, Jan. 2017.
- [11]. S. G. Schalk, J. Huang, J. Li, L. Demi, H. Wijkstra, P. Huang, and M. Mischi, “3-D Quantitative Dynamic Contrast Ultrasound for Prostate Cancer Localization,” *Ultrasound Med. Biol.*, vol. 44, no. 4, pp. 807–814, 2018.
- [12]. R. R. Wildeboer, R. J. G. van Sloun, S. G. Schalk, C. K. Mannaerts, J. C. van der Linden, P. Huang, H. Wijkstra, and M. Mischi, “Convective-Dispersion Modeling in Three-Dimensional Contrast-Ultrasound Imaging for the Localization of Prostate Cancer,” *IEEE Trans. Med. Imaging*, 2018.
- [13]. R. R. Wildeboer, A. W. Postema, L. Demi, M. P. J. Kuenen, H. Wijkstra, and M. Mischi, “Multiparametric dynamic contrast-enhanced ultrasound imaging of prostate cancer,” *Eur. Radiol.*, vol. 27, no. 8, pp. 3226–3234, 2017.
- [14]. R. Montironi, R. Mazzuccheli, M. Scarpelli, A. Lopez-Beltran, G. Fellegara, and F. Algaba, “Gleason grading of prostate cancer in needle biopsies or radical prostatectomy specimens: contemporary approach, current clinical significance and sources of pathology discrepancies,” *BJU Int.*, vol. 95, no. 8, pp. 1146–1152, 2005.
- [15]. T. Saidov, C. Heneweer, M. Kuenen, J. von Broich-Oppert, H. Wijkstra, J. de la Rosette, and M. Mischi, “Fractal dimension of tumor microvasculature by DCE-US: preliminary study in mice,” *Ultrasound Med. Biol.*, vol. 42, no. 12, pp. 2852–2863, 2016.
- [16]. O. Ukimura, J. A. Coleman, A. de la Taille, M. Emberton, J. I. Epstein, S. J. Freedland, G. Giannarini, A. S. Kibel, R. Montironi, G. Ploussard, M. J. Roobol, V. Scattoni, and J. S. Jones, “Contemporary Role of Systematic Prostate Biopsies: Indications, Techniques, and Implications for Patient Care,” *Eur. Urol.*, vol. 63, no. 2, pp. 214–230, Feb. 2013.

Contrast-enhanced Ultrasound and Computed tomography for Detection and Quantification of Endoleaks in EVAR

R. Kubale¹, A. Massmann¹, P. Fries¹, F. Frenzel¹, M. Lehnhard¹, K. Schlüter², A. Bücken¹, P. Minko¹

¹Klinik für Diagnostische und Interventionelle Radiologie, Homburg/Saar, Germany

²Klinik für Allgemeine Chirurgie, Viszeral-, Gefäß- und Kinderchirurgie, Homburg/Saar

Introduction

Endovascular aortic repair (EVAR) is associated with an endoleak rate type 2 of more than 20% . Regular controls are mandatory. Most often contrast-enhanced CT is used. The aim of this study was to compare contrast enhanced ultrasound (CEUS) for detection (1-3), quantification and follow-up of endoleaks using the dynamic properties of CEUS.

Methods

115 Patients underwent EVAR during 11/2012-10/2018 including hybrid-technique using chimney/periscope/double-barrel technique (n=24), for treatment of infra-/suprarenal true and mycotic aneurysms using various types of stentgrafts from six different vendors. Patients were followed up (mean follow-up 417 days) using CT-Angiography (CTA) (n=270) and CEUS (n=155). CEUS was performed blinded to the results of CTA with the use of i.v. application of sulphur hexafluoride (SonoVue, Bracco, Italy) on an Acuson S2000 with 4C1 and 6C1 scan heads (Siemens, Germany). Additionally, pairs of CTA-/CEUS-examinations were reviewed simultaneously by two experienced radiologists. For CEUS quantification software VueBox 6.0 and 7.0, Bracco was used. After linearization and standardization Time to Peak (TP), Rise Time (RT), Peak Enhancement (PE) and wash-in curves were calculated (fig.1) and correlated – if available - with results of perfusion CT (fig. 2: Somatom Force, SyngoVia, Siemens).

Results

61 patients (9 females; mean age 72.5±8.4) underwent 101 combined CTA-/CEUS-examinations. Endoleaks were detected by CEUS in 56% and by CTA in 48% of cases. Mismatch in detection of endoleaks was observed in 9%, in 4% related to artifacts in CEUS (1 false-negative and 3 false-positive). In 5%, CEUS proved advantageous over CTA due to dynamic assessment of late endoleaks not detected in CT due to an occurrence of more than 20 sec or beam hardening artifacts in CTA caused by embolization materials. In 7/11 patients different dynamic parameter of RT and TTP could be evaluated showing 4 types of early and late appearance with and without a short rise time (fig.3). In 6/7 patients prognosis concerning the persistence of the endoleak was possible.

Conclusions

1. Although CEUS is difficult during the first 3 days after the intervention due to postoperative artifacts and limiting postinterventional air inclusions, after that, both methods are comparable in detecting and classifying type and origin of endoleaks. After multiple interventions (embolization, coiling) CEUS is superior to CT due to beam hardening artifacts.
2. The difference of time to peak in combination combined with rise time was helpful for evaluating the prognosis and improve the differentiation of Type II and Type I / III endoleak.

References

- [1]. Jung E, Krauss M, Ritter W et al. 3D-Gefäßultraschall mit Power Mode zur Planung und Therapiekontrolle abdomineller, perkutan implantierter Aortenstentgrafts. Fortschr Röntgenstr 2000; 172: 888–893
- [2]. Clevert D, Sommer W, Meimarakis G. Contrast-enhanced ultrasound compared with multislice computed tomography for endovascular aneurysm repair surveillance. Ultrasound 2011; 19: 11–19
- [3]. Partovi, Sasan et al. Contrast enhanced Ultrasound after endovascular aortic repair – current status and future perspectives. Cardiovascular diagnosis and Therapy 2015, 454

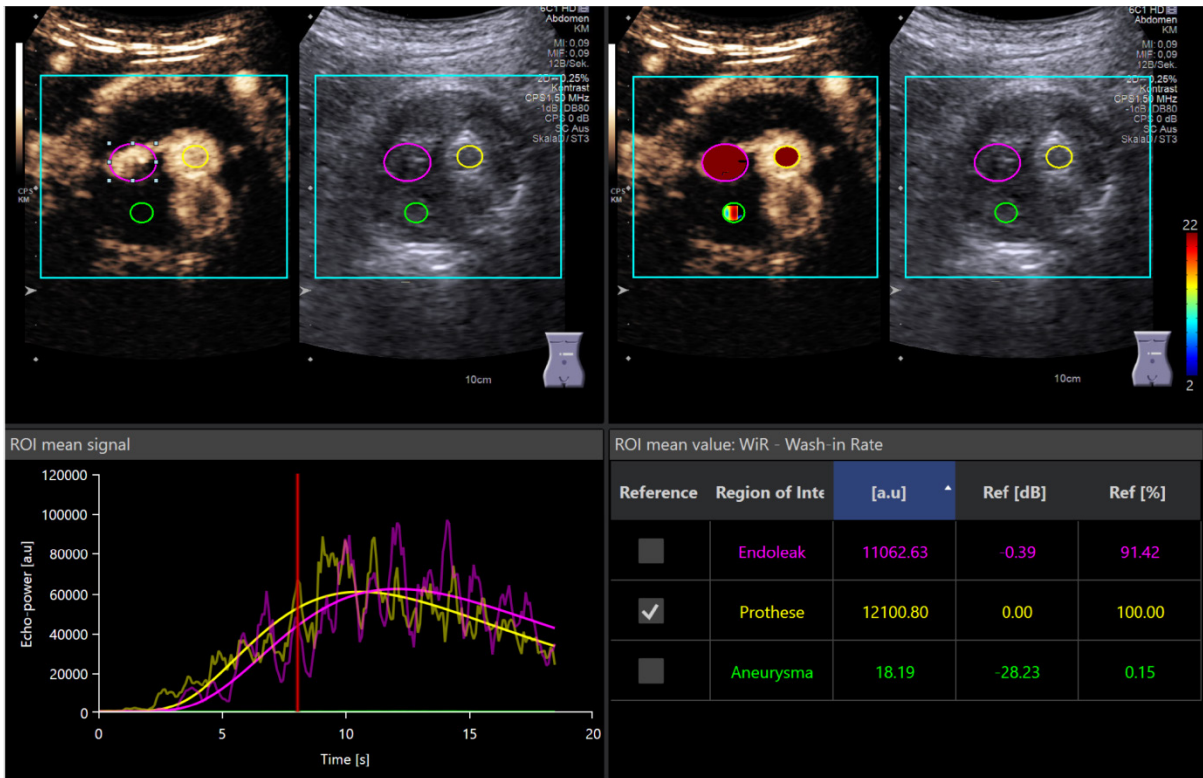
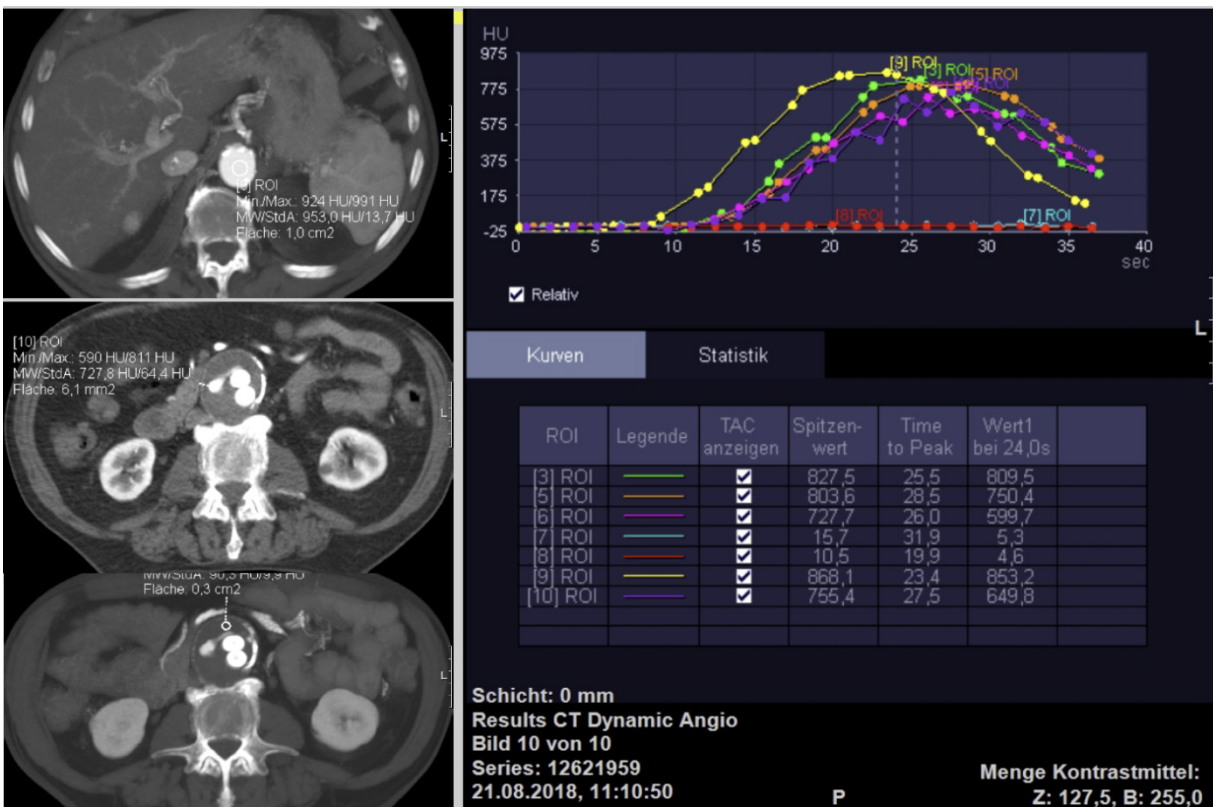


Fig.1: CEUS-Evaluation of an endoleak after less than 2 seconds with a very short rise time (yellow ROI: prothese, red ROI: endoleak, green ROI: occluded part of thze aneurysm). No occlusion of the endoleak during the next 6 month.



2: Dynamic CT of the above patient showing a synchronous enhancement of prostheses (orange and green) and endoleak (purple curve). The enhancement of the proximal aorta is shown in yellow, the occluded part of the aneurysm is marked in red.

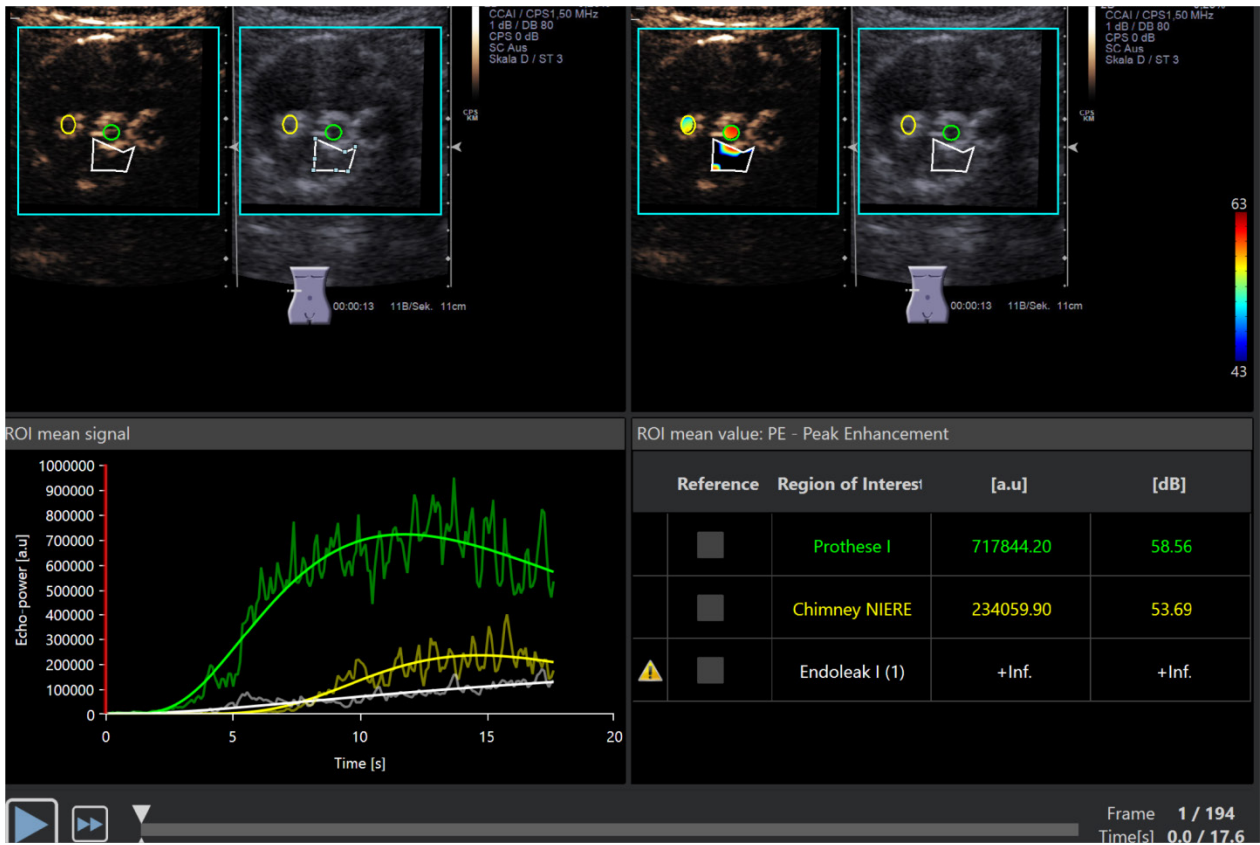


Fig. 3: CEUS-Evaluation of an endoleak coming very late and a very long rise time (green ROI: prothese, white ROI: endoleak, green ROI: chimney for the kidney). Spontaneous occlusion after 3 month.

Ultrafast Three-Dimensional Microbubble Imaging Predicts Tissue Damage Following Nonthermal Brain Ablation

Ryan M. Jones¹, Dallan McMahon^{1,2}, Kullervo Hynynen^{1,2,3}

¹Physical Sciences Platform, Sunnybrook Research Institute, Toronto, ON, Canada

²Department of Medical Biophysics, University of Toronto, Toronto, ON, Canada

³Institute of Biomaterials and Biomedical Engineering, University of Toronto, Toronto, ON, Canada

Corresponding author: rmjones@sri.utoronto.ca

Introduction

Nonthermal ablation via focused ultrasound and contrast agent microbubbles is under pre-clinical investigation for non-invasive brain surgery [1-7]. Existing sources of variability during the procedures can lead to inconsistent treatment outcomes and bioeffect generation outside of the intended target volume(s) [1,6,7], warranting the development of systems and methods for online monitoring and control prior to clinical translation. Our group has shown that three-dimensional (3D) microbubble imaging can be used to calibrate ultrasound exposure levels for inducing transient blood-brain barrier permeabilization without causing overt tissue damage [8]. In separate work, megahertz-rate processing of the acquired volumetric imaging data uncovered details regarding the spatiotemporal evolution of microbubble activity *in vivo* that were missed when temporal averaging was carried out over the duration of ultrasound on-time [9]. Here we investigate ultrafast 3D microbubble imaging for predicting the spatial distribution of tissue necrosis induced following nonthermal brain ablation.

Methods

Experiments were performed on craniotomized rabbits (≈ 2 cm x 2 cm window, 3-4 kg) using a multi-frequency transmit/receive ultrasound phased array consisting of 256 transducer modules (3 concentric cylindrical PZT4 elements, $f_0 = 306/612/1224$ kHz, inner/outer diameter = $1.4\lambda/2.0\lambda$, $\lambda =$ wavelength) sparsely distributed over a 31.8 cm diameter hemispherical shell [8]. Pulsed ultrasound ($f_0 = 612$ kHz, pulse length = 10 ms, pulse repetition frequency = 1 Hz, duration = 120 s) was electronically steered over a 2 x 2 point square grid (axial plane, side length = 6 mm) starting simultaneously with an intravenous microbubble infusion (200 μ l/kg DefinityTM over 90 s, 10 x maximum allowable clinical imaging dose) using a 3D subharmonic imaging-based feedback approach [8] that was modified to enable multi-point exposure level calibration. For all grid points, channel data were acquired throughout each transmit pulse (capture length = 14 ms, sampling rate = 10 MS/s) using the array elements tuned to the subharmonic frequency ($f_0/2 = 306$ kHz). Exposures were carried out at 0/50/100/150% of the peak negative pressure required to detect spatially-coherent subharmonic activity *in vivo* (p_{sub}) via multi-channel 3D beamforming [8]. The locations of the different exposure levels were randomized between animals. Short-time analysis of the acoustic emissions data (moving, non-overlapping rectangular beamforming windows spanning ultrasound on-time, integration time = 1 μ s) was performed offline. MRI was carried out at 3T to assess the induced tissue effects. Animals were sacrificed 48 hr post-treatment for histological examination.

Results

Multi-point exposure level calibration via 3D subharmonic imaging was feasible *in vivo* ($p_{\text{sub}} = 0.67 \pm 0.19$ MPa, intra-grid p_{sub} range = 0.14 ± 0.05 MPa, *in-situ* estimates). No statistical differences were found in the peak negative pressure subharmonic threshold between subgroups when the grid points were stratified based on either the exposure level or the target location within the brain ($p > 0.60$, one-way ANOVA). T_2^* -weighted (T_2^*w) MR images acquired immediately post-sonication displayed regions of signal hypointensity induced by the exposures at 100% p_{sub} and 150% p_{sub} , but not at lower target levels (Fig. 1). Hematoxylin-eosin (H&E) stained tissue sections associated the T_2^*w MRI signal hypointensities with the presence of red blood cell (RBC) extravasations and regions of tissue necrosis, the spatial extent

of which were both found to increase with increasing exposure level (Fig. 1). H&E histology also revealed small zones of RBC extravasations and tissue necrosis resulting from exposures at 50% p_{sub} that were not evident on T_2^*w MRI (Fig. 1). Ultrafast 3D subharmonic imaging data correlated well with the spatial distribution of T_2^*w MRI signal hypointensities (Fig. 1).

Conclusions

Volumetric imaging of ultrasound contrast agents *in vivo* over microsecond timescales shows promise as a method for predicting the spatial morphology of tissue damage induced following nonthermal brain ablation. The information provided by ultrafast 3D microbubble imaging is expected to aid in the development of active exposure control strategies for bubble-mediated ultrasound treatments both in the brain and in other parts of the body.

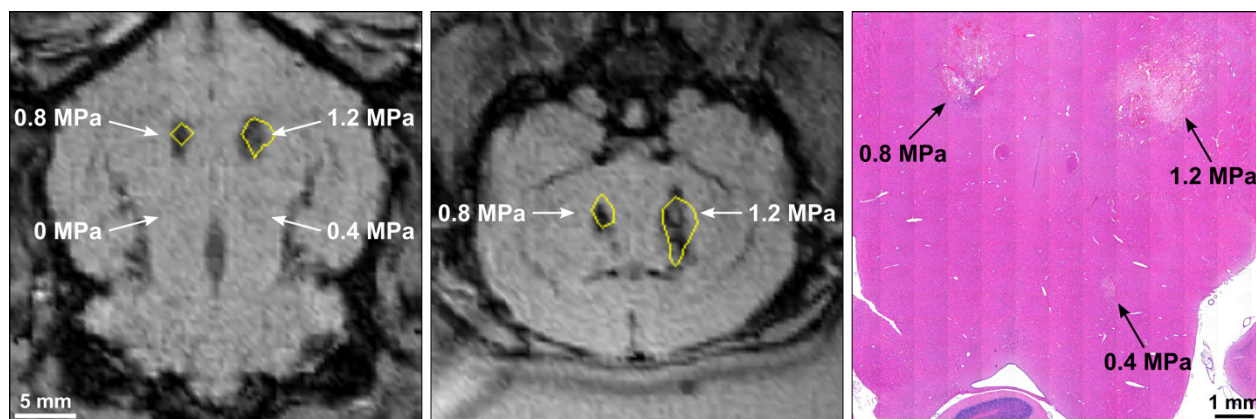


Figure 1: Spatial correlation of ultrafast 3D microbubble imaging data with ultrasound-induced tissue damage in rabbit brain *in vivo*. Axial (left) and coronal (middle) T_2^*w MR images acquired immediately post-sonication demonstrate regions of signal hypointensity induced by the exposures at 0.8 MPa (100% p_{sub}) and 1.2 MPa (150% p_{sub}). Yellow contours: -8 dB source field intensity distributions from the corresponding anatomical plane (1 MHz imaging volume rate, spatial-peak source field intensity location/magnitude integrated over each pulse for the full treatment duration). Axial H&E stained tissue section from the same animal 48 hours post-sonication (right) shows regions of RBC extravasations and lightly stained necrotic areas (arrows).

References

- [1]. McDannold NJ, Vykhodtseva NI, Hynynen K, Microbubble contrast agent with focused ultrasound to create brain lesions at low power levels: MR imaging and histologic study in rabbits, *Radiology*, 241:95-106, 2006.
- [2]. Vykhodtseva N, McDannold N, Hynynen K, Induction of apoptosis *in vivo* in the rabbit brain with focused ultrasound and Optison®, *Ultrasound Med Biol*, 32:1923-1929, 2006.
- [3]. Burke CW, Klibanov AL, Sheehan JP, Price RJ, Inhibition of glioma growth by microbubble activation in a subcutaneous model using low duty cycle ultrasound without significant heating, *J Neurosurg*, 114:1654-1661, 2011.
- [4]. Huang Y, Vykhodtseva NI, Hynynen K, Creating brain lesions with low-intensity focused ultrasound with microbubbles: a rat study at half a megahertz, *Ultrasound Med Biol*, 39:1420-1428, 2013.
- [5]. McDannold N, Zhang Y-Z, Power C, Jolesz F, Vykhodtseva N, Nonthermal ablation with microbubble-enhanced focused ultrasound close to the optic tract without affecting nerve function, *J Neurosurg*, 119:1208-1220, 2013.
- [6]. Arvanitis CD, Vykhodtseva N, Jolesz F, Livingstone M, McDannold N, Cavitation-enhanced nonthermal ablation in deep brain targets: feasibility in a large animal model, *J Neurosurg*, 124:1450-1459, 2016.
- [7]. McDannold N, Zhang Y, Vykhodtseva N, Nonthermal ablation in the rat brain using focused ultrasound and an ultrasound contrast agent: long-term effects, *J Neurosurg*, 125:1539-1548, 2016.
- [8]. Jones RM, Deng L, Leung K, McMahon D, O'Reilly MA, Hynynen K, Three-dimensional transcranial microbubble imaging for guiding volumetric ultrasound-mediated blood-brain barrier opening, *Theranostics*, 16:2909-2926, 2018.
- [9]. Jones RM, Hynynen K, Ultrafast three-dimensional imaging of contrast agent microbubble dynamics *in vivo* during pulsed ultrasound exposures in the brain. 18th Annual International Symposium for Therapeutic Ultrasound, 2018.

Single-cycle ultrasound drug delivery and passive acoustic mapping in the brain in vivo

Sophie V. Morse¹, Harry J. Davies¹, Matthew J. Copping¹, Tiffany G. Chan², Mengxing Tang¹, Nicholas J. Long², James J. Choi¹

¹NSB Laboratory, Department of Bioengineering, Imperial College London, London, United Kingdom

²Department of Chemistry, Imperial College London, London, United Kingdom

Corresponding author: j.choi@imperial.ac.uk

Introduction

Patients suffering from brain diseases, such as Alzheimer's and brain cancer, currently have no effective treatment available to them because drugs cannot cross the blood-brain barrier (BBB) [1]. The only method that can allow drugs into the brain non-invasively, locally and reversibly is focused ultrasound and microbubbles [2]. We have recently developed a new rapid short-pulse (RaSP) sequence that delivers drugs in vivo with minimal disruption to the microenvironment when compared to the more commonly used long-pulse sequences [3]. Using 5-cycle pulses emitted in a RaSP sequence, we altered the BBB permeability for less than 10 minutes, rather than hours or days, and released less neurotoxic blood proteins into the brain when compared to 10,000-cycle long pulses [3].

A crucial component to delivering drugs and delivering them safely is to ensure that the in vivo stimulated microbubble activity is of the intended magnitude and distribution. Passive acoustic mapping (PAM) methods can image this cavitation activity, but current algorithms cannot locate the activity with good precision due to the poor axial resolution [4-5]. Here, we will explore the use of a novel axial temporal position (ATP) algorithm that, when combined with the short pulses used in RaSP sequences, has the potential to improve the axial resolution of PAM and provide a better understanding of the cavitation activity generated in vivo.

Methods

Focused ultrasound was emitted in a RaSP sequence, consisting of microsecond pulses emitted at a rapid kHz rate (center frequency: 1.25 MHz, peak-rarefactional pressure: 530 kPa, pulse length: 1 cycle, phase: 220°, pulse repetition frequency: 1.25 kHz, burst length: 10 ms, burst repetition frequency: 0.5 Hz, number of pulses: 126). The ultrasound treatment was applied *in vivo* to the left murine hippocampus (n = 6) during the systemic injection of SonoVue[®] microbubbles and a fluorescently-tagged Texas Red 3 kDa dextran (model drug). The right hippocampus was used as a control. Dextran delivery was assessed post-mortem by cutting the brain into 30 µm slices with a cryostat and by acquiring fluorescence images. Acoustic emissions from the microbubbles were captured with an L7-4 linear array (center frequency: 5.2 MHz, number of elements: 128), positioned through the central cut-out of the therapeutic transducer. The ATP-PAM algorithm was used to reconstruct the spatial and temporal position of the acoustic emissions during ultrasound treatment. Given prior information regarding the speed of sound and distance between the transmitting transducer and the receiving linear array, the time of flight to and from all axial positions was calculated. Delay and sum beamforming was then performed across a window of data dependent on the number of cycles, center and sample frequency. Each axial position corresponded to a constrained window of sample data.

Results

The permeability of the BBB was altered using a 1-cycle pulse in all treated brains (Figure 1 (left)). To our knowledge, this is the lowest energy pulse reported to alter the BBB. Since the ATP-PAM resolution is dependent on the pulse length of the therapeutic beam, we were able to generate passive acoustic maps with exceptional resolution in vivo (Figure 1(Right)). Tail artefacts normally present in maps produced by

other algorithms, such as time exposure acoustics (TEA-PAM) and robust capon beamformer (RCB-PAM), were eliminated using ATP-PAM. Brain regions where drug delivery was observed corresponded to regions where activity was shown in the cumulative energy maps. Regions with highest activity on the acoustic maps also corresponded to regions where higher drug delivery was detected.

Conclusions

Short therapeutic pulses are here shown for the first time to enable drug delivery to the brain by emitting just 1 cycle pulses. In addition, our novel ATP-PAM algorithm was used to monitor microbubble activity *in vivo* with improved axial resolution, allowing acoustic sources to be resolved down to biologically relevant length scales. The combination of 1 cycle RaSP sequences and an appropriate high resolution monitoring system could enable safe and efficient drug delivery with more precise targeting of ultrasound treatment.

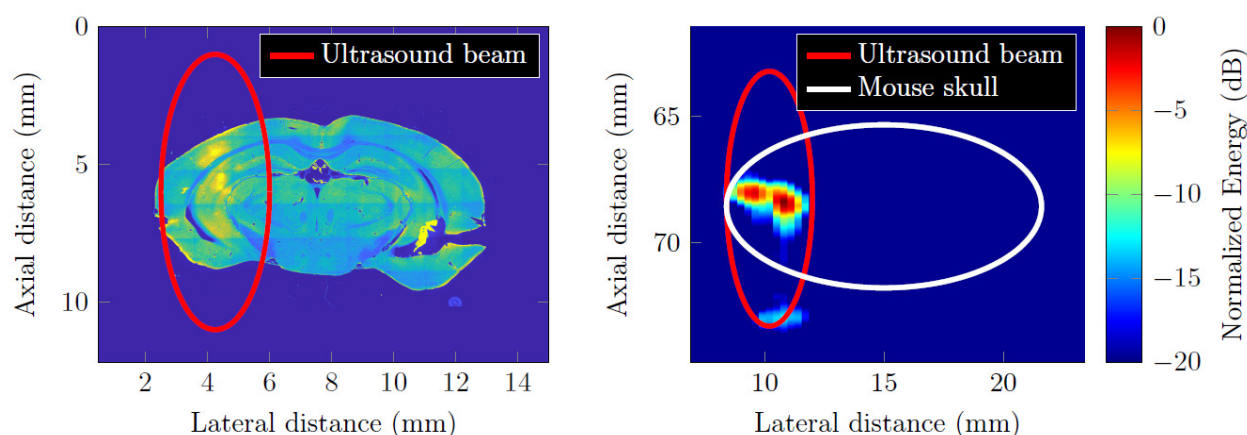


Figure 1. Drug delivery and acoustic energy map of an ultrasound and microbubble treated mouse brain. (Left) Fluorescence microscopy image of drug delivery to the left hippocampus of the murine brain using rapid short-pulse (RaSP) sequences emitting only 1 cycle pulses. The circle indicates the ultrasound beam. **(Right)** Cumulative energy map of microbubble activity in the left hippocampus acquired using a novel axial temporal position passive acoustic mapping (ATP-PAM) algorithm. Approximate brain and focal beam regions are indicated within circles.

References

- [1]. Pardridge, WM, The blood-brain barrier: bottleneck in brain drug development 2005, *NeuroRx: Journal of American Society for Experimental NeuroTherapeutics*, 2(1): 3-14.
- [2]. Hynynen, K et al, Noninvasive MR imaging-guided focal opening of the blood-brain barrier in rabbits 2001, *Radiology*, 220(3): 640-646.
- [3]. Morse, SV et al, Rapid short pulse ultrasound delivers drugs uniformly across the murine blood-brain barrier with negligible disruption 2019, *Radiology*, (in publication).
- [4]. Coviello, C et al, Passive acoustic mapping utilizing optical beamforming in ultrasound therapy monitoring 2015, *The Journal of the Acoustical Society of America*, 137.
- [5]. Gyongy, M et al, Passive spatial mapping of inertial cavitation during HIFU exposure 2010, *IEEE Transactions on Biomedical Engineering*, 57(1): 48-56.

Predictive Real-Time Monitoring of Cavitation-Enhanced Immunotherapies by Passive Acoustic Mapping

Christophoros Mannaris^{1*}, *Prateek S. Katti*^{1,2,3*}, *Cameron A. B. Smith*¹, *Cliff Rowe*⁴,
*Christian Coviello*⁴, *Joanna Hester*³, *Robert Carlisle*¹, *Constantin Coussios*¹

¹*Biomedical Ultrasonics, Biotherapy & Biopharmaceuticals Laboratory (BUBBL)
Institute of Biomedical Engineering, Department of Engineering Science,
University of Oxford, OXFORD, UK*

²*Center for Interventional Oncology, National Institutes of Health
10 Center Drive, BETHESDA, USA*

³*Nuffield Department of Surgical Science, University of Oxford
John Radcliffe Hospital, OXFORD, UK*

⁴*OxSonics Ltd
The Magdalen Centre, Oxford Science Park
Robert Robinson Avenue, OXFORD, UK*

*Corresponding author: christophoros.mannaris@eng.ox.ac.uk
contributed equally to the work being presented

Introduction

Therapeutic antibodies which act to turn on immune responses against cancer by blocking immune checkpoints are demonstrating potent therapeutic efficacy across a wide range of cancers, but typically only a fraction of patients treated clinically respond. We hypothesise that poor penetration and inadequate distribution of these large therapeutic agents in solid tumours is a key contributor to the observation of inconsistent therapeutic responses and propose the use of sustained ultrasound-induced inertial cavitation as a tool to overcome this barrier.

Passive acoustic mapping (PAM) [1] now provides unprecedented opportunity to qualify and quantify spatio-temporal variations in cavitation activity during treatment. Here, building on data acquired from over 300 tumour-bearing mice treated with ultrasound and simultaneous intravenous administration of a cavitation nucleation agent and a drug, we pose the question as to whether quantification of the real-time PAM signal during treatment can be predictive of drug delivery and longer-term therapeutic outcomes.

Methods

Bilateral CT26 tumour-bearing mice were utilised to assess the delivery and distribution of a fluorescently labelled (VivoTag, Perkin Elmer, MA, USA) therapeutic antibodies (BioXCell, West Lebanon, NH, USA) with and without inertial cavitation seeded by gas-stabilised solid nanoparticles (OxSonics, UK). 0.5 MHz ultrasound with peak rarefactional pressures of 1-2 MPa and duty cycles in the range 0.05-5% was delivered using a pair of orthogonal single element transducers, while real time PAM monitoring was carried out using two orthogonal linear arrays (L11-5, Verasonics, WA, USA) placed coaxially with each of the two therapeutic transducers. Tumours were immediately excised and delivery quantification was performed using an IVIS Spectrum Imaging system (Perkin Elmer, Waltham, MA, USA). The optimal ultrasound exposure parameters that maximized drug delivery enhancement relative to the contralateral non-ultrasound-treated tumour were first identified by correlating the type, intensity, spatial distribution and overall persistence of cavitation activity to drug delivery across the ultrasound-treated tumour. The optimal conditions were then used in 4 independent therapy studies where different combinations of non-therapeutic isotype (IgG) and checkpoint inhibitor antibodies (including aPD1 and aPD1) were intravenously co-injected with the cavitation nucleation agent and delivered to single-CT26 tumour-bearing mice using ultrasound, with monitoring of 90-day survival across all groups.

Results

During the parameter optimization study, an enhancement in antibody delivery was observed in 23/24 of all cavitation treated tumours relative to each of the 24 contralateral controls across the range of acoustic parameters tested. Consistent 2 to 3-fold enhancements in antibody delivery were achieved in groups treated with higher duty cycles (5%) and longer pulse durations (>1000 cycles), irrespective of the antibody used. Real-time PAM of all ultrasound-treated tumours evidenced sustained inertial cavitation activity throughout the 10-minute treatment period, with little evidence of non-inertial cavitation. A treatment-specific cavitation dose was derived by integrating the PAM-positive pixels over the tumour ROI over time, which was directly correlated to the observed enhancement in drug delivery. Preliminary analysis of the PAM signal recorded during the subsequent therapeutic studies indicates that the PAM-derived cavitation dose is predictive of non-responders, partial responders and full responders.

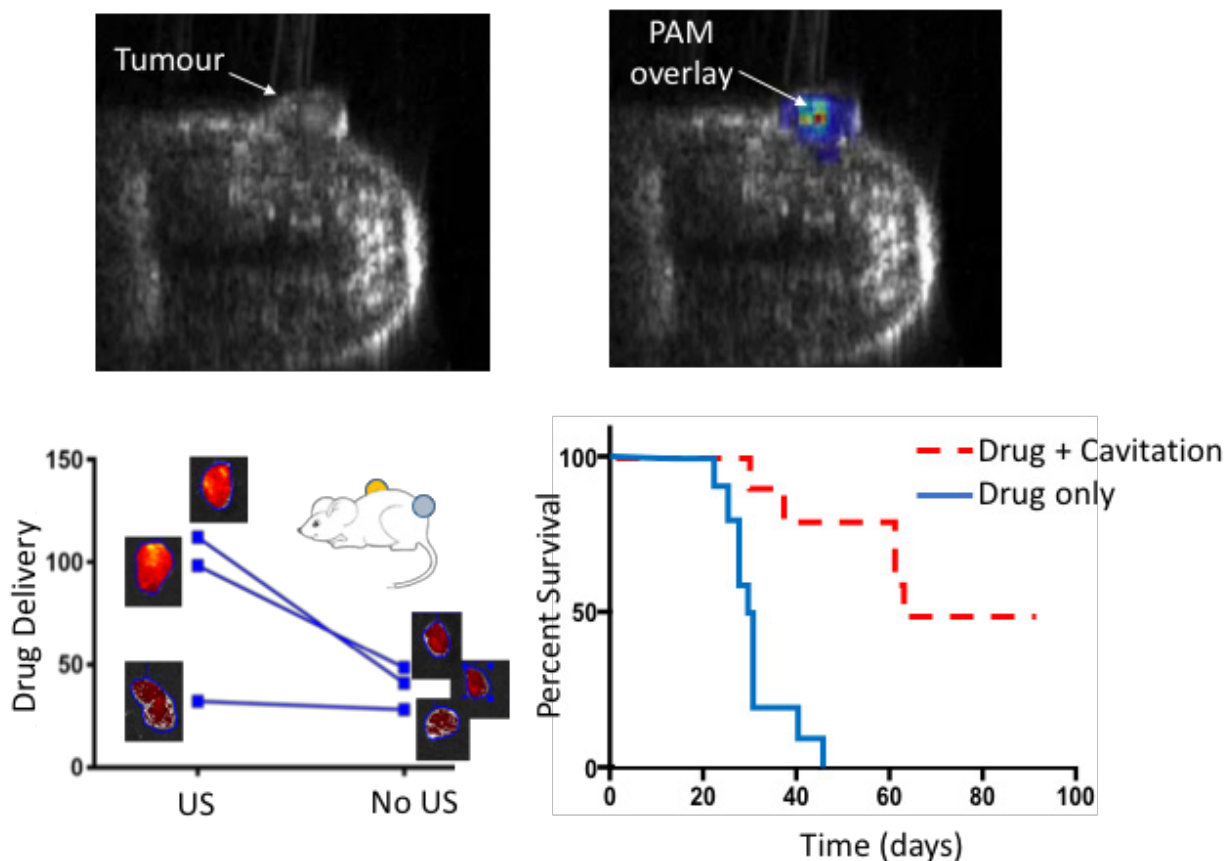


Figure 2: Passive acoustic mapping (PAM) was utilized to qualify and quantify the impact of spatio-temporal variations in cavitation activity during treatment in drug delivery and survival studies (500+ procedures). Drug-delivery studies tracked florescent-antibody accumulation in bilateral tumour bearing mice where one tumour was sonicated after systemic administration of nanobubbles and drug. Efficacy studies compared survival outcomes of single-tumor bearing mice administered nanobubbles and therapeutic antibody alone or with ultrasound.

Conclusions

Passive Acoustic Mapping (PAM) of cavitation activity provides a real-time means of monitoring and optimizing therapeutic antibody delivery during treatment that is predictive of drug delivery enhancement and potentially predictive of therapeutic outcomes.

Reference

- [1]. C. Coviello et al., "Passive acoustic mapping utilizing optimal beamforming in ultrasound therapy monitoring," J. Acoust. Soc. Am., 2015.

Perfusion-Guided Monitoring of Tumor Response to Sonoporation and Prediction of Liposomal Doxorubicin Uptake Using Microbubble Contrast Agents

Aditi Bellary¹, Arelly Villarreal¹, Rojin Eslami¹, Quincy Undseth¹, Sonia Hernandez², Bianca Lec², Jessica Kandel², Mark Borden³, Sumbul Shaikh⁴, Rajiv Chopra⁴, Shashank Sirsi^{1,4}

¹Department of Biomedical Engineering, University of Texas at Dallas, Richardson, TX, USA

²Department of Surgery, University of Chicago Medical School, Chicago, IL, USA

³Department of Mechanical Engineering, University of Colorado at Boulder, Boulder, CO, USA

⁴Department of Radiology, University of Texas Southwestern Medical Center, Dallas, TX, USA

Corresponding author: Shashank.Sirsi@utdallas.edu

Introduction

Microbubble ultrasound contrast agents (UCAs) are frequently used for *in vivo* imaging applications to monitor changes in tumor perfusion. Additionally, volumetric changes of microbubbles in an ultrasound field can promote drug extravasation into tumor tissue by a technique called “sonoporation”. In this study, we demonstrate that UCAs can simultaneously be used to both monitor and modulate tumor vasculature permeability using 2D and 3D quantitative contrast enhanced ultrasound imaging (qCEUS). Our study demonstrates that qCEUS parameters correlate strongly with sonoporation-mediated chemotherapeutic uptake in tumors using liposomal doxorubicin (L-DOX). Thus, qCEUS can provide real-time feedback that can be used to evaluate and control drug dosages that are delivered to tumor tissue during personalized therapy. Furthermore, we show that sonoporation can be used to effectively improve L-DOX delivery to neuroblastoma tumor models, which is not achievable using L-DOX administration alone. Therefore, the technique we are developing can have clinically significant implications in poorly perfused tumors and/or tumors that do not exhibit an enhanced permeability and retention (EPR) effect, on which

the majority of current nanoparticle delivery strategies are predicated.

Methods

Matrigel plugs were used as mock tumors that promote neovascular growth when injected subcutaneously in mice. The matrigel was mixed with 1 μ g basic fibroblast growth factor and heparin, then injected subcutaneously into 6-8 week old CD-1 mice. The vasculature was allowed to grow for 10-14 days in the matrigel plug then imaged using lipid-stabilized microbubble contrast agents. Microbubbles were fabricated using the commercially available lipids 1,2-distearoyl-*sn*-glycero-3-phosphocholine (DSPC) and 1,2-distearoyl-*sn*-glycero-3-phosphoethanolamine-N-[methoxy(polyethylene glycol)-2000] (DSPE-PEG2K) mixed at a 9:1 ratio in a lipid suspension at 2 mg/mL in PBS and emulsified with hydrophobic perfluorobutane gas. Microbubbles were injected systemically via tail vein injections (5 X 10⁷ MBs in 100 μ L at a rate of 50 μ L/min) and perfusion was monitored using an Acuson Sequoia 512 ultrasound imaging scanner with a 15L8 probe and proprietary LabVIEW software to analyze US video data. A custom motorized stage was built

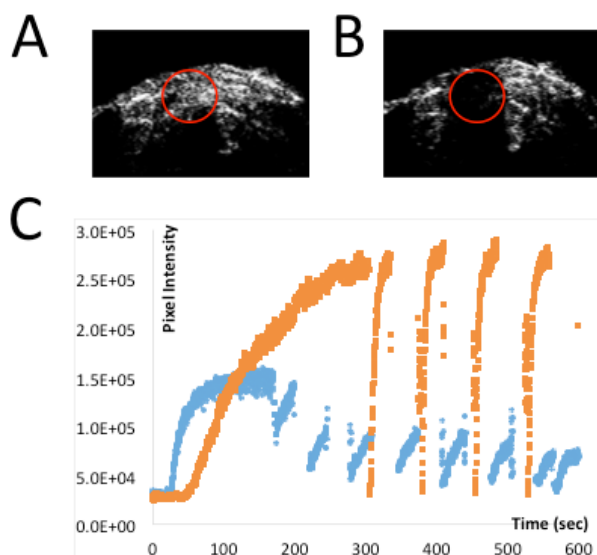


Figure 1. Perfusion-guided imaging of matrigel plug tumor models using q-CEUS imaging techniques to provide real-time feedback of sonoporation effects. A) Non-linear 2D imaging of tumors showing contrast enhancement before sonoporation. B) Focused ultrasound destruction of microbubble contrast agents *in vivo*. C) Time-intensity curves from two different matrigel mock tumors given the same concentration of bubbles and focused ultrasound energy (multiple treatments). qCEUS used to monitor bioeffects effects of focused ultrasound treatment on tumor vasculature.

to acquire 3D ultrasound images. Additionally, a rotating syringe pump was designed to administer sustained contrast agent infusions to the tumors. After gauging initial perfusion, matrigel plugs were sonoporated using a therapeutic ultrasound machine at 3 W/cm^2 (1 MHz, 10% duty cycle) for 10 minutes with a high dose of microbubbles (1×10^9 MBs) mixed with 25 mg/kg L-DOX. Matrigel plugs (along with liver, contralateral kidney, and heart) were excised to assess drug uptake using an acidified isopropanol extraction to recover doxorubicin. The doxorubicin was quantified with a fluorescent plate reader.

Results

Matrigel sonoporation resulted in significantly higher levels of doxorubicin uptake compared to non-sonoporated controls (~5 fold increase, $p < 0.05$). Organ distribution of doxorubicin outside of the tumor was not altered, meaning that its therapeutic index was increased. Our custom software allows for 3D vascular perfusion imaging throughout the entire tumor volume as well as 2D destruction-replenishment imaging. 3D imaging of the tumors was performed to establish a baseline of vascular perfusion prior to L-DOX delivery via sonoporation. The data reveals a strong correlation between initial tumor perfusion and L-DOX accumulation, indicating that qCEUS imaging can be employed as a predictor of whether tumors are amenable to L-DOX uptake. We also noted that reperfusion kinetics are detectably altered during sonoporation, suggesting that qCEUS can effectively show the degree of vessel permeabilization. Reperfusion rates of UCAs correlated strongly with doxorubicin uptake in tumors as well, implying that perfusion-guided therapy can be harnessed to increase localized drug deposition in tumors.

Conclusions

Currently we are able to demonstrate significantly improved L-DOX uptake in mock tumors using ultrasound-mediated sonoporation. Our preliminary data in NGP neuroblastoma models shows higher uptake and intratumoral drug penetration of doxorubicin in sonoporated tumors. In this study we found quantitative 2D and 3D perfusion imaging to be an excellent predictor of drug uptake and sonoporation efficiency in tumors, which has substantial clinical impact in the design of tailored drug treatment regimens for patients.

Image-guided bubble-enhanced thermal ablation

Dingjie Suo, Eric Juang, Sara Keller, Conner Pitts, Mike Averkiou

Department of Bioengineering, University of Washington, Seattle, WA, USA

Corresponding author: dsuo@uw.edu

Introduction

High-intensity focused ultrasound (HIFU) is used for thermal ablation of uterine fibroids and a variety of cancer types such as liver, pancreas, prostate, kidney, breast, and bone metastasis. By focusing all ultrasound energy in a small area, HIFU can raise the temperature by 60 °C (or more) and induce necrosis. The size of the thermal lesion, which correlates with the focal spot, is in the order of a few mm and therefore the induced heating does not affect or damage the surrounding areas on the pre- and post-focal regions. More recently, HIFU has been used in the brain for locally-controlled thermal treatment of Parkinson's disease, essential tremor, and neuropathic pain [1]. However, in brain applications, most of the acoustic energy is either absorbed or reflected by the skull and thus very high intensities are required to produce thermal lesions. In addition, the thermal lesion location is restricted to a small area due to geometric and boundary limitations. Even with strong focusing, there is a concern that the acoustic energy may cause unwanted tissue damage or skin and skull burns.

Controlled bubble-enhanced heating (BEH) has been suggested as a method to considerably lower the required acoustic energy for a certain temperature elevation. By adding microbubble ultrasound contrast agents, it is possible to initiate controlled cavitation and generate spatially and temporally controlled thermal lesions. Other recent studies have also suggested that BEH can be effective in vitro and in vivo [2, 3]. To further optimize BEH and use it clinically, the bubble dynamics and heat transfer mechanisms should be investigated.

The main objective of the present work was to study and perform BEH in vitro. We have first evaluated the microbubble behavior at higher temperatures in the range 20-60 °C. Next, we used HIFU with and without microbubbles to heat glycerol in vitro. The increase in temperature was measured with fine wire thermocouples. A focused 1 MHz transducer and 2 different types of microbubbles were used. Next, we investigated BEH in gel phantoms with embedded bubbles under image guidance.

Methods

We evaluated microbubble behavior at higher temperatures by imaging microbubbles flowing in an ATS flow phantom with an ultrasound scanner (Philips iU22) at three temperatures: 22, 40, and 60 °C. The experimental setup is shown in Fig. 1(a). The image intensity in a region of interest (ROI) in the middle of the flow channel was measured at three different mechanical indices (MIs), 0.05, 0.33, and 0.83. Images were collected at 0.5 Hz frame rate (every 2 sec) in order to allow time for fresh bubbles to enter the ROI after bubble destruction with the higher MI's (0.33 and 0.83). We collected 60 sec video loops and extracted time-intensity curves (TIC) with QLab analysis software. Two different types of microbubbles were used: one custom type that we make at the lab, and one commercial.

The experimental setup used for the in vitro BEH study is shown in Fig. 1(b). The 1 MHz focused transducer moves with a 3-axis computer-controlled micropositioner. The temperature changes in the sample were measured by two fine wire thermocouples, one at the focus and one far enough from the focus that it effectively records the fluid ambient temperature. An imaging probe (C5-1, Philips, Bothell, WA) is used to align the thermocouple with the transducer focus and then monitor the microbubble activity. We have evaluated the following parameters on their effect on BEH: acoustic pressure (1–3 MPa), duty cycle

(20%-100%), microbubble concentration ($10^4 - 10^6$ bubbles/ml), and type of microbubbles. First, we have induced BEH in glycerol contained in an enclosure with acoustic windows by generating bubbles with inertial cavitation and next by diluting ultrasound contrast agents.

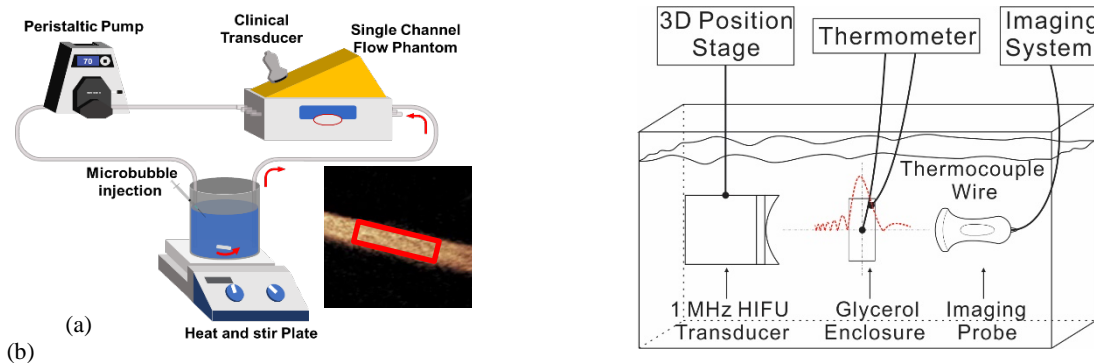


Figure 1. (a) Flow phantom setup for evaluating microbubble behavior at higher temperatures. (b) Experimental setup for temperature measurement of BEH in glycerol.

Results

In Fig. 2 we show TICs extracted from video loops from the flow phantom [Fig. 1(a)] at various temperatures and MIs. The custom microbubbles (a-c) were affected more by the temperature, especially at 60 °C, and the image intensity was lower and decayed faster at all 3 MIs than that in 20 and 40 °C. The commercial (d-f) microbubbles were affected minimally by the temperature only at 60 °C [see red line in Fig. 2(f)].

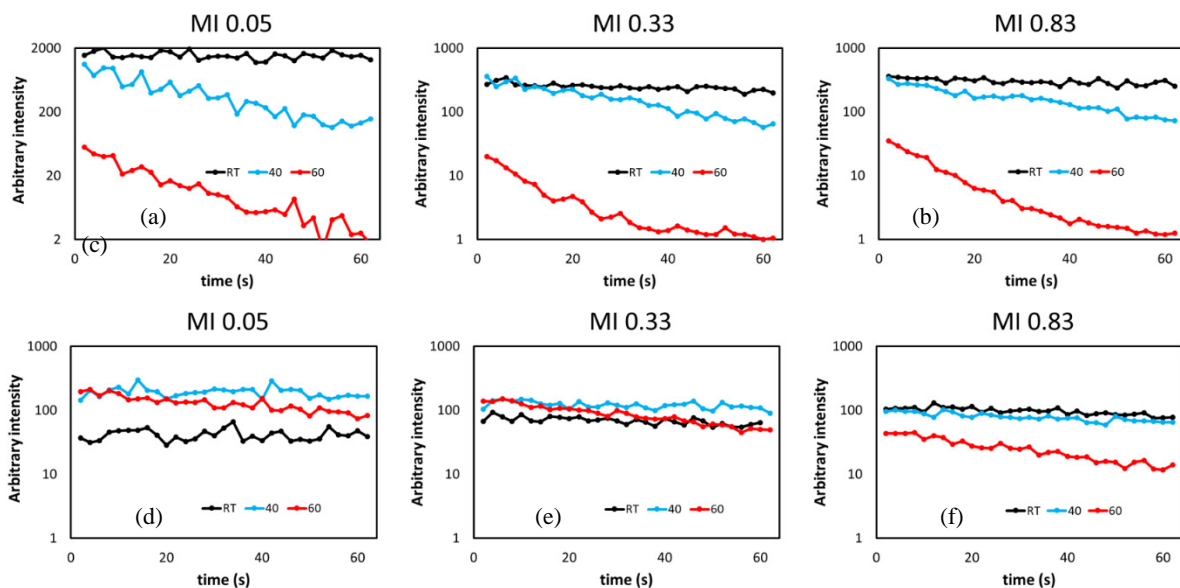


Figure 2. Image intensity of a ROI in a tube with custom (a-c) and commercial (d-f) microbubbles, at 3 different MIs.

The temperature rise induced by HIFU in whole glycerol (without microbubbles) at various acoustic pressures is shown in Fig. 3(a). As the acoustic pressure increases the temperature rise measured at the focus also increased linearly up to a pressure of about 2 MPa. At 2 MPa, the temperature rise is about 20 °C. At higher pressures, the temperature rise undergoes a sudden increase, indicating the existence of cavitation activity and the formation of microbubbles at the focus. The time necessary for this cavitation activity to be initiated decreases as the acoustic pressure increases. We assume that the threshold of inertial cavitation in glycerol is temperature dependent and thus this type of bubble-enhanced heating is

initiated above a certain temperature and only when cavitation nuclei are present. We also note that there is no noticeable temperature rise at the location of the second thermocouple which is placed outside the focal area.

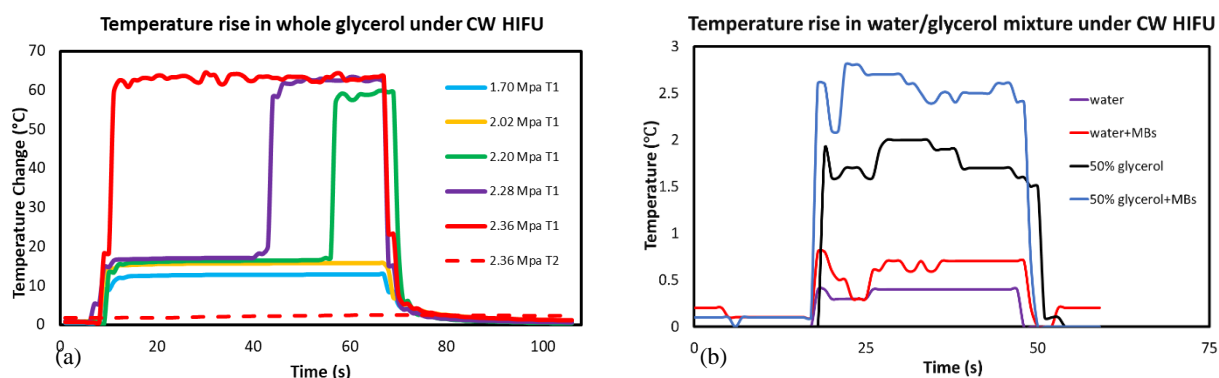


Figure 3. (a) HIFU-induced temperature rise in glycerol. One thermocouple is placed at the focus (T1) and another one 1 cm away from the focus (T2). Inertial cavitation causes a jump in temperature rise. (b) HIFU-induced temperature rise in 50-50% glycerol-water mixture with diluted microbubbles.

In Fig. 3(b) we show the temperature rise in the presence of microbubbles. It is interesting to note that adding microbubbles even in water (red line) resulted in a temperature rise increase. The same is observed in the 50-50% glycerol-water mixture (blue versus black line). The measured temperature rise in both Fig. 3(a) and (b) are less than predicted by theory (Bioheat equation) due to the fact that acoustic streaming moves the fluid away from the focus. In future work, we plan to repeat these experiments in gels to avoid fluid motion and streaming, and in machine-perfused pig livers.

Conclusions

Clinically approved commercial microbubbles were found to be more stable at elevated temperatures at all MIs tested and with only a small reduction in scattering intensity at 60 °C. This implies that they are suitable for BEH studies. Acoustic cavitation was observed at pressures between 2 and 3 MPa and was found to dramatically increase the temperature (by about 40 °C) of glycerol. With similar pressures and by introducing microbubbles we were able to induce controlled BEH in a water-glycerol mixture. Controlled BEH is feasible and can reduce the acoustic intensity required to elevate tissue temperature during HIFU.

References

- [1]. W. J. Elias et al., "A randomized trial of focused ultrasound thalamotomy for essential tremor," *New England Journal of Medicine*, vol. 375, no. 8, pp. 730-739, 2016.
- [2]. N. J. McDannold, N. I. Vykhodtseva, and K. Hynynen, "Microbubble contrast agent with focused ultrasound to create brain lesions at low power levels: MR imaging and histologic study in rabbits," *Radiology*, vol. 241, no. 1, pp. 95-106, 2006.
- [3]. P. Zhang and T. Porter, "An in vitro study of a phase-shift nanoemulsion: a potential nucleation agent for bubble-enhanced HIFU tumor ablation," *Ultrasound in medicine & biology*, vol. 36, no. 11, pp. 1856-1866, 2010.

Image-guided therapy with ultrasound and microbubbles: a tool to monitor in vivo events in real time

Zhongmin Du¹, Talent Shevchenko¹, Galina B. Diakova¹, Chen Ting Chin^{2,3}, Ralf Seip^{2,4},
Balasundar Raju^{2,5}, William Shi^{2,5}, Alexander L Klibanov¹

¹Cardiovascular Division and Cardiovascular Research Center, University of Virginia, Charlottesville VA USA, ²Philips Research, Briarcliff Manor, NY; Current addresses: ³Shenzhen University, Shenzhen, China; ⁴Sonacare Medical, Charlotte, NC; ⁵Philips Research, Cambridge MA.
Corresponding author: sasha@virginia.edu

Introduction

Imaging is used to direct the location of the focal zone of therapeutic ultrasound application, to point the intervention specifically towards the disease site. Even more importantly, imaging can be used to observe immediate and delayed effects of therapy application, such as monitoring blood flow as well as the immediate and delayed inflammatory status of the treated tissues. Here we present two examples of such observations. First, induction of inflammation by microbubble destruction in the tumor vasculature, that leads to immediate accumulation of neutrophils, which is observed by targeted ultrasound imaging with neutrophil-targeted microbubbles. Second example is for the efficacy of therapeutic drug delivery via ultrasound-triggered release of doxorubicin from liposome-microbubble complexes: depending on the acoustic pressure applied, tumor perfusion may be blocked and drug delivery inhibited.

Methods

Microbubbles were prepared by sonication of decafluorobutane gas, and coated with a monolayer shell of phosphatidylcholine and PEG stearate. When necessary, phosphatidylserine (PS) or biotin-PEG-phosphatidylethanolamine were added as microbubble shell components. Doxorubicin was extracted into biotinylated liposomes prefilled with ammonium citrate, by remote-loading process; these liposomes were attached to biotinylated microbubbles via streptavidin. As the animal model, we used MC38 murine colon adenocarcinoma cells (a generous gift of J. Schlom, NIH) grown subcutaneously in the hind leg of C57BL/6 mice. Tumor therapy studies were performed by either (a) high pressure daily ultrasound treatments of the tumors following intravenous administration of plain phosphatidylcholine microbubbles, until complete disappearance of the tumors or (b) ultrasound treatments of the tumors following intravenous administrations, 2-3 times a week, for two weeks, of the microbubble-liposome-doxorubicin complexes (injected dose of 6 mg/kg doxorubicin, with ~1pg per one microbubble-liposome pendant complex). Controls included non-insonated animals, or animals that have received no microbubble or microbubble-liposome-drug contrast administrations. Euthanasia was performed if tumor burden reached 10% of the body mass, or if the skin above the tumor mass had ruptured.

High pressure (5 MPa) ultrasound treatment was performed by the action of Philips TIPS (1.2 MHz, 100,000 cycles, repeated at 1 s intervals, 3x10 pulses). Treatment was initiated 30 sec after microbubbles or microbubble-liposome-drug constructs administration. Low pressure insonation was administered with a 1 MHz physical therapy ultrasound apparatus, Birtcher Megason, which operated, as a 3 sec “on”, 10 sec “off”, cycles at 0.6 W/cm². Real-time monitoring of microbubble perfusion during ultrasound application was performed by ultrasound imaging.

Ultrasound imaging of inflammatory response to ultrasound action was performed following administration of phosphatidylserine-containing microbubbles or control PS-free microbubbles: imaging of the insonated tumor was performed using contrast ultrasound imaging mode, an hour after high-power insonation, and up to 30 min after administration of PS microbubbles. PS-microbubble studies were repeated next day after insonation. Ultrasound imaging was performed using CPS contrast mode of Sequoia 512 scanner with 15L8 probe.

Results

We have observed a significant (nearly 3-fold) improvement in median survival time of animals that have received ultrasound-microbubble treatments; some of the experimental animals maintained tumor growth suppression for several months after initiation of the experiment. Transient reduction of blood flow, that resolved after several minutes, was observed in the insonated tumors. Significant accumulation in the tumor vasculature of the neutrophil-specific PS microbubbles, but not of the control PS-free microbubbles, was observed by ultrasound imaging within an hour following therapeutic ultrasound application. Extended retention of the PS-microbubble ultrasound signal beyond 10 min may point towards engulfment of microbubbles by neutrophils adherent on the vessel wall. When PS-microbubble study was repeated next day, no selective adhesion in the tumor vasculature was observed. These results were confirmed by histological assessment with neutrophil-specific staining: on the day of the study, adherent intravascular neutrophils could be observed, but on the following day, a significant number of inflammatory cells was present in the tissue, but not within the vasculature.

In case when following doxorubicin-liposome-microbubble administration, high-pressure TIPS insonation was applied, we have observed cessation of blood flow in the tumor mass, so during the residence time of acoustically active microbubble complexes in the bloodstream we would not be able to expect successful passage of microbubble complexes through the tumor vasculature, and tumor deposition. Therefore, the study was amended to apply low-pressure continuous sine wave ultrasound, using a physical therapy ultrasound apparatus. In that case, blood flow in the tumor vasculature was not interrupted, and suppression of tumor growth was observed in the insonated samples that received microbubble-liposome-doxorubicin complexes. In the control samples, where doxorubicin-free bubbles were combined with ultrasound treatment, or doxorubicin-liposome-microbubble complexes were administered without insonation, tumor growth was not suppressed.

Conclusions

Contrast ultrasound imaging allows rapid assessment of the efficacy of therapeutic intervention and status during ultrasound-assisted tumor therapy protocols. Use of neutrophil-targeted phosphatidylserine bubbles allows assessment of the mechanism of antitumor action. Direct observation of the blood flow in the tumor vasculature by contrast ultrasound imaging allows monitoring of drug complex passage, to guide successful drug delivery and therapeutic intervention.

The magnificent bubble: More than just air

Fabian Kiessling^{1,2}

¹*Institute for Experimental Molecular Imaging/RWTH Aachen University, Aachen, Germany*

²*Fraunhofer MEVIS, Institute for Medical Image Computing, 52074 Aachen, Germany*

Corresponding author: fkiessling@ukaachen.de

Introduction

Microbubbles are used as ultrasound contrast agents since decades to enhance the signal of the blood. They are well tolerated by the patients and have proven to enhance the diagnostic accuracy of ultrasound examinations e.g. of the liver and the cardiovascular system. However, microbubbles can do more than just adding vascular contrast. Modification of their surfaces with targeting ligands can turn them into molecular imaging probes, and the conjugation or incorporation of additional imaging markers can render them multimodal. Besides these diagnostic aspects, microbubbles can act as local transmitters of acoustic energy and be used to permeate vessels, tissues and cell membranes [1].

Methods & Results

In this talk, I will report on our experiences in microbubble-based diagnosis and therapy. This will include examples of using contrast-enhanced ultrasound (CE US) for the characterisation of tumors and the assessment of antitumor therapies. In this context, I will introduce motion-model ultrasound localization microscopy (mULM) as a novel method to obtain superresolution images of tissue vasculature and multiple vascular characteristics in laboratory animals and patients [2]. It will also be shown how tissue characterisation by CE US can be improved by analyzing the image features in a radiomics approach [3]. Besides this, examples of molecularly targeted ultrasound imaging will be provided illustrating that the molecular information about vascular inflammation and activation is complementary and sometimes superior to morphological and functional features of the vasculature [4, 5]. At this point, I will introduce our poly(butylcyanoacrylate) (PBCA) microbubble platform and motivate the use of multimodal microbubbles in basic research to bridge different resolution scales. The final part of my talk will be dedicated to therapeutic applications. I will point to the high loading capacity of the shell of PBCA microbubbles and show how imaging agents like dyes or nanoparticles can be incorporated. When using these microbubbles for sonopermeabilisation the imaging agents are released during microbubble destruction and accumulate in the tissue indicating the opening of biological barriers and acting as biomarkers of drug accumulation [6]. Finally, the mechanisms of sonopermeabilisation will be discussed. Here, I will show that in contrast to brain tissue where the vascular wall needs to be opened as dominant barrier for drug delivery, enhanced stroma penetration and improved perfusion may be the most crucial features in peripheral tumors [7]. This hypothesis will be strengthened by our initial clinical data from breast cancer patients treated with neoadjuvant chemotherapy, where sonopermeabilisation leads to a significant increase in tumor perfusion.

Conclusions

There is a huge potential for CE US to advance diagnostics and therapy which is not exploited in clinical practice yet. Many of the emerging ultrasound applications could considerably easy be moved from preclinical to clinical evaluation and further refined by the introduction of novel transducer and image processing technologies. This could also stimulate the clinical introduction of new microbubbles dedicated to molecular imaging or sonopermeabilisation.

References

- [1]. Rix A, Lederle W, Theek B, Lammers T, Moonen C, Schmitz G, Kiessling F, Advanced Ultrasound Technologies for Diagnosis and Therapy 2018, *J Nucl Med*, 59, 740-746.
- [2]. Opacic T, Dencks S, Theek B, Piepenbrock M, Ackermann D, Rix A, Lammers A, Stickeler E, Delorme S, Schmitz G, Kiessling F, Motion Model Ultrasound Localization Microscopy for Preclinical and Clinical Multiparametric Tumor Characterization 2018, *Nat Commun*, 9, 1527.
- [3]. Theek B, Opacic T, Magnuska Z, Lammers T, Kiessling F, Radiomic analysis of contrast-enhanced ultrasound data 2018, *Sci Rep*, 8, 11359.
- [4]. Baetke SC, Rix A, Tranquart F, Schneider R, Lammers T, Kiessling F, Lederle W, Squamous cell carcinoma xenografts: use of VEGFR2-targeted microbubbles for combined functional and molecular US to monitor antiangiogenic therapy effects 2016, *Radiology*, 278, 430-40.
- [5]. Palmowski M, Huppert J, Ladewig G, Hauff P, Reinhardt M, Mueller MM, Woenne EC, Jenne JW, Maurer M, Kauffmann GW, Semmler W, Kiessling F, Molecular profiling of angiogenesis with targeted ultrasound imaging: early assessment of anti-angiogenic therapy effects. *Mol Cancer Ther* 2008, 7: 101-09.
- [6]. Lammers T, Koczera P, Fokong S, Gremse F, Ehling J, Vogt M, Pich A, Storm G, van Zandvoort M, Kiessling F, Theranostic USPIO-loaded microbubbles for mediating and monitoring blood-brain barrier permeation 2015, *Adv Funct Mater*, 25, 36-43.
- [7]. Theek B, Baues M, Ojha T, Möckel D, van Bloois L, Veettil SK, Steitz J, Storm G, Kiessling F, Lammers T, Sonoporation enhances liposome accumulation and penetration in tumors with low EPR 2016, *J Control Release*, 231, 77-85.

Sequence design for ultrasound imaging of polyvinyl alcohol microbubbles

H. Chen¹, D. Evangelou¹, D. Grishenkov¹

¹Department of Biomedical Engineering and Health Systems, KTH Royal Institute of Technology, Stockholm, Sweden

Corresponding author: hongjian@kth.se

Introduction

Nonlinear behavior of the ultrasound contrast agent (UCA) offers a unique feature to be distinguished from the surrounding tissue. In a recent years several methods were developed to enhance the nonlinear response of UCA. Crucial for efficient differentiation of the nonlinear response of UCA from the surrounding tissue is to design the contrast pulse sequence specific to the unique nonlinear properties that the particular UCA is offering.

In the previous study, the nonlinear response from a novel polyvinyl alcohol (PVA) microbubbles (MB), in ultra-harmonic region was investigated over a pressure range from 50 kPa to 300 kPa. In this study, five contrast pulse sequences and reference B-mode sequence were designed to visualize PVA MB. The performance of those sequences were evaluated and compared.

Methods

An experimental setup for ultrasound tests consists of a tissue-mimicking phantom (Model 524 Peripheral Vascular Doppler Flow Phantom, ATS Laboratories) with 2 wall-less channels of a diameter 6 and 8 mm respectively. A peristaltic pump was employed to drive the fresh sample through the phantom. The PVA MBs with the outer diameter of $3.40 \pm 0.85 \mu\text{m}$ were fabricated following protocol from Cavalieri et al.[1]. The aqueous suspension of PVA MB with the concentration of 10^6 mL^{-1} was employed.

Six ultrasound sequences: 1) B-mode 2) ultra-harmonic 3) pulse inversion (PI) 4) subharmonic pulse inversion 5) ultra-harmonic pulse inversion and 6) contrast pulse sequence 4 (CPS4); were designed for the image acquisition. The characteristics of the transmission and receiving part of the sequence are listed in table 1. Pulse duration for all excitation pulses was equal to 1 cycle.

Table 1. Characteristics of the imaging sequences.

Sequence name	Transmission part	Receiving part
B-mode	Single pulse was excited at 6 MHz	Full bandwidth of the probe.
Ultra-harmonic	Single pulse was excited at 6 MHz	A band-pass filter was employed to limit the receiving echoes at frequency around 9 MHz with 6 dB bandwidth about 2.75 MHz.
PI	Two pulse was excited at 6 MHz with 180 degree phase difference	Full bandwidth of the probe.
Sub-harmonic PI	Two pulse was excited at 6 MHz with 180 degree phase difference	A band-pass filter was employed to limit the receiving echoes at frequency around 3 MHz with 6 dB bandwidth about 2.75 MHz.

Ultra-harmonic PI	Two pulse was excited at 6 MHz with 180 degree phase difference	A band-pass filter was employed to limit the receiving echoes at frequency around 9 MHz with 6 dB bandwidth about 2.75 MHz.
CPS4	Two groups of pulses were excited at 6 MHz. Each group contains two pulses with 180 degree phase difference	Two band-pass filters with center frequency round 3 and 9 MHz bandwidth about 2.75 MHz were employed for the echo receiving of the two pulse groups respectively.

A L7-4 ultrasound linear array transducer was controlled by programmable ultrasound system Verasonics Research System (Verasonics Inc., Kirkland WA, USA), to generate the desired transmission pulse and to acquire the response echoes. In all acquisitions, excitation voltage was kept at 60V peak to peak. The beam was focused at the center of the channel. The peak negative pressure at the focus points was estimated to be about 400 kPa. Ten gray scale ultrasound images of the channels cross section were obtained for all imaging techniques. Contrast to tissue ratio (CTR) and contrast to noise ratio (CNR) were calculated based on the intensity of the gray scale images using the following equation:

$$CTR = 20 \log_{10} \frac{\langle I_S \rangle}{\langle I_T \rangle}$$

$$CNR = 20 \log_{10} \frac{\langle I_S \rangle}{\langle I_N \rangle}$$

where, $\langle I_S \rangle$ is mean pixel intensity of the region of interest (ROI) containing sample, $\langle I_T \rangle$ is mean pixel intensity of ROI containing tissue-mimicking material, $\langle I_N \rangle$ is the pixel intensity of ROI containing degassed water.

The ROIs of sample, tissue and noise were selected within the channel containing MBs suspension, within tissue mimicking phantom and within the channel containing degassed water, respectively. Fig. 1 demonstrates all three ROIs located at the same depth around the ultrasound focus.

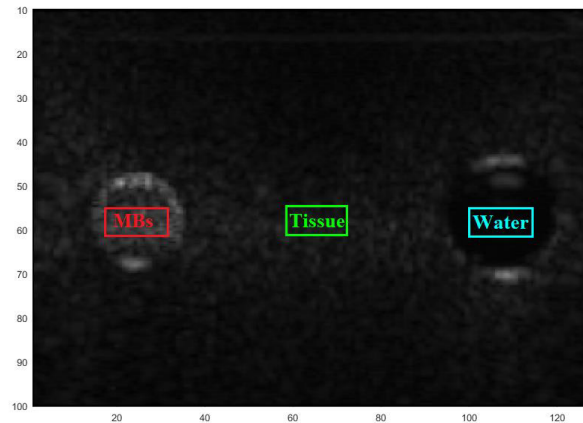


Fig. 1. Example of the ROIs selection: MBs (right), Tissue (middle) and water (left)

Results

Fig. 2 demonstrates the gray-scale images for each of the 6 implemented ultrasound imaging techniques described in the method section. In each of these images, the contrast between the 6mm tube, the 8mm tube and the in-between tissue-mimicking phantom was calculated and averaged over 10 images.

The visual inspection of the images reveals that fundamental B-mode sequence (Fig. 2a) fails to differentiate MBs from the surrounding tissue. An application of the band-pass filter around ultra-harmonic (Fig. 2b) decrease overall brightness of the image but did not provide any enhancement. On the

contrary, contrast specific PI technique (Fig. 2c) suppresses linear response from the tissue and highlights harmonic response from the MBs suspension. Further improvement can be obtained by the application of advanced contrast pulse sequence CPS4 that increases the signal intensity and also unify the response through the whole lumen of the tube.

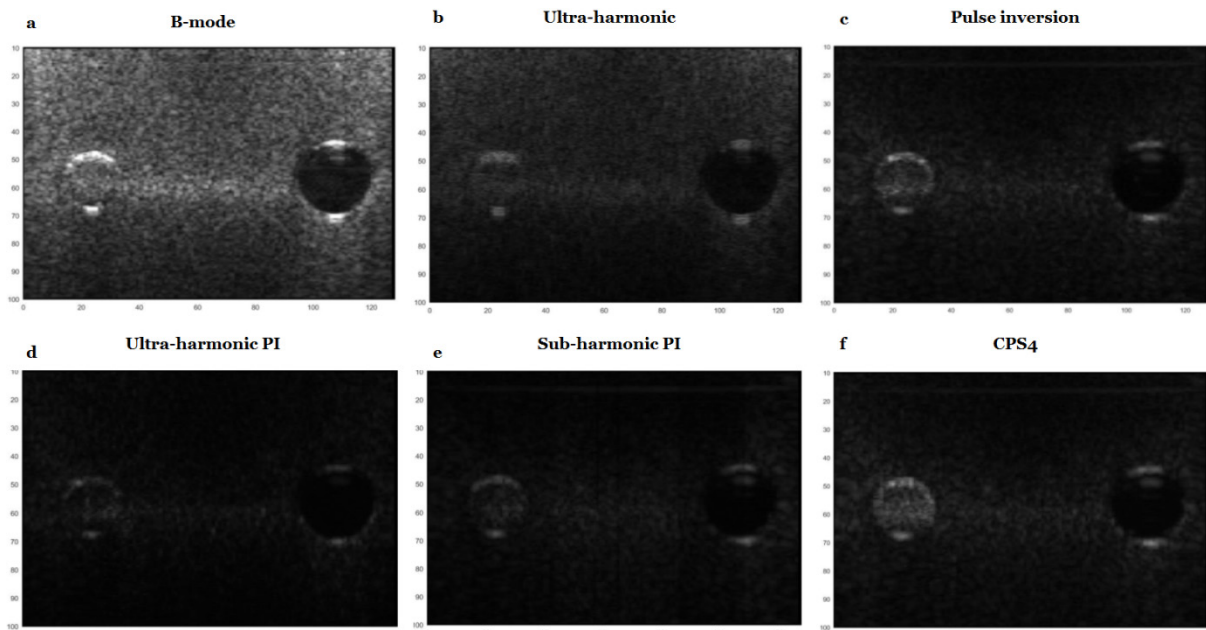


Fig. 2 Gray scale images for 6 imaging techniques. a) B-mode b) ultra-harmonic v) PI d) subharmonic PI e) ultra-harmonic PI and f) CPS4. The smaller channel on the left in each image contains PVA MB sample. The bigger channel on the right in each image contains degassed water.

The mean CTR and CNR of all six imaging techniques over are shown in Fig. 3.

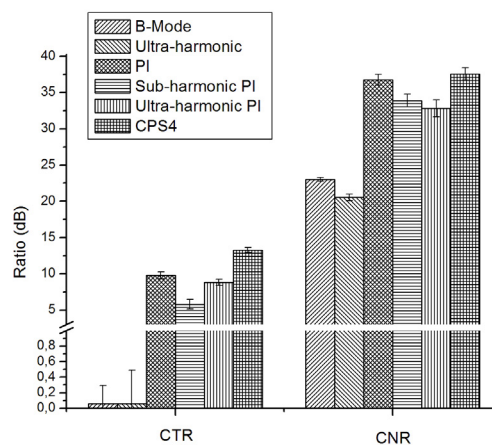


Fig. 3. Result of CTR and CNR for all imaging techniques

Worth mentioning is that all PI imaging techniques have considerable higher CTR and CNR than non-PI imaging techniques.

According to Poehlmann et al. the resonance frequency of polymer MBs is between 12 - 14 MHz [2]. It is expected that the excitation at half the resonance frequency (6MHz) and detection with the application of the filter around sub- (3MHz) or ultra-harmonic frequency (9 MHz) will further improve the detectability of UCA. However, current study reveals the opposite, i.e. both CTR and CNR were decreased between 2 to 5 dB for sub- and ultra-harmonic PI in comparison to the full-bandwidth PI. A

potential explanation could be that the sensitivity of the transducer reduces at the sub-harmonic and ultra-harmonic part of the frequency bandwidth.

Nevertheless, the combination of sub- and ultra-harmonic PI imaging, that constitute the contrast pulse sequence imaging technique (CPS4), overcome the sensitivity problem and through synergetic effect demonstrates highest CTR and CNR, of about 13 and 37 dB respectively. Those values are approximately 12 dB higher than obtained for conventional B mode.

To further improve the performance of the imaging sequence, several modifications can be made. MBs suspension with a narrow size distribution of the diameter will also have narrow distribution of the resonance frequencies. As a result, it is expected that responses at sub- and ultra-harmonics will be also more concentrated and easier to identify. Moreover, setting excitation frequency closer to the distinctive resonance frequency allows for more energy to be absorbed and scattered by MBs. Last but not least, the study will also benefit from the precise control of the pressure at the focused area, which ensures that the MBs oscillate in the nonlinear regime.

Conclusions

In this study the performance of six imaging techniques with PVA MBs was evaluated. Combination of sub-harmonic, ultra-harmonic and PI techniques demonstrated the best performance reaching 37.55 dB in CNR and 13.27 dB in CTR.

References

- [1]. Cavalieri, F., El Hamassi, A., Chiessi, E., Paradossi, G., Villa, R., & Zaffaroni, N. (2006). Tethering functional ligands onto shell of ultrasound active polymeric microbubbles. *Biomacromolecules*, 7(2), 604-611.
- [2]. Poehlmann, M., Grishenkov, D., Kothapalli, S. V., Härmak, J., Hebert, H., Philipp, A., ... & Paradossi, G. (2014). On the interplay of shell structure with low-and high-frequency mechanics of multifunctional magnetic microbubbles. *Soft Matter*, 10(1), 214-226.

Assessment of the Superharmonic Response of Microbubble Contrast Agents for Acoustic Angiography As A Function of Microbubble Parameters

Isabel G. Newsome¹, Thomas M. Kierski¹, Paul A. Dayton¹

¹*Joint Department of Biomedical Engineering, University of North Carolina and North Carolina State University, Chapel Hill, NC, USA*

Corresponding author: padayton@email.unc.edu

Introduction

Acoustic angiography (AA) is a superharmonic contrast-enhanced ultrasound imaging technique for high-resolution, three-dimensional microvascular imaging. This technique utilizes a dual-frequency imaging strategy, exciting microbubble contrast agents at a low frequency and receiving the superharmonic signals generated at a high frequency, allowing separation of the microvasculature from the surrounding tissue. Because AA relies on superharmonic production by microbubbles, the sensitivity of the technique could be improved by optimizing microbubble parameters for AA. Previous literature has illustrated differences in microbubble scatter depending on microbubble size and composition; however, most previously reported data has utilized a relatively narrow frequency bandwidth centered around the excitation frequency, not the higher harmonics. Here, we evaluate the superharmonic response of 14 microbubble contrast agents using a broadband dual-frequency system.

Methods

The contrast agents evaluated in this work are listed in Table 1. The size and stock concentration of all contrast agents was measured before data collection, and microbubbles were diluted to a matched concentration of 10^8 #/mL for comparison. A transducer with two confocally-aligned single elements was used to transmit at 4 MHz and receive at 25 MHz. Mechanical index was varied from 0.2 to 1.2. The experimental setup is depicted in Fig. 1. After digitization, RF data was processed in MATLAB, and superharmonic production was quantified by the area under the normalized frequency spectrum (AUC) of the RF data within the -6 dB bandwidth (8.5 to 35.7 MHz) of the receive element.

Table 1. Summary of microbubble contrast agents.

<u>Group</u>	<u>Name</u>	<u>Shell</u>	<u>Core</u>	<u>Size Distribution</u>	<u>Manufacturer</u>
Clinical and Preclinical	Definity	lipid	C ₃ F ₈	polydisperse	Lantheus Medical Imaging
	Optison	protein	C ₃ F ₈	polydisperse	GE Healthcare
	Micromarker	lipid	N ₂ & C ₄ F ₁₀	polydisperse	FUJIFILM VisualSonics, Inc.
Gas Core	DFB	lipid	C ₄ F ₁₀	polydisperse	Dayton Lab
	OFB	lipid	C ₃ F ₈	polydisperse	Dayton Lab
	SF ₆	lipid	SF ₆	polydisperse	Dayton Lab
Lipid Shell	C16-2L	lipid	C ₃ F ₈	polydisperse	Dayton Lab
	C16-3L	lipid	C ₃ F ₈	polydisperse	Dayton Lab
	C18-2L	lipid	C ₃ F ₈	polydisperse	Dayton Lab
	C20-2L	lipid	C ₃ F ₈	polydisperse	Dayton Lab
Bubble Diameter	SIMB1-2	lipid	C ₄ F ₁₀	size-sorted	Advanced Microbubbles Laboratories
	SIMB3-4	lipid	C ₄ F ₁₀	size-sorted	Advanced Microbubbles Laboratories
	SIMB4-5	lipid	C ₄ F ₁₀	size-sorted	Advanced Microbubbles Laboratories
	SIMB5-8	lipid	C ₄ F ₁₀	size-sorted	Advanced Microbubbles Laboratories

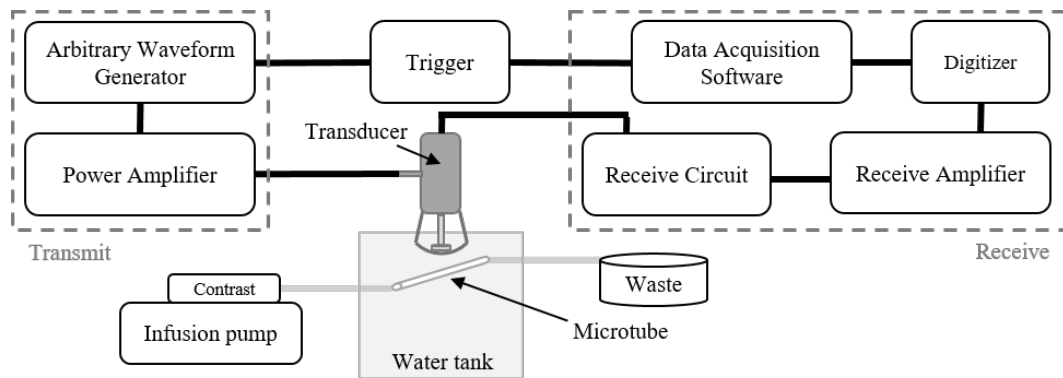


Figure 1: Schematic diagram of the experimental setup.

Results

Our results are summarized in Fig. 2. In a comparison of two clinical agents, Definity and Optison, and one preclinical agent, Micromarker, Optison produced the smallest superharmonic signals, while Definity and Micromarker behaved similarly. Results comparing perfluorocarbon and sulfur hexafluoride core microbubbles indicated greater superharmonic production for bubbles containing perfluorocarbons. Microbubbles with longer acyl chains (18-20 C atoms) in their lipid shells generated greater superharmonic signals than those with shorter acyl chains (16 C atoms). Finally, as microbubble diameter increased from 1 to 4 μm , superharmonic generation decreased.

Conclusions

This study demonstrates that the superharmonic response of microbubbles follows different trends than shown in prior studies using a narrower frequency bandwidth centered around the excitation frequency. As such, the data presented here may not hold true for other contrast-enhanced ultrasound techniques performed within the bandwidth of a single clinical transducer. Future work will apply these results *in vivo* to optimize the sensitivity of acoustic angiography.

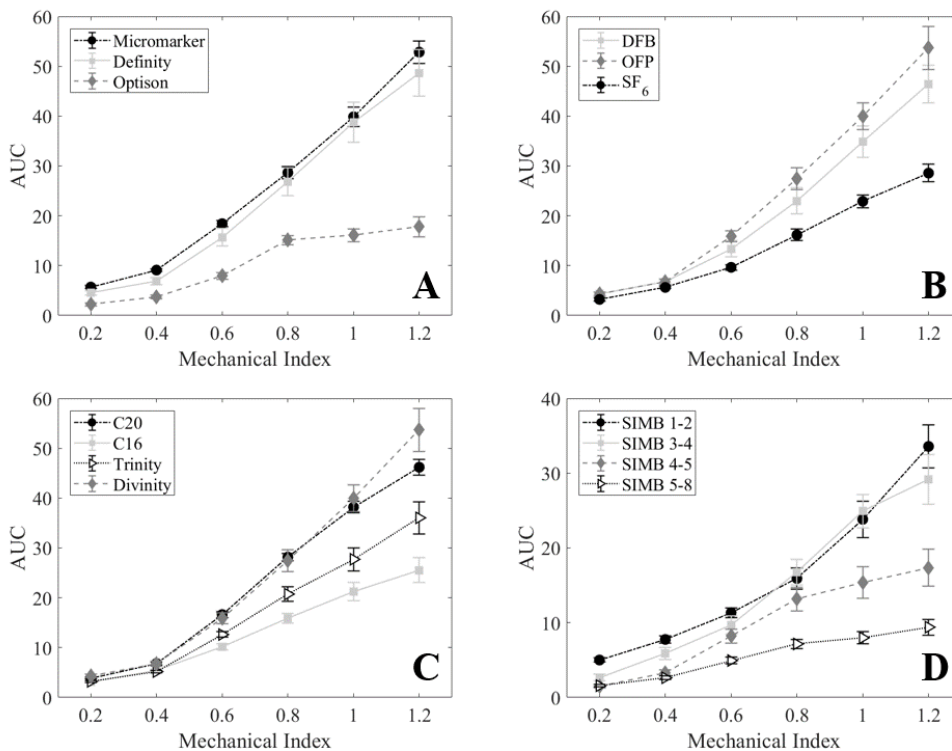


Figure 2: Comparison of superharmonic response for A) clinical and preclinical agents, B) microbubbles with different gas cores, C) microbubbles with different lipid shells, and D) microbubbles of varying diameter.

Longitudinal Follow-up Analyses for Quantification of Contrast-Enhanced Ultrasound Imaging

H. Robert¹, A. Helbert¹, T. Bettinger¹, I. Tardy¹, T. Rognard¹

¹Geneva Research Center, Bracco Suisse SA, Plan-les-Ouates, Switzerland
Corresponding author: hugo.robert@bracco.com

Introduction

With the development of contrast-enhanced ultrasound (CEUS) in a wide range of applications for pre-clinical and clinical purposes, there is a need for quantitative solutions to overcome the limitations of visual assessment of contrast enhancement. Perfusion quantification of CEUS has become mandatory for research purposes, as demonstrated by more than 300 publications on CEUS which rely on quantification software. Also, to enable monitoring of the treatment response, the combination of such quantification analyses with a follow-up tool could be a valuable asset.

Methods

Current quantification method for CEUS relies on the kinetics of Ultrasound Contrast Agent (UCA) uptake in the early phase following the injection of UCA. The average intensity within a Region Of Interest (ROI) is displayed as a function of time in the form of a Time-Intensity Curve (TIC), which describes the wash-in and wash-out of the UCA in the ROI.

For this purpose, VueBox® (Bracco Suisse SA) enables linearization of the video signal recorded in DICOM datasets for all the ultrasound platforms allowing contrast imaging [1]. Fully automatic in-plane motion compensation and patented curve-fitting models allow a quantitative perfusion assessment [2,3], but also the visualization of parametric images by integrating perfusion information at the pixel level using color coding. Recently, VueBox® 7.0 also upgraded with a follow-up tool to visualize in a single window various perfusion parameters over time for a single subject.

To assess the value of combining quantification analyses with the new follow-up tool, cases of chemo-induced rat mammary tumors were analyzed. Pre-pubescent female animals received a single intraperitoneal injection of N-Nitroso-N-methylurea (NMU). When animals developed mammary tumors, the lesions were treated by an antiangiogenic agent (Sunitinib). For each animal, CEUS examinations (with bolus injection of the targeted contrast agent named BR55) were performed prior, during and after the treatment. Each acquisition was quantified off-line using VueBox® with the GI-Perfusion package. Finally, all the VueBox® analyses for each animal were processed in the follow-up tool to evaluate the response to the therapy.

Results

The use of the follow-up tool clearly facilitated the monitoring of tumor growth, perfusion and possible response to therapy, with a significant gain in time to perform the analyses and obtain the trends of the perfusion plus anatomical parameters.

In the present example of one animal shown in Figure 1, results obtained using the follow-up tool indicate that tumor progression occurs during the week prior the first sunitinib dosing. At day 11, Peak Enhancement (PE), Wash-In Area Under the Curve (WiAUC) and area values represent 6%, 50% and 43% of the initial value. Throughout the 13 days of treatment with a dose of 5 mg/kg/day, evolution charts show a stagnation of WiAUC and Area, but an increase of PE by a factor 1.3, suggesting that the treatment was not efficient. Then, when the dose was increased to 20 mg/kg/day during 7 days, the graphs showed a strong decrease of PE, WiAUC and area parameters divided by a factor of 2.2, 2.2 and 1.7 respectively. These results suggest that sunitinib treatment is effective both at an anatomical and functional levels by inducing a tumoral shrinkage and the diminution of the tumoral perfusion. Moreover, these parameters seem to be relevant indicators of the treatment efficacy. Finally, 15 days after the treatment was stopped,

PE and WiAUC perfusion parameters strongly increased by a factor of 2.9 and 2.2 respectively, indicating a resumption of the tumoral perfusion. Tumor area was also multiplied by a factor 1.75.

Conclusions

The implementation of the longitudinal follow-up tool into the VueBox® quantification software has proved to be valuable, providing a clear and easy way to quantitatively evaluate the treatment response in preclinical animal model.



Figure 1 – Evolution charts and Time Intensity Curves results dashboard. 7 days after the first imaging, the animal was treated for 13 days with daily gavage of 5 mg/kg of Sunitinib. The dose was then increased to 20 mg/kg of Sunitinib for 7 days. The treatment was finally stopped, and imaging was performed during 15 days. Red arrows represent the daily gavage of Sunitinib. B-Mode snapshots are shown in the “Area” chart to highlight tumor size over time (at day 1, 18, 29 and 38). Contrast snapshots at the peak are shown in the “Peak Enhancement” chart to highlight the maximum perfusion intensity over time (also at day 1, 18, 29 and 38).

References

- [1]. Arditi M, Frinking P, Zhou X, Rognin N, A New Formalism for the Quantification of Tissue Perfusion by the Destruction-Replenishment Method in Contrast Ultrasound Imaging 2006, IEEE Trans Ultrason Ferroelectr Freq Control, 1118–1129, 2006.
- [2]. F. Tranquart, L. Mercier, P. Frinking, E. Gaud, M. Arditi, Perfusion Quantification in Contrast-Enhanced Ultrasound (CEUS) – Ready for Research Projects and Routine Clinical Use 2012, Ultraschall in Med, 33: S31–S38, 2012.
- [3]. C. Greis, Quantitative evaluation of microvascular blood flow by contrast-enhanced ultrasound (CEUS) 2011, Clinical Hemorheology and Microcirculation, 137–149, 2011.

Measuring the effect of Radiotherapeutic Radiation on Commercially Available Microbubbles

*Gonzalo Collado*¹, *Sophie V. Heymans*², *Koen Van Den Abeele*², *Klazina Kooiman*¹,
*Hendrik Vos*¹, *Jan D'hooge*³, *Nico de Jong*¹

¹*Department of Biomedical Engineering, Erasmus Medical Center, Rotterdam, The Netherlands*

²*Department of Physics, KU Leuven Campus KULAK, Kortrijk, Belgium*

³*Department of Cardiovascular Sciences, KU Leuven, Leuven, Belgium*

Corresponding author: g.colladolar@erasmusmc.nl

Introduction

Recent studies in radiotherapy have shown for some tumors a higher effectivity of larger single-dose irradiations [1]. To avoid damaging the surrounding healthy cells, single-dose therapies would require not only a good planning, but a delivered-dose measurement. So far, no dosimetric technique has emerged as a golden standard [2].

Based on the results from *Verboven et Al.* [3], that show a linear decrease in the attenuation with delivered dose for some microbubbles, we want to assess the feasibility of commercial Ultrasound Contrast Agents as possible non-invasive internal dosimeters. Here we study the temporary and permanent effects of high energy photon irradiation on the size, concentration and acoustic response of SonoVue, Definity and Optison populations.

Methods

One vial of each type, SonoVue, Definity and Optison, was activated according to the manufacturer indications. Bubble samples diluted in a closed container were placed in a water tank. A Linear Particle Accelerator was used to produce a 6 MV photon beam delivering a total dose of 15 Gy. Both transmission and scattering were measured before, during and after irradiation using three transducers. Broadband and narrowband acoustic pulses with 2.25 MHz center frequency and peak negative pressure below 50 kPa were used. After the acoustic measurements, the samples were counted and sized using a Multisizer 3 (Coulters Beckman).

Control measurements were done using a new sample from the same vial, following the same steps, and keeping the same time duration, without starting the beam irradiation. Unfortunately, there was a 15 minutes delay for the counting and sizing measurement of the irradiated samples, which may have led to deviations in these measurements. For each vial, the study of two irradiated samples and two control samples was performed.

Results

The size distribution and bubble concentration of the irradiated and control samples were compared. We notice a slight deviation, likely due to the time different handling time.

Searching for temporary effects, the transmission and scattering signals of the irradiated samples were compared just before and just after starting the photon irradiation. No difference in amplitude or frequency content was found.

For both irradiated and control samples, total attenuation was calculated and the same behaviour was found, i.e. the value was decreasing over time. This effect was probably due to either bubble disruption or the flotation of larger bubbles. The total decrease was compared and the irradiated samples had lower final attenuation, in the order of 1 dB (Fig. 1). The scattering signal level was analysed and an increase over time was found. We attribute this effect to the attenuation drop. The second harmonic is below the noise level due to the high attenuation caused by a high bubble concentration.

Conclusions

No remarkable difference was found in the scattering and attenuation signals before and during radiation, which suggest that there is no direct transient effect. The size distribution, concentration and acoustic responses of irradiated samples were compared with a control, finding only differences in the acoustic response. A permanent drop in attenuation in the order of 1 dB after a 15 Gy dose agrees with previous results [3]. Nevertheless, the effect is hardly repeatable and below a clinically relevant value.

Both points together suggest that SonoVue, Definity and Optison are not directly suitable as dosimetric Ultrasound Contrast Agents. Other paths should be explored.

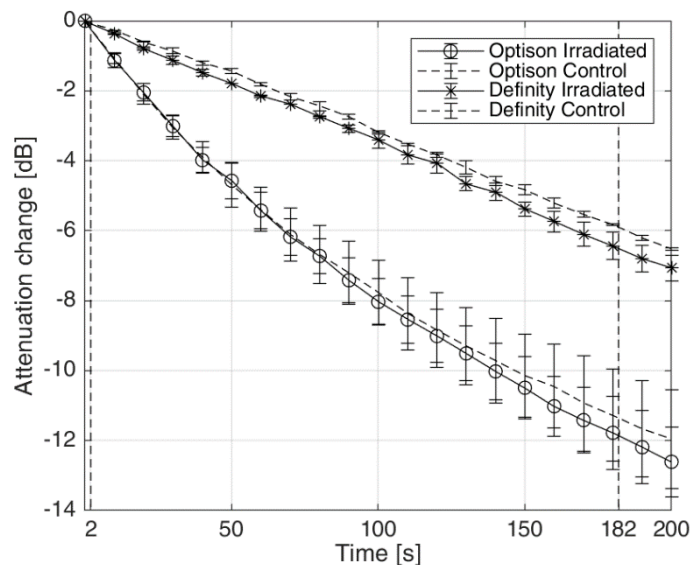


Figure 1. Attenuation drop as function of time. Both vertical lines represent the start and end of X-ray irradiation

Acknowledgment

This project has received funding from the European Union's Horizon 2020 research and innovation Program under grant agreement 766456 (AMPHORA).

References

- [1]. Yamada Y, Bilsky MH, Lovelock DM, Venkatraman ES, Toner S, Johnson J, Zatcky J, Zelefsky MJ, Fuks Z, High-Dose, Single-Fraction Image-Guided Intensity-Modulated Radiotherapy for Metastatic Spinal Lesions, *Int. J. Radiation Oncology Biol. Phys.*, Vol 71: 484-490, 2008.
- [2]. Mijnheer B, Beddar S, Izewska J, Reft C, In vivo dosimetry in external beam radiotherapy, *Med. Phys.*, Vol 40(7), July 2003
- [3]. Verboven E, D'Agostino E, Callens M, Pfeiffer H, Verellen D, D'hooge J, Van Den Abeele K., Ultrasound based dosimetry for radiotherapy: in-vitro proof of principle, *IEEE International Ultrasonics Symposium Proceedings*, 2014.

Segmentation of stationary microbubbles: the foundation for targeted molecular imaging

Ryan Hammond¹, Zin Khaing¹, Charles Tremblay-Darveau² Christoph Hofstetter¹, Matthew Bruce¹

¹University of Washington, Seattle, USA

²Philips Medical Systems, Bothell, USA

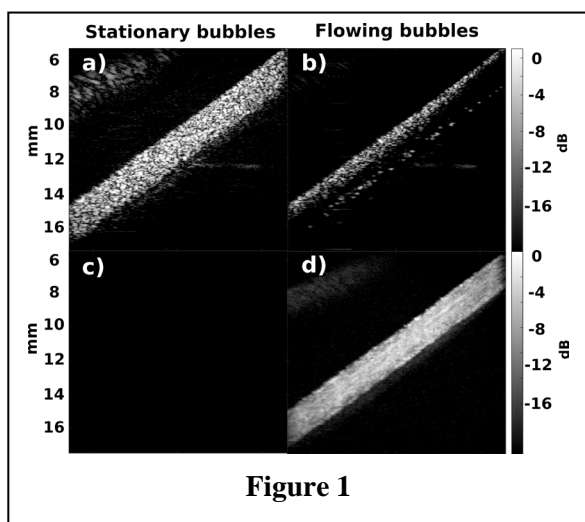
Corresponding author: mbruce@uw.edu

Introduction

The use of targeted microbubbles to image the molecular expression of various vascular factors is an active area of research. In contrast to non-targeted ultrasound imaging of microbubbles, ultrasound molecular imaging consists of detecting and separating signals from a small fraction of molecularly attached microbubbles from freely circulating, non-attached microbubbles, assuming that only a small fraction (1% or less) of the injected targeted microbubbles actually bind to molecular targets.[1-2] Different indirect approaches have been used to separate bound microbubbles from those freely flowing in the vasculature.[1-3] In this work, we present a direct approach to classify bound microbubbles in the presence of surrounding free-flowing microbubbles, through processing of a nonlinear Doppler acquisition.

Methods

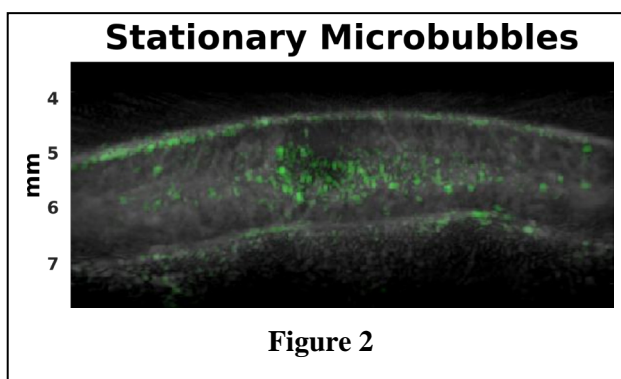
The Vantage ultrasound research platform (Verasonics, USA) was used to program plane-wave nonlinear Doppler sequences, using a 15 MHz linear array transducer (Vermon, France).[4-5] A singular value decomposition of the nonlinear Doppler sequence was then used to separate the lowest frequency microbubble Doppler signals of stationary microbubbles from the higher frequency Doppler signals of flowing microbubbles.[6] The separation of stationary and flowing microbubbles was demonstrated both in both *in-vitro* and *in-vivo* experiments. The *in-vitro* setup consisted of an infusion pump pushing microbubbles through a 2mm diameter dialysis tube with a peak velocity of 3 cm/sec. Nonlinear Doppler acquisitions were acquired at two flow states: 1) stationary microbubbles. 2) flowing microbubbles. For *in-vivo* experiments, a rat spinal cord injury model was used to visual changes in blood flow. Access to the dorsal spinal cord for both injury and ultrasound imaging was obtained by laminectomy, where the laminae were surgically removed. [4] A contusion injury of the thoracic spinal cord (Infinite Horizon, USA) was then performed followed by ultrasound imaging. Bolus injections of Definity (Lantheus, USA) were administered via a tail vein followed by nonlinear Doppler acquisitions. This approach enabled visualization of flowing microbubbles in the microcirculation and macrocirculation as well as microbubbles whose passage through the vasculature had been impeded surrounding the contusion injury.



Results

Figure 1a and 1b illustrate the lowest frequency singular vectors capturing the component of stationary microbubble signals. Figure 1b shows microbubbles collecting on the upper wall of the dialysis tube in the presence of flowing microbubbles. Figure 1c and 1d show the higher frequency components of the decomposition of the nonlinear Doppler signal. The absence of flowing microbubbles for the no-flow microbubble state leads to a corresponding absence in higher frequency Doppler signals as shown in Figure 1c. Figure 2 illustrates the nonlinear signal of

microbubbles in a median sagittal slice of a rat's spinal cord following injury. The background greyscale image of Figure 2 shows the perfusion signal composed of a group of the lowest frequency singular vectors, with the hypoechoic region outlining the disruption of the microcirculation from the contusion injury. The central region of the spinal cord is composed of grey matter having a higher vascular density and resulting brighter perfusion signal. The separation of the stationary microbubble signals (i.e. the very



lowest frequency singular vectors) is shown in green over the perfusion microbubble signal shown in grey. The stationary microbubble signal predominantly accumulated in the area of injury. The alteration in kinetics of these microbubbles passage through the vasculature might be due to multiple factors. Trauma to the spinal cord tissue leads to endothelial defects, clots and vasospasm, which impede blood flow in areas surrounding the spinal cord injury. Moreover, marked increases in the intraspinal pressure arising from haemorrhage and edema result in a loss of perfusion pressure. Lastly, a neuroinflammatory response to spinal cord injury leads to the accumulation of leukocytes in the area of injury.[7] The retention of microbubbles has been observed in regions of inflammation, where it was demonstrated that microbubbles can adhere to activated leukocytes attached to the endothelium following ischemic injury.[1]

Conclusions

We demonstrate an approach to segment stationary microbubbles from surrounding flowing microbubbles in both in-vitro and in-vivo experiments. Non-targeted microbubbles were seen to collect surrounding a contusion injury of a rat spinal cord. This work demonstrates a potential to separate bound targeted microbubbles from free-flowing microbubbles without having to wait for the clearance of microbubbles from vasculature. This would enable the imaging of bound microbubbles to a molecular target, when the number of microbubbles available for binding is maximal (i.e. in the presence of free flowing microbubbles).

References

- [1]. Lindner, Jonathan R., et al. "Noninvasive imaging of inflammation by ultrasound detection of phagocytosed microbubbles." *Circulation* 102.5 (2000): 531-538.
- [2]. Abou-Elkacem, Lotfi, Sunitha V. Bachawal, and Jürgen K. Willmann. "Ultrasound molecular imaging: Moving toward clinical translation." *European journal of radiology* 84.9 (2015): 1685-1693.
- [3]. Turco, Simona, et al. "Quantitative ultrasound molecular imaging by modeling the binding kinetics of targeted contrast agent." *Physics in Medicine & Biology* 62.6 (2017): 2449.
- [4]. Khaing, Zin Z., et al. "Contrast-enhanced ultrasound to visualize hemodynamic changes after rodent spinal cord injury." *Journal of Neurosurgery: Spine* (2018): 1-8.
- [5]. Tremblay-Darveau, Charles, et al. "Visualizing the tumor microvasculature with a nonlinear plane-wave Doppler imaging scheme based on amplitude modulation." *IEEE transactions on medical imaging* 35.2 (2016): 699-709.
- [6]. Demené, Charlie, et al. "Spatiotemporal clutter filtering of ultrafast ultrasound data highly increases Doppler and fUltrasound sensitivity." *IEEE transactions on medical imaging* 34.11 (2015): 2271-2285.
- [7]. Shechter, Ravid, and Michal Schwartz. "CNS sterile injury: just another wound healing?." *Trends in molecular medicine* 19.3 (2013): 135-143.

Catheter-based, instrumented, flow focusing microfluidics device for production, counting and sizing of monodisperse microbubbles optimized for sonothrombolysis

J. M. Robert Rickel, Adam J. Dixon, Yanjun Xie and John A. Hossack

*Biomedical Engineering Department, University of Virginia,
Charlottesville, VA 22908, USA
Corresponding author: jh7fj@virginia.edu*

Introduction

The use of flow focusing microfluidic devices (FFMDs) have been investigated over recent years as a means for creating a stream of microbubbles suitable for imaging or drug delivery. Although an FFMD provides an exceptional degree of control over size of produced microbubbles, the method also has some serious limitations. The microbubbles are frequently relatively large ($> 5 \mu\text{m}$ diameter), possess a short *in vivo* lifetime (a few minutes), may require an additional “washing” step and production rates are low relative to many requirements (typically $< 10^6/\text{s}$). We previously determined that we can accommodate, or even exploit, these same limitations for a specific application – sonothrombolysis¹. Thrombolysis is a challenge in the context of stroke, deep vein thrombosis and pulmonary embolism. The limitations of our FFMD generated microbubbles necessitate that the FFMD be placed near to the intended sonothrombolysis site – i.e. near the tip of catheter introduced to the vicinity of the target blood clot. We have previously demonstrated basic prototype FFMD catheter devices and now add capabilities to support the potential pathway to translation to clinical usage. This necessitates that the *in situ* device perform several basic “quality control” functions on generated microbubbles. These include: 1) a means to count microbubbles, 2) a means to size-quantify microbubbles, 3) a means to test for basic forms of device malfunction (e.g. “stable operation” or no production due to either “liquid flood” or “gas flood”) and 4) a means to assess the progress of the thrombolytic process. These requirements can be viewed as a form of minimal *in situ* “quality control” that would be necessary to inform a physician using the device that the catheter is operating properly and for visualizing or monitoring the clot erosion process.

Methods

We have developed a Micro Coulter Particle Counter (μCPC) as part of the microfluidic device to enable electrical impedance-based microbubble characterization (counting and sizing)². The counter comprises a Wheatstone bridge to facilitate measurements of differential impedance, and consequent voltage potential, as a non-conducting microbubble passes through the sensing zone adjacent to a pair of electrodes near the outlet of the FFMD. In this presentation, we satisfy the requirement to assess progress of the clot erosion process by using a small piezoelectric transducer to probe blood / clot during the sonothrombolysis procedure. This may use the same transducer as intended for delivery sonothrombolysis ultrasound or a second one optimized for imaging (*i.e.* high frequency). In the current case, we chose to use the transducer intended for sonothrombolysis delivery. It was necessary to use a principal component analysis (PCA) method to reduce problematic near field reverberation arising from the transducer lying in a tightly constrained catheter package.

Results

The μCPC is capable of accurate counting (no detectable error) and sizing (at least down to our minimum diameter of $8 \mu\text{m}$), over the extent of any envisaged operating parameter set (*i.e.* all viable liquid and gas permutations relevant to our devices). Pairs of electrodes in the inlet liquid and gas channels enable facile detection of “liquid flood” (lower impedance) or “gas flood” (higher impedance). A PCA

approach applied to the transducer echo analysis reduced problematic reverberation energy by 99% and enabled detection of small blood echo signals that were otherwise undetectable. Over a period of 120 minutes of usage, signal correlation reduced from $r^2 > 0.95$ to $r^2 \sim 0.70$ indicating the viability of the approach for detecting clot erosion related echo changes. An initial prototype device, comprising a functional μ CPC-FFMD catheter device, approximately 1.5 mm in cross-sectional dimension, is also presented.

Conclusions

We have previously described the unique potential of relative small numbers of large, but unstable, microbubbles generated from an FFMD device placed at the tip of a catheter. The potential has been previously explored *in vitro* and *in vivo* in a small animal stroke model. Although the pathway to any future clinical adoption is prolonged, a necessary initial step is to show a viable technical pathway to assuring the most basic “quality control” and safety essential from a physician’s, and a medical device regulator’s, perspective. The results in this presentation demonstrate a capacity to count and size a stream of produced microbubbles, identify critical fault conditions (“liquid flood” and “gas flood”) and use of an ultrasound transducer in a catheter to assess the clot erosion progress.

References

- [1]. Dixon AJ, Rickel JMR, Shin BD, Klibanov, AL Hossack JA, Ann Biomed Eng. 2018 Feb;46(2):222-232
- [2]. Rickel JMR, Dixon AJ, Klibanov AL, Hossack JA, Lab Chip, 2018,18, 2653-2664.

High frame rate echoPIV reveals the transient flow patterns in heart failure patients

Jason Voorneveld¹, Lana B.H. Keijzer², Mihai Strachinaru^{1,2}, Dan J. Bowen², Jeffrey S.L. Goei², Antonius F.W. van der Steen¹, Folkert Ten Cate², N. de Jong¹, Hendrik J. Vos¹, Annemien E. van den Bosch², Johan G. Bosch¹

¹Department of Biomedical Engineering, Thorax Center, Erasmus MC, Rotterdam, Netherlands

²Department of Cardiology, Thorax Center, Erasmus MC, Rotterdam, Netherlands

Corresponding author: j.vorneveld@erasmusmc.nl

Introduction

Study of left ventricular (LV) flow patterns may reveal early stage biomarkers of cardiac dysfunction[1]. However, standard clinically available techniques for flow estimation, such as color and pulsed-wave (PW) Doppler, are limited to measuring only the axial velocity components. Echo-particle image velocimetry (echoPIV) is an image processing technique that tracks the displacement of ultrasound contrast agent (UCA) microbubbles to estimate flow patterns in 2D. However, echoPIV using standard line-scanning echocardiography (~50 fps) is known to severely underestimate the high velocity flows associated with diastolic filling [2]. High frame rate (HFR) echocardiography, using diverging wave transmission sequences, can be beneficial with frame rates 100x that of standard line-scanning echocardiography. We have shown previously, in an *in vitro* LV model, that HFR echoPIV can accurately estimate the high velocity flows associated with diastolic filling [3]. In this study we assess whether the use of HFR echoPIV can also estimate the transient and high velocity diastolic flow patterns in patients with heart failure.

Methods

Preliminary data from a single patient (out of a 20 patient group) with heart failure was scanned using both a clinical scanner (Phillips EPIQ 7, Phillips) and an open research scanner (Verasonics Vantage 256, Verasonics). The clinical scanner was used to obtain PW Doppler estimates at the mitral valve and aortic outflow tract, as well as to verify that the desired UCA concentration was obtained in the LV. Continuous infusion of UCA (SonoVue®, Bracco) was administered at 0.6 ml/min using an infusion pump (VueJect BR-INF 100, Bracco). For the HFR acquisitions, a P4-1 probe (center frequency = 1.5 MHz, ATL) was used to transmit two-angled (-7°, 7°) diverging-waves in a pulse-inversion sequence at a PRF of 4900 Hz, resulting in an imaging frame rate of 1225 Hz. For echoPIV analysis a custom PIV implementation was used that calculated correlation for each angle separately [3]. Subsequently, correlation compounding was performed on 5 frames of each angle to further improve SNR (10 frames total correlation compounding), resulting in a vector-frame rate of 244 Hz. Normalized cross-correlation was performed in the polar domain with an iterative, window refinement and deformation scheme [4]. Kernel size was 10° by 10mm for 3 iterations, followed by 5° by 5mm for 2 iterations, with an overlap of 75%, resulting in a final grid resolution of 1.25° by 1.25 mm. Post-processing included a 3-element temporal moving average and 3x3 gaussian spatial smoothing filter.

Results

HFR echoPIV vector sequences were obtained at 244 Hz, allowing for detailed flow structures to be followed as they develop and traverse the scan-plane (Figure 1. Right). The diastolic jet velocities corresponded well with the PW Doppler spectrum obtained in the same location (Figure 1. Top-left). Systolic correspondence was also good but the **systolic HFR echoPIV data had more variance than in the diastolic position** (Figure 1. Bottom-left).

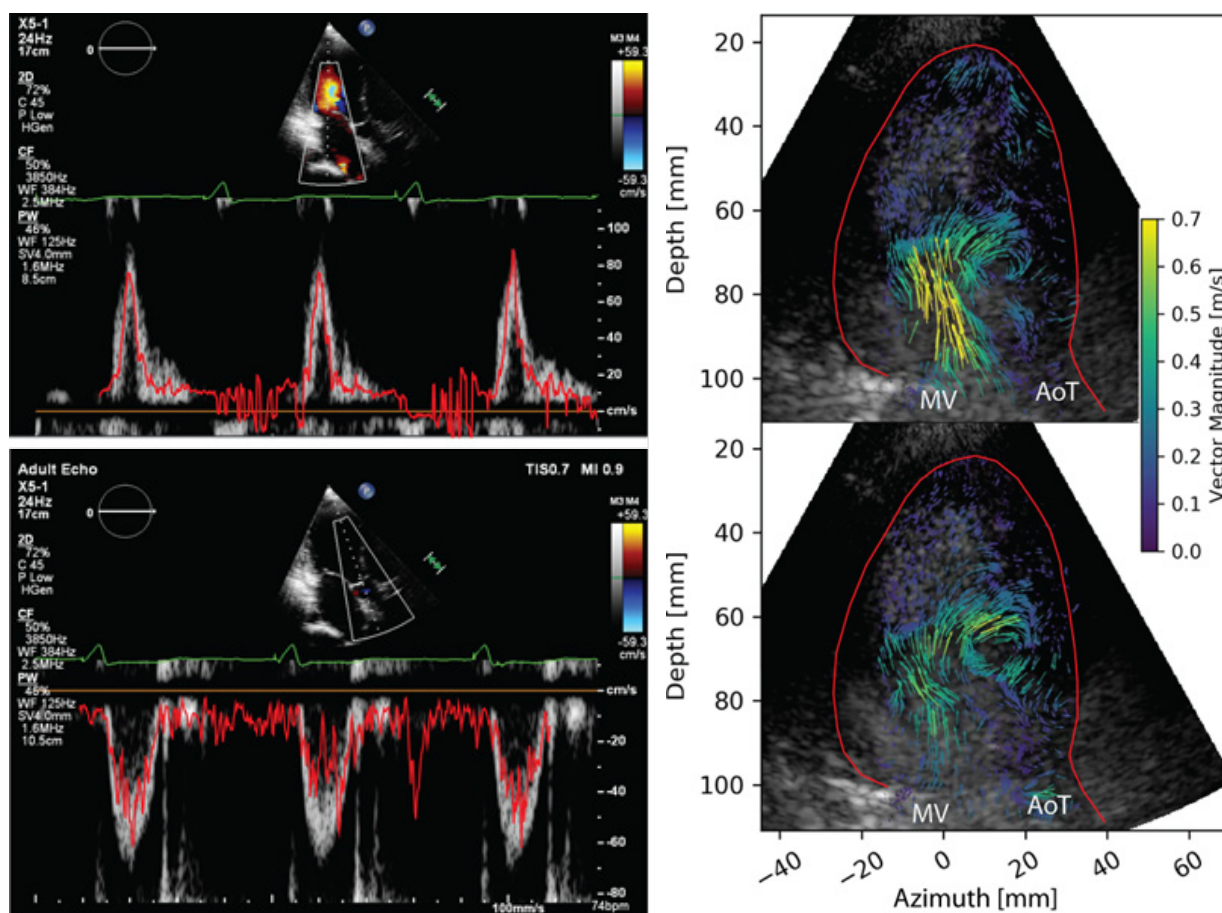


Figure 1: **Left:** Mean velocity measured in the diastolic (*top*) and systolic (*bottom*) jets using HFR echoPIV overlaid (red curves) on PW Doppler spectrum from clinical machine in the same position. **Right:** HFR echoPIV snapshots during early filling (*top*) and 30ms later (*bottom*) showing central vortex development.

Conclusions

High frame rate echoPIV could measure the high velocity diastolic and systolic jets of the left ventricle in 2D, with good correspondence to PW Doppler. Additionally, the high temporal resolution of the calculated vectors may reveal transient flow structures that would otherwise go unnoticed when using low frame rate imaging sequences.

References

- [1]. Sengupta, P. P. et al. Emerging trends in CV flow visualization. *JACC Cardiovasc. Imaging*, 5, 305–316, 2012.
- [2]. Prinz, C. et al. Can echocardiographic particle image velocimetry correctly detect motion patterns as they occur in blood inside heart chambers? A validation study using moving phantoms. *Cardiovasc. Ultrasound*, 10, 24, 2012.
- [3]. Voorneveld, J. et al. High Frame Rate Ultrasound Particle Image Velocimetry for Estimating High Velocity Flow Patterns in the Left Ventricle. *IEEE Trans. Ultrason. Ferroelectr. Freq. Control*, 1–1, 2017. doi:10.1109/TUFFC.2017.2786340
- [4]. Thielicke, W. & Stamhuis, E. J. PIVlab – Towards User-friendly, Affordable and Accurate Digital Particle Image Velocimetry in MATLAB. *J. Open Res. Softw.* 2, 2014.

Microbubble Contrast Agents for Coherent Multi-Transducer Ultrasound Imaging

Laura Peralta, Kirsten Christensen-Jeffries, Rachel Paley, Joseph V. Hajnal, Robert J. Eckersley

Department of Biomedical Engineering, School of Biomedical Engineering & Imaging Sciences, King's College London, London, UK

Corresponding author: laura.peralta_pereira@kcl.ac.uk; kirsten.christensen-jeffries@kcl.ac.uk;

Introduction

Recently, a coherent multi-transducer ultrasound imaging system has been developed by our group [1]. Such a method allows coherent combination of all the received radio frequency (RF) data sets from the multiple probes of the system. As a result, one larger effective aperture is obtained, improving the ultrasound imaging performance. The approach relies on the detection of multiple isolated point-like targets within the imaging region, which are in the common field of view (FoV) of the transducers that form the system.

This study proposes the use of microbubbles to generate the point-like targets that the coherent multi-transducer method requires. A sparse population of microbubbles is introduced into the imaging region of interest, which are then detected and localized through a similar approach to that in ultrasound super-resolution ultrasound imaging [2]. Finally, the optimum beamforming parameters, including transducer positions and average speed of sound, are calculated using the localized microbubbles and following the approach proposed by the coherent multi-transducer method [1].

Methods

The feasibility of microbubbles as reference points to localise multiple transducers with enough precision to coherently increase the effective aperture of the imaging system was investigated using an ultrasound phantom. The ultrasound phantom was immersed in a water tank containing a dilute suspension of Sonovue (Bracco, Milan) microbubbles (40 μ l SonoVue in 2.2 l water). The microbubble suspension was stirred to ensure a uniform distribution within the FoV.

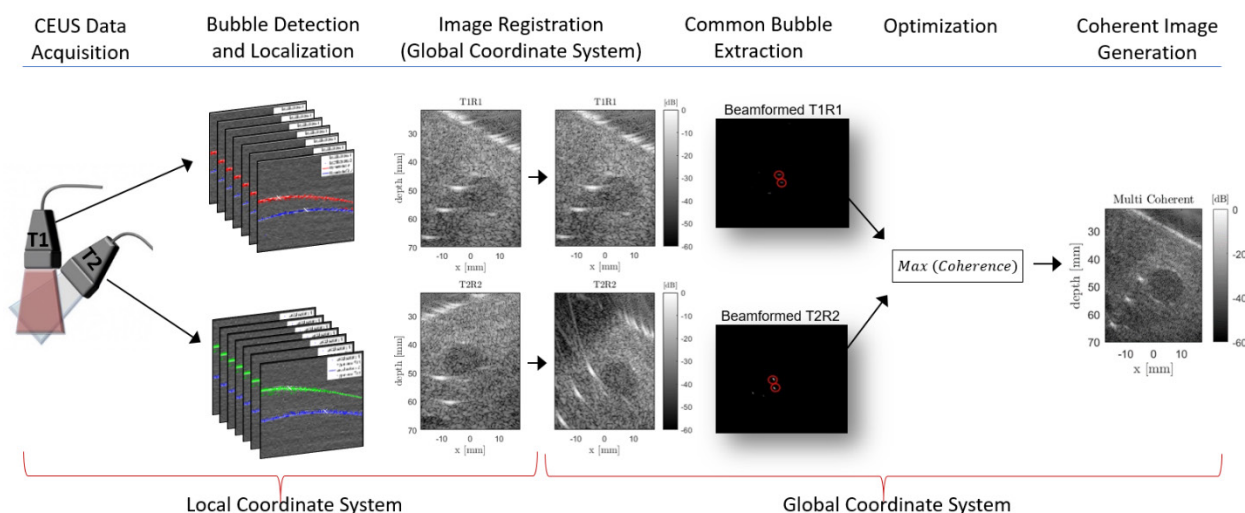


Figure 1. Schematic diagram of the proposed methodology

The experimental imaging setup consists of two synchronised 256-channel Ultrasound Advances Open Platform (ULA-OP 256) systems (University of Florence, Italy). Each ULA-OP 256 system was used to drive an LA332 ultrasonic linear array (Esaote, Italy) and transmit a plane wave (PW) at 3 MHz and pulse repetition frequency of 7 kHz, in an alternating sequence. The experimental sequence starts with probe 1 transmitting a PW into the common FoV. Then, the backscattered ultrasound field is received by both transducers. This sequence is repeated but transmitting with probe 2 and again recording the backscattered echoes with both transducers. Since every transmitted PW is received by both probes, including the transmitting one, the experimental sequence yields four RF datasets in total. Using this sequence, RF data of the ultrasound phantom immersed in the microbubble suspension was acquired over 3 minutes.

Microbubbles present in the common FoV of both transducers were detected, localized and then used as input to the coherent multi-transducer ultrasound imaging method [3]. The optimum beamforming parameters were calculated by maximising the spatial coherence of (1) the echoes backscattered from the microbubbles and (2) from the point-like targets of the phantom, as originally described in the coherent multi-transducer ultrasound imaging method [1]. A schematic diagram of the proposed method is shown in Fig.1.

Results

All RF data acquired by both probes in one sequence (four RF datasets in total) was coherently beamformed into an improved image. Resulting images obtained using microbubbles and the classical approach were compared. There were not significant differences in the optimum parameters that define probe localisation and average speed of sound between both methods.

Conclusions

In this work, the feasibility of microbubbles to optimize the beamforming parameters in a coherent multi-transducer ultrasound imaging system has been investigated. Preliminary results show potentials of microbubble contrast agents for this use.

References

- [1]. Peralta, L., Gomez, A., Hajnal, J. V., and Eckersley, R. J., "Feasibility study of a coherent multi-transducer US imaging system," in [Ultrasonics Symposium (IUS), 2018 IEEE International], IEEE (2018).
- [2]. Christensen-Jeffries, K., Browning, R. J., Tang, M.-X., Dunsby, C., and Eckersley, R. J., "In vivo acoustic super-resolution and super-resolved velocity mapping using microbubbles," *IEEE transactions on medical imaging*, vol. 34, no. 2, pp. 433–440, 2015.
- [3]. Christensen-Jeffries, K., Harput, S., Brown, J., Wells, P. N., Aljabar, P., Dunsby, C., Tang, M.-X., and Eckersley, R. J., "Microbubble axial localization errors in ultrasound super-resolution imaging," *IEEE transactions on ultrasonics, ferroelectrics, and frequency control*, vol. 64, no. 11, pp. 1644–1654, 2017.

Contrast-Enhanced Ultrasound for velocimetry in the diseased aorto-iliac tract

Stefan Engelhard^{1,3,4}, ***Majorie van Helvert***¹, ***Jason Voorneveld***², ***Guillaume Lajoinie***³, ***Hendrik Vos***², ***Johan Bosch***², ***Erik Groot Jebbink***^{1,4}, ***Michel Versluis***^{3,4}, ***Michel Reijnen***^{1,4}.

¹ Department of Vascular Surgery, Rijnstate Hospital, Arnhem, The Netherlands

² Department of Biomedical Engineering, Thorax Center, Erasmus MC, Rotterdam, The Netherlands

³ Physics of Fluids group, TechMed centre, University of Twente, Enschede, The Netherlands

⁴ Multimodality Medical Imaging Group, TechMed centre, University of Twente, Enschede, The Netherlands

Corresponding author: s.a.j.engelhard@utwente.nl

Introduction

Blood flow quantification in the aorto-iliac arteries is challenging due to complex flow phenomena near the aortic bifurcation. These flow phenomena are clinically relevant as they can affect atherosclerotic disease progression and stent patency. High-frame-rate, contrast-enhanced ultrasound (HFR-CEUS) in combination with particle image velocimetry (PIV), or echoPIV, can be used to quantify blood flow in real-time. However, the clinical application of echoPIV remains challenging. For example, calcifications found in stenotic lesions may lead to imaging artifacts. Furthermore, the potential of HFR-CEUS in stents in-vivo is unexplored. Here, we present a first preliminary study of the clinical applicability of HFR-CEUS imaging, for the purpose of PIV blood flow quantification, in patients with atherosclerotic lesions in the aorto-iliac tract, with and without stents.

Method

9 patients with a stenotic lesion in the aorto-iliac tract were included, of which 6 were treated with supervised exercise therapy and 3 patients by endovascular stent placement. All patients underwent 4 HFR-CEUS measurements and a CTA scan within 3 weeks after treatment. In the conservatively treated patients this means the start of exercise therapy. Different transmit voltages (5V and 10V) and contrast dosages (0.5mL and 1.0mL) were used for the HFR-CEUS measurements. Intravascular contrast signal in the HFR-CEUS images was compared between healthy regions, stented regions and diseased regions with and without calcifications, using the CTA scan as a reference for vessel geometry and tissue characteristics. A further analysis of the Contrast-to-Background ratio of signal intensity in these regions is presently on-going.

Results

The imaged vessels, the aorta and iliac arteries, were located at a depth of 20-70 mm on the HFR-CEUS images. The average Mechanical Index (MI) at this depth was: 0.04-0.06 (transmit voltage 5 V) and 0.08-0.12 (transmit voltage 10 V). During diastole, implying a slow blood flow, minor bubble destruction was observed in 2 out of 9 patients in the 10 V measurement.

In stented vessels, the contrast signal was lower when compared to neighboring unstented vessel regions, but contrast was clearly visible. Calcifications lead to shadowing and a substantial drop in the contrast signal, making the microbubbles undetectable in heavily calcified lesions.

Conclusion

Blood flow quantification with echoPIV in diseased aorto-iliac arteries is expected to be feasible, both in stented and non-stented regions. Calcifications, however, may cause a significant signal drop in the HFR-CEUS images, making accurate PIV analysis in these particular areas very challenging. Improved imaging methods for UCA visualization (e.g. angular compounding) may assist the clinical application of echoPIV near calcified stenotic lesions.

Detection of significant prostate cancer: Contrast-enhanced ultrasound and multiparametric MRI-targeted biopsy in comparison with standard systematic biopsy

Christophe K. Mannaerts¹, Marc. R.W. Engelbrecht², Arnoud W. Postema¹, Olivia. A.P. Lodeizen¹, Rob A.A. van Kollenburg¹, Ruud J.G. van Sloun³, Rogier R. Wildeboer³, Massimo Mischì³, Theo M. de Reijke¹, Hessel Wijkstra.^{1,3}

¹*Dept. of Urology, Amsterdam UMC, University of Amsterdam, Amsterdam, The Netherlands.*

²*Dept. of Radiology, Amsterdam UMC, University of Amsterdam, Amsterdam, The Netherlands.*

³*Dept. of Electrical Engineering, Eindhoven University of Technology, The Netherlands*

Corresponding author: c.k.mannaerts@amc.uva.nl

Introduction

Transrectal ultrasound (TRUS)-guided systematic biopsy (SBx) has been the cornerstone of prostate cancer (PCa) diagnosis for decades. Due to its ability to detect significant PCa while reducing over-detection of insignificant PCa, multiparametric magnetic resonance imaging (mpMRI) has evolved as an increasingly appealing tool [1]. Targeted biopsy (TBx) of mpMRI suspicious lesions is therefore currently recommended for previously biopsied men [2]. However, the role of mpMRI before the first biopsy is currently unclear. mpMRI-TBx misses non-negligible significant PCa while resources, such as radiologic and urologic expertise and MRI gantry time, and costs for reimbursement also represent a logistic and financial challenge [3]–[6].

Meanwhile, contrast-enhanced ultrasound (CEUS) has been considered as an alternative imaging modality for PCa diagnosis based on the fact that ultrasound is widely available, less expensive in machine purchase, portable and familiar to the urologist [7]. In CEUS, a suspension of gas-filled microbubbles is used for visualization of the microvascular network of the prostate based on the hypothesis that this vascular network undergoes alterations caused by angiogenesis [8]. Over the years, we have developed several quantification algorithms to extract these angiogenetic features by modeling the transport of a contrast bolus through the prostate vasculature as a convective-dispersion process from two-dimensional (2D) CEUS recordings. These algorithms are generally referred to as contrast-ultrasound dispersion imaging (CUDI) [9]. Various CUDI parameters related to contrast-agent dispersion and velocity have been proven to be useful for the localization of PCa in studies compared to radical prostatectomy specimens [10]–[12].

Based on the fact that radical prostatectomy data is biased (men must test positive for PCa and choose to have surgery), this work aimed at evaluating the diagnostic potential of CEUS with CUDI in a clinical setting, with prostate biopsy as the reference standard. In this IRB approved, prospective clinical trial, the significant PCa detection rates for mpMRI-TBx and CEUS/CUDI-TBx with standard SBx in biopsy-naïve men (e.g. men with no previous prostate biopsy) with a suspicion of PCa were compared.

Methods

150 biopsy-naïve men with a suspicion of PCa based on an elevated prostate-specific antigen (PSA) level and/or suspicious digital rectal examination (DRE) at the Amsterdam UMC, University of Amsterdam were included. After signing informed consent, all included men underwent mpMRI and CEUS imaging during the first visit and prostate biopsy in the second visit. As a consequence, all men served as their own control. Prebiopsy mpMRI consisted of T2-weighted, diffusion-weighted and dynamic contrast-enhanced imaging in line with ESUR guidelines [13]. 2D CEUS imaging consisted of 4 prostate plane recordings using a 2.4 mL bolus injection of SonoVue® (Bracco, Milan, Italy) on a Philips iU22 ultrasound scanner with a C10-3V endorectal probe (Philips Healthcare, Bothell, USA). The 2D CEUS recordings were subsequently extracted from the device and subjected to CUDI quantification analyses.

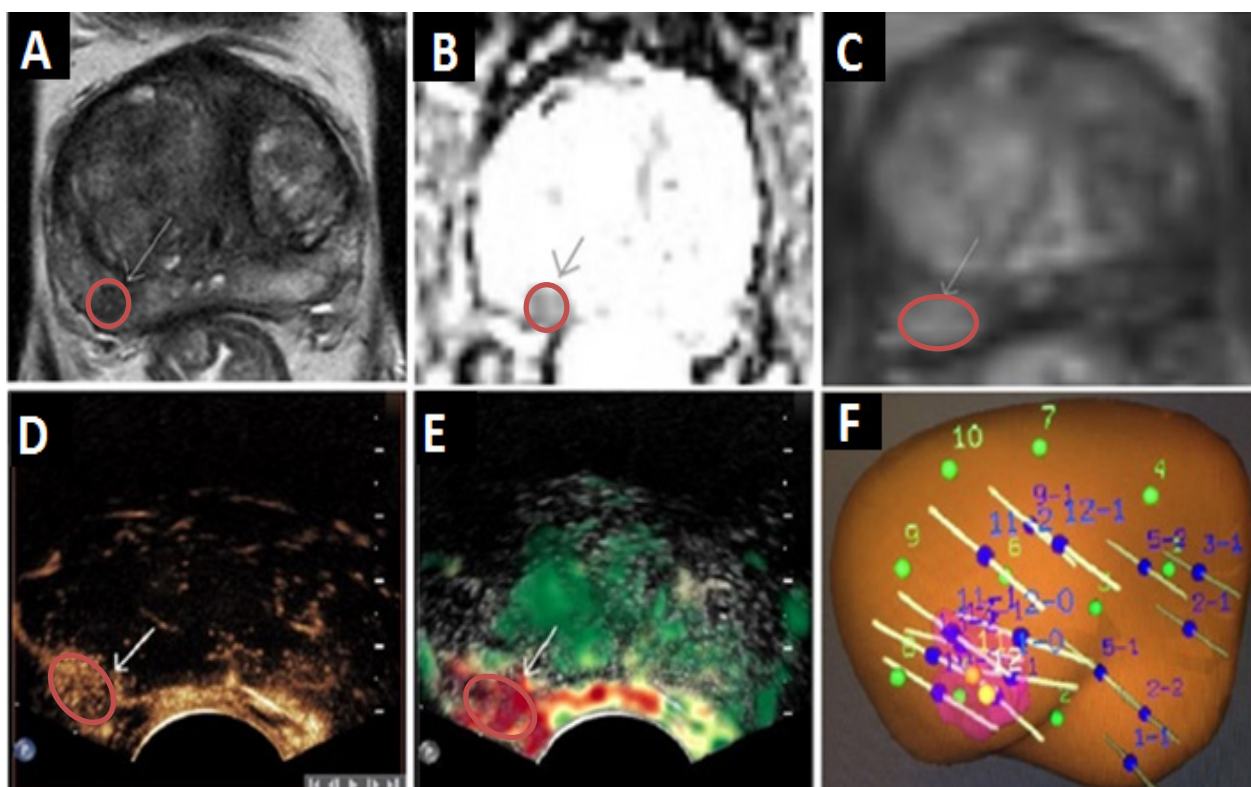
Four different CUDI parametric maps were generated, representing spatiotemporal correlation, Péclet number, flow velocity and a combination of these parameters. We refer to earlier publications for a more elaborate explanation of these individual techniques [10]–[12].

The mpMRI and CEUS with CUDI parametric maps were evaluated in a blinded fashion by a radiologist and ultrasound performer with PIRADSV2 (Prostate Imaging and Reporting Data System) and a 1 to 5 Likert Scale, respectively [14]. Hereafter, an operator blinded for mpMRI and CEUS/CUDI imaging performed a TRUS-guided 12-core SBx. A second operator performed a cognitive TBx from CEUS/CUDI suspicious lesions (Likert score ≥ 3) and a TBx from mpMRI suspicious lesions (PI-RADS ≥ 3) using a MRI-TRUS fusion device (Artemis®, Eigen, Grass Valley, CA, USA). Detection rates of significant PCa (defined as Gleason score (GS) ≥ 7) and insignificant PCa (defined as GS=6) were compared between the different biopsy regimens. Negative (NPV) and positive predictive values (PPV) of mpMRI and CEUS for significant PCa were also determined.

Results

Data of 140 men was available for final analysis. Men had a median PSA of 6.2 ng/mL (IQR: 4.6 – 8.0). A total of 78 men (56%) had PCa. 61 men (44%) had significant PCa (GS ≥ 7) while 17 men (12%) had insignificant PCa (GS=6). Figure 1 demonstrates a study example.

Figure 1. Study example: 66 years old men with a PSA of 5.8 ng/mL and a suspicious DRE on the right



A, B and C: mpMRI imaging: **A:** T2-weighted image, **B:** Diffusion-weighted ADC map, **C:** Dynamic Contrast-Enhanced image. **D and E:** US imaging: **D:** contrast-enhanced image (single frame), **E:** CUDI parametric image. In all MRI and US imaging modalities a clear lesion (circle and arrows) is visible. **F:** Artemis® image fusion: Suspicious lesion in pink with biopsy tracking (SBx and TBx). Biopsy **Results:** mpMRI- and CEUS-TBx: Gleason score 4+3=7 PCa; SBx: Gleason score 3+4=7 PCa.

	SBx	MRI-TBx	CEUS-TBx		
Imaging					
Negative imaging; no biopsy	-	91 (65)	59 (42)		
Biopsy performed	140 (100)	49 (35)	81 (58)		
Biopsy outcome					
All PCa, n (%)	76 (54)	41 (29)	p<0.001*	42 (30)	p<0.001*
Insignificant PCa (GS=6), n (%)	21 (15)	1 (1)	p<0.001*	4 (3)	p<0.001*
Significant PCa (GS≥7), n (%)	55 (39)	40 (29)	p=0.004*	39 (28)	p=0.002*
3+4	35 (25)	18 (13)		21 (15)	
4+3	13 (9)	14 (10)		9 (6)	
8	2 (1)	5 (4)		5 (4)	
9-10	5 (4)	3 (2)		4 (3)	

Table 1. Comparison of PCa detection between the different biopsy regimens

*p-values indicate a statistically significant difference with the McNemar test between SBx outcome with the outcome of interest (MRI-TBx or CEUS-TBx)

As seen in Table 1, SBx detected more significant PCa (39%) and insignificant PCa (15%) as compared to MRI-TBx (29% and 1%) and CEUS-TBx (28% and 3%), respectively (all p<0.05). The NPV and PPV of mpMRI for significant PCa was 81% (74/91) and 82% (40/49). The NPV and PPV of CEUS/CUDI for significant PCa was 83% (49/59) and 48% (39/81), respectively.

Conclusions

This work is the first to compare the diagnostic value of mpMRI-TBx and CEUS/CUDI-TBx with standard SBx for detection of significant PCa. Despite avoidance of biopsy in men without PCa and men with insignificant PCa, an MRI-TBx or CEUS/CUDI-TBx only approach missed non-negligible significant PCa as compared to SBx. mpMRI and CEUS have a comparable detection rate (29% vs 28%) and NPV (81% vs 83%) for significant PCa, but mpMRI provided a higher PPV (82% vs 48%) compared to CEUS.

We recognize that biopsy-core histopathology as reference standard has limitations by its tendency to harbour both random and systematic errors, as recently confirmed by the PROMIS trial [15]. However, we addressed the more pragmatic clinical question as to whether an mpMRI-TBx or CEUS/CUDI-TBx could replace SBx biopsy. If the NPV and PPV of mpMRI and CEUS/CUDI were sufficiently high in comparison with the reference standard of SBx, then in practice one could indeed avoid the need for SBx.

In the future, we hope to further improve our CUDI quantification analysis. Further assessment of possible benign disease in false-positive regions of interest and more extensive machine learning strategies might elucidate on the relation between CUDI parameters and underlying physiology and improve our currently low PPV. Furthermore, three-dimensional (3D) CEUS, shortening the procedure time and alleviating the limitation of being bound to a 2D plane, might be used in the future to enable full 3D modelling of the kinetic behaviour of microbubbles in the prostate and improve NPV by reducing the risk of missing a lesions [16], [17].

Acknowledgments

This research was conducted in the framework of a research grant from the Dutch Cancer Society entitled: Improved prostate cancer detection and localization by contrast enhanced dispersion imaging (#UVA 2013-5941)

References

- [1]. V. Kasivisvanathan et al., "MRI-targeted or Standard Biopsy for Prostate-Cancer Diagnosis," *N Engl J Med*, vol. 378, no. 19, pp. 1767–1777, 2018.
- [2]. N. Mottet et al., "EAU-ESTRO-SIOG Guidelines on Prostate Cancer. Part 1: Screening, Diagnosis, and Local Treatment with Curative Intent," *Eur. Urol.*, vol. 71, no. 4, pp. 618–629, 2017.
- [3]. P. C. Moldovan et al., "What Is the Negative Predictive Value of Multiparametric Magnetic Resonance Imaging in Excluding Prostate Cancer at Biopsy? A Systematic Review and Meta-analysis from the European Association of Urology Prostate Cancer Guidelines Panel," *Eur. Urol.*, vol. 72, no. 2, pp. 250–266, 2017.
- [4]. G. Ploussard et al., "Positive pre-biopsy MRI: are systematic biopsies still useful in addition to targeted biopsies?," *World J. Urol.*, no. 0123456789, 2018.
- [5]. R. Faria et al., "Optimising the Diagnosis of Prostate Cancer in the Era of Multiparametric Magnetic Resonance Imaging: A Cost-effectiveness Analysis Based on the Prostate MR Imaging Study (PROMIS)," *Eur. Urol.*, vol. 73, no. 1, pp. 23–30, 2018.
- [6]. J. Walz, "The 'PROMIS' of Magnetic Resonance Imaging Cost Effectiveness in Prostate Cancer Diagnosis?," *Eur. Urol.*, vol. 73, no. 1, pp. 31–32, 2018.
- [7]. A. Grey and H. U. Ahmed, "Multiparametric ultrasound in the diagnosis of prostate cancer," vol. 26, no. 1, pp. 114–119, 2016.
- [8]. G. Russo, M. Mischi, W. Scheepens, J. J. De La Rosette, and H. Wijkstra, "Angiogenesis in prostate cancer: Onset, progression and imaging," *BJU Int.*, vol. 110, no. 11 C, pp. 794–808, 2012.
- [9]. M. Mischi, M. P. Kuenen, and H. Wijkstra, "Angiogenesis imaging by spatiotemporal analysis of ultrasound contrast agent dispersion kinetics," *IEEE Trans Ultrason Ferroelectr Freq Control*, vol. 59, no. 4, pp. 621–629, 2012.
- [10]. M. P. J. Kuenen, M. Mischi, and H. Wijkstra, "Contrast-ultrasound diffusion imaging for localization of prostate cancer," *IEEE Trans. Med. Imaging*, vol. 30, no. 8, pp. 1493–1502, 2011.
- [11]. M. P. Kuenen, T. A. Saidov, H. Wijkstra, J. J. de la Rosette, and M. Mischi, "Spatiotemporal correlation of ultrasound contrast agent dilution curves for angiogenesis localization by dispersion imaging," *IEEE Trans Ultrason Ferroelectr Freq Control*, vol. 60, no. 12, pp. 2665–2669, 2013.
- [12]. R. J. van Sloun, L. Demi, A. W. Postema, J. J. de la Rosette, H. Wijkstra, and M. Mischi, "Ultrasound-contrast-agent dispersion and velocity imaging for prostate cancer localization," *Med. Image Anal.*, vol. 35, pp. 610–619, 2017.
- [13]. J. O. Barentsz et al., "ESUR prostate MR guidelines 2012," *Eur. Radiol.*, vol. 22, no. 4, pp. 746–757, 2012.
- [14]. J. C. Weinreb et al., "PI-RADS Prostate Imaging - Reporting and Data System: 2015, Version 2," *Eur. Urol.*, vol. 69, no. 1, pp. 16–40, 2016.
- [15]. H. U. Ahmed et al., "Diagnostic accuracy of multi-parametric MRI and TRUS biopsy in prostate cancer (PROMIS): a paired validating confirmatory study," *Lancet*, vol. 389, no. 10071, pp. 815–822, 2017.
- [16]. S. G. Schalk et al., "4-D spatiotemporal analysis of ultrasound contrast agent dispersion for prostate cancer localization: A feasibility study," *IEEE Trans. Ultrason. Ferroelectr. Freq. Control*, vol. 62, no. 5, pp. 839–851, 2015.
- [17]. R. R. Wildeboer et al., "Convective-Dispersion Modeling in Three-Dimensional Contrast-Ultrasound Imaging for the Localization of Prostate Cancer," *IEEE Transactions on Medical Imaging*, 2018.

Ultrasound-mediated intravesical chemotherapy: *ex vivo* evaluation

Noboru Sasaki¹, Nobuki Kudo², Mitsuyoshi Takiguchi¹

¹*Department of Veterinary Clinical Sciences, Hokkaido University, Sapporo, Japan*

²*Division of Bioengineering and Bioinformatics, Hokkaido University, Sapporo, Japan*

Corresponding author: n.sasaki@vetmed.hokudai.ac.jp

Introduction

Bladder cancer is the ninth most common cancer worldwide. Almost 70% are non-muscle invasive bladder cancer (NMIBC) at the initial diagnosis. The standard therapy is transurethral resection of visible tumors, followed by intravesical chemotherapy or Bacillus Calmette-Guérin (BCG) therapy. However, 50-70% of patients relapse within 5-year and up to 30% progress to muscle invasive cancer [1]. Although radical cystectomy remains the standard therapy after the BCG failure, it may have impacts on quality of life. In addition, current shortage of BCC requires non-BCG alternative intravesical therapy [2].

Drug delivery using ultrasound (US)-triggered microbubble cavitation would be one of the most promising tools for intravesical chemotherapy. Intravesical instillation enables microbubbles to directly attach to the surface of bladder. Since NMIBC limited in urothelium/lamina propria, US-triggered microbubble cavitation in bladder would be effective with high tumor specificity. We previously showed the temporal and spatial profile of drug delivery by US-triggered microbubble cavitation in a bladder cancer model [3]. In this *ex vivo* study, we evaluated the feasibility of the US-triggered microbubble cavitation for intravesical chemotherapy.

Methods

Two freshly excised dog bladders were used in this study. The bladders were filled with 20 mL saline containing cisplatin and microbubbles. The concentrations of cisplatin and microbubbles were 0.5 µg/mL and 6×10^6 microbubbles/mL, respectively. A linear array probe (PLT-704SBT; Cannon Medical Systems) was attached to the bladder. The probe was operated in the pulsed subtraction imaging mode of a diagnostic US machine (Aplio-XG SSA-790; Cannon Medical Systems). The transmitting frequency was 5 MHz and the MI value on the screen was 1.39. The bladder was placed on an acoustic absorber and was exposed to US for 2 mins. After the exposure, bladder wall samples were taken from three different regions (Fig. 1). Tissue samples were washed with phosphate buffered solution and were divided into two pieces. One piece was digested in 60% nitric acid overnight for platinum quantification using an inductively coupled plasma mass spectrometry (Agilent 7700x ICP-MS). The others was placed in neutral-buffered 10% formalin at room temperature and was used for histological evaluation.

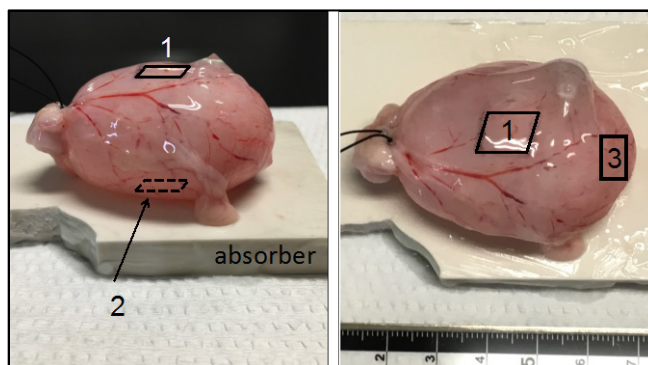


Figure 1. Resected bladder.

Tissue samples were taken from three regions. #1 was the sonicated region, #2 was the contralateral side of sonicated region, and #3 was a region distant from the sonicated region.

Results

Figure 2 shows the platinum concentration of the tissue samples taken from three different regions of the bladder. Although platinum was detectable in all three regions, the platinum concentration in the sonicated region was higher than that of other two regions. There were not any observable differences in bladder mucosa in hematoxylin and eosin staining.

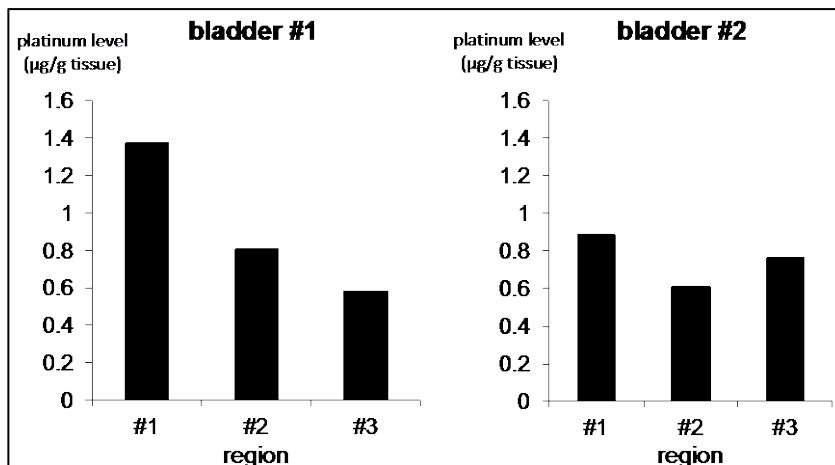


Figure 2. Platinum concentration in bladder wall.

Platinum level in bladder wall was measured by ICP-MS. #1 was the sonicated region, #2 was the contralateral side of sonicated region, and #3 was a region distant from the sonicated region.

Conclusions

This preliminary study shows the feasibility of US-triggered microbubble cavitation for intravesical chemotherapy. Meanwhile, passive diffusion of intravesical cisplatin may have some impacts on US-assisted intravesical chemotherapy. Further studies are needed to evaluate pharmacokinetics of intravesical cisplatin and to optimize treatment procedures.

References

- [1]. Eifler JB, Scarpato KR, Clark PE, Management of noninvasive bladder cancers, *Current Opinion in Oncology*, 27: 185-190, 2015.
- [2]. Veeratterapillay R, Heer R, Johnson MI, Persad R, Bach C, High-risk non-muscle-invasive bladder cancer - Therapy options during intravesical BCG shortage, *Management of noninvasive bladder cancers, Current Urology Reports*, 16: 68, 2016.
- [3]. Sasaki N, Ishi K, Kudo K, et al., Spatial and temporal profile of cisplatin delivery by ultrasound-assisted intravesical chemotherapy in a bladder cancer model, *PLoS One*, 12: e0188093, 2017.

Ultrasound-sensitive liposomes for macromolecular drug delivery

*Maria B. C. de Matos*¹, *Roel Deckers*², *Guillaume Lajoinie*³, *Raymond Schiffelers*⁴, *Robbert Jan Kok*¹

¹ *Department of Pharmaceutics, Utrecht Institute for Pharmaceutical Sciences, Utrecht University, The Netherlands*

² *Imaging Division, University Medical Center Utrecht, The Netherlands*

³ *Physics of Fluids Group, MESA+ Institute for Nanotechnology, University of Twente, The Netherlands*

⁴ *Laboratory Clinical Chemistry & Haematology, University Medical Center Utrecht, the Netherlands*

Corresponding author: r.j.kok@uu.nl

Introduction

Ultrasound-sensitive liposomes (USL) are liposomes that have been loaded with perfluorocarbon (PFC) nanoemulsions that can respond to external ultrasound stimuli. By applying ultrasound, PFC droplets undergo phase transition from liquid to gas thus rupturing the lipid bilayer of the USL and releasing the drug [1,2]. The use of toxic proteins and other biotherapeutics have gained relevance in the cancer treatment arena due to their high potency. The toxic protein mistletoe lectin-1 (ML1, 60 kDa) has been studied in the context of cancer treatment using thermosensitive liposomes as nanocarriers [3], but the release was limited by the underlying release mechanism of this class of liposomes. The objective of this study was to investigate the feasibility of USL for encapsulation and triggered release of ML1.

Methods

The 200 nm-size liposomes were prepared by thin film hydration method and extrusion and were composed of DPPC, cholesterol and DSPE-PEG₂₀₀₀ (DSPE-PEG₂₀₀₀ content 5, 10, 20% mol; USL5, USL10, USL20, respectively). ML1 was encapsulated in the liposomes and used as active ingredient. Oil in water nanoemulsions were composed of perfluoropentane (PFC5) as oil-like phase and DPPC as surfactant and were prepared by sonication (Branson sonifier, 20 kHz), followed by extrusion (100 nm). USLs were finally obtained by mixing and sonicating liposomes and nanoemulsion in 1:1 v/v. Plain liposomes, i.e. not containing nanoemulsion, were prepared similarly. Sucrose gradients were used to separate free drug, un-encapsulated emulsions, empty liposomes and USL. The resulting fractions were characterized in terms of size/PDI, stability at storage conditions, phosphate content, HIFU triggered release, and bioactivity of released ML1 against CT26 colon adenocarcinoma cells.

High-intensity focused ultrasound (HIFU) release experiments were performed with a single element focused ultrasound transducer (Imasonic, Besançon, France) operated at 1.3 MHz, Duty Cycle = 1%, Pulse Repetition Period = 50 ms. The dimensions of the focal point were 1×1×3 mm³ (at -3 dB). A PCR tube (Bio rad, California USA), containing 3 µL of USL in 167 µL buffer, was positioned in the focal point and sonicated for 1 minute at different pressures ranging between 1 and 50 MPa. Time dependent release experiments were performed at constant acoustic pressure (2 and 25 MPa) and exposure times varying between 30 s and 8 min. For *in vitro* proof of concept experiments, the PCR tube containing 3 µL of USL in 167 µL cell culture medium, was positioned in the focal point and sonicated for 1 minute at 2 and 25 MPa. The mixture was then transferred to the cells and incubated during 4 h, without any further purification (i.e. no separation between released cargo and USL), to allow released ML1 uptake. After the incubation/uptake period, the medium was replaced by drug-free medium and MTS was measured 44 h later. The goal was to assess the integrity of the protein after HIFU exposure and to determine if the released amounts could induce cell killing.

Results

USL5 and USL10 complied with all requirements: homogeneous size, storage stability, HIFU triggered release (Figure 1A) and *in vitro* tests, contrarily to USL20, that revealed colloidal instability during the first days after preparation. The best release conditions were found to be in the range of 2-25MPa, therefore we used the two extremes to continue with the experiments. Plain liposomes also released their cargo upon HIFU treatment as showed before [4] but the release was 4-fold improved when the PFC5 nanoemulsion was located inside the liposomes. State of the art confocal live cell imaging of CT26 cells allowed visualization of the uptake of the ML1 that was released from USLs after HIFU treatment. Released ML1 potently inhibited tumor cell viability, reaching 60-70% killing of the cancer cells (Figure 1B).

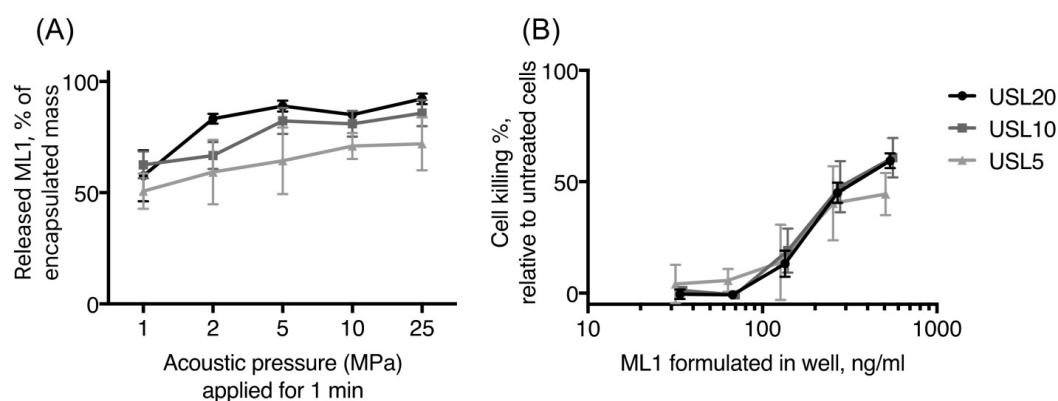


Fig. 1. – HIFU triggered release of ML1 toxin from USLs (A). After HIFU treatment of USL, the released ML1 inhibited cell viability as measured by MTS (B). In both graphs, black line corresponds to liposomal formulation USL20, dark-grey to USL10 and light-grey to USL5.

Conclusion

We demonstrate that USL can be used for triggered delivery of macromolecules including cytotoxins that can induce tumor cell death. The detailed analysis of the acoustic behavior of the nanoemulsion and USL is ongoing. Encapsulation of cytotoxic proteins in USL can be an attractive approach to increase their safety, target site accumulation and enhance their potential to induce cytotoxicity, by a combination of nanoparticle driven tumor uptake followed by local HIFU stimulation and consequent cargo release.

References

- [1]. Lin CY, Javadi M, Belnap DM, Barrow JR, Pitt WG, Ultrasound sensitive eLiposomes containing doxorubicin for drug targeting therapy, *Nanomedicine: Nanotechnology, Biology, and Medicine*, 10: 67-76, 2014.
- [2]. Javadi M, Pitt WG, Belnap DM, Tsosie NH, Hartley JM, Encapsulating Nanoemulsions Inside eLiposomes for Ultrasonic Drug Delivery, *Langmuir*, 28: 14720-14729, 2012.
- [3]. de Matos, MBC, Beztsinna N, Heyder C, Fens MHAM, Mastrobattista E, Schiffelers RM, Lenewit G, Kok RJ, Thermosensitive liposomes for triggered release of cytotoxic proteins, *European Journal of Pharmaceutics and Biopharmaceutics*, 132: 211-221, 2018.
- [4]. Oerlemans C, Deckers R, Storm G, Hennink WE, Nijssen JFW, Evidence for a new mechanism behind HIFU-triggered release from liposomes, *Journal of Controlled Release*, 168: 327-333, 2013.

Cytotoxicity evaluation of sonodynamic therapy combined with microbubble contrast agent *in vitro*

M. Tamošiūnas¹, J. Kulbacka², S. Šatkauskas¹

¹ Biophysical Research group, Faculty of Natural Sciences, Vytautas Magnus University, Vileikos 8, Kaunas 44404, Lithuania

² Department of Molecular and Cellular Biology, Medical University of Wrocław, Borowska 211A, 50-556 Wrocław, Poland

Corresponding author: mindaugas.tamosiunas@vdu.lt

Introduction

Ultrasound (US) application activates tetrapyrrole sensitizers causing cell killing effects via elevated oxidative stress, referred to as sonodynamic therapy (SDT). In response to sonication, the cells may also undergo irreversible sonoporation (SP) resulting cell damage and reversible SP facilitating the intracellular delivery of tetrapyrrole sensitizers. Our study quantitatively separates the cytotoxic effects produced by sonoporation and sonodynamic therapy when combining US, microbubble (MB) contrast agent and sensitizer treatment.

Methods

Human malignant melanoma Me45 cells were exposed to 0.3 – 1.1 MPa acoustic peak negative pressures (PNP) generated by 6 mm diameter US transducer (Sonitron 2000, Richmar, USA) operating at 1 MHz frequency, continuous wave mode. For sonodynamic reaction, 150 µl of Me45 cells were suspended in electroporation medium (10⁶ cells/ml) with addition of sensitizer chlorin e6 (Ce6, Frontier Sci., USA) at 170 µM final concentration. Cells in SP group, w/o Ce6, were added with air-filled MBs at 390:1 or 66:1 MB-cell ratio prepared by using BG7573 (Bracco, Switzerland) lipids. Cells in US control group were insonicated without MBs administration. US transducer was placed 2 mm bellow exposure chamber, made of thin (70 µm) plastic of 12 mm internal diameter and 6 mm height, and US was applied for 2, 10, 25, 60, 120 and 180 s. After insonication the cells were incubated for 10 min at 20 °C, then allowed to grow for 24 h (or 72 h) incubated at 37 °C in 5 % CO₂ for cell viability determination by MTT assay. Cell apoptosis was additionally analysed using TUNEL assay, visualized using an ApopTag kit (Millipore, USA) after 120 h incubation. Intracellular accumulation of Ce6 was compared between SDT groups using fluorescence microscopy (Leica DMI8, Germany; ex 540 – 580 nm, dichroic 585 nm; em. 592 – 668 nm; exposure 3 s) and spectrofluorimetry (AvaSpec ULS2048L, Avantes, Netherlands; 473 nm excitation coupled to Y-shaped fiber bundle FC-UV400-2-SR) within 1 h after insonication.

Results

Me45 cell membrane permeability to Ce6 was significantly enhanced by US application, increasing Ce6 fluorescence in cell cytoplasm. Compared with US control groups, Ce6 mediated sonodynamic therapy induced higher cytotoxicity at the same insonication conditions, evaluated by MTT assay. Me45 cell apoptosis was detected by TUNEL assay after sonodynamic reaction. The most efficient sonodynamic activation of sensitizer Ce6 was produced by relatively low PNP (0.3 MPa) US treatment applied for 1min interval, without additional contrast agent MBs added, resulting in 50 % decrease of cell viability. The application of MBs at 390:1 MB-cell ratio induced the highest effect of irreversible cell sonoporation, however with low significance of sonodynamic cytotoxicity. Maximum 70 % of cells were killed by US induced MB cavitation, applying 0.6 MPa PNP for 2 min, whereas only ~5 % of cells were additionally affected by SDT.

Conclusion

The ability of MB cavitation to induce cell apoptosis extends its application area of into a field of SDT, however the highest induced cytotoxicity *in vitro* was related to MB cavitation, but not to sonodynamic reaction.

Bleomycin plus ultrasound and microbubbles to treat feline oral squamous cell carcinoma, as a model for human head and neck cancer, study design of the BUBBLEFISH Trial

Josanne S. de Maar¹, Charis Rousou², Maurice M.J.M. Zandvliet³, Stefanie Veraa³,
Chrit T.W. Moonen¹, Roel Deckers¹

¹Imaging Division, University Medical Center Utrecht, Utrecht, The Netherlands

²Department of Pharmaceutical Sciences, Utrecht University, Utrecht, The Netherlands

³Department of Clinical Sciences of Companion Animals, Faculty of Veterinary Medicine, Utrecht, The Netherlands

Corresponding author: j.s.demaar@umcutrecht.nl

Introduction

Head and Neck Squamous Cell Carcinoma (HNSCC) is a common group of malignancies in humans. Most patients present with locally advanced disease, where primary surgery is often not an option. Despite treatment with combined modalities, approximately half of the patients develop (often incurable) local recurrences. Therefore, there is a clear clinical need for improved local therapy in HNSCC.

The combination of ultrasound and microbubbles (USMB) has been shown to increase local tumor uptake and to enhance the efficacy of several drugs.[1] In particular, the nonpermeant drug bleomycin may benefit from the combination with USMB. *In vitro*, USMB increased bleomycin cytotoxicity,[2,3] while *in vivo*, adding USMB to bleomycin improved growth inhibition of HNSCC in mice.[2]

Feline Oral Squamous Cell Carcinoma (FO SCC) patients provide a valuable model for evaluation of HNSCC therapies. The combination of bleomycin chemotherapy with USMB could become a low-burden alternative treatment for these cats, and simultaneously provide valuable information for clinical translation of the USMB technique.

Here we present the design of a veterinary study with the objective to evaluate the safety, feasibility and efficacy of bleomycin plus USMB in FO SCC patients. As a preparation for this veterinary study we confirmed the efficacy of bleomycin plus USMB in a HNSCC cell-line, and compared the sonoporation efficacy between an optimized single element set-up and a clinical US imager that will be used during the veterinary study.

Methods

In vitro experiments. We performed *in vitro* experiments using an unfocused single element transducer (Precision Acoustics, Dorchester, United Kingdom) with a diameter of 20 mm. FaDu cells were sonicated in CLINicells (Mabio) in the presence of SYTOX green (conc. 2.1µM) or bleomycin (5 µg/mL, 2 hours incubation) and microbubbles (700µL per CLINicell, SonoVue, Bracco, conc. 1-5x10⁸ bubbles/mL) with different ultrasound transducers and settings (see table 1 for overview of performed experiments). Cell viability was evaluated 24 hours after sonoporation with an Alamar Blue assay.

Table 1. Overview of experiments and used ultrasound parameters

	SYTOX/BL M	f (MHz)	Cycli/pulse	PRF (kHz)	Pneg (MPa)	Rel. I (dB)	Indicated MI	Exposure time (s)	US area (cm ²)
Single element transducer	YES/YES	1.5	150	1.0	0.4 0.5 0.6	-	-	60	25
EPIQ 7, Probe S12-4	YES/NO	4	67	1.8	-	-3 -1.5 0	0.2 0.3 0.4	10	±4.2
EPIQ 7, probe S8-3	YES/NO	3	46	1.8	-	-1.5 0	0.3 0.3	10	±4.2

Veterinary study design. We will perform a single-arm prospective study, in 10 feline companion animals with spontaneously arisen FOSCC without other suitable treatment options except for palliative care. During procedural sedation, intravenous bleomycin (10.000 IU/m²) will be combined with USMB treatment of the oral tumor, which can be repeated to a maximum of three sessions in two weeks. Ultrasound parameters will be based on *in vitro* experiments performed with the clinical ultrasound device. Feasibility of the treatment, adverse events, clinical performance and body condition score will be monitored, questionnaires will be used to evaluate quality of life. Clinical response will be evaluated by measurement of the tumor after 1, 2 and 5 weeks.

Results

In vitro experiments

Bleomycin or USMB alone had little effect on cell viability, whereas the combination of bleomycin and USMB significantly reduced the cell viability. The cell viability decreased with increasing US pressure when applied as combination (Fig. 1a). SYTOX green uptake was highest (31%) after USMB with the single element transducer at 0.6MPa Pneg. (Fig. 1b). After USMB with the US imager and the S8-3 probe at 0dB, SYTOX green uptake (i.e 23%) approached that of the single element transducer. The S12-4 probe increased SYTOX green uptake to a lesser extent and achieved a maximum uptake similar to that of the single element transducer at 0.5MPa Pneg (i.e. 5%).

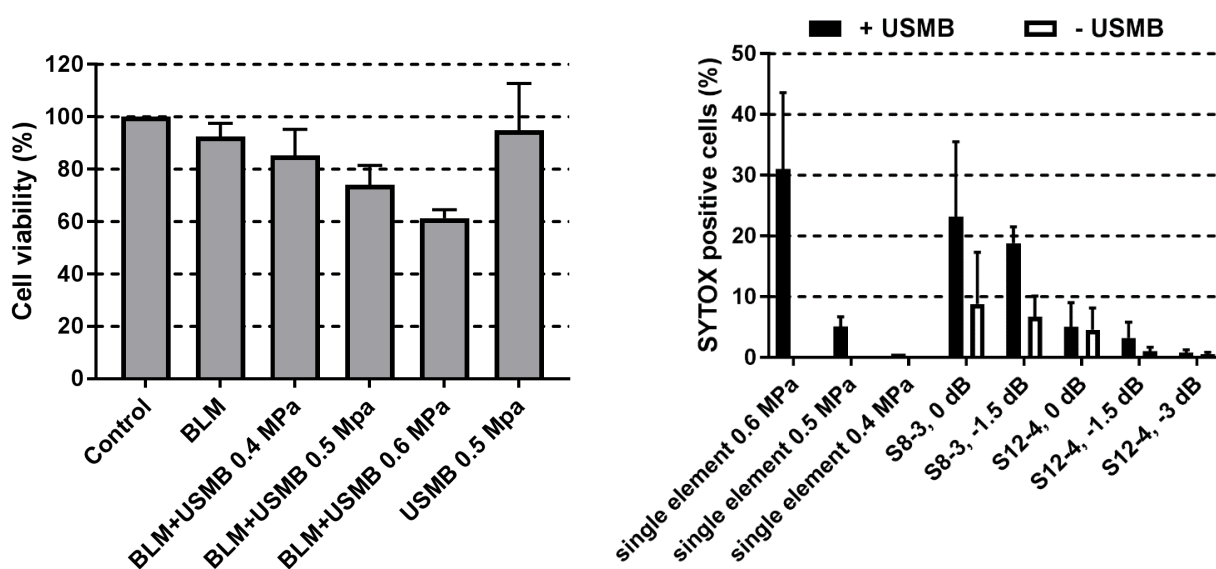


Figure 1a. Cell viability 24 hours after bleomycin + USMB b.SYTOX green uptake

Veterinary study We expect to start patient inclusion in the beginning of 2019.

Conclusions

USMB treatment increases the cytotoxic effect of bleomycin on FaDu cells *in vitro*. Cell permeability can also be increased *in vitro* using a clinical ultrasound device, which will be used in the planned veterinary study.

References

- [1]. Lammertink BHA, Bos C, Deckers R, Storm G, Moonen CTW, Escoffre J-M, Sonochemotherapy: from bench to bedside, *Frontiers in Pharmacology*, 6(138): 1-17, 2015.
- [2]. Iwanaga K, Tominaga K, Yamamoto K, Habu M, Maeda H, Akifusa S, Tsujisawa T, Okinaga T, Fukuda J, Nishihara T, Local delivery system of cytotoxic agents to tumors by focused sonoporation, *Cancer Gene Therapy*, 14: 354-363, 2007.
- [3]. Lamanuskas N, Novell A, Escoffre J-M, Venslauskas M, Šatkauskas S, Bouakaz A, Bleomycin delivery into cancer cells *in vitro* with ultrasound and SonoVue® or BR14® microbubbles, *Journal of Drug Targeting*, 21(4): 407-414, 2013.

Drug delivery across the blood-brain barrier using short 300-kHz pulses of ultrasound and microbubbles

*Matthew J. Copping¹, Gerard Hernandez Mir¹, Sophie V. Morse¹, Tiffany G. Chan³,
Magdalena Sastre², James J. Choi¹*

¹*Department of Bioengineering, Imperial College London, London SW7 2AZ, UK*

²*Department of Medicine, Imperial College London, London W12 0NN, UK*

³*Department of Chemistry, Imperial College London, London SW7 2AZ, UK*

Corresponding author: j.choi@imperial.ac.uk

Introduction

The blood-brain barrier (BBB) is a specialised interface between the blood and the brain interstitial fluid that prevents therapeutic agents from entering the brain [1]. As a result the BBB impedes the treatment of brain diseases, such as Alzheimer's disease, which currently has no effective treatment [2]. By use of ultrasound and lipid shell microbubbles the blood-brain barrier permeability can be altered in a non-invasive, localised and temporary manner allowing for a wider range of compounds to be delivered to the brain in a safe and well documented way [3]. We have recently demonstrated that short pulses of ultrasound emitted in a rapid short pulse (RaSP) sequence can produce short-duration blood-brain barrier permeability changes and reduce the brain's exposure to neurotoxic blood proteins [4]. However, those studies were performed in mice with pulses with a centre frequency of 1-MHz, which does not easily pass through the thick human skull. The purpose of this study is to determine whether short ultrasound pulses at 300-kHz can deliver drugs across the blood-brain barrier and characterise how different acoustic parameters alter the drug delivery pattern.

Methods

Fluorescently tagged model drugs (Texas Red 3 kDa dextran and FITC 645 Da biotin) were injected intravenously into wild type mice (C57BL/6) after a bolus injection of SonoVue[®] or homemade lipid microbubbles. During and after the injections focused ultrasound pulses (centre frequency 0.3 MHz, pulse length 1-5 cycles, peak-rarefactional pressures: 0.1 - 0.4 MPa) were non-invasively applied to the left hemisphere of the mouse's brain in bursts of rapidly emitted pulses (pulse repetition frequency 0.1 – 3.75 kHz). A total of 125 bursts were emitted at a burst repetition frequency of 0.5 Hz with 13-250 pulses per burst. The in vivo cavitation activity was monitored by capturing the microbubble response recorded on a centrally mounted passive cavitation detector for analysis.

After sonication, the mice were euthanised and perfused with formalin (10%). The mouse brains were removed, cryoprotected in sucrose (15-30%) for 24 hours, sectioned and imaged using fluorescence microscopy.

Results

Drugs were delivered across the blood-brain barrier using a low-pressure 1-cycle, 300-kHz pulse. The acoustic pressure threshold for drug delivery was between 0.1 and 0.2 MPa. Increasing levels of drug delivery were observed from 0.2 to 0.4 MPa. At lower pressures it was found that a greater number of pulses were required per burst to achieve increased BBB permeability. It was observed that the energy of the microbubble acoustic emissions decayed with every pulse within each burst. This suggested that microbubbles replenished the target tissue during the interval between bursts. The average acoustic emission energy from each pulse was observed to decrease at a fast rate for the first 10-15 pulses of each burst and settled to a lower decay rate for the remaining pulses. For a large proportion of bursts microbubble emissions were still persistent after at least 38 pulses for many of the parameter sets tested. Co-injecting dextran and biotin suggests a BBB permeabilisation size dependence, with the smaller biotin

often being more prevalent in the brain post-sonication than the larger dextran, particularly at lower pressures tested (0.2 MPa or less). Further to this it was observed that the biotin distribution was often more uniform than the dextran distribution.

Conclusions

Here we demonstrate increased BBB permeability using bursts of short and rapid pulses of ultrasound at a clinically applicable frequency with the transducer driven with a single input cycle per pulse. This study shows a wide range of parameters which have been explored in an attempt to optimise low-frequency BBB permeabilisation specifically with clinical translation in mind and hope to show that single cycle rapidly pulsed ultrasound may be used to create safe BBB permeability enhancement in humans in the future.

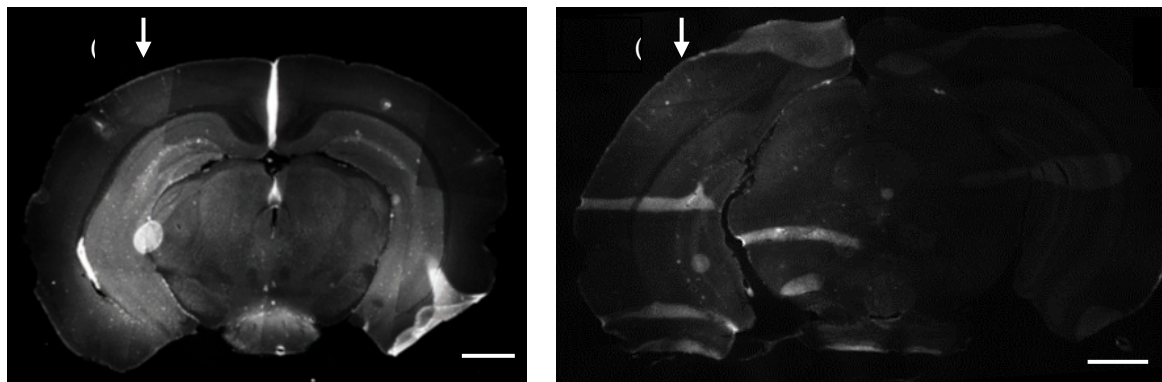


Figure 1. Drug delivery across the blood-brain barrier using 1-cycle 300 kHz pulses at (a) 0.2 MPa and (b) 0.3 MPa. The left hippocampus of the mouse brain was sonicated at a pulse repetition frequency of 1.25 kHz, 38 pulses per burst and a burst repetition frequency of 0.5 Hz for a total of 125 bursts. Each pulse was 1-cycle-long and with a centre frequency of 300 kHz. At the start of sonication 100 μ l of microbubbles were injected into the mice intravenously followed by 100 μ l of the model drug, with injections completed by the 30th burst. Regions of high intensity indicate the presence of a model drug having permeated the blood-brain barrier. Some artefacts can be seen in each image which occurred during cryo-sectioning. Scale bars indicate 1000 μ m.

References

- [1]. N. Joan Abbott, Adjanie A. K. Patabendige, Diana E. M. Dolman et. al., Structure and function of the blood-brain barrier, *Neurobiology of Disease*, 37 (1): 13-25, 2010.
- [2]. Pardridge, WM, The blood-brain barrier: bottleneck in brain drug development 2005, *NeuroRx: Journal of American Society for Experimental NeuroTherapeutics*, 2(1): 3-14.
- [3]. Arnold B. Etame, Roberto J. Diaz, Christian A. Smith, et. al., Focused ultrasound disruption of the blood brain barrier: a new frontier for therapeutic delivery in molecular neuro-oncology, *Neurosurg Focus*, 32 (1): E3, 2014.
- [4]. Morse SV, Pouliopoulos AN, Chan TG et al, Rapid short pulse ultrasound delivers drugs uniformly across the murine blood-brain barrier with negligible disruption 2019, *Radiology*, (in publication).

3D tumor spheroid model for in-vivo therapeutic predictions of Sonochemotherapy

Rahul Misra¹, Raffi Karshafian²

*¹Institute of Bioengineering science & Technology (iBEST),
Keenan Research Centre, St. Michael's Hospital,
Department of Physics, Ryerson University,
Toronto, ON, Canada
Corresponding author: misra.rahul87@gmail.com*

Introduction

Delivering chemotherapeutic agents with the use of microbubble-assisted ultrasound is also referred to as sonochemotherapy. Microbubbles can be locally activated by a targeted ultrasound beam, which can result in several bio-effects. For drug delivery, microbubble-assisted ultrasound is used to increase vascular- and plasma membrane permeability for facilitating drug extravasation and the cellular uptake of drugs in the treated region, respectively. The therapeutic effects can also be produced by bursting the microbubble (localized in tumors) under certain ultrasound intensity. 3D cell cultures possess several in vivo features of tumors such as cell-cell interaction, hypoxia, drug penetration, response and resistance, and production/deposition of extracellular matrix. All of these factors shift growth dependence away from the phenotype of unrestrained proliferation, which is dominant in standard 2D cultures. Furthermore, the study of cancer cell dynamics in a 3D context allows us to recapitulate the architecture of living tissue and to better investigate the pathobiology of tumor. 3D Spheroids could fill the gap between conventional 2D in vitro testing and animal models, and many researchers recommend the use of 3D cell cultures in drug screening programs as support for conventional 2D monolayer studies and before activating animal protocols.

Methods

To develop a robust spheroid model for USMB studies, it is crucial to monitor the growth, size mortality and metabolic activity of the spheroid structure. Using Geltrex as extracellular matrix, tumor spheroids are grown in "Ultra-low Attachment" microplate (Corning) seeding MDA-MB-231 cells in well. Different conditioning regimens of Geltrex (0-6%) and cell density (5000-10,000 cells/well) were tested to optimise the cell aggregation (scattered, loose or compact aggregates) and to develop spheroids of different sizes (200-2000 μm). Metabolic activity of the spheroids was measured by the colorimetric resazurin test involving the reduction of resazurin into resorufin by metabolically active mitochondria of cells. The growth and proliferation of each spheroid in the well was monitored over time through high content imaging using Image express microscopic system. Based on the metabolic activity and viability, optimum size of spheroids for further studies was determined. The qualitative viability analysis of ultrasound and chemo drug treated spheroids was assessed by the Live/Dead® kit (Viability/Cytotoxicity kit, Molecular Probes™) and compared with control. The in-vitro drug uptake and penetration was investigated by high content imaging of thin section of spheroids. The spheroid model was developed such that it resembles the heterogeneity of real tumors with complex hypoxic regions. Using Image-iT Green Hypoxia Reagent (Thermo Scientific), USMB+drug treated spheroids was studied for hypoxic analysis using confocal imaging.

Results

200-2000 μm size of tumor spheroids was developed and monitored for their metabolic activity. These spheroids show well developed hypoxic core, observed with high content imaging system. The drug uptake in USMB treated spheroids was significantly increased (4-5 fold). With the help of fluoresce

microscopy, it was observed that the fluorescent drug molecules of Doxorubicin were diffused through the inner regions of spheroids by USMB treatment and produced DNA damage as observed through COMET assay. The 3D clonogenic cytotoxicity and survival were investigated and it was observed that the post USMB treatment the growth of tumor spheroids was stopped representing the loss of clonogenicity.

Conclusions

3D Spheroid model found to be relevant for predicting the behavior of USMB therapeutic treatments in xenografts. The 3D tumor model gave more clear understanding of clinical complications and implementation of sonochemotherapy. The tumor spheroids shown the potential of Ultrasound and bubbles for delivering the drugs and how effectively and deep these drug molecules can penetrate the tumors. This model is also helpful in optimizing the USMB parameters for treating xenografts and getting maximum therapeutic benefits.

References

- [1]. Denekamp J, Hobson B. Endothelial-cell proliferation in experimental tumours. *Br. J. Cancer.* 1982;46:711–720.
- [2]. Less JL, Skalak EM, Sevic EM, Jain RK. Microvascular architecture in a mammary carcinoma: branching patterns and vessel dimensions. *Cancer Res.* 1991;51:265–273.
- [3]. Intaglietta M, Myers RR, Gross JF, Reinhold HS. Dynamics of microvascular flow in implanted mouse mammary tumours. *Bibl. Anat.* 1977;15(1):273–276.
- [4]. Chaplin DJ, Olive PL, Durand RE. Intermittent blood flow in a murine tumour: Radiobiological effects. *Cancer Res.* 1987;47:597–601.
- [5]. Chaplin DJ, Trotter MJ, Durand RE, Olive PL, Minchinton AI. Evidence for intermittent radiobiological hypoxia in experimental tumour systems. *Biomed. Biochim. Acta.* 1989;48:255–259.

STAT3 Decoy Oligonucleotide-carrying Microbubbles with Pulsed Ultrasound for Enhanced Therapeutic Effect in Head and Neck Tumors

Thiruganesh Ramasamy, Xucai Chen, Bin Qin, Jennifer Grandis, Flordeliza S. Villanueva

Center for Ultrasound Molecular Imaging and Therapeutics, Heart and Vascular Institute, University of Pittsburgh, Pittsburgh, USA

Corresponding author: villanuevafs@upmc.edu

Introduction

The signal transducer and activator of transcription 3 (STAT3) is an oncogenic transcription factor that has been implicated in carcinogenesis, tumor progression and drug resistance in many cancers, including head and neck squamous cell carcinoma (HNSCC) [1,2]. The main objective of this study was to develop and compare 2 microbubble (MB) delivery vehicles: cationic lipid-based microbubbles (MBs) vs. MB-liposome complex to enhance localized delivery of STAT3 decoy. For this purpose, decoy oligonucleotide (ODN) was loaded in microbubbles and combined with ultrasound-targeted microbubble cavitation (UTMC). The present study was undertaken to develop UTMC technology to enhance focal delivery of the STAT3 decoy in human HNSCC tumors.

Methods

Two types of MBs were prepared to load STAT3 Decoy. The synthesis of STAT3 decoy-loaded cationic lipid microbubbles (Mod-159) was reported previously [3]. Cationic liposome containing STAT3 Decoy was prepared by extrusion method first and conjugated to lipid MB via biotin-streptavidin interaction to form liposome-MB complex (LPX). To evaluate *in vitro* anticancer efficacy, human squamous carcinoma cell line CAL-33 cells were plated and incubated for 24 h until nearly confluent. Cells were treated with ultrasound and respective MBs at a concentration equivalent to 10 MB/cell with MBs maximally loaded with decoy. UTMC was performed with a single element immersion transducer (1 MHz, 0.50 MPa PNP, 10 μ s pulse duration, 1 ms pulse interval) for 10 s. Treatment efficacy was evaluated using a viability assay, apoptosis assay, and Hoechst 33342 staining. Anticancer efficacy *in vivo* was performed in a HNSCC-based xenograft model in mice. Therapeutic ultrasound was applied (1 MHz, 0.7 MPa PNP, 100 μ s pulse duration repeated 5 times with 1 ms pulse interval every 2 s) during 15 min of STAT3 Decoy MB infusion for a total of 3 treatments at 3-day intervals. UTMC with MB carrying STAT3 decoy mutant (Mutant Decoy MB) and untreated (NT) groups were used as controls. The tumor was serially imaged using a high-resolution 3-D ultrasound imaging system (Vevo 2100, VisualSonics). Tumor volume was automatically computed from the 3-D reconstructions of the outlines drawn on the cross-sectional images. Survival rate was calculated based on animal sacrifice once the tumor volume reached 1,000 mm³. The antitumor efficacy was evaluated in terms of tumor volume and survival rate. Statistical comparison for survival index was performed by Log-rank (Mantel-Cox) Test using GraphPad Prism (version 7.0) software. In a separate group of animals, tumors were extracted 48 h after UTMC and analysed for gene expression.

Results

UTMC with both species of STAT3 decoy-loaded MB showed significantly more cytotoxicity compared to that of mutant control ($p < 0.05$). UTMC *in vitro* with Mod159 carrying STAT3 decoy showed significantly lower cell viability ($p < 0.05$) of $56.8 \pm 8.4\%$ compared to $84.5 \pm 8.8\%$ for LPX in CAL-33 cell line, indicating superior therapeutic efficacy compared to the LPX formation. Therefore, Mod159 was used for all subsequent *in vitro* and *in vivo* experiments. Flow cytometric analysis of Annexin V/propidium iodide-stained cells demonstrated that compared to the mutant control-loaded MBs, STAT3

decoy-loaded MBs + UTMC caused significant ($p < 0.05$) apoptosis of CAL33 cells, indicating that cell death was mainly attributed to the induction of apoptosis at the *in vitro* level. *In vivo* studies illustrated that UTMC with STAT3 Decoy MB had strong antitumor effect, with significant reduction in the tumor burden in xenograft mice compared to that of UTMC with decoy mutant-loaded MB and untreated animal groups ($p < 0.05$, **Figure 1A**). Kaplan-Meier survival curves were concordant with the aforementioned results, with STAT3 decoy-treated group having 100% of mice still surviving at day 15 compared to a survival rate of 33% and 14% for mutant and NT group, respectively ($p < 0.05$, **Figure 1B**). Relative to the mutant control group, tumors in the STAT3 decoy-treated mice exhibited ~45% and ~38% ($p < 0.05$) decrease in downstream target gene expression of Bcl-xL and cyclin D1, respectively, by protein analysis. Consistent with the immunoblot analysis, there was approximately 30% reduction in Bcl-xL and cyclin D1 mRNA transcripts in STAT3 decoy treated mice (PCR analysis).

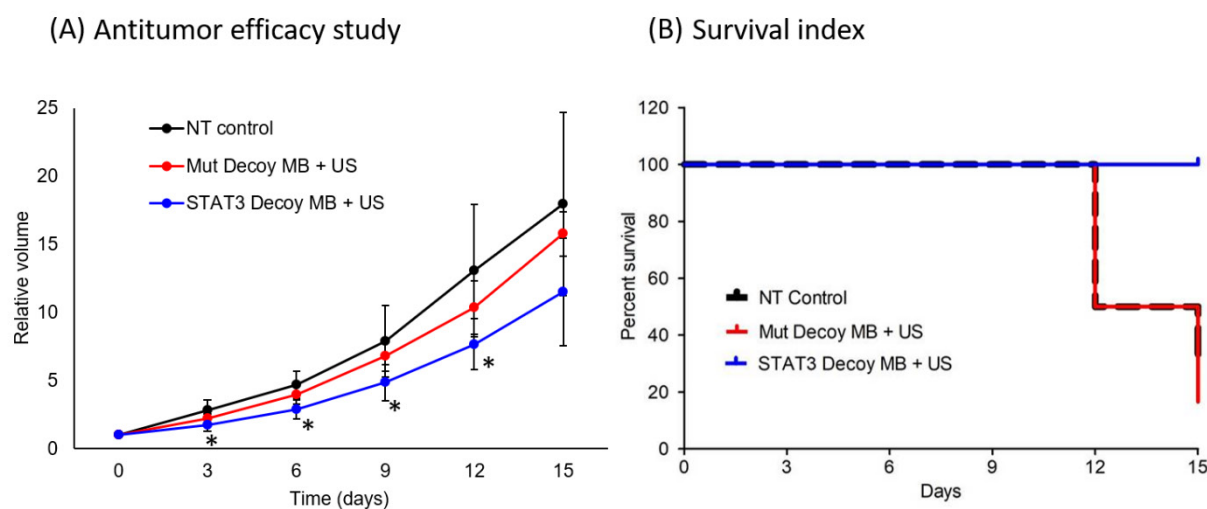


Figure 1: (A) Antitumor efficacy of UTMC with STAT3 decoy MB *in vivo* in a subcutaneous xenograft model of human head and neck cancers in mice with CAL-33 cells; (B) Kaplan–Meier survival analysis. Asterisks (*) indicate $p < 0.05$ for STAT3 Decoy MB + US vs Mut Decoy MB + US.

Conclusions

This study demonstrated the potential of oligonucleotide-loaded microbubbles and US in the treatment of human head and neck cancers. UTMC with STAT3 decoy-loaded MBs significantly reduced human tumor burden in xenograft mice, resulting in a higher survival rate compared to that of mutant decoy-treated and non-treated tumor-bearing animals.

References

- [1]. Chai EZP, et al, Targeting transcription factor STAT3 for cancer prevention and therapy, *Pharmacology & Therapeutics* 2016;162: 86–97.
- [2]. Grandis JR, et al, Constitutive activation of STAT3 signaling abrogates apoptosis in squamous cell carcinogenesis *in vivo*, *Proc Natl Acad Sci USA* 2000;97: 4227-32.
- [3]. Kopechek JA, et al, Ultrasound targeted microbubble destruction-mediated delivery of a transcription factor decoy inhibits STAT3 signaling and tumor growth, *Theranostics* 2015;5: 1378-1387.

Targeted microbubbles as a novel therapy for *Staphylococcus aureus* biofilms on cardiac devices

Joop J.P. Kouijzer¹, Kirby R. Lattwein¹, Inés Beekers¹, Nico de Jong^{1,2}, Antonius F.W. van der Steen^{1,2}, Alexander L. Klibanov³, Willem J.B. van Wamel⁴, Klazina Kooiman¹

¹ Department of Biomedical Engineering, Thoraxcenter, Erasmus MC, Rotterdam, the Netherlands

² Acoustical Wavefield Imaging, Delft University of Technology, Delft, the Netherlands

³ Cardiovascular Division, Department of Medicine, University of Virginia, Charlottesville, Virginia, United States of America

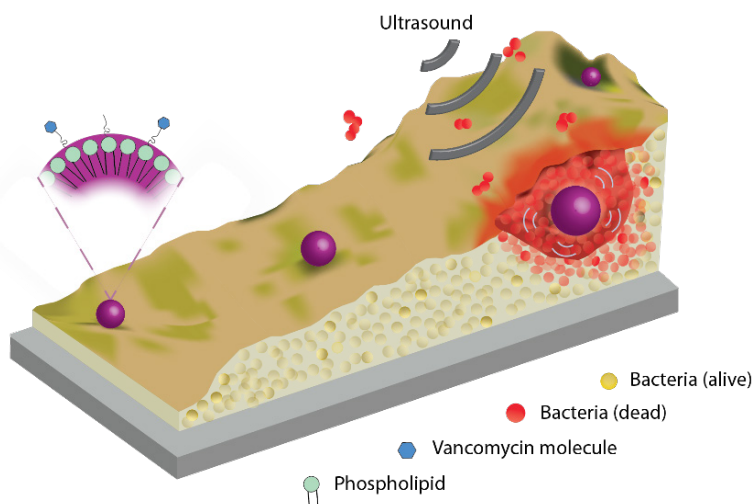
⁴ Department of Medical Microbiology and Infectious Diseases, Erasmus MC, Rotterdam, the Netherlands
Corresponding author: j.kouijzer@erasmusmc.nl

Introduction

Infective endocarditis (IE) is a life-threatening infection of the cardiac valves, endocardial surface, or artificial implants such as cardiac devices. Cardiac device infections have mortality rates of ~29% for pacemakers, implantable cardioverter defibrillators (ICDs), and cardiac resynchronization therapy devices (CRTs)¹, ~30% for prosthetic valves², and ~50% for left ventricular assist devices (LVADs)³. Removal of the devices is either not possible or a major undertaking with a risk of death or significant complications¹. The infections are biofilm infections⁴, i.e. device-bound, matrix-enclosed microbial communities. Treating these infections is a major challenge because bacteria embedded in a biofilm are up to 1,000 times more resistant to antibiotics than non-embedded bacteria⁵. A targeted, non-invasive treatment is desperately needed, but currently unavailable because of the complex disease.

We have recently shown that sonobactericide, the combination of ultrasound (US), microbubbles, and therapeutics, shows great potential to treat IE *in vitro*⁶. However, *in vivo* targeted microbubbles will be crucial as rapid blood flow will hamper contact of non-targeted microbubbles with the IE-biofilm. This study aimed to produce novel targeted microbubbles and treat *Staphylococcus aureus* (*S. aureus*) biofilms with ultrasound-activated targeted microbubbles, see Figure 1. We focused on *S. aureus* because cardiac device biofilm infections are mainly caused by Gram-positive *Staphylococci* (~60%)^{4,7,8}. Moreover, *S. aureus* is associated with longer hospital stays, elevated costs, and the highest mortality rate^{9,10}.

Figure 1. 3D Illustration of the hypothesized effect on a biofilm caused by ultrasound-activated bound targeted microbubbles. After insonification of the targeted microbubbles with ultrasound, bacteria killing and detachment can be achieved.



Methods

The antibiotic vancomycin was used as the targeting component and was chemically coupled via its amine group to DSPE-PEG(3400)-NHS. DSPC was used as the main phospholipid component of the microbubble shell with perfluorobutane (C₄F₁₀) as the gas core. DiD was used to fluorescently label the microbubbles. Non-targeted microbubbles were made without vancomycin. For the in-house manufacturing of the microbubbles a probe sonicator was used¹¹.

IbiTreat μ -Slides (ibidi GmbH, Germany) were used as cardiac device mimics to grow biofilms with an *S. aureus* clinical isolate of IE. Each channel was filled with a diluted bacterial suspension in IMDM (1·10⁴ CFU/mL). Slides were incubated at 37 °C under agitation (150 rpm) for 24 hours.

Ibidi channels containing the biofilms were incubated with vancomycin-targeted or non-targeted microbubbles ($5 \cdot 10^6$ MBs/ml) and allowed to adhere prior to confocal microscopy. The ibiTreat μ -Slide was mounted in the set-up such that the bound microbubbles were on top of the biofilm. Unbound microbubbles floated to the topside of the channel due to the upward buoyancy force of the microbubble. Live and dead bacteria were stained using respectively Syto9 and propidium iodide (PI). To assess specificity of the vancomycin-targeted microbubbles, a competition assay was performed with vancomycin concentrations ranging from 0 to 1 mg/ml added prior to the addition of the targeted-microbubbles. For treatment, a low (250 kPa) and high (1 MPa) peak negative acoustic pressure ultrasound pulse ranging from 100 to 10,000 cycles at a frequency of 2 MHz were investigated. The ultrasound frequency of 2 MHz was chosen as this is a clinically representable echocardiography frequency¹². Microbubble behaviour during insonification was recorded with the Brandaris 128 ultra-high speed camera coupled to a custom build Nikon A1R confocal microscope.

Results

The vancomycin-targeted microbubbles bound to the *S. aureus* biofilm whereas non-targeted microbubbles did not, as shown in Figure 2A and B. Figure 2c and 2d show representative images of the upper area of the ibiTreat μ -Slide, i.e. the location where non-bound microbubbles would float up to. Interestingly, the vancomycin-targeted microbubbles present at the upper area were covered with bacteria (Figure 2c) whereas non-targeted microbubbles were not (Figure 2d). Moreover, the vancomycin competition assay showed that increasing concentrations of vancomycin added prior to the addition of the targeted microbubbles significantly reduced the amount of bound targeted microbubbles to the biofilm.

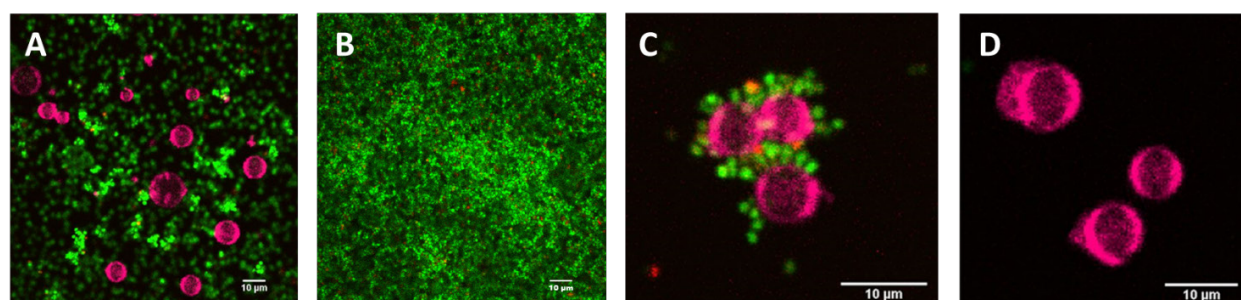


Figure 2. Microbubble binding to *S. aureus*. (A) Vancomycin-targeted microbubbles bound to the biofilm. (B) Non-targeted microbubbles did not bind to the biofilm. (C) In the upper area of the IbiTreat μ -Slides vancomycin-targeted microbubbles were decorated with bound bacteria. (D) In the upper area of the IbiTreat μ -Slides non-targeted microbubbles were not decorated with bacteria. For the confocal microscopy, living bacteria were stained with Syto9 (green), dead bacteria with PI (red), and microbubbles with DiD (pink).

Insonification of the bound targeted microbubbles with the two diverse ultrasound settings resulted in a different microbubble-biofilm interaction. The high acoustic pressure (1 MPa) burst of 100 cycles of ultrasound resulted in microbubble collapse with minimal visual impact on the biofilm. By contrast, the long bursts of 10,000 cycles of ultrasound at a low acoustic pressure (250 kPa) resulted in substantial biofilm- destructive behaviour (Figure 3). During insonification, the targeted microbubbles formed clusters by migrating towards each other, a phenomenon known as Bjerknes forces^{13,14}. This resulted in deformation and removal of the biofilm (Figure 3B). Also, a greater amount of movement of bacteria was noticed in the path where the microbubble had been.

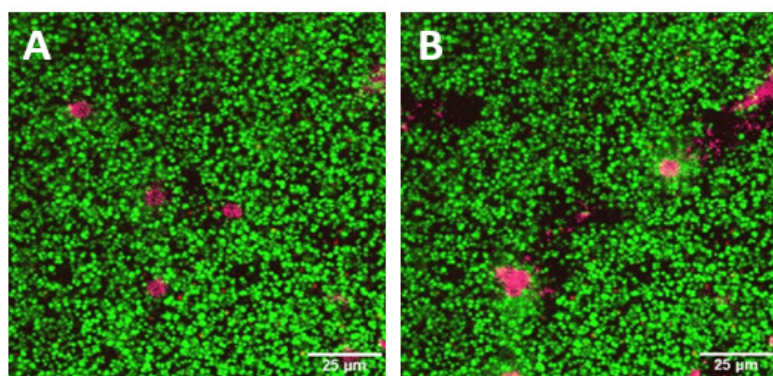


Figure 3. Biofilm reducing effect of vancomycin-targeted microbubbles in combination with ultrasound. (A) Before and (B) after insonification. The targeted bound microbubbles formed clusters and the biofilm partly detached. For the confocal microscopy, living bacteria were stained with Syto9 (green), dead bacteria with PI (red), and microbubbles with DiD (pink).

Conclusions

Vancomycin-targeted microbubbles were developed that specifically bound to *in vitro* *Staphylococcus aureus* biofilms. In addition, ultrasound insonification of these bound targeted microbubbles had a mechanical effect on the biofilm. Deformations and detachment of the biofilm were observed when 2 MHz ultrasound was applied at a low acoustic pressure (250 kPa) for 10,000 cycles. This successful detachment of bacteria from biofilms by targeted microbubbles may assist in the treatment of infective endocarditis in a more efficient and less invasive manner. Therapeutics may need to be given alongside to prevent the detached bacteria from readhering.

Acknowledgements

The authors thank Michiel Manten, Geert Springeling, Robert Beurskens, and Phoei Ying Tang from the Department of Biomedical Engineering, Thoraxcenter, Erasmus MC, the Netherlands for technical assistance. Financial support from the Erasmus MC Foundation (fellowship to K.K.) is gratefully acknowledged. This project has received funding from the European Research Council (ERC) under the European Union's Horizon 2020 research and innovation programme (grant agreement No 805308).

References

- [1]. Sandoe JA, Barlow G, Chambers JB, Gammage M, Guleri A, Howard P, Olson E, Perry JD, Prendergast BD, Spry MJ, Steeds RP, Tayebjee MH, Watkin R, British Society for Antimicrobial C, British Heart Rhythm S, British Cardiovascular S, British Heart Valve S and British Society for E. Guidelines for the diagnosis, prevention and management of implantable cardiac electronic device infection. Report of a joint Working Party project on behalf of the British Society for Antimicrobial Chemotherapy (BSAC, host organization), British Heart Rhythm Society (BHRS), British Cardiovascular Society (BCS), British Heart Valve Society (BHVS) and British Society for Echocardiography (BSE). *The Journal of antimicrobial chemotherapy*. 2015;70:325-59.
- [2]. Lalani T, Chu VH, Park LP, Cecchi E, Corey GR, Durante-Mangoni E, Fowler VG, Jr., Gordon D, Grossi P, Hannan M, Hoen B, Munoz P, Rizk H, Kanj SS, Selton-Suty C, Sexton DJ, Spelman D, Ravasio V, Tripodi MF, Wang A and International Collaboration on Endocarditis-Prospective Cohort Study I. In-hospital and 1-year mortality in patients undergoing early surgery for prosthetic valve endocarditis. *JAMA internal medicine*. 2013;173:1495-504.
- [3]. Thyagarajan B, Kumar MP, Sikachi RR and Agrawal A. Endocarditis in left ventricular assist device. *Intractable Rare Dis Res*. 2016;5:177-84.
- [4]. Werdan K, Dietz S, Loffler B, Niemann S, Bushnaq H, Silber RE, Peters G and Muller-Werdan U. Mechanisms of infective endocarditis: pathogen-host interaction and risk states. *Nat Rev Cardiol*. 2014;11:35-50.
- [5]. Lewis K. Persister cells and the riddle of biofilm survival. *Biochemistry (Mosc)*. 2005;70:267-74.
- [6]. Lattwein KR, Shekhar H, van Wamel WJB, Gonzalez T, Herr AB, Holland CK and Kooiman K. An in vitro proof-of-principle study of sonobactericide. *Scientific reports*. 2018;8:3411.
- [7]. Hussein AA, Baghdy Y, Oussama M, Wazni OM, Brunner MP, Kabbach G, Shao M, Gordon S, Saliba WI, Wilkoff BL and Tarakji KG. Microbiology of Cardiac Implantable Electronic Device Infections. *JACC Clinical Electrophysiology*. 2016;2:498-505.
- [8]. Koval CE, Rakita R and Practice ASTIDCo. Ventricular assist device related infections and solid organ transplantation. *American journal of transplantation : official journal of the American Society of Transplantation and the American Society of Transplant Surgeons*. 2013;13 Suppl 4:348-54.
- [9]. Slipczuk L, Codolosa JN, Davila CD, Romero-Corral A, Yun J, Pressman GS and Figueredo VM. Infective endocarditis epidemiology over five decades: a systematic review. *PloS one*. 2013;8:e82665.
- [10]. Mokhles MM, Ciampichetti I, van Domburg R, Cheng JM, Bogers AJ and Witsenburg M. Infective endocarditis in a tertiary referral hospital: long-term follow up. *The Journal of heart valve disease*. 2012;21:118-24.
- [11]. Klibanov AL, Rasche PT, Hughes MS, Wojdyla JK, Galen KP, Wible JH, Jr. and Brandenburger GH. Detection of individual microbubbles of ultrasound contrast agents: imaging of free-floating and targeted bubbles. *Invest Radiol*. 2004;39:187-95.
- [12]. remkau FW. General principles of echocardiography. In: R. Lang, Goldstein, S. A., Kronzon, I., Khandheria, B. K., Mor-Avi, V., ed. *ASE's Comprehensive Echocardiography*: Elsevier; 2015.
- [13]. Lazarus, C., Pouliopoulos, A.N., Tinguely, M., Garbin, V. & Choi, J.J. Clustering dynamics of microbubbles exposed to low-pressure 1-MHz ultrasound. *J Acoust Soc Am* 142, 3135 (2017).
- [14]. Schmidt, B.J., Sousa, I., van Beek, A.A. & Bohmer, M.R. Adhesion and ultrasound-induced delivery from monodisperse microbubbles in a parallel plate flow cell. *J Control Release* 131, 19-26 (2008).

Therapeutic applications of ultrasound for retinal drug delivery using *in vitro* and *ex vivo* models

Charis Rousou¹, Roel Deckers², Gert Storm¹, Chrit Moonen², Enrico Mastrobattista¹

¹Department of Pharmaceutical Sciences, Utrecht Institute for Pharmaceutical Sciences, Utrecht University, Utrecht, The Netherlands

²Imaging Division, University Medical Center Utrecht, Utrecht, The Netherlands
Corresponding author: e.mastrobattista@uu.nl

Introduction

The unique anatomy and presence of biological barriers between the different ocular tissues make drug delivery to the posterior segment of the eye one of greatest challenges in ophthalmology [1-2]. Currently, the most widely applied method for treatment of posterior eye-segment diseases is injection of therapeutic compounds in the vitreous. This administration route is often related to severe adverse effects (e.g. retinal detachment, ocular inflammations, increase of the intraocular pressure). Therefore, there is a need for development of novel minimally invasive techniques that allow for efficient administration of drugs while preserving patient comfort.

The aim of this study is to compare the ultrasound and microbubbles (USMB) induced intracellular uptake of a model drug by retinal pigment epithelial cells (ARPE-19) and a commonly used cell line in our lab (FaDu). Additionally, the temporal window of the uptake by ARPE-19 cells is investigated *in vitro*. Furthermore, an *ex vivo* model has been developed in order to study the effects of USMB on extracorporeal arterially perfused porcine eyes. This latter method allows for preservation of integrity and complexity of the ocular tissues, which is essential for retinal drug delivery applications.

Methods

In vitro model

To study the intracellular uptake after USMB exposure, a cell membrane impermeable fluorescent dye (Sytox Green) was used as model drug. Human-derived retinal pigment epithelial cells (ARPE-19) or human pharyngeal squamous carcinoma cells (FaDu) were seeded in cell culture cassettes (CliniCell, Mabio, France) one day prior the US experiment. Immediately before US exposure, microbubbles (2×10^7 microbubbles/ml) were mixed with Sytox Green (2 μ M) and culture medium, and were injected in the CliniCell. Subsequently, US was applied using an unfocused single-element transducer (frequency = 1.5 MHz, PRF = 1 kHz, duty cycle = 10%, sonication time = 60 s, and $P_{neg} = 0.5$ MPa).

For the temporal window experiments ARPE-19 cells were used and the ultrasound parameters were kept the same. However, additional samples were used where Sytox Green was added 15, 60, or 120 minutes post-sonication. At each time point cells were incubated with Sytox Green for 20 minutes in a 37 °C incubator. Subsequently cells were fixated with PFA and cell nuclei were stained with DAPI.

For all samples fluorescence microscopy images were acquired (Keyence, BZ-9000) and Sytox Green positive cells showing a fluorescent signal above a fixed threshold were counted automatically (ImageJ). The percentage of Sytox Green positive cells was calculated by comparing the Sytox Green positive cells with the total number of cells as counted from the DAPI images.

Ex vivo model

Fresh porcine eyes are enucleated at a local abattoir directly after animal termination, and transported to the laboratory. Using an operational microscope the ophthalmic artery is localized and isolated. An incision is created and a cannula is inserted in the ophthalmic artery. Subsequently, the cannula is

connected to a syringe pump which perfuses the eye at a flow of 0.1 ml/hr. Successful cannulation can be tested by perfusion of the eye with a dye (e.g. fluorescein).

Results

The results from the uptake of Sytox Green by ARPE-19 cells, indicated the highest uptake when the dye was present during sonication (Figure 1, A), with the number of positive cells reaching 98% (Figure 1, B). The number of Sytox Green positive cells decreased by increasing time between sonication and addition of the model drug. However, even 120 minutes after sonication there was uptake of the dye by 30% of the cells, indicating that the sonoporation effect can still be potent a few hours after exposure to ultrasound. In contrast, using the same US parameters, only 19% of FaDu cells showed uptake when the dye was present during sonication. The duration of USMB-enhanced cell membrane permeability was previously investigated by Lammerking et al. for other cell lines [3].

In Figure 2, an example of retinal perfusion with fluorescein in an extracorporeal, cannulated porcine eye is shown. The images represent different perfusion time points depicting firstly the native blood that was remained inside the retinal blood vessels (Figure 2, A). Subsequently, fluorescein arrived in the retinal arteries (Figure 2, B) and a few seconds later in the retinal veins (Figure 2, C).

Conclusions

In this study, it was shown that USMB can be used for the internalization of low molecular weight model drugs in retinal pigment epithelial and pharyngeal squamous carcinoma cells. Almost all ARPE-19 cells show Sytox Green uptake in comparison to only 19% of the FaDu cells. Investigation of the duration of the cell membrane permeability indicated that the number of Sytox Green positive cells decreased by increasing time between sonication and addition of the model drug.

We hereby present an *ex vivo* porcine ocular model which can be used as an experimental platform to test novel drug delivery systems or surgical techniques. This model allows for preservation of the complex physiology of the ocular tissues, while controlled perfusion and viability can be reached. In the future, this system will be used to study the effect of USMB on the retinal tissue. Fluorescent dyes of various molecular weights will be used and the uptake by the retinal cells will be studied using fluorescence microscopy of the retina. Additionally, histopathological evaluation will be performed in order to study the safety of the method.

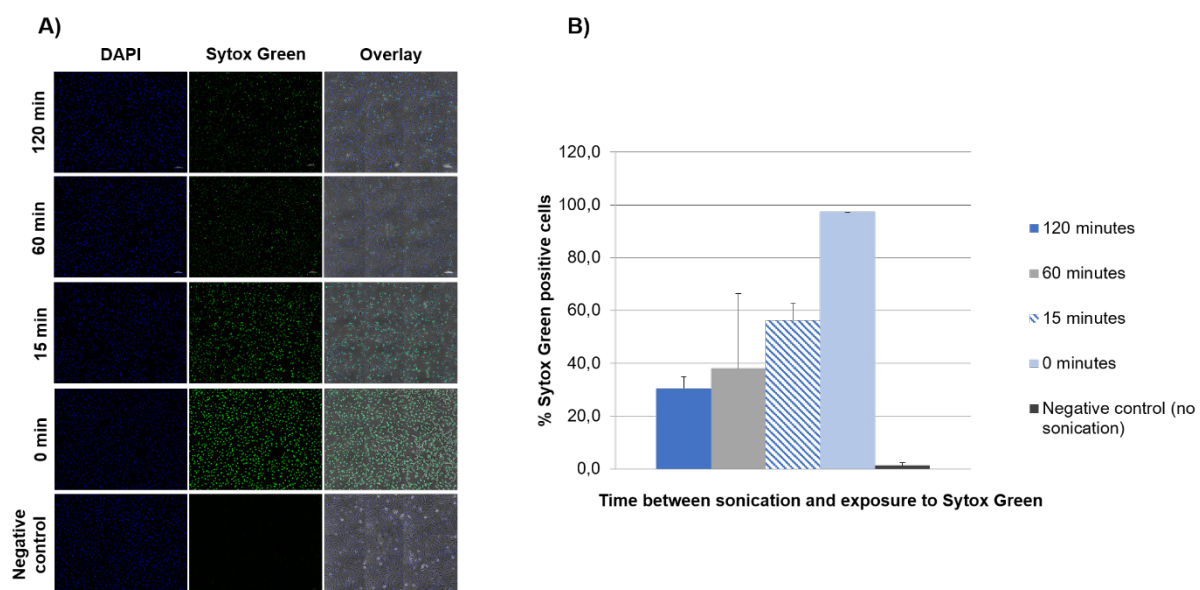


Figure 1: (A) Fluorescent microscopy images of ARPE-19 cells after exposure to USMB. Sytox Green was added 15 min, 30 min, 60 min and 120 min after sonication of cells. In one sample Sytox Green was

added just prior to sonication (0 min). The highest uptake of the fluorescent dye was observed when the dye was present during sonication. Left: DAPI, middle: Sytox Green, right: overlay of phase contrast, DAPI and Sytox green images. (B) Percentage of the number of Sytox Green positive cells corresponding to the different points of addition of Sytox Green.

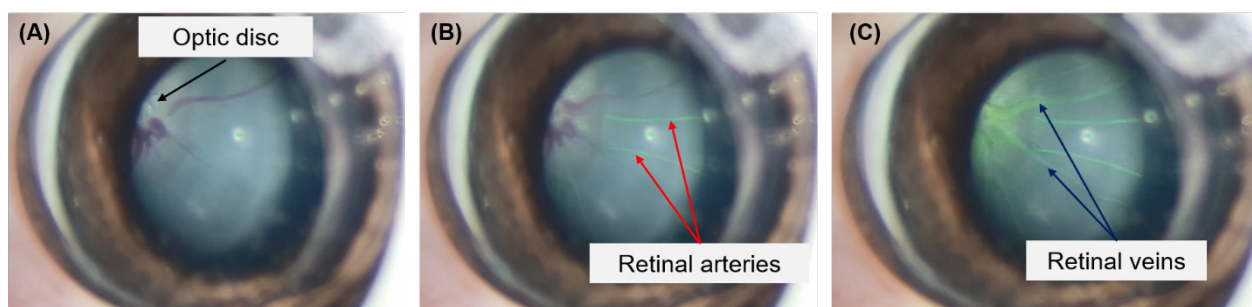


Figure 2: Operational microscopy images of the retinal vessels of an *ex vivo* arterially perfused porcine eye during the perfusion with fluorescein. Before the perfusion starts the native blood is still observed (A). When fluorescein is injected the retinal arteries are firstly filled with the dye (B). A few seconds later, the retinal veins are also perfused (C).

Funding

This work was supported by the European Union's Horizon 2020 research and innovation program under the Marie Skłodowska-Curie [grant agreement No. 722717].

References

- [1]. Del Amo EM et al., Pharmacokinetic aspects of retinal drug delivery, *Prog. Retin. Eye Res.*, 57:134–185, 2017.
- [2]. Díaz-Coránguez M, Ramos C, Antonetti DA, The inner blood-retinal barrier: Cellular basis and development, *Vision Res.*, 139: 123–137, 2017
- [3]. Lammertink B, Deckers R, Storm G, Moonen C, Bos C, Duration of ultrasound-mediated enhanced plasma membrane permeability, *Int. J. Pharm.*, 482:92–98, 2015

Contrast enhanced ultrasound treatment enhances tumor perfusion in breast cancer patients – first results

A. Rix¹, B. Flege², T. Opacic¹, N. Simons², P. Koczera¹, K. Kraus², E. Stickeler², F. Kiessling¹

¹Institute for Experimental molecular Imaging, RWTH Aachen, Aachen, Germany

²Clinic for Gynecology and Obstetrics, University Hospital RWTH Aachen, Aachen, Germany

Corresponding author: fkiessling@ukaachen.de

Introduction

Pathological remission under neoadjuvant chemotherapy is a reliable surrogate marker for clinical outcome, with improved overall and breast cancer specific survival in patients reaching a complete pathological response. One possibility to improve response rates could be an enhanced accumulation of therapeutic substances in the tumor tissue. This could be achieved by mechanical manipulation of the tumor vasculature using shear forces resulting from the local destruction of ultrasound contrast agents [1]. The present study shows initial results of the impact of destructive contrast enhanced ultrasound (dCEUS)-treatment on tumor vascularity during neoadjuvant chemotherapy (CTx) in breast cancer patients.

Methods

The study was approved by the RWTH Aachen University ethics committee, registered on clinicaltrials.gov (NCT03385200) and written informed consent was obtained from all participants. N = 8 patients with primary breast cancer who received neoadjuvant CTx were allocated in a blinded manner to either a control or therapy group. In all patients tumor size was measured (Toshiba Aplio 500 equipped with 10MHz PLT 1005BT transducer, mechanical index (MI) 0.07, thermal index (TI) below 0.4) prior to each chemotherapy cycle. Tumor perfusion was assessed by slow administration of 0.5 ml Sonovue (Bracco, Italy) before and after infusion of CTx. Patients of the therapy group additionally received 18 minutes of CEUS-treatment during CTx infusion, consisting of 6 consecutive injections of 0.5 ml Sonovue with continuous destruction of the contrast agent in the tumor area (Philips iU22 equipped with 15 MHz L17-5 transducer, MI 0.7, TI 0.2). Before and after each injection multiple pictures of the tumor were recorded to assess the percentage of perfused tumor area. Data were post-processed and analyzed using IamalyticsPreclinical (Gremse IT). All results are presented as mean +/- standard deviation.

Results

Peak enhancement (PE) in tumors of the control group decreased after CTx (pre CTx 5.19 +/- 8.08 signal intensity (SI) [a.u.], post CTx 1.4 +/- 1.5 SI [a.u.]), whereas PE in tumors of the CEUS-treatment group predominantly increased from 1.78 +/- 3.05 SI [a.u.] to 4.76 +/- 3.15 SI [a.u.]. Furthermore, maximum intensity over time (MIOT) curves showed an increase in maxMIOT in tumors after CEUS-treatment (pre CTx 20.57 +/- 26.68 SI [a.u.]; post CTx 43.55 +/- 31.21 SI [a.u.]), whereas a decrease could be observed in tumors of the control group (pre CTx: 33 +/- 35 SI [a.u.]; post CTx: 24 +/- 20 SI [a.u.]).

Conclusions

Promising initial results of CEUS-treatment in breast cancer patients show an increase in tumor perfusion indicated by an increase in PE, as well as an increase in the relative blood volume estimated from MIOT curves. An increase in tumor perfusion and relative blood volume could contribute to an enhanced accumulation of chemotherapy in the tumor tissue and therefore lead to a better therapeutic efficacy. Nevertheless, more patients have to be included in the study to verify this hypothesis

Reference

[1]. Dimcevski G, Kotopoulis S, Bjane T et al. Ultrasound and microbubble enhanced treatment of inoperable pancreatic adenocarcinoma 2016, J Clin Oncol 34

Ultrasonic Induction of Apoptosis of Pancreatic Cancer through Activation of the Mechanosensitive Channel Piezo1

Yue Song¹, Qunying Li¹, Tongcun Huang¹, Hang Zhou¹, Fuqiang Qiu¹, Pintong Huang¹

¹Department of Ultrasound, The Second Affiliated Hospital of Zhejiang University School of Medicine, Hangzhou 310009, China

Introduction

Due to locally advanced disease and the prevalence of extreme desmoplasia of pancreatic cancer, patients always lose the opportunity of surgery and are insensitive to radiotherapy or chemotherapy, so a novel therapeutic intervention conducted by Norway researchers via ultrasound combined with microbubbles has caused wide attention.^[1] But the underlining mechanism still remains undiscovered. In our study, we found that low frequency ultrasound combined with microbubbles can cause apoptosis of pancreatic cancer. Piezo1^[2], a mechanosensitive channel, has played an irreplaceable role in this course.

Methods

Annexin V-PI staining was used to assess apoptosis of pancreatic cancer under different ultrasonic parameters combined with microbubbles and the optimal combination was chosen. To explore the electrophysiological character of Piezo1, patch-clamp recording and calcium imaging was obtained in virtue of three different typical cell lines. Then we tried to illuminate the function of mitochondria via the following two methods, first, JC-1 staining was used to test the membrane potential; second, the ATP concentration was detected. Finally, we used western blot to prove the expression of apoptosis related proteins.

Results

Low frequency ultrasound combined with microbubbles can lead to apoptosis of pancreatic cancer. Piezo1 played an important role in this course. We found that the inhibitor of Piezo1 can alleviate the extent of apoptosis. Calcium increased in the soma when ultrasound was used. Cells suffered from mitochondrial dysfunction including decreased membrane potential and ATP content and the expression of apoptosis related proteins was increased in the ultrasound intervened group.

Conclusions

Low frequency ultrasound combined with microbubbles can lead to apoptosis of pancreatic cancer. This can be explained by the Piezo1 induced calcium influx and the consequent dysfunction of mitochondria in this process.

References

- [1]. DIMCEVSKI G, KOTOPOULIS S, BJANES T, et al. A human clinical trial using ultrasound and microbubbles to enhance gemcitabine treatment of inoperable pancreatic cancer [J]. *Journal of controlled release : official journal of the Controlled Release Society*, 2016, 243(172-81).
- [2]. ROMAC J M, SHAHID R A, SWAIN S M, et al. Piezo1 is a mechanically activated ion channel and mediates pressure induced pancreatitis [J]. *Nature communications*, 2018, 9(1): 1715.

Sonoporation efficacy and intracellular mechanisms: Cancer cells vs. healthy cells.

Ragnhild Haugse^{1,2}, ***Anika Langer***², ***Stein-Erik Gullaksen***², ***Silje Maria Sundøy***², ***Bjørn Tore Gjertsen***², ***Spiros Kotopoulos***^{3,4}, ***Emmet McCormack***^{2,5}.

¹*Hospital Pharmacy in Western Norway, Bergen, Norway*

²*Department of Clinical Medicine, University of Bergen, Bergen, Norway,*

³*Department of Clinical Science, University of Bergen, Bergen, Norway,*

⁴*National Centre for Ultrasound in Gastroenterology, Haukeland University Hospital, Bergen, Norway*

⁵*Department of Internal Medicine, Haematology Section, Haukeland University Hospital, Bergen, Norway*

Corresponding author: emmet.mc.cormack@uib.no

Introduction

The use of ultrasound and microbubbles to enhance therapeutic efficacy is commonly known as sonoporation. In combination with chemotherapy sonoporation has been found to enhance the efficacy of cancer therapy both in preclinical trials [1, 2] and in a Phase I clinical trial [3]. The primary mechanism of sonoporation has typically been defined as the formation of transient pores in cell membranes caused by the ultrasound itself, or by the microbubbles excited by ultrasound. The main hypothesis for the improved treatment efficacy is that the formation of pores enhances drug uptake into the cells. The exact mechanisms leading to improvement in therapy is however not clearly understood, and there is limited knowledge on the intracellular mechanisms following sonoporation. Thus, the primary aim of this study was to interrogate a multitude of intracellular pathways following sonoporation. Furthermore, it is not yet fully known how various ultrasound parameters and microbubble formulations influence drug uptake and cellular response; parameters which must be optimised to maximise sonoporation efficacy. We aim to elucidate the intracellular mechanisms of sonoporation in two cell types, at three ultrasound conditions, using two commercially available ultrasound contrast agents.

Methods

The leukemic cell-line MOLM-13 and healthy peripheral blood mononuclear cells (PBMC) were treated at three different levels of ultrasound intensities ($I_{SPTA} = 74, 501 \text{ \& } 2079 \text{ mW/cm}^2$) with and without microbubbles (SonoVue[®] and Sonazoid[™]) using a custom-made plate sonicator [4]. Calcein, a cell impermeable fluorescent dye, was used as a model drug. The percentage of calcein positive cells and fluorescence intensity (analysed by flow cytometry) was used as marker for sonoporation efficacy. Cell viability was assessed immediately following treatment and 24 hours later (Trypan Blue, Hoechst 33343, and colony forming assay).

Flow cytometry was used to elucidate the phosphorylation status of 18 intracellular proteins immediately, 30 minutes, and 2 hours after treatment. Western Blot analysis was performed to validate responses.

Results

In agreement with existing literature our results show that sonoporation significantly enhances uptake of the model drug. Thereby, ultrasound intensity correlated to the percentage of calcein positive cells and the calcein concentration within the cells. The addition of microbubbles further increased both the number of cells with calcein uptake and the intracellular concentration. At clinically diagnostic ultrasound intensities (*i.e.*, below 720 mW/cm^2) Sonazoid[™] was more efficient than SonoVue[®] as it resulted in a higher percentage of calcein positive cells ($p < 0.0001$). When surpassing the clinical diagnostic threshold, Sonazoid[™] resulted in cells taking up more calcein than SonoVue[®] ($p < 0.001$).

Interestingly healthy blood cells (PBMCs) demonstrated approximately 4-fold less uptake of calcein in comparison to MOLM-13 cells at similar conditions.

Accordingly, significant changes in intracellular signalling pathways were only found in MOLM-13 cells. Specifically an increase in phosphorylation of ERK and p38 (MAP-Kinases), transcription factor

CREB, ER-stress protein eIF2 α , Akt (PI3K-pathway) and STAT3 (JAK/STAT-pathway) could be shown. Other proteins such as FAK or Src showed no change in phosphorylation.

Conclusions

Our results show that sonoporation efficacy is determined by many factors such as ultrasound conditions, microbubble formulation, and type of cell treated. In addition, sonoporation can significantly alter intracellular signalling and cell viability but this depends on the type of cell. As the sonoporation effect was significantly larger in all aspects on the cancerous MOLM-13 cells versus the healthy PBMC cell this can be an advantage for cancer therapy using sonoporation.

References

- [1]. Kotopoulos, S., et al., Sonoporation-Enhanced Chemotherapy Significantly Reduces Primary Tumour Burden in an Orthotopic Pancreatic Cancer Xenograft. *Molecular Imaging and Biology*, 2014. 16(1): p. 53-62.
- [2]. Kotopoulos, S., et al., Sonoporation with Acoustic Cluster Therapy (ACT(R)) induces transient tumour volume reduction in a subcutaneous xenograft model of pancreatic ductal adenocarcinoma. *J Control Release*, 2017. 245: p. 70-80.
- [3]. Dimceviski, G., et al., A human clinical trial using ultrasound and microbubbles to enhance gemcitabine treatment of inoperable pancreatic cancer. *J Control Release*, 2016. 243: p. 172-181.
- [4]. Yddal, T., et al., Open-source, high-throughput ultrasound treatment chamber. *Biomed Tech (Berl)*, 2015. 60(1): p. 77-87.

Ultrasound Responsive Bioactive Microbubbles for the Eradication of Biofilms

Gareth LuTheryn^{1,4}, Charlotte Hind⁵, Peter Glynn-Jones¹, Jeremy S Webb^{2,3,4},
J. Mark Sutton⁵, Dario Carugo^{1,3}

¹ Faculty of Engineering and Physical Sciences, University of Southampton, Southampton, UK. ² Centre for Biological Sciences, University of Southampton, Southampton, UK. ³ Institute for Life Sciences, University of Southampton, Southampton, UK. ⁴ National Biofilms Innovation Centre, University of Southampton. ⁵ National Infection Service, Public Health England, Porton Down, Salisbury, Wiltshire, UK.
Corresponding author: G.LuTheryn@soton.ac.uk

Introduction

Biofilm formation remains one of the most pervasive means by which bacteria may thrive cooperatively within a given environment, by augmenting their ability to capture resources and share information. Given that over 90% of chronic infections are attributed to underlying presence of biofilms, the subsequent risk to public health is clear^[1]. A treatment strategy that has been suggested in the past to facilitate healing of chronic wounds, is the administration of nitric oxide. However, the therapeutic application of nitric oxide has historically been problematic, due to its high reactivity with exogenous molecules such as oxygen and endogenous scavengers like haemoglobin^[2]. A solution to this problem is to utilise shelled microbubbles as carrier for nitric oxide; the typical architecture of the microbubble consists of a polymer, protein or phospholipid layer, which usually encapsulates a fluorinated gas core^[3]. The microbubble shell can therefore protect the nitric oxide core from its external environment, allowing the release of nitric oxide to be spatially and temporally controlled by the administration of ultrasound. This provides the unique opportunity to capitalise on the bioactive effect of nitric oxide, combined with the mechanical action of an oscillating microbubble^[4].

Methods

Nitric oxide microbubbles (NOMBs) with respective mean post-production diameters of 2.85 μm (SD ± 2.002) and 3.306 μm (SD ± 1.897) composed of 1,2-distearoyl-sn-glycero-3-phosphocholine (DSPC) or 1,2-dibehenoyl-sn-glycero-3-phosphocholine (DBPC) and polyoxyethylene (40) stearate (PEG40s), in a 9:1 molar ratio were generated by sonication. For dynamic tests an antibiotic-NOMB suspension in volumetric ratios of 1:1 to 1:10 was applied to a *Pseudomonas aeruginosa* biofilm, which was grown on a polypropylene coupon in a CDC bioreactor^[5]. The suspension was allowed to interact with the biofilm for 15-60 minutes, before being exposed to pulsed ultrasound for five minutes (1 MHz, 0.6 MPa). In all experiments, the US frequency was 1 MHz and a sub-inhibitory concentration for biofilm eradication ($< 10 \mu\text{g/ml}$) of the aminoglycoside gentamicin was used. In static tests a NOMB suspension was applied to *P. aeruginosa* biofilms grown at the fluid-air interface of wells on a microtiter plate, after 60 minutes the NOMB suspension was removed and the remaining biomass stained using 1% (aq) crystal violet. In both dynamic and static experiments, microbubbles with a core of ambient 'room' air (RAMBs) were used as a control for the effect of the constituent gas core.

Results

The sub inhibitory concentration of gentamicin alone used in dynamic experiments, achieved on average < 1 -Log reduction in viable cells. However, the administration of NOMBs and ultrasound achieved up to a 3-Log reduction in the number of viable cells, with an average reduction of 99.68% and 95.93% for DBPC and DSPC respectively (Figure 1). Microbubbles with an air core were unable to achieve a Log reduction greater than 1, reducing the number of viable cells by 92.92%. The static incubation of DSPC and DBPC NOMBs achieved on average a 23.96% and 63.28% reduction in total biomass respectively, whereas air filled microbubbles caused an apparent increase in biomass of 9.71% compared to untreated control biofilms.

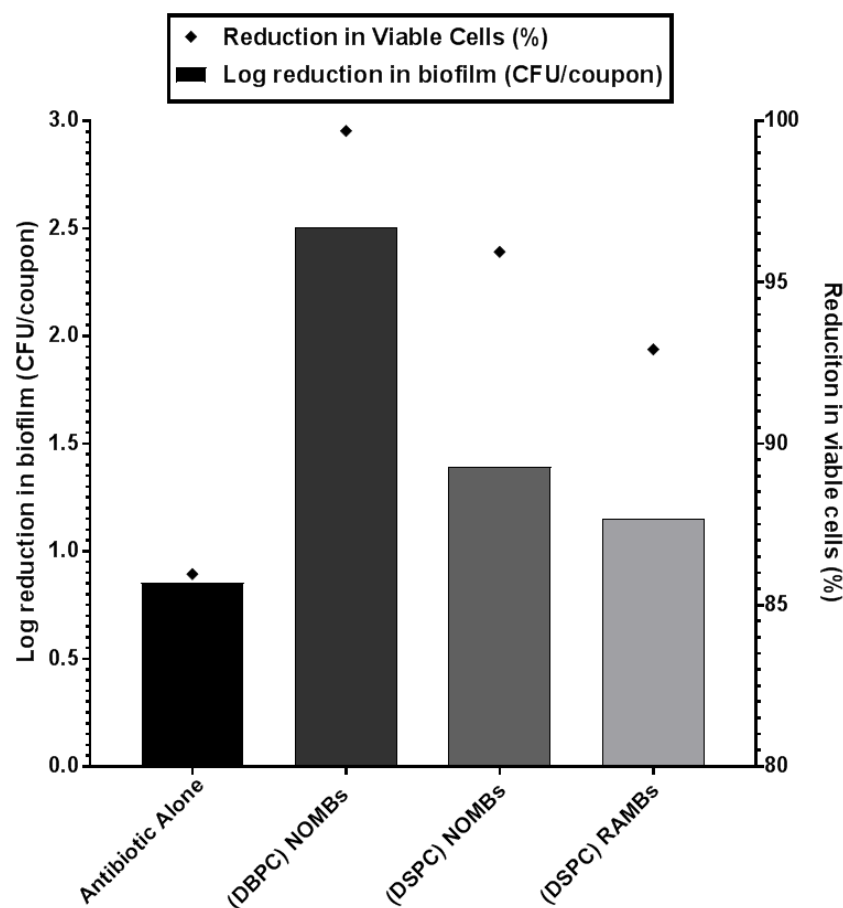


Figure 1 - The relative log reduction and associated percentage decrease in the number of viable biofilm cells, achieved by exposing a suspension containing microbubbles and a sub-inhibitory concentration of the antibiotic gentamicin to pulsed ultrasound for 5 minutes (1 MHz, 0.6 MPa). The antibiotic:microbubble suspension was applied in volumetric ratio of 1:10, nitric oxide microbubbles (NOMBs) or room air microbubbles (RAMBs) composed of either a DBPC or DSPC and PEG40s shell were used.

Conclusions

Building upon our previous work utilising microbubbles for the elimination of bacterial biofilms, this research is providing a new insight into the application of bioactive microbubbles (BOMBs). The most promising aspect of this work is that not only are NOMBs capable of significantly enhancing the efficacy of sub-inhibitory concentrations of antibiotics, but there is clear evidence that they are capable of inducing dispersal. Building on this early success, it is our aim to enhance the contact of NOMBs with the biofilm with the use of charge. Though the biofilm constituents vary significantly, the net charge remains consistent. Our early data on this area of work shows promise; cationic charged microbubbles are capable of sustaining an interaction with a negatively charged surface, upon exposure to increasing levels of fluid shear stress.

References

- [1]. G. Han and R. Ceilley, "Chronic Wound Healing: A Review of Current Management and Treatments.," *Adv. Ther.*, vol. 34, no. 3, pp. 599–610, Mar. 2017.
- [2]. R. P. Howlin et al., "Low-Dose Nitric Oxide as Targeted Anti-biofilm Adjunctive Therapy to Treat Chronic *Pseudomonas aeruginosa* Infection in Cystic Fibrosis," *Mol. Ther.*, vol. 25, no. 9, pp. 2104–2116, Sep. 2017.
- [3]. S. M. Fix, M. A. Borden, and P. A. Dayton, "Therapeutic gas delivery via microbubbles and liposomes," *J. Control. Release*, vol. 209, pp. 139–149, 2015.
- [4]. E. Stride and N. Saffari, "Microbubble ultrasound contrast agents: A review," *Proc. Inst. Mech. Eng. Part H J. Eng. Med.*, vol. 217, no. 6, pp. 429–447, 2003.
- [5]. R. E. Touzel, J. M. Sutton, M. E. Wand. *J Hosp Infect.* 2016 Feb;92(2):154-60.

Ultrasound-mediated delivery of DNA-coated gold nanoparticles across the blood-brain barrier

Tiffany G Chan^{1,2}, ***Sophie V Morse***³, ***Matthew J Copping***^{2,3}, ***James J Choi***³, ***Ramon Vilar***¹

¹*Department of Chemistry, Imperial College, London, UK*

²*Centre of Excellence in Neurotechnology, Imperial College, London, UK*

³*Department of Bioengineering, Imperial College, London, UK*

Corresponding author: r.vilar@imperial.ac.uk

Introduction

Functionalised nanoparticles have been widely studied as versatile platforms for *in vivo* imaging and therapy. In particular, nanoparticles coated with a dense layer of DNA are promising due to their high tailorability, ability to enter over fifty different cell types without the need for an external transfecting agent and lack of toxicity [1-5]. However, due to their size, the use of nanoparticles to image and/or treat the brain is limited as they are often unable to cross the blood-brain barrier (BBB). As of now, the only method to disrupt the BBB in a non-invasive, transient and targeted manner is with focused ultrasound and microbubbles [6]. To date, focused ultrasound-mediated BBB disruption has been used to deliver a variety of small molecules into the brains of rodents and non-human primates, but there are significantly fewer examples involving nanoparticles. A reason for this is that the dependency of focused ultrasound-mediated delivery on nanoparticle size has not been investigated, making it difficult to design nanoparticles tailored for this application: larger nanoparticles allow for higher payloads of drug to be delivered to the target location, but may not be delivered as efficiently into the brain using focused ultrasound. In this work, we have synthesised a range of DNA-coated gold nanoparticles of different sizes, show that they can be successfully delivered into the brains of mice using focused ultrasound and investigate the size-dependency of focused ultrasound-mediated nanoparticle delivery across the BBB [7].

Methods

Three sets of gold nanoparticles of different sizes were synthesised and coated with Cy5-labelled DNA strands. Synthesised DNA-coated gold nanoparticles (hydrodynamic diameters: 21.6 ± 3.3 nm (A), 23.3 ± 2.6 nm (B) and 25.2 ± 1.9 nm (C)) were delivered into the left thalamus of C57LB/6 mice using focused ultrasound (frequency = 1 MHz, peak-negative pressure = 530 kPa, pulse length = 10 ms, pulse repetition frequency = 0.5 Hz, sonication duration = 250 s; $n = 5$ for each set of nanoparticles). Following sonication, brains were sectioned into 30 μ m sections, imaged and stained with haemotoxylin and eosin. The efficiency of delivery using focused ultrasound-mediated BBB disruption was investigated by calculating the normalised optical density – the average fluorescence intensity in the targeted region normalised by the control region – from fluorescence images. A two-sided Student's *t*-test was performed to assess statistical significance.

Results

Successful BBB disruption in the left thalamus was observed in all experiments. Signal corresponding to the gold nanoparticle cores was seen in brightfield images at the same location as fluorescence signal from the attached Cy5-labelled DNA strands, suggesting that the synthesised nanoparticles remained intact as they crossed the BBB. Furthermore, the smallest nanoparticles used in this study were delivered across the BBB six times more efficiently than the largest nanoparticles using the same ultrasound parameters (Fig. 1). In agreement to prior work, the size-dependency observed suggests that the increased BBB permeability induced by focused ultrasound and microbubbles is primarily due to enhanced paracellular transport rather than enhanced vesicular transport [8].

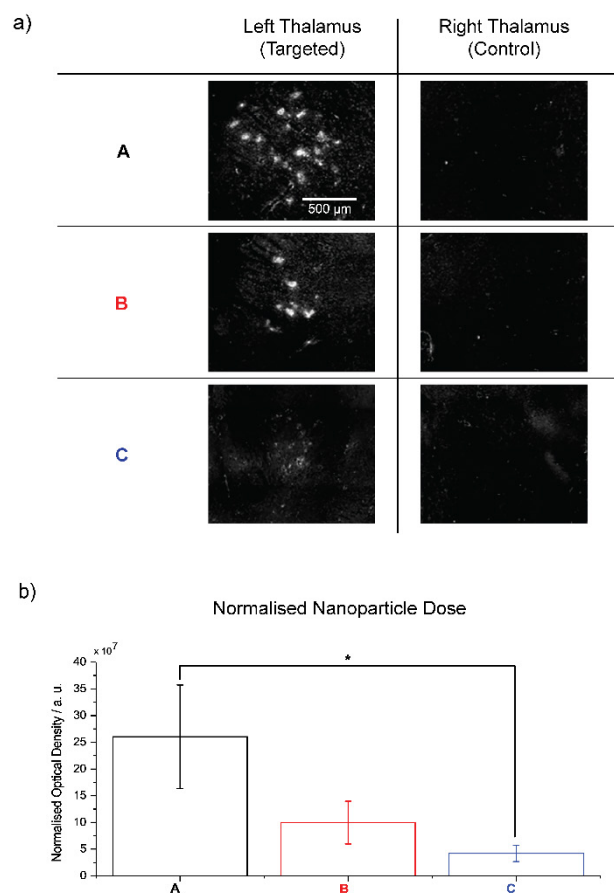


Figure 1. a) Representative fluorescence images from the delivery of Cy5-labelled DNA-coated gold nanoparticles (hydrodynamic diameters: 21.6 ± 3.3 nm (A), 23.3 ± 2.6 nm (B) and 25.2 ± 1.9 nm (C)) across the BBB using focused ultrasound. b) Normalised optical density was calculated from fluorescence images as a measure of the nanoparticle dose delivered across the BBB ($n = 5$ for each set of nanoparticles; $p < 0.05$).

Conclusions

Fluorescently-labelled DNA-coated gold nanoparticles of different sizes were synthesised and delivered across the BBB in mice using focused ultrasound. To the best of our knowledge, this is the first time that DNA-coated nanoparticles have been delivered across the BBB *in vivo* using focused ultrasound. In addition to this, more efficient delivery across the BBB was observed for the smallest nanoparticles tested. Since the difference in diameter between the smallest and largest nanoparticles used in this study is < 5 nm, nanoparticle diameter is an important criterion to take into account if one wishes to deliver nanoparticles into the brain using focused ultrasound.

References

- [1]. J. I. Cutler, E. Auyeung, C. A. Mirkin, *J. Am. Chem. Soc.*, 2012, 134, 1376-1391
- [2]. D. S. Seferos, A. E. Prigodich, D. A. Giljohann, P. C. Patel, C. A. Mirkin, *Nano Lett.*, 2009, 9, 308-311
- [3]. D. A. Giljohann, D. S. Seferos, A. E. Prigodich, P.C. Patel, C. A. Mirkin, *J. Am. Chem. Soc.*, 2009, 131, 2072-2073
- [4]. M. D. Massich, D. A. Giljohann, D. S. Seferos, L.E. Ludlow, C. M. Horvath, C. A. Mirkin, *Mol. Pharm.*, 2009, 6, 1934-1940
- [5]. N. L. Rosi, D. A. Giljohann, C. S. Thaxton, A. Lytton-Jean, M. S. Han, C.A. Mirkin, *Science*, 2006, 312, 1027-1030
- [6]. K. Hynynen, N. McDannold, N. Vykhodtseva, F. A. Jolesz, *Radiology*, 2001, 220, 640-646
- [7]. T. G. Chan, S. V. Morse, M. J. Copping, J. J. Choi, R. Vilar, *ChemMedChem*, 2018, 13, 1311-1314
- [8]. H. Chen, E. E. Konofagou, *J. Cereb. Blood Flow Metab.*, 2014, 34, 1197-1204

The role of microbubble composition in sonoporation

Oliver Vince¹, Miles Aron¹, Sarah Peeters², Vanessa Johanssen², Michael Gray¹, Nicola Sibson², Eleanor Stride¹

¹*BUBBL, Institute of Biomedical Engineering, University of Oxford, UK*

²*Institute for Radiation Oncology, University of Oxford, UK*

Corresponding author: oliver.vince@eng.ox.ac.uk

Introduction

The permeabilisation of cell membranes when exposed to ultrasound (US) and microbubbles (MBs) has considerable potential for improving therapeutic delivery, and similar mechanisms are thought to underlie ultrasound mediated blood brain barrier disruption (US-BBBD). Recent studies have demonstrated that transfer of material takes place between phospholipid-coated MBs and cell membranes. This study investigates the effect of this transfer on cancer cell membrane fluidity and sonoporation *in vitro* using MBs formulated with different phospholipids and subsequently on US-BBBD *in vitro* and *in vivo*.

Methods

MBs were formulated using phosphatidylcholines of different molecular weights and/or lysophosphatidylcholines (lyso-MBs). MBs were separated from unincorporated lipid and emulsifier solution by centrifugation. Quantitative fluorescence microscopy techniques were used to quantify changes in the molecular packing, viscosity and permeability to model drugs of cancer cells under mild ultrasound exposure *in vitro* (1 MHz, 250 kPa peak to peak, 10% DC, 15s exposure). MBs were size and concentration matched before all experiments and no significant difference in acoustic emissions was observed. Similar experiments were then performed using an *in vitro* BBB model consisting of a monolayer of MDCK cells whose transendothelial electrical resistance (TEER) could be measured.

To assess US-BBBD *in vivo*, Evans Blue (EB), Gadolinium-DTPA (Gd) and MBs were coinjected approximately 120s after the start of ultrasound exposure (500kHz, 200, 300 and 400kPa peak to peak, 1% DC, 5 mins exposure (2 and 3 mins pre and post injection respectively)). Cavitation activity was measured by comparing the acoustic emissions before and after MB injection. Pre/post T1-weighted MRI was used to assess Gd extravasation; histological analysis was used to assess EB and IgG extravasation.

Results

Removal of unincorporated emulsifier from the MB solution, reducing the lipid chain length and incorporating lysolipid into the MB shells all significantly decreased the molecular packing of cancer cell membranes in the absence of US. Lyso-MBs were also found to give a ~6 fold increase in sonoporation *in vitro* ($p < 0.0001$), while remaining non-toxic to cells in the absence of US over the timescales tested. Lyso-MBs were found to be more stable than control-MBs consisting of the same material without lysolipid. Lysolipid was also found to transiently reduce the TEER of a cell monolayer, indicating temporary cell-cell tight junction opening.

In the absence of US, both control-MBs and lyso-MBs are stable and safe to inject in mice without altering the BBB. At the three ultrasound pressures tested, Lyso-MBs are as effective as control-MBs at causing US-BBBD, as detected from the percentage hyperintensity across the whole brain on the post-Gd T1 weighted images.

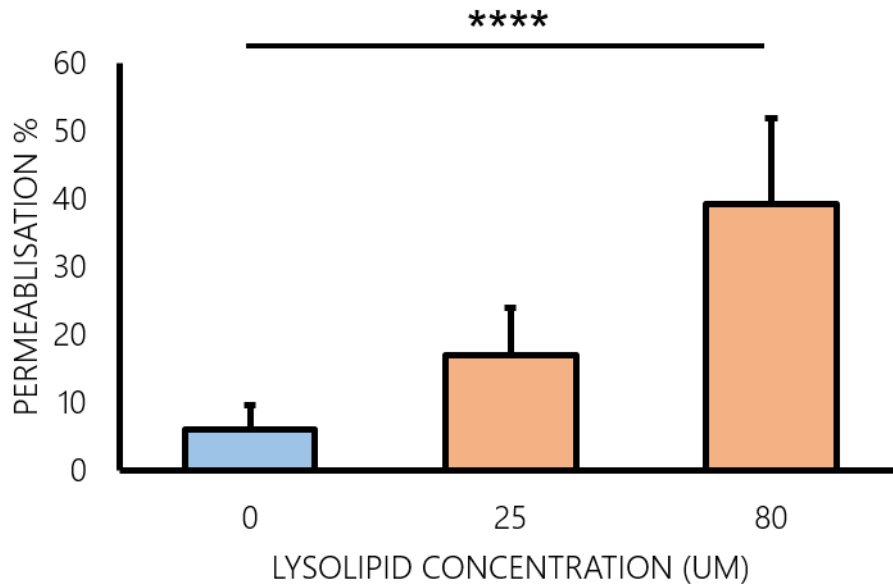


Figure 1: The effect of the concentration of lysolipid in the microbubble formulation on *in vitro* cell sonoporation as measured by uptake of propidium iodide, a cell nuclear stain. Lyso-MBs do not increase the permeabilisation of cell membranes in the absence of ultrasound when compared to control-MBs (data not shown).

Conclusions

The composition of the microbubble shell plays an important role in both cell membrane fluidity and sonoporation *in vitro*. Lyso-MBs significantly increase the percentage of cells sonoporated in an *in vitro* setup, and remain non-toxic to cells in the absence of ultrasound.

Lyso-MBs also present a stable, non-toxic and effective agent for *in vivo* US-BBBD at low ultrasound pressures as measured using Gd and MRI. Histological analyses and experimentation using different ultrasound conditions are ongoing and will be discussed. The merits and a comparison of each of the methods of measuring US-BBBD will be presented. Plans to further optimise the composition of the microbubble shell for sonoporation and US-BBBD will also be discussed.

Clinical Translation of Sonoreperfusion Therapy for Treatment of Microvascular Obstruction

Filip Istvanic¹, Gary Yu¹, Francois Yu¹, Jeff Powers², Xucai Chen¹, John Pacella¹

¹*Center for Ultrasound Molecular Imaging and Therapeutics, Department of Medicine, University of Pittsburgh, Pittsburgh, PA, USA*

²*Philips Ultrasound, Bothell, WA, USA*

Corresponding author: pacellajj@upmc.edu

Introduction

Microembolization during percutaneous coronary intervention for acute myocardial infarction causes microvascular obstruction (MVO). We have previously shown that sonoreperfusion therapy using ultrasound (US) and microbubbles restores microvascular perfusion in an in vitro model of MVO, and that reperfusion efficacy increases with US pulse length and with US acoustic pressure [1]. In preparation for clinical translation of this technique, we compared the reperfusion efficacy of an experimental US system (modified Philips EPIQ) capable of long US pulses to that of a clinical US system (Philips Sonos 7500) with short US pulses in a rat hindlimb model of MVO. We hypothesized that the experimental long-pulse US delivery system would relieve MVO to a greater extent than would the short-pulse US delivery system.

Methods

We used our previously developed rat hindlimb model of MVO [2]. This model was created by injecting microthrombi into the arterial circulation of the hindlimb muscle via the contralateral femoral artery. Lipid encapsulated microbubbles were infused through the femoral artery while therapeutic US was delivered to the obstructed microvasculature for two 10-minute sessions using one of four US conditions: (1) Sonos 7500 in ultraharmonic mode; 1.3 MHz, 1.3 MPa (MI=1.1), 27 μ s pulse length (total), time triggered, 1 frame every 3 sec; spatial peak time average intensity (I_{SPTA}) 0.5 mW/cm²; (2) Sonos 7500 in ultraharmonic mode; 1.3 MHz, 1.3 MPa (MI=1.1), 27 μ s pulse length (total), time triggered, 23 frames every 3 sec; I_{SPTA} 11.6 mW/cm²; (3) EPIQ in SonoLysis mode; 1.6 MHz, 0.5 MPa, 1 ms pulse length, time triggered, 8.3 frames every 3 sec; I_{SPTA} 23.0 mW/cm²; and (4) EPIQ in SonoLysis mode; 1.6 MHz, 1.44 MPa, 1 ms pulse length, time triggered, 1 frame every 3 sec; I_{SPTA} 23.0 mW/cm². Control rats were injected with microthrombi but did not receive US therapy.

Contrast enhanced US perfusion imaging (Sequoia, CPS, 7 MHz) of the microvasculature was conducted at four timepoints: (1) baseline (BL); (2) 10 min after microthrombi injection (MVO); (3) post-treatment 1 (Tx1); and (4) post-treatment 2 (Tx2). DEFINITY® microbubble contrast agent was infused through the jugular vein during perfusion imaging. Microvascular blood volume (MBV) calculated from video intensity-time data measured in hindlimb muscle regions of interest was used as a measure of reperfusion efficacy. Measurements were analyzed using repeated measures two-way ANOVA with Tukey's HSD for post-hoc analysis to compare reperfusion efficacy across experimental groups and within experimental groups over time.

Results

MBV was similar across all experimental groups at baseline and after microthrombi injection, yielding an MVO state with markedly reduced MBV. MBV for each group over all time points are shown in **Fig. 1** with accompanying indications of post-hoc statistical significance ($p < 0.05$ for statistical significance of post-hoc comparisons).

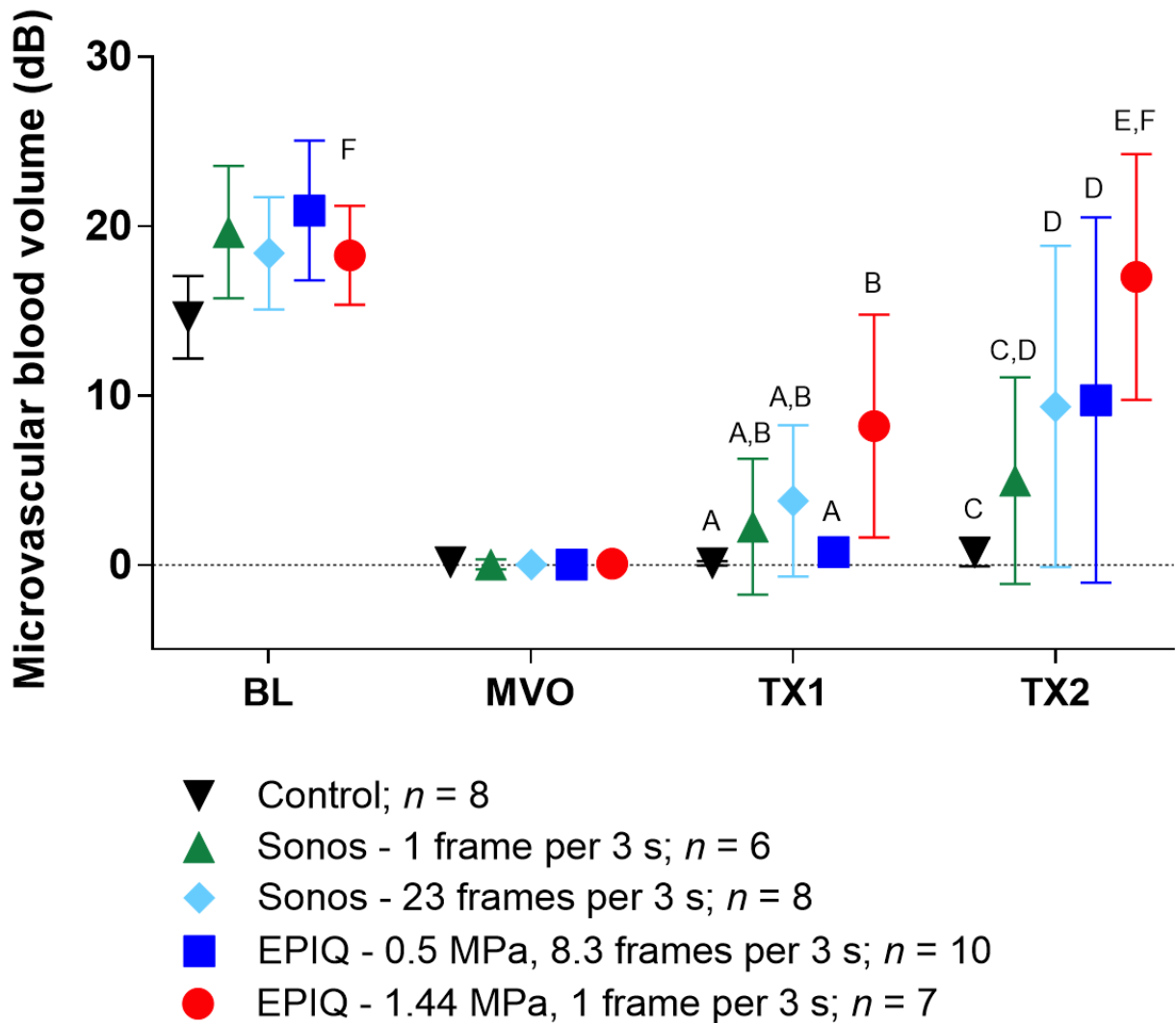


Figure 1: Microvascular blood volume in the treated hindlimb for all experimental groups. Data points and error bars represent mean and SD. Time points of measurement include baseline prior to treatment (BL), 10 min after microthrombi injection (MVO), immediately after first 10-min US treatment (TX1), and immediately after second 10-min US treatment (TX2). Groups marked with the same letter are not statistically different.

Repeated measures two-way ANOVA resulted in significant time, treatment, and interaction effects ($p < 0.005$). For post-hoc analysis between different experimental groups after the first 10-minute treatment, only the EPIQ high pressure group showed significantly higher blood volume relative to the control group. Additionally, the EPIQ high pressure group had significantly higher blood volume than did the EPIQ low pressure group. After the second 10-minute treatment, only the EPIQ high pressure group showed significantly higher blood volume relative to all other experimental groups, while the EPIQ low pressure and Sonos multi-frame groups had higher blood volumes than did the control group. For within treatment group comparisons over time, the EPIQ high pressure group was the only treatment to show a restoration of blood volume to baseline values, while all other treatment groups had significantly lower blood volumes after the second treatment compared to baseline.

Conclusions

These data demonstrate the superior reperfusion efficacy of a long pulse, high acoustic pressure US delivery system. This observation corroborates our previous *in vitro* findings that longer pulse lengths and higher acoustic pressures are associated with greater reperfusion efficacy [1]. Of note, the EPIQ high pressure group (1.44 MPa, I_{SPTA} 23.0 mW/cm²) was significantly more efficacious at restoring MBV than was the energy-matched EPIQ low pressure group (0.5 MPa, I_{SPTA} 23.0 mW/cm²), suggesting that higher acoustic pressures enhance reperfusion efficacy when accounting for total energy delivered to the obstructed microvasculature. Additionally, the EPIQ low pressure group (0.5 MPa, I_{SPTA} 23.0 mW/cm²) was just as efficacious at restoring MBV as was the one-half energy-matched Sonos multi-frame group (1.3 MPa, I_{SPTA} 11.6 mW/cm²), suggesting that higher acoustic pressures can elicit comparable reperfusion efficacy using less total energy. Results obtained from this study demonstrate that clinically available US systems may allow for sonoreperfusion after MVO using long pulses coupled with high acoustic pressures.

References

- [1]. Leeman JE et al. Effect of acoustic conditions on microbubble-mediated microvascular sonothrombolysis. *Ultrasound Med Biol* 2012;38(9):1589-98.
- [2]. Pacella JJ et al. Treatment of microvascular microembolization using microbubbles and long-tone-burst ultrasound: an in vivo study. *Ultrasound Med Biol* 2015;41(2):456-64.

Ultrasound-mediated antitumor efficacy of liposomal doxorubicin conjugated polymer microbubbles with reduced cardiotoxicity in a mouse model of soft tissue sarcoma

Mingyu He¹, Xucai Chen¹, Linda Lavery¹, Flordeliza S. Villanueva¹

¹Center for Ultrasound Molecular Imaging and Therapeutics,
University of Pittsburgh, Pittsburgh, PA, USA
Corresponding author: villanuevafs@upmc.edu

Introduction

Doxorubicin (Dox) is one of the most widely used chemotherapeutic agents and is standard of care for the treatment of sarcomas and other cancers. Unfortunately, Dox also induces cardiac damage in a dose-dependent manner [1]. Anti-tumor efficacy, similarly dependent on Dox dose, is compromised when dosage must be decreased due to cardiotoxicity. An alternative preparation, pegylated liposomal Dox (Doxil[®]), putatively reduces cardiotoxicity [2]. However, in clinical studies, Doxil[®] did not improve the maximal tolerated dose compared to free Dox, and prolonged circulation of encapsulated Dox caused a new dose-limiting toxicity, palmar-plantar erythrodysesthesia (PPE)[3]. Thus, an optimal delivery platform for Dox remains elusive.

Microbubbles (MBs) are intravenously injectable gas-filled microspheres that are clinically used as ultrasound (US) contrast agents. Polymer MBs are also suitable drug or gene carriers that can prolong the half-life of the therapeutic substances and undergo disease site-specific US-triggered unloading of cargo via navigation of the US beam [4, 5]. In this study, we developed polymer MBs carrying liposomal Dox with US targeted microbubble cavitation (UTMC) directed at the tumor site to inhibit tumor growth in a murine sarcoma model while reducing cardiotoxicity.

Methods

Liposomal Dox-loaded polymer MBs, called Dox lipopolyplexes (DoxLPX), were developed ($\sim 6 \times 10^{-7}$ $\mu\text{g}/\text{MB}$) (Fig. 1). The polymer MBs used in this study were composed of an outer layer of crosslinked human albumin, an inner shell of (poly-D,L-lactide, PLA) and a core of nitrogen gas. The liposomal Dox was conjugated to MBs via biotin-avidin interaction. C57BL/6 mice received a subcutaneous injection of 2×10^6 MCA205 cells in the lower flank near the base of the tail to establish soft tissue sarcoma (STS). Treatments commenced when tumor volume grew to 40-80 mm^3 . A complex US waveform (1 MHz, 5- μs duration at 1,000 kPa followed by 495- μs duration at 170 kPa, repeated 500 times in 1 ms intervals every 2.5 sec), optimized for Dox release, was delivered for 15 min aiming the tumor site during intravenous (i.v.) infusion of DoxLPX (5 mg/kg equiv. Dox per treatment). Controls received an equivalent dose of i.v. liposomal Dox+MB co-administration with the same US regime or free i.v. Dox, i.v. liposomal Dox, i.v. saline and US mediated i.v. empty LPX carrier. Treatments were given every 3.5 days (total 4 treatments).

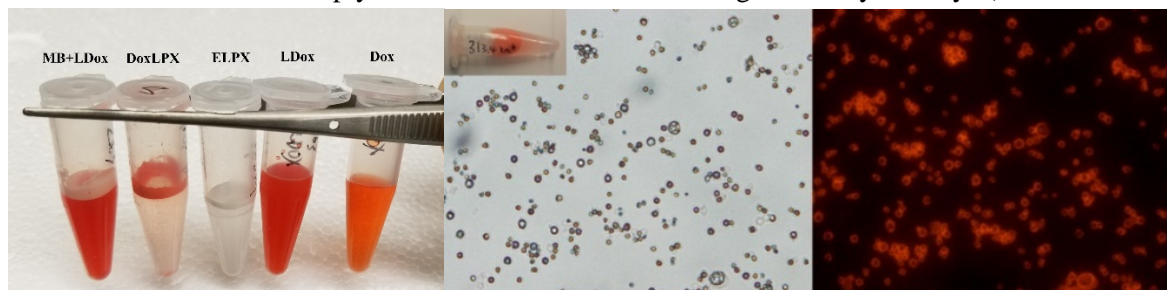


Figure 1. Intravenous administered formulations (left), from left: MB+liposomal Dox co-administration, DoxLPX, Empty LPX, liposome Dox, free Dox; and DoxLPX under microscope, brightfield (middle) and fluorescence image (right).

Tumor volume and cardiac function were serially monitored with high-resolution ultrasound imaging (Vevo 2100). Tumor volume was plotted vs. time and the tumor doubling time was calculated. Left ventricular ejection fraction (EF), fractional shortening (FS), global radial strain, and left ventricle (LV)

mass were calculated using the Vevo LAB software. Apoptosis signal (caspase-3 activity) in heart tissue and histologic myocardial fibrosis in DoxLPX+US treated animals was compared with that from controls.

Results

Treatment with US+empty LPX carrier (without drug) did not show therapeutic efficacy. DoxLPX + US treated mice had numerically the smallest mean normalized tumor volume of all the groups, which was significantly smaller than that in mice treated with free Dox and liposomal Dox treated tumors on day 17.5 (Fig. 2). Compared to free Dox and liposomal Dox, DoxLPX + US treatment was associated with enhanced accumulation of Dox in the tumors, inhibited tumor growth rates, and increased median survival time. Intravenous co-administration of MB and liposomal Dox + US generally caused tumor growth inhibition, but the magnitude was highly variable, such that overall difference in tumor size vs. mice treated with free Dox or liposomal Dox was not statistically significant. Echocardiographic analysis and histological staining suggested that DoxLPX + US attenuated adverse effects of Dox on cardiac function; i.e. fewer animals had a decline in EF, FS or an increase in LV mass, and histologic analysis showed less myocardial collagen deposition compared to the other Dox-treated groups.

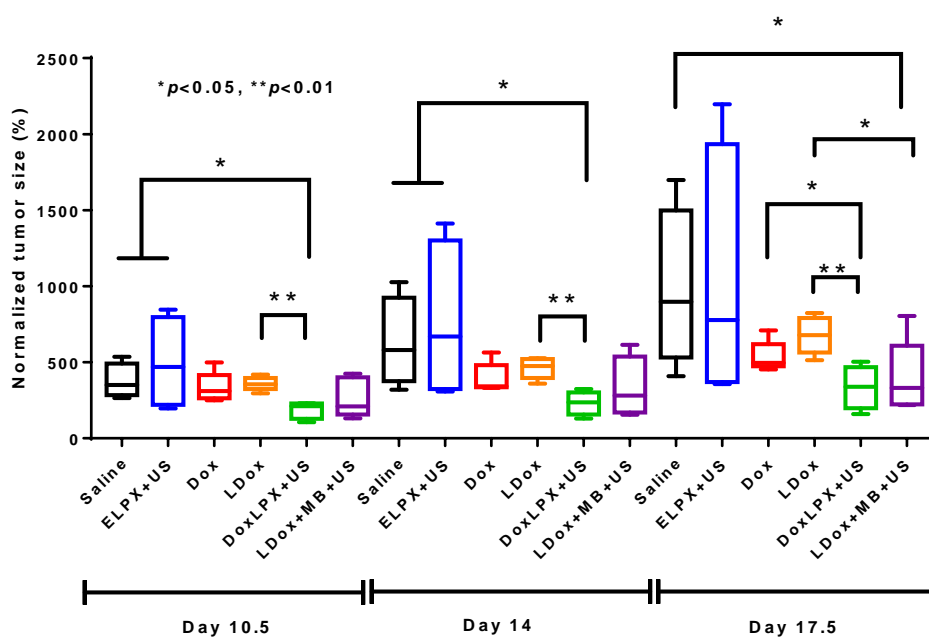


Figure 2. Normalized tumor size of C57BL/6J mice soft tissue sarcoma tumor model (MCA205) with US mediated DoxLPX, MB+LDox or ELPX treatments. Saline, free Dox and liposomal Dox were used as controls on day 10.5, 14 and 17.5.

Conclusions

DoxLPX-loaded MBs combined with ultrasound targets doxorubicin delivery to the tumor site, resulting in tumor growth inhibition equivalent to that achieved by free Dox, and with relative sparing of cardiotoxicity.

References

- [1]. Ewer MS et al., Cardiotoxicity of anticancer treatments, *Nature Reviews Cardiology*, 2015;12:547-559.
- [2]. Duggan ST et al., Pegylated liposomal doxorubicin: a review of its use in metastatic breast cancer, ovarian cancer, multiple myeloma and AIDS-related Kaposi's sarcoma, *Drugs*, 2011; 71: 2531-2558.
- [3]. Lorusso D et al., Pegylated liposomal doxorubicin-related palmar-plantar erythrodysesthesia ('hand-foot' syndrome), *Annals of Oncology*, 2007; 18(7): 1159-1164.
- [4]. Yu FTH et al., Low intensity ultrasound mediated liposomal doxorubicin delivery using polymer microbubbles, *Molecular Pharmaceutics*, 2016; 13: 55-64.
- [5]. Eisenbrey JR et al., Development and optimization of a doxorubicin loaded poly(lactic acid) contrast agent for ultrasound directed drug delivery. *J. Controlled Release* 2010;143: 38-44.

Classification of histotripsy liquefaction *in vitro* with passive cavitation imaging

Kenneth B. Bader¹, Kevin J. Haworth², Adam D. Maxwell³, and Christy K. Holland²

¹*Department of Radiology, University of Chicago, Chicago, IL, USA*

²*Department of Internal Medicine, Division of Cardiovascular Health and Disease, University of Cincinnati, Cincinnati, OH, USA*

³*Department of Urology, University of Washington School of Medicine, Seattle, WA, USA*
Corresponding author: baderk@uchicago.edu

Introduction

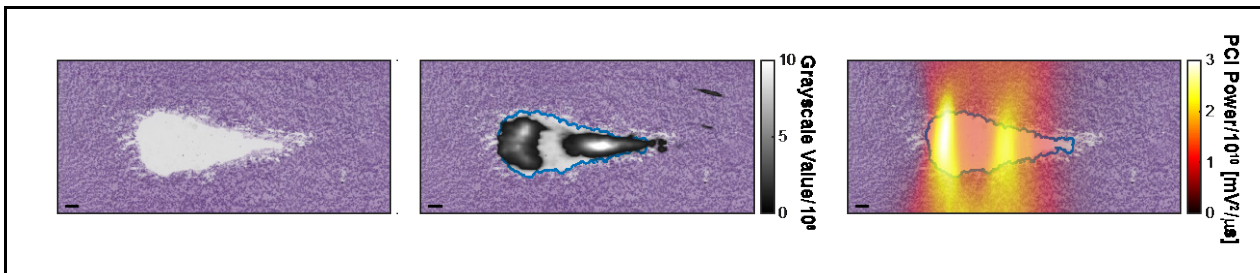
Histotripsy is a focused ultrasound therapy that utilizes the mechanical action of bubble clouds to liquefy tissue [1]. Conventional B-mode imaging, the primary method for histotripsy image guidance, can detect the presence of a bubble cloud via echogenicity but does not quantify the degree of bubble activity [2], [3]. Variability in tissue properties and the immediate physiological response to the histotripsy insonation also limit quantitative assessment of liquefaction with B-mode imaging [2]-[4]. Acoustic emissions generated by bubbles are a surrogate for the strength and type of their mechanical activity. Passive cavitation imaging maps bubble-generated acoustic emissions spatially and temporally [5]-[7]. The purpose of this study was to investigate passive cavitation imaging as a means to classify histotripsy-induced liquefaction location within an *in vitro* phantom.

Methods

Prostate tissue phantoms composed of agarose and evaporated milk [8] were exposed to histotripsy pulses with a 1-MHz fundamental frequency over a range of pulse durations (5 – 20 μ s) and peak negative pressures (12 – 23 MPa). A total of 2000 shocked histotripsy pulses were applied at a 20-Hz rate, and five replicates were performed for each set of insonation conditions. During application of the histotripsy pulse, acoustic emissions generated by the bubble cloud were recorded passively with a linear array (L7-4, ATL Inc., Bothell, WA). Emissions were processed with a delay, sum, and integrate beamformer to generate passive cavitation images [7]. To assess bubble cloud echogenicity, a plane-wave B-mode image was acquired with the same imaging array 1 ms after transmission of the histotripsy pulse.

Following insonation, the phantom was sectioned and stained (periodic acid-Schiff) to delineate the liquefaction extent. Passive cavitation and plane-wave B-mode images were co-registered with stained sections of the phantom (Fig. 1). Receiver operator characteristic (ROC) analysis was conducted based on the beamformed acoustic emission power or grayscale value along the central axis of the liquefaction zone. The analysis was only performed along the central axis of the liquefaction zone due to the documented limited axial resolution of the point spread function for a linear array [5]. Data was analyzed in aggregate across all pulse durations and peak negative pressures. The threshold acoustic power or grayscale value for phantom liquefaction was extracted from the ROC curve at the point closest to a true positive rate of 1, and false positive rate of 0 [9]. The accuracy, sensitivity, and specificity of each imaging modality prediction for phantom liquefaction were extracted from the ROC curves at the threshold point.

Fig 1. (Left) Histotripsy liquefaction zone in prostate phantom. (Center) Plane wave B-mode image co-registered with gross observation of phantom liquefaction. (Right) Passive cavitation image co-registered with gross observation of phantom liquefaction. The histotripsy pulse (20- μ s pulse duration, 23-MPa peak negative pressure) propagated from left to right in the image. The extent of the liquefaction zone is outline in blue for the center and right panels. The bar in the lower left corner of each panel corresponds to 1 mm.



Results

Bubble cloud activity was initiated for all insonation conditions, as evidenced by strong acoustic emissions and hyperechogenicity (Fig. 1). The area under the ROC curve was greater for passive cavitation images compared to plane-wave B-mode images ($p < 0.05$, Fig. 2). The threshold acoustic power and grayscale values were $9.36 \times 10^{10} \pm 6.42 \times 10^8$ $\text{mV}^2/\mu\text{s}$ and $1.94 \times 10^8 \pm 1.66 \times 10^3$, respectively. The corresponding accuracy, sensitivity, and specificity were $90 \pm 3\%$, $81 \pm 5\%$, and $93 \pm 2\%$ for passive cavitation images, and $83 \pm 1\%$, $49 \pm 6\%$, and $95 \pm 1\%$ for plane-wave B-mode images, respectively. The accuracy and sensitivity were significantly greater for passive cavitation relative to plane-wave B-mode images ($p < 0.05$). Specificity was not significantly different between the two imaging modalities (Fig. 3).

Fig 2. Receiver operator characteristics for aggregated plane-wave B-mode grayscale and passive cavitation image acoustic power prediction of phantom liquefaction. The dashed black line represents an area under the ROC curve of 0.5 (i.e. random guessing).

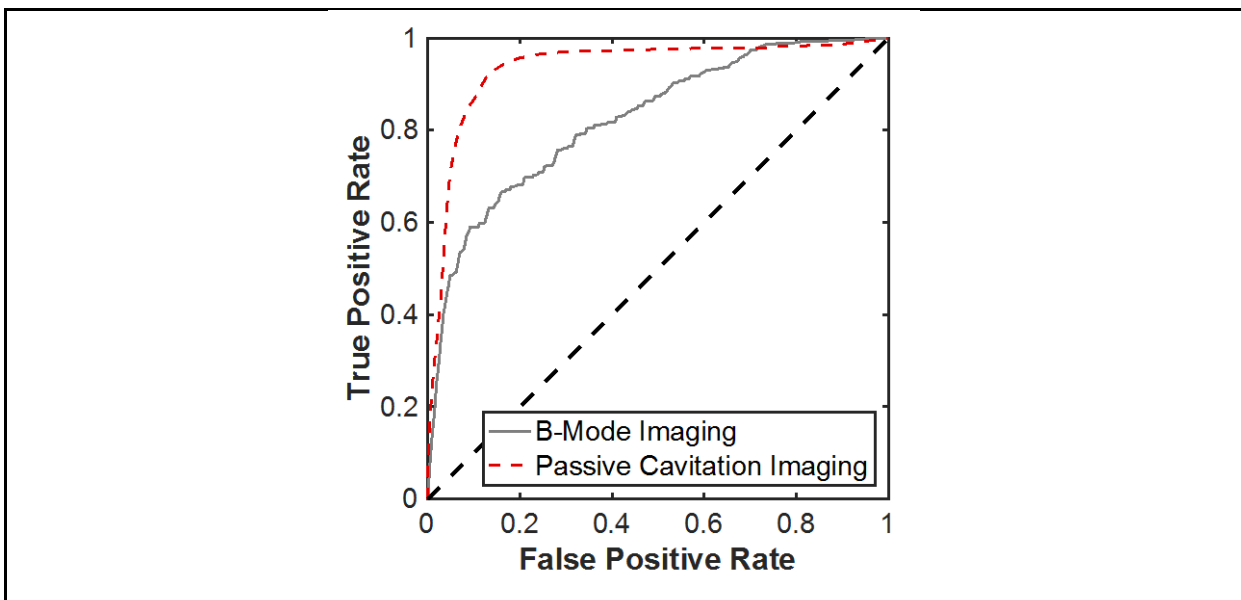
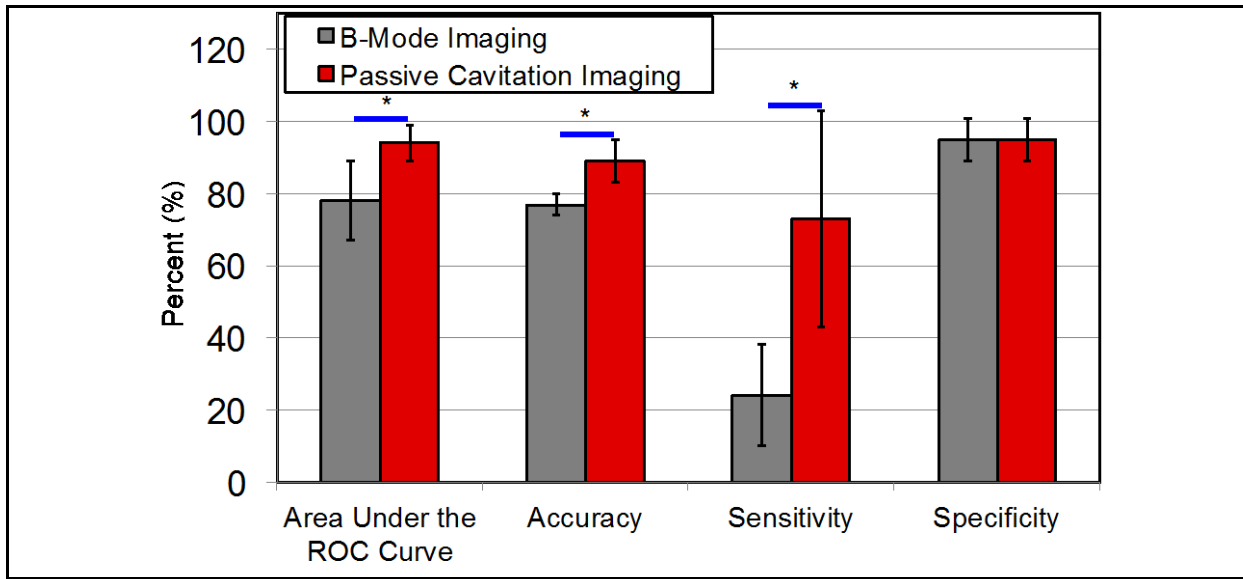


Fig 3. The area under the ROC curve, accuracy, sensitivity, and specificity of plane wave B-mode and passive cavitation imaging for predicting phantom liquefaction. Blue bars with an asterisk denote statistically significant difference in the data ($p < 0.05$).



Conclusions

Though temperature is monitored to predict thermal tissue ablation, mechanical ablation lacks an equivalent means to assess the mechanism of therapeutic action and therefore treatment efficacy. Here, acoustic emissions mapped with passive cavitation imaging were used to assess overall mechanical activity of histotripsy-induced bubble clouds. These results highlight a stronger correlation between histotripsy-induced liquefaction and passive cavitation images compared to plane wave B-mode images, albeit within the context of a limited passive cavitation image range resolution.

References

- [1]. V. A. Khokhlova, J. B. Fowlkes, W. W. Roberts, G. R. Schade, Z. Xu, T. D. Khokhlova, T. L. Hall, A. D. Maxwell, Y.-N. Wang, and C. A. Cain, "Histotripsy methods in mechanical disintegration of tissue: Towards clinical applications," *Int. J. Hyperthermia*, vol. 31, no. 2, pp. 145–162, Mar. 2015.
- [2]. X. Zhang, R. M. Miller, K.-W. Lin, A. M. Levin, G. E. Owens, H. S. Gurm, C. A. Cain, and Z. Xu, "Real-time feedback of histotripsy thrombolysis using bubble-induced color Doppler," *Ultrasound Med. Biol.*, vol. 41, no. 5, pp. 1386–1401, May 2015.
- [3]. Y.-F. Zhou, "High intensity focused ultrasound in clinical tumor ablation," *World J. Clin. Oncol.*, vol. 2, no. 1, pp. 8–20, 2011.
- [4]. E. Vlaisavljevich, J. Greve, X. Cheng, K. Ives, J. Shi, L. Jin, A. Arvidson, T. Hall, T. H. Welling, G. Owens, W. Roberts, and Z. Xu, "Non-Invasive Ultrasound Liver Ablation Using Histotripsy: Chronic Study in an In Vivo Rodent Model," *Ultrasound Med. Biol.*, vol. 42, no. 8, pp. 1890–1902, Aug. 2016.
- [5]. M. Gyöngy, M. Arora, J. A. Noble, and C. C. Coussios, "Use of passive arrays for characterization and mapping of cavitation activity during HIFU exposure," presented at the IEEE Ultrasonics Symposium (IUS), 2008, pp. 871–874.
- [6]. V. A. Salgaonkar, S. Datta, C. K. Holland, and T. D. Mast, "Passive cavitation imaging with ultrasound arrays," *The J. Acoust. Soc. Am.*, vol. 126, no. 6, p. 3071, 2009.
- [7]. K. J. Haworth, K. B. Bader, K. T. Rich, C. K. Holland, and T. D. Mast, "Quantitative Frequency-Domain Passive Cavitation Imaging," *IEEE Trans. Ultrason., Ferroelect., Freq. Contr.*, vol. 64, no. 1, pp. 177–191, Jan. 2017.
- [8]. K. B. Bader, M. J. Crowe, J. L. Raymond, and C. K. Holland, "Effect of Frequency-Dependent Attenuation on Predicted Histotripsy Waveforms in Tissue-Mimicking Phantoms," *Ultrasound Med. Biol.*, vol. 42, no. 7, pp. 1701–1705, Jul. 2016.
- [9]. M. H. Zweig and G. Campbell, "Receiver-operating characteristic (ROC) plots: a fundamental evaluation tool in clinical medicine.," *Clin. Chem.*, vol. 39, no. 4, pp. 561–577, Apr. 1993.

Ultrafast radial modulation imaging

P. Muleki-Seva¹, K. Xu¹, M. Tanter¹, O. Couture¹

¹ ESPCI Paris, PSL Research University, CNRS, INSERM, Institut Langevin, 75012 Paris, France

Corresponding author: pauline.muleki@gmail.fr

Introduction

Radial modulation imaging improves the detection of microbubbles at high frequency [1-4], where other nonlinear techniques, as pulse inversion and amplitude modulation, often lock the emission pulse frequency close to the bubble resonance frequency (below 10 MHz), and consequently limit image resolution. Radial modulation imaging uses two ultrasonics excitations: a low-frequency excitation to manipulate microbubbles diameter and a higher frequency excitation to image them. The synchronization between the imaging pulses in RMI is non-trivial because microbubbles need to be interrogated in the compression and in the rarefaction phase and not between them (ie, in nodes of the modulation pressure) and the time-delay difference corresponding to the dispersion of the imaging pulse by the modulation pulse have to be corrected [2, 5]. We propose to simplify RMI by sampling the oscillations of microbubbles induced by the modulation pulse with ultrafast imaging. Ultrafast nonlinear imaging allows to increase microbubbles contrast when compared to conventional ultrasound imaging [6-7]. For radial modulation imaging, we suggest that the modulation frequency can be filtered more efficiently, in the slow-time, on long ensembles of images comparably to ultrasensitive Doppler [8]. We describe an implementation of ultrafast RMI (uRMI) where a beat frequency between the modulation pulse and the ultrafast pulse-repetition frequency is exploited to separate microbubbles from tissue phantom *in vitro*. In this way, recording microbubbles in different states of the modulation period translates to a modulated images set in the spectral domain of the slow-time. The microbubbles images may then be evaluated by demodulation of the images through a lock-in-amplifier.

Methods

Diluted Sonovue (1/3000) was injected in a flow phantom with a flow speed from 0 to 20 mL/min. It was insonified by two confocal transducers, one array at 15MHz and a single element at 1 MHz. The 1-MHz transducer generated a continuous excitation close to 1 MHz using a function generator. The 15-MHz probe was connected to a Verasonics Vantage and performed ultrafast imaging with plane waves (300 kPa, 1 cycle, PRF 1/60 μ s). One thousand images were acquired for each acquisition, with a varying number of compounding angles. Ultrafast radial-modulation imaging consisted in addressing the microbubbles at different stage of their oscillations. The 1-MHz modulation wave was modulated in frequency so that high-frequency pulses reached microbubble at 3, 4, 5 or 10 modulation-states. Radio-frequency data were beamformed and filtered by a lock-in-amplifier in the slow time. Reconstruction of images was performed by combining coherently the compounding angles. The contrast-to-tissue ratio was estimated for the sum in intensity of the 1000 processed images. Acquisitions were repeated 3 times to study the effect of the number of sampled modulation states, the number of angles of imaging plane waves acquisitions, the amplitude of the modulation pulse and the flow speed. The uRMI technique was also compared to other techniques to detect microbubbles: amplitude modulation at 15 MHz, microbubble disruption and SVD filter.

Results

In our experimental conditions, a contrast-to-tissue ratio from 7.2 to 14.8 dB was obtained with uRMI at 15 MHz. This contrast-to-tissue ratio was stable with the number compounding angles. It increased with the amplitude of excitation of the low frequency and with the number of microbubbles modulation-states. It decreased with the flow speed. Without flow, uRMI (10 dB) provided a better contrast-to-tissue ratio than SVD filter (8 dB), microbubbles disruption (6 dB) and amplitude modulation (4 dB) (Figure 1). In

presence of flow, SVD filter provided the best contrast-to-tissue ratios (16 to 17 dB). The inherent limitation of uRMI and RMI techniques were the decorrelation of microbubbles through a higher flow velocity or a lower frame rate. This shows the complementarity of uRMI and SVD filtering of ultrafast imaging of microbubbles, which works well in the presence of flow.

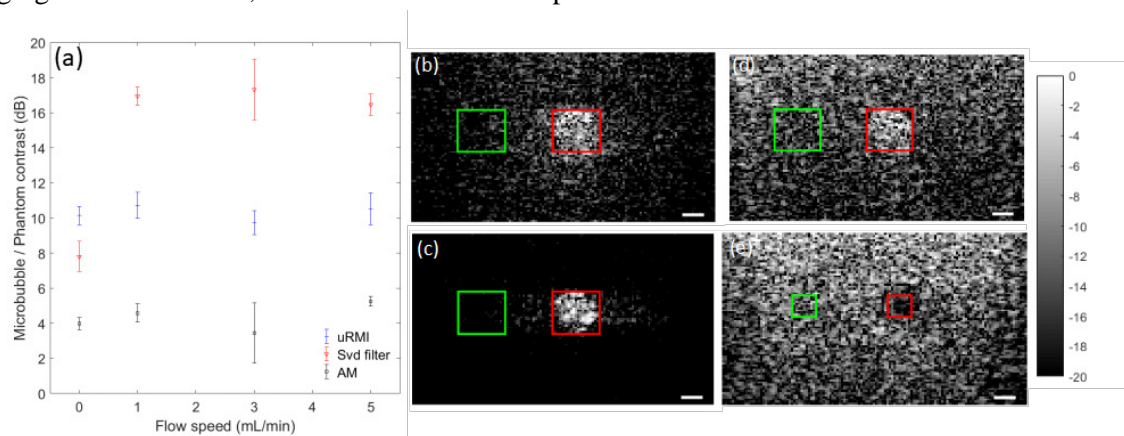


Figure 1. Contrast-to-tissue ratio between microbubbles in the vessel and the phantom as a function of the flow speed (3 angles, 4 modulation-states, 100 kPa low-frequency acquisition) and for amplitude modulation, SVD filtering (a). Examples of images for uRMI (b), SVD filter (c), amplitude modulation (d) and subtraction of an image with microbubbles to an image without microbubbles (e). The red and green rectangles correspond to the ROI of the vessel phantom and the agar, respectively. The scale bar represents 1 mm and the colorbar is in dB.

Conclusion

In this study, we showed that RMI can be improved when combined to ultrafast imaging. This technique may then be suitable to improve the detection of targeted microbubbles in ultrasound molecular imaging applications. Moreover, it could be used to detect microbubbles moving extremely slowly in the finest vessels to improve ultrasound localization microscopy [9-11]. Furthermore, RMI may be less destructive than other nonlinear techniques as linear radial oscillations are enough to detect microbubbles whereas strong nonlinear oscillations (close from destruction regime) are needed for nonlinear contrast sequences.

References

- [1]. Shariff HH, Bevan PD, Karshafian R, Williams R and Burns PN, Radial Modulation Imaging: Raising the Frequency for Contrast Imaging, In *Ultrasonics Symposium*, 2006: 104-107, 2006.
- [2]. Angelsen BA and Hansen R, SURF Imaging-A new method for ultrasound contrast agent imaging, In *Ultrasonics Symposium*, 2007: 531-541, 2007.
- [3]. Chérin E, Brown J, Måsøy S-E, Shariff H, Karshafian R, Williams R, Burns PN and Foster FS, Radial modulation imaging of microbubble contrast agents at high frequency, *Ultrasound in medicine & biology*, 34(6): 949-962, 2008.
- [4]. Masoy S-E, Standal O, Nasholm P, Johansen TF, Angelsen B and Hansen R, SURF imaging: In vivo demonstration of an ultrasound contrast agent detection technique, *IEEE UFFC*, 55(5): 1112-1121, 2008.
- [5]. Hansen R and Angelsen BA, SURF imaging for contrast agent detection, *IEEE UFFC*. 56(2): 280-290. 2009.
- [6]. Couture O, Bannouf S, Montaldo G, Aubry JF, Fink M, and Tanter M, Ultrafast imaging of ultrasound contrast agents, *Ultrasound in medicine & biology*, 35(11): 1908-1916, 2009.
- [7]. Couture O, Fink M and Tanter M, Ultrasound Contrast Plane Wave Imaging, *IEEE UFFC*. 59(12): 2676-2683. 2012.
- [8]. Bercoff J, Montaldo G, Loupas T, Savery D, Mézière F, Fink M and Tanter M, Ultrafast compound Doppler imaging: Providing full blood flow characterization, *IEEE UFFC*, 58(1): 134-147, 2011.
- [9]. Couture O, Besson B, Montaldo G, Fink M and Tanter M, Microbubble ultrasound super-localization imaging (MUSLI), In *Ultrasonics Symposium*, 2011: 1285-1287, 2011.
- [10]. Couture O, Hingot V, Heiles B, Muleki-Seya P and Tanter M, Ultrasound localization microscopy and super-resolution: A state of the art, *IEEE UFFC*, 65(8): 1304-1320 2018.
- [11]. Errico C, Pierre J, Pezet S, Desailly Y, Lenkei Z, Couture O and Tanter M, Ultrafast ultrasound localization microscopy for deep super-resolution vascular imaging, *Nature*, 527(7579): 499, 2015.

The Bubble Counter: a unique device for the precise control of microfluidically formed monodisperse microbubbles

Emmanuel Gaud¹, Gilles Casqueiro¹, Anne Lassus¹, Peter Frinking¹, Guillaume Lajoinie², Tim Segers^{1,2}, Gonzalo Collado Lara^{1,2}, Michel Versluis²

¹Bracco Suisse SA, CH-1228 Plan-les-Ouates, Geneva, Switzerland

²Physics of Fluids group, Technical Medical center, MESA+ Institute for Nanotechnology, University of Twente, Enschede, The Netherlands

Corresponding author: emmanuel.gaud@bracco.com

Introduction

The Bubble Counter is a sophisticated device developed by the University of Twente, as a part of a collaboration with Bracco, aiming to produce Monosize phospholipid-shell microbubbles in a reproducible and robust manner. With this device, microbubbles are produced using microfluidic flow-focusing technology, i.e. by focusing a gas thread between two liquid flows through a nozzle of a microfluidic chip. The gas thread destabilizes due to capillary instability and pinches off to produce microbubbles (Figure 1). Accurate control of the gas pressure, liquid flow and nozzle size allows producing highly calibrated microbubbles. A critical point of this technology is, however, to accurately control the liquid flow and gas pressure in the chip, which are very sensitive to the surface state of the glass chip, the presence of impurities and ambient temperature. For this purpose, the Bubble Counter was developed which counts and sizes the microbubble flow in the nozzle of the microfluidic chip in real-time during production.

Methods

The Bubble Counter consists of a laser and built-in microscope system allowing counting and sizing the microbubbles in real-time and control the phospholipid liquid flow and the gas pressure through a dedicated feedback loop system. Counting and sizing of microbubbles is performed directly in the nozzle of the chip using a violet laser beam (Figure 1). The laser beam is converted into a sheet by a custom optical bench and focused on the chip nozzle by the microscope lens. The microbubbles crossing the nozzle modulate the laser light that is collected by a photodiode whose signal is recorded on an integrated oscilloscope. The analysis of this signal allows determining different parameters such as bubble production frequency and bubble passing time, which, together with other known flow parameters such as liquid flow, laser sheet width and nozzle geometry, allow the calculation of the size of the bubbles produced in the nozzle.

The knowledge in real time of the size of the produced bubbles has allowed the implementation of a feedback loop driving the production. Any drift from the desired size is compensated by automatically adjusting the phospholipid liquid flow rate while the gas pressure is kept constant. The feedback loop ensures the monodispersity of microbubble production over a long period of time as well as the repeatability of the size of the produced bubbles for a given setpoint value.

Results

The Bubble Counter device is capable to produce monosize microbubbles with diameter between 8 and 12 μm measured by the laser (Figure 2A) which corresponds to a final size of about 2 times smaller after a stabilization period of 24 hours. The production rate reaches between 0.5 MHz and 1.5 MHz depending on the bubble size (i.e. between 0.5 and 1.5 million bubbles per second). Monosize microbubble samples were characterized (after stabilization) by Coulter Multisizer measurement (Figure 2B). The monodispersity was evaluated by the Geometric Standard Deviation (GSD) of the size distribution. Thus, microbubble samples were considered monodisperse when fulfilling the ad hoc criteria of $\text{GSD} \leq 1.1$. The robustness of the production controlled by the feedback loop was assessed and it was observed that, for a given setpoint, the size (after stabilization) of the produced samples showed a relative standard deviation lower than 5% in the range 3-5.5 μm and lower than 10% in the range 5.5-7 μm .

Conclusion

In conclusion, the Bubble Counter is a unique device aimed at improving the production of monosize microbubbles by real-time automated counting and sizing. A major advantage of the feedback loop is that it automatically controls the monodispersity of microbubble size over a long period of time, contrarily to manually controlled systems for which this has to be checked continuously. Our data demonstrate the robustness of this platform to generate monodisperse microbubbles over a large size ranging from 3.5 to 7 μm . These results could be exploited for the scale-up of microbubble production by integrating a parallelization of the microfluidic chips.

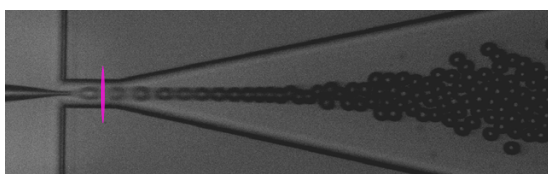


Figure 1: Microfluidic chip nozzle with the laser sheet.

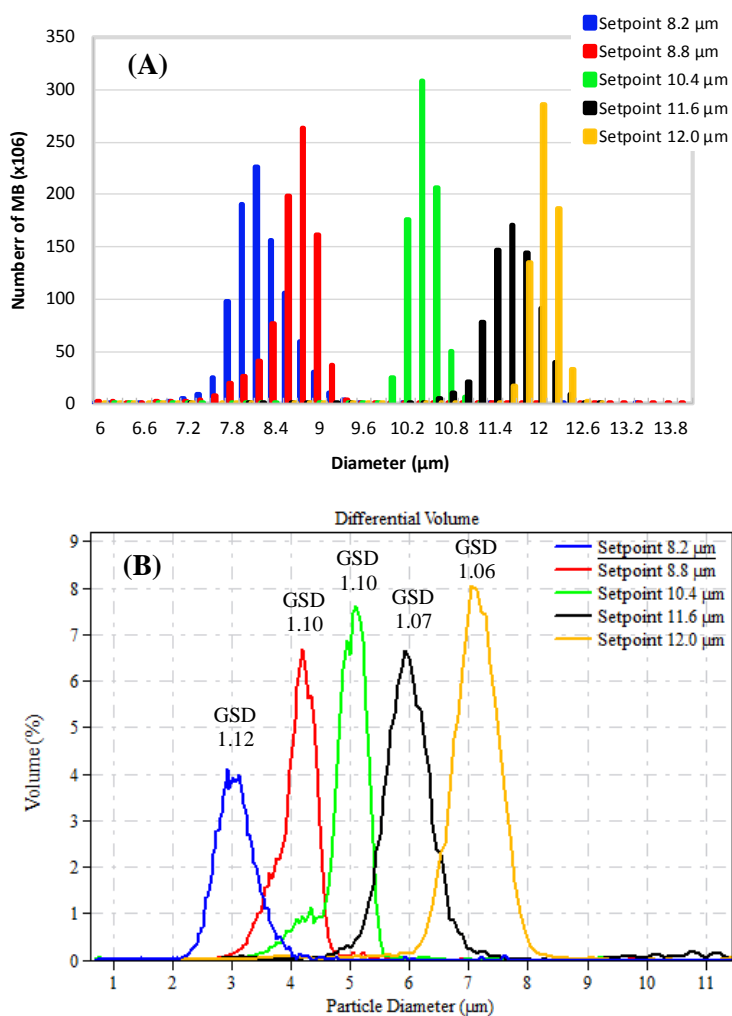


Figure 2: Microbubble size distributions for different size setpoints measured (A) on chip by the laser during production and (B) by Coulter Multisizer after 24h stabilization.

Blood flow patterns analysis in the left ventricle by dynamic contrast-enhanced ultrasound at low frame rates

P. Chen¹, R. J. G. van Sloun¹, S. Turco¹, H. Wijkstra^{1,2}, P. Houthuizen³, M. Misch¹

¹*Biomedical Diagnostics Lab, Eindhoven University of Technology, Eindhoven, the Netherlands*

²*Department of urology, Academic Medical Center University Hospital, Amsterdam, the Netherlands*

³*Department of cardiology, Catharina Hospital, Eindhoven, the Netherlands*

Corresponding author: p.chen1@tue.nl

Introduction

Heart-failure is one of the leading causes of death worldwide. About 5.7 million adults suffer from heart-failure in the United States [1]. Many cases are associated with cardiac dyssynchrony. In these cases, a clinically-proven treatment option is cardiac resynchronization therapy (CRT), which aims at improving pumping efficiency. Several clinical studies have also shown that impairment of the left ventricle (LV) function occurs at a very early stage in the course of heart-failure [2]. Therefore, recent guidelines give special emphasis on the diagnosis of LV dysfunction for management of heart-failure patients [3]. The ventricular function is strongly associated with blood flow patterns, that are determined by coordinated myocardial and valvular dynamics. Therefore, visualization of the spatial and temporal distribution of these patterns, aiding the diagnosis of LV dysfunction, has gained attention [2].

Current techniques for visualization of blood flow are typically based on speckle-tracking using ultrafast ultrasound acquisitions. High frame rates are required to spatially track the fast motion of blood. As a result, these techniques are not suitable for low frame-rate, as typical in e.g. 3D ultrasound imaging, as the speckle decorrelates significantly between frames [4]. To address this limitation, we propose a novel technique for the visualization of LV blood-flow patterns by dynamic contrast-enhanced ultrasound (DCE-US) at low frame rates. By this technique, the dynamic velocity vector field and the relative pressure in the LV are estimated, and flow features related to the LV pumping efficacy are then derived. A preliminary validation of the method was performed by comparing the estimated flow features on 18 patients (9 responders, 9 non-responders) before and after CRT.

Methods

Ultrasound acquisitions were performed at the Catharina Hospital (Eindhoven, the Netherlands) under approval granted by the local ethics committee. DCE-US imaging was performed with a Philips iE33 ultrasound scanner (Philips Healthcare, Andover, MA, USA), at a frame rate of 23 Hz and pixel spacing of about 0.4 mm in both directions.

The acquired 2D imaging data was pre-processed by a spatial Gaussian filter to reduce the impact of spatially incoherent noise [5]. An interpolation (time up-sampling) by a factor of 2 was performed to attain a virtual frame rate of 46 Hz.

Velocity vectors were estimated by combining time-delay estimates and inter-pixel distance vectors within a circular kernel [6, 7]. As shown in Fig. 1, time intensity curves (TICs) at each kernel point were extracted by collecting pixel intensities over time at a set of neighboring pixels. Time-delays are obtained by maximizing the cross-correlation between the obtained TICs. Since velocities vary considerably during the cardiac cycle, multiple (one per cardiac cycle) moving time windows are first applied to collect TIC samples from the same phase of subsequent cardiac cycles, determined by synchronized electrocardiography (see Fig.1). Finally, the time delay is estimated by maximizing the cross-correlation between the TICs obtained for each phase of the cardiac cycle. The window length determines the actual temporal resolution of the estimator. In this way, a higher temporal resolution is obtained by processing multiple cardiac cycles for the duration of the full TIC. Based on distance vectors between all pairs in the circular kernel, the velocity vector at a specific location can then be obtained. By moving the kernel across

the entire LV, the spatiotemporal velocity vector field is constructed. A regularization strategy based on the Navier-Stokes equation is then applied to mitigate the impact of noise on the velocity estimates [8]. The relative pressure is finally calculated from the regularized velocity vector field using the Navier-Stokes equation, which describes the motion of viscous fluid as a function of the relative pressure.

Flow features such as vorticity, changes in relative pressure (dp/dt) in the LV outflow tract, and viscous energy loss are then derived from the estimated velocity vector field and relative pressure. Blood flow patterns are characterized in terms of these features, as they reflect the ejection efficiency. Since the goal of CRT is improving pumping efficiency, we evaluated the proposed method by comparing the proposed flow features on 18 heart-failure patients (9 responders, 9 non-responders) who underwent CRT.

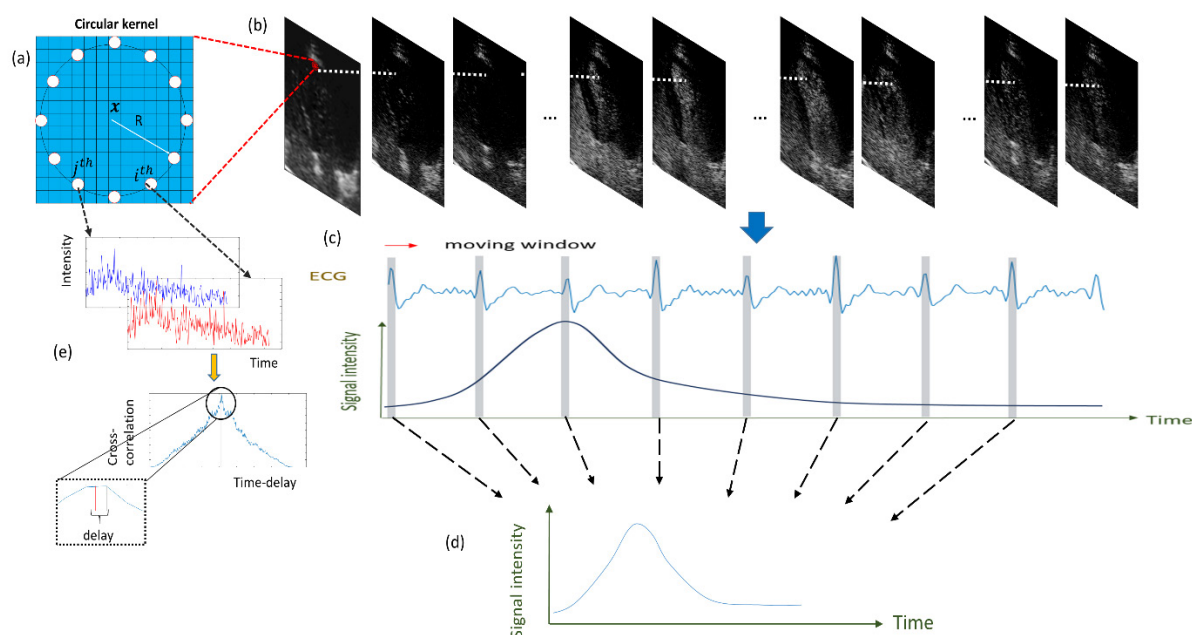


Fig. 1: An illustration of the time-delay estimation scheme: (a-b) TICs extraction by collecting pixel intensities along the DCE-US loop at each point of the circular kernel; (c-d), a moving window is used to collect TIC samples from the same phase of the cardiac cycle; (d) time-windowed TICs are obtained; (e) the time-delay is calculated by maximizing the cross-correlation between each pair of time-windowed TICs.

Results

The velocity vector field and relative pressure at four phases during the cardiac cycle are shown in Fig. 2. During diastole, a pressure gradient can be observed across the left atrium and ventricle. This pressure difference, generated by relaxation and deformation of the LV, accelerates the blood from the atrium into ventricle through the mitral valve, thereby forming a vortex. With the flow filling the LV, the pressure gradient decreases, and the initial pressure differences are reversed, decelerating and redirecting the flow. From late diastole to the isovolumetric contraction phase, a counterclockwise vortex appears in the central region of the LV close to the apex. The closer to the center of this vortex, the lower the pressure. During systole, the high pressure at the apex accelerates blood towards the aortic-valve region along the wall. With blood flowing out of the LV, the pressure gradient reverses at the end of systole.

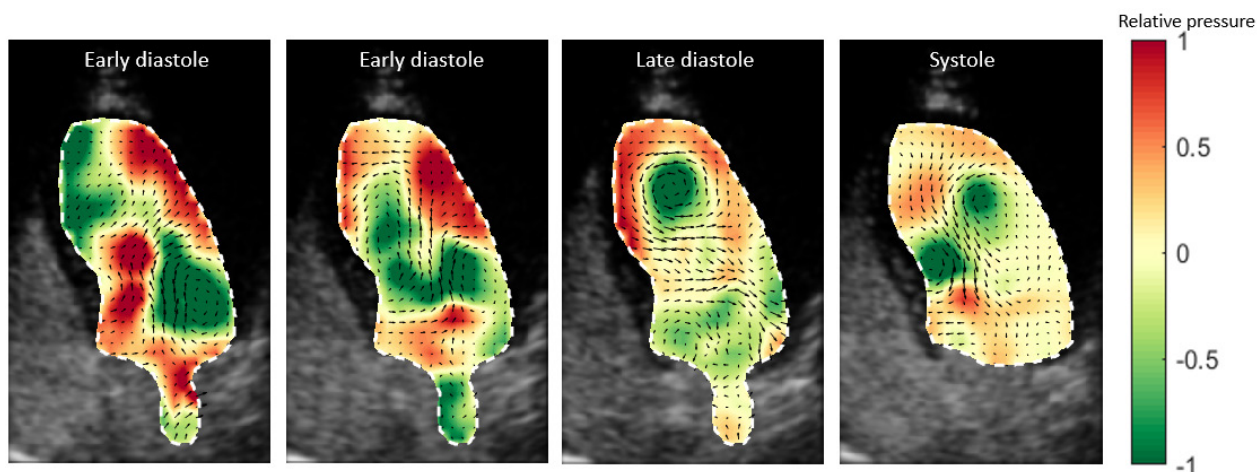


Fig. 2: Dynamic velocity vector field and relative pressure in the LV.

By analysing the obtained flow features, we observed that, after CRT, the responder group evidenced a significant ($p < 0.05$) increase in vorticity and peak dp/dt , and a non-significant decrease in viscous energy loss. No significant difference was found in the non-responder group. Relative feature variations before and after CRT evidenced a significant difference ($p < 0.05$) between responders and non-responders for all the features.

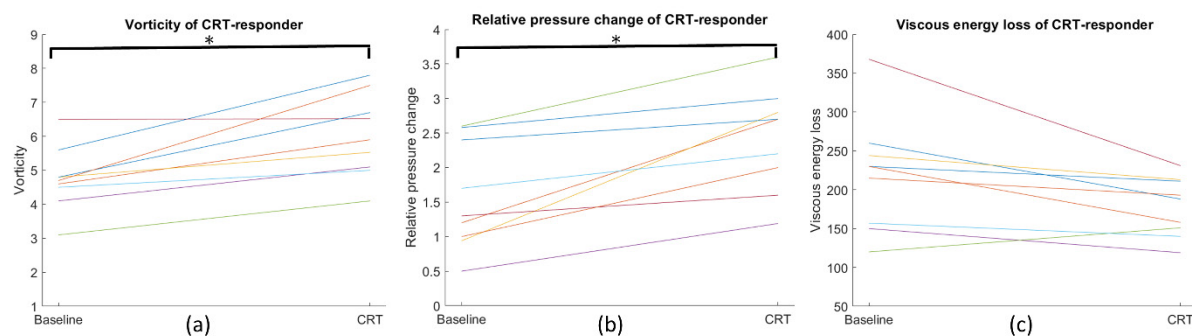


Fig. 3: Flow features for CRT responders at baseline and 3 months after treatment: (a) vorticity; (b) relative pressure change (peak dp/dt), and (c) viscous energy loss. Significant differences (p -value < 0.05) are indicated by an asterisk.

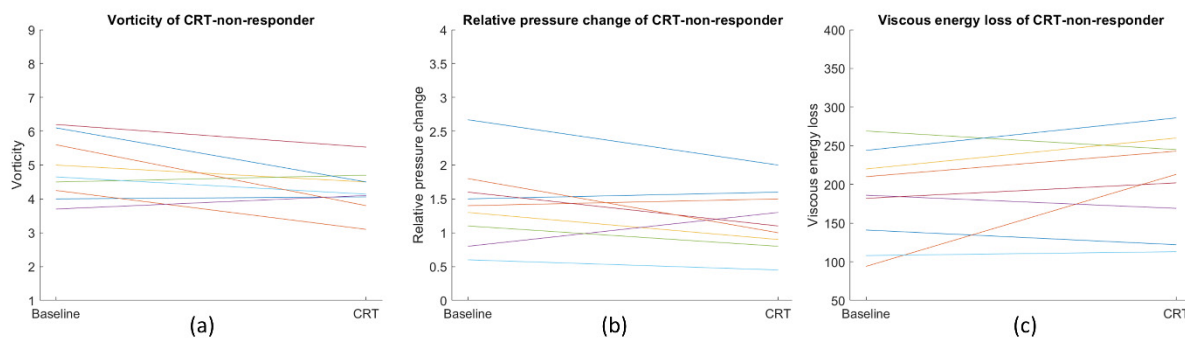


Fig. 4: Flow features for CRT non-responders at baseline and 3 months after treatment: (a) vorticity; (b) relative pressure change (peak dp/dt), and (c) viscous energy loss.

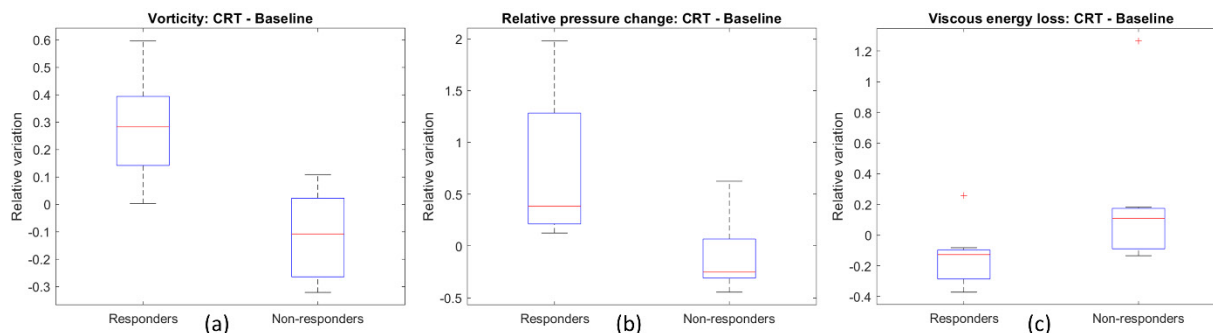


Fig. 5: Relative variation between baseline and 3 months after treatment for each flow feature in the responder and non-responder group: (a) vorticity; (b) relative pressure change (peak dp/dt), and (c) viscous energy loss. Relative variation for all these features are significant.

Conclusions

The proposed technique enables visualization and analysis of blood flow patterns by low-frame-rate DCE-US. It might represent a valuable option for 3D contrast-enhanced ultrasound, for which the volume rates are especially low. Our results also show the potential clinical value of the proposed method in the context of CRT.

In the future, the feasibility of the proposed method for 3D DCE-US will be investigated. Moreover, further validation of the method based on simulations with realistic heart model will also be performed.

References

- [1]. Mozzafarian D, et al, On behalf of the American Heart Association Statistics Committee and Stroke Statistics Subcommittee. Heart disease and stroke statistics-2016 update: a report from the American Heart Association., *Circulation*, 133: e38-e360, 2016.
- [2]. Cimino S, et al, In vivo analysis of intraventricular fluid dynamics in healthy hearts, *Eur. J. Mech. B/Fluids*, 35: 40-46, 2012.
- [3]. ESC Guidelines for the diagnosis and treatment of acute and chronic heart failure, *Eur. Heart J.*, 29: 2388-2442, 2008.
- [4]. Gao H, et al, left ventricular 2D flow pattern estimation of the heart by combining speckle tracking with Navier-Stokes based regularization, *Proc. IEEE Ultrason. Symp.*, 1068-1071, 2010.
- [5]. Bourne R, *Fundamentals of digital imaging in medicine*. Springer Science & Business Media, 2010.
- [6]. Van Sloun R.J.G., et al, Entropy of Ultrasound-Contrast-Agent velocity fields for angiogenesis imaging in prostate cancer, *IEEE Tran. Med. Imaging*, 36: 826-837, 2016.
- [7]. Van Sloun R.J.G., et al, Contrast-enhanced ultrasound tractography for 3D vascular imaging of the prostate, *Scientific Reports*, 2018
- [8]. Gao H, et al, 2-D left ventricular flow estimation by combining speckle tracking with Navier-Stokes-Based regularization: an in silico, in vitro and in vivo study, *Ultrasound Med. Biol*, 41: 99-113, 2015.

High Dynamic Range Non-linear Ultrasound Imaging

Jemma Brown¹ and Robert J. Eckersley¹.

¹ *Department of Biomedical Engineering, School of Biomedical Engineering and Imaging Sciences, King's College London, London SE1 7EH, U.K. (e-mail: jemma.brown@kcl.ac.uk; robert.eckersley@kcl.ac.uk).*

Introduction

The non-linear response of microbubbles (MBs) provides the opportunity to extract the MB signal from surrounding tissue using non-linear processing techniques. Previously, several methods have been proposed to exploit this potential [1]. Since the non-linear components of the MB signals are much weaker than the linear, the receive gain of the ultrasound US system must be high to capture the non-linear response. However, this can cause the signal from strong tissue scattering to become saturated and then breakthrough the filtering process. This is a common problem in commercial ultrasound systems, with the saturated signal appearing as bright structures in the contrast enhanced image. In this work a simple high dynamic range (HDR) acquisition strategy for non-linear imaging is proposed.

Methods

The non-linear MB signal is isolated through the combination of sequential frames acquired at the maximum system gain (high gain) and frames acquired the highest gain before saturation occurs (low gain). The received low gain signal is amplified during post processing and the data lost due to saturation of the high gain pulse replaced with that from the low gain acquisition. Amplitude modulation [2] is then applied to the reconstructed data to extract the MB signal without being limited by the saturation.

This was tested in-silico. k-Wave, a simulation package used to model acoustic wave propagation in tissue [3], has been combined with the Marmottant model [4] of microbubble dynamics to simulate 2D plane wave ultrasound images received with different gains. Improvement to images of a region of contrast and superficial fat and muscle layers was quantified using contrast to tissue (CTR) and contrast to acoustic noise ratio (CANR) values.

Improvement using the technique was also quantified in vitro using a 200 μm copper wire provided a strong linear scatterer approximately 20 mm from the probe. A diluted solution of SonovueTM (Bracco) MBs was drawn through a 200 μm cellulose tube using a syringe pump at a range of 30 $\mu\text{l}/\text{min}$. Plane wave ultrasound data was acquired using the programmable ULA-OP system (MSD Lab, University of Florence) [5]. A pulse repetition frequency of 4kHz was used to ensure as little MB flow between frames as possible. The pulse sequence $[A_{\text{low_gain}}, -A_{\text{low_gain}}, (A/2)_{\text{low_gain}}, A_{\text{high_gain}}, -A_{\text{high_gain}}, (A/2)_{\text{high_gain}}]$ where A is the pulse amplitude.

Results

Figure 1 shows the simulation geometry and an example of the improvement possible using this HDR technique in silico. Figure 1(A) shows an impedance map of the tissue structures and the positions of the MB contrast region and transducer. Layers of fat and muscle generated strong linear reflections which are saturated upon receive. Figure 1(B) shows that using high gain generates a stronger contrast signal from the MBs compared to the low gain image on the left. However, the regions defined within the white rectangles show the artefact introduced due to signal saturation. The right-hand column presents the HDR image where the strong contrast signal is captured, without the saturation artefact.

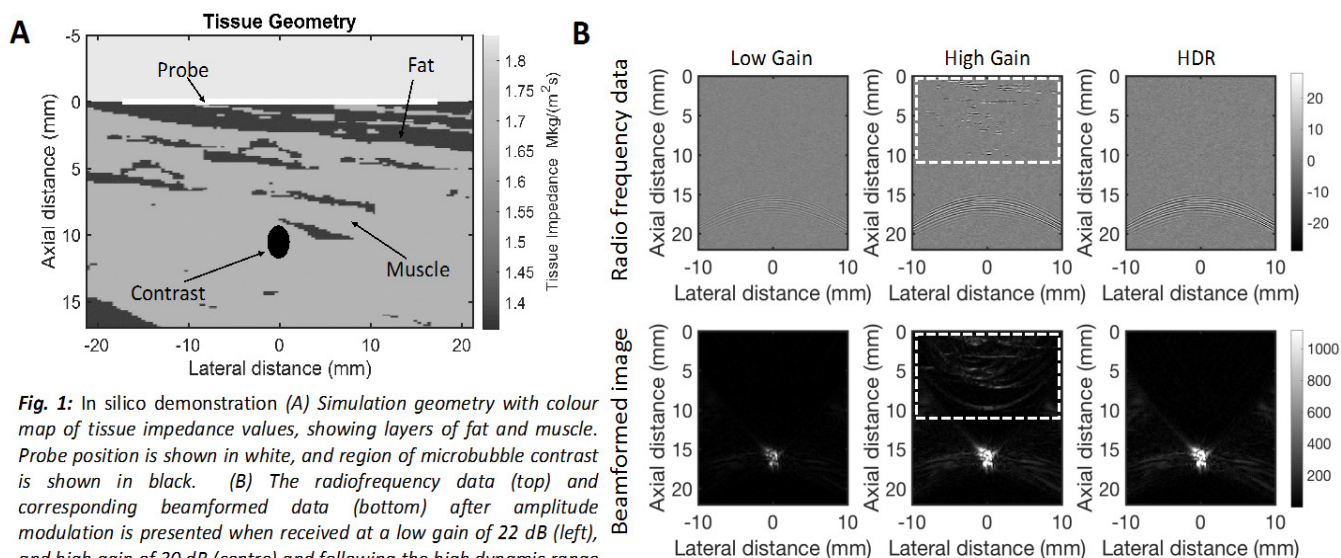


Fig. 1: In silico demonstration (A) Simulation geometry with colour map of tissue impedance values, showing layers of fat and muscle. Probe position is shown in white, and region of microbubble contrast is shown in black. (B) The radiofrequency data (top) and corresponding beamformed data (bottom) after amplitude modulation is presented when received at a low gain of 22 dB (left), and high gain of 30 dB (centre) and following the high dynamic range processing (right). The areas enclosed by the white rectangles show where error due to image saturation occurs.

The in vitro results showed a mean 9.3 dB increase in CTR for HDR images compared to those filtered with AM using the high gain data and a 29% average increase in CANR for HDR images compared to those filtered using the low gain data.

Conclusions

Overall, the problem of visualising MB non-linear signal, without saturation of strong linearly scattering structure, has not previously been sufficiently addressed for contrast enhanced ultrasound imaging. This proposed method does not affect MB behaviour as transmit pulse is unchanged, can be easily implemented on existing systems and, despite its simplicity, can significantly improve image quality.

References

- [1]. Phillips, P. Contrast pulse sequences (CPS): imaging nonlinear microbubbles. in Ultrasonics Symposium, 2001 IEEE. 2001. IEEE.
- [2]. Brock-Fisher, G.A., M.D. Poland, and P.G. Rafter, Means for increasing sensitivity in non-linear ultrasound imaging systems. 1996, Google Patents.
- [3]. Treeby, B. E., Jaros, J., Rendell, A. P., & Cox, B. (2012). Modelling nonlinear ultrasound propagation in heterogeneous media with power law absorption using a k-space pseudospectral method. The Journal of the Acoustical Society of America, 131(6), 4324-4336.
- [4]. Marmottant, P., van der Meer, S., Emmer, M., Versluis, M., de Jong, N., Hilgenfeldt, S., & Lohse, D. (2005). A model for large amplitude oscillations of coated bubbles accounting for buckling and rupture. The Journal of the Acoustical Society of America, 118(6), 3499-3505.
- [5]. Tortoli, P., et al., ULA-OP: An advanced open platform for ultrasound research. IEEE transactions on ultrasonics, ferroelectrics, and frequency control, 2009. 56(10): p. 2207-2216.

Repeatability of contrast enhanced ultrasound to measure cerebral blood flow using the middle cerebral artery as a reference

A. J. Kortenbout^{1,2}, A.W.J. Scholten^{1,2}, E.J. Vinke³, G.P.R. Lajoinie², S.A.J. Engelhard², J. Eyding⁴, C. L. de Korte^{2,5}, C.H. Slump⁶, M. Versluis², J.G. van der Hoeven¹, R. van Kaam¹, C.W.E. Hoedemaekers¹

¹Intensive Care, Radboud University Medical Centre, Nijmegen, the Netherlands

²Physics of Fluids group, Technical Medical (TechMed) Centre, University of Twente, Enschede, The Netherlands

³Department of Radiology and Nuclear Medicine, Erasmus MC, Rotterdam, The Netherlands

⁴Department of Neurology, Klinikum Dortmund gGmbH, Dortmund, Germany

⁵MUSIC, Radboud University Medical Centre, Nijmegen, the Netherlands

⁶Robotics and Mechatronics, University of Twente, Enschede, the Netherlands

Corresponding author: Astrid.Hoedemaekers@Radboudumc.nl

Introduction

In patients with acute brain injury, optimal cerebral perfusion and oxygenation is necessary. Therefore, adequate cerebral blood flow (CBF) is essential. [1] Contrast enhanced ultrasound (CEUS) is a promising technique for bedside quantification of CBF. However, previous research showed that intra- and inter individual variability in the measurements was high. [2] One of the possible causes of variation, might be the distance travelled by the ultrasound contrast agent (UCA). [3] When arrival of the UCA in the middle cerebral artery (MCA) is taken as reference for measurement of CBF in the microcirculation, this systemic blood flow derived source of variability may be reduced. We investigated whether repeatability of CEUS quantification of CBF in the microcirculation improves by using the MCA as a reference for arrival of UCA. We also investigated the influence of the injection rate and dose of UCA and of changes in CBF on repeatability in vitro.

Methods

We performed a post-hoc analysis of data derived from a previously published study to measure feasibility and repeatability of CEUS for the quantification of CBF in vivo. [2] CEUS was performed 3 times in 10 healthy volunteers. In the CEUS measurements, 3 regions of interest (ROIs) were selected in the microcirculation and the MCA was selected as reference (figure 1). In these regions, time intensity curves (TICs) were created. The coefficient of variation (CV), defined as standard deviation divided by the mean, expressed as % of the mean, was calculated for both the standard perfusion parameters and several time difference parameters, with MCA as reference (figure 2). For the in-vitro measurements, an in-vitro flow phantom simulated the circulation from peripheral bubble injection towards the internal carotid artery (ICA), whereafter it divided into the MCA, and other vessels. Dual probe imaging with a Verasonics (Vantage 256) machine was performed of the ICA and MCA. Different contrast injection rates, dosages and CBFs were studied and the CVs were calculated.

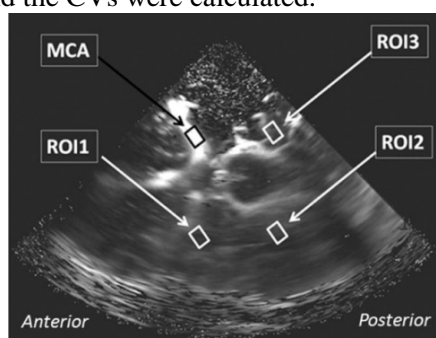


Figure 1: An transcranial contrast enhanced ultrasound image of the mesencephalic plane, MCA = middle cerebral artery, ROI = Region of Interest [2]

Results

The results of the in-vivo data are presented in figure 2. The CV of the time-related parameter time of peak intensity (T_{pi}) was lowest (median CV of 8.2%). The CV of the other time-related parameter time to peak (TTP) was relatively low as well (median CV of 17.7%). The time difference between arrival of UCA in the MCA and the peak intensity of the ROI in the microcirculation, (TD) had the highest repeatability of the time difference parameters (CV below 15%). Since T_{pi} measures the time between injection to peak intensity, this parameter is highly influenced by cardiac output or the dispersion of UCA in the large central circulation. [4] TTP is a more representative measurement, since it is calculated with the arrival of the UCA in the ROI as reference. This suggest that using a different reference point for arrival of the UCA in the ultrasound field, might improve repeatability.

The in-vitro results show that the injection rate of 0.125 mL/s with an dosage of 1 mL had the lowest CV with a maximal CV of 15% for the ICA and 10% for the MCA. Normal CBF (10 ml/s) had the lowest CVs, with the PI being the most reliable parameter. However, we observed large differences in CVs with the chosen combination of injection rate and dosage when varying the CBF. In addition, we did not observe a pattern in these results, because the CVs inconstantly changed with increasing and decreasing the flow.

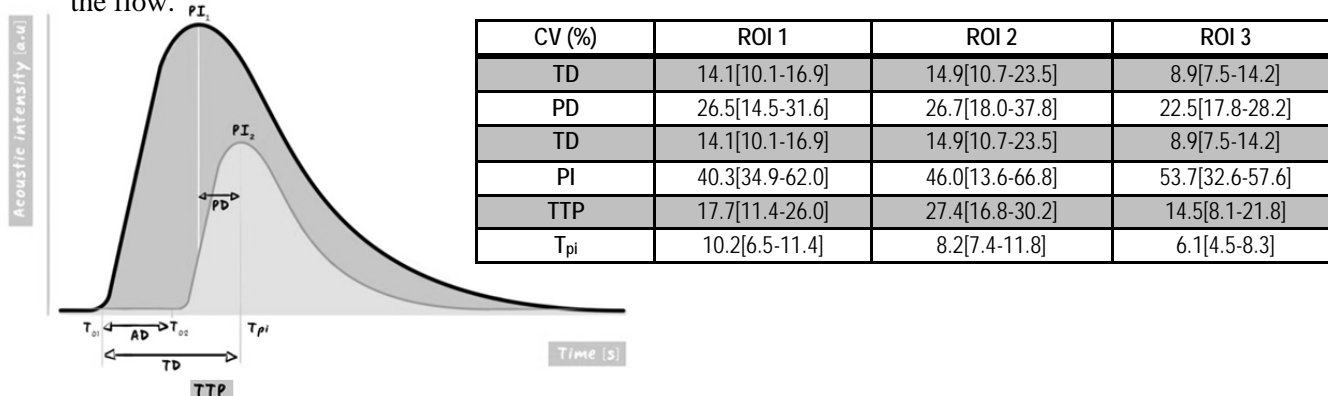


Figure 2 Left: the dark time intensity curve (TIC) is of MCA as reference and the lighter TIC is of a region of interest in the microcirculation. PI indicates peak intensity of both TICs, T_0 is de arrival of ultrasound contrast agent. TD is the time difference between T_{01} and PI of microcirculation. PD is the time difference between both PI and AD is the time difference between both T_0 . TTP is the time difference between T_0 and time of PI (T_{pi}) [5] Right: Coefficient of variation (CV) of parameters in the different regions. Data are expressed as the median value with interquartile ranges

Conclusions

CEUS has the potential to measure CBF at the bedside. When the MCA is used as a reference for measurement of CBF in the microcirculation, repeatability improved in vivo. The injection rate and dosage of microbubbles are an important modulator of the variability of CEUS. In addition, differences in flow seem to strongly influence the optimal injection speed and dose, thus contributing to the high rate of variability. Therefore, we conclude that there is a significant interaction between flow, speed of injection and dose of microbubbles. Further studies are necessary to elucidate this interaction to optimise the validity of CEUS.

References

- [1]. Dagal, A. and A.M. Lam, Cerebral blood flow and the injured brain: how should we monitor and manipulate it? *Curr Opin Anaesthesiol*, 2011. 24(2): p. 131-7.
- [2]. Vinke, E.J., et al., Repeatability of Bolus Kinetics Ultrasound Perfusion Imaging for the Quantification of Cerebral Blood Flow. *Ultrasound in Medicine & Biology*, 2017. 43(12): p. 2758-2764.
- [3]. Tang, M.X., et al., Quantitative contrast-enhanced ultrasound imaging: a review of sources of variability. *Interface Focus*, 2011. 1(4): p. 520-39.
- [4]. Wei, K., et al., Quantification of Myocardial Blood Flow With Ultrasound-Induced Destruction of Microbubbles Administered as a Constant Venous Infusion. *Circulation*, 1998. 97(5): p. 473-483
- [5]. de Vries, A.L.E. Drawing of time intensity curve. Quantification of cerebral blood flow with contrast enhanced ultrasound, Master-thesis A.J. Kortenbout University of Twente - Radboudumc, 26-01-2018

Motion Compensation for High Frame-rate Contrast-enhanced Echocardiography using Diverging Waves

Luzhen Nie¹, David M. J. Cowell¹, Thomas Carpenter¹, James R. McLaughlan^{1,2},
Arzu A. Çubukçu³, and Steven Freear¹

¹*School of Electronic and Electrical Engineering, University of Leeds, Leeds, LS2 9JT, U.K.*

²*Leeds Institute of Cancer and Pathology, University of Leeds, Leeds, LS9 7TF, U.K.*

³*East Cheshire NHS Trust Macclesfield, SK10 3BL, U.K.*

Corresponding author: l.nie@leeds.ac.uk and s.freear@leeds.ac.uk

Introduction

Ultrasound imaging constitutes an important aid for diagnosis of cardiac dysfunction. It is advantageous over other imaging modalities, such as CT and MRI, being relatively cheap and easily accessible. The list of its applications is expanding to encompass a wider range of diagnostic information including 2-D or 3-D blood flow estimation, elasticity of the myocardium, wall motion and myocardial perfusion with microbubbles. Instead of using sequential focused beams to form the image line by line, a B-mode image can be reconstructed by transmitting a single diverging wave. The image contrast and resolution can be improved at the receiving side by coherent summation of echoes from multiple transmissions. Diverging wave imaging thus allows for a high frame rate (HFR) up to 6 kHz which is two orders of magnitude faster than the most clinical scanners. This HFR capability underpins a number of novel techniques, such as transient shear wave elastography, intracardiac flow velocimetry and coupling myocardium and vortex dynamics, for better understanding of cardiac function. However, spatial coherent compounding of diverging waves is susceptible to tissue motion artifacts as highlighted in [1]. Doppler-based methods have been proposed to compensate for motion between multiple diverging wave transmissions prior to compounding, but the maximum velocity without aliasing is bound to $cPRF/4f_0$ [1], where c indicates the speed of sound and f_0 is the center frequency of the ultrasound pulse. This threshold could be small compared to the blood flow in the left ventricle (LV) when correction of microbubble motion is needed in HFR contrast-enhanced echocardiography (CEE) using diverging waves [2]. Image registration algorithms such as the one adapted from MRI have been used to correct motion artifacts in coherent diverging wave imaging in [2]. As opposed to image registration, the correlation-based motion tracking method could be also used for motion estimation and compensation in HFR CEE using diverging waves. In this study, a correlation-based method for 2-D motion compensation was proposed for HFR CEE, and compared to the state-of-the-art image registration method. The motion estimation field for compensation was then further processed to render flow vectors in the LV, allowing for a triplex cardiac imaging technique, consisting of B mode, contrast mode and 2-D vector flow imaging with a HFR of 250 Hz.

Methods

A. Imaging Setup

The pulsing scheme for diverging wave imaging was adapted from [1]. The 4-cycle 2.78 MHz ultrasound pulses with either a full or half amplitude were transmitted, emulating diverging waves using the full aperture at each steering angle and enabling amplitude modulation (AM) for contrast enhanced imaging. The sector angle which was determinant to the imaging field of view was set to 90° and unchanged during beam steering for compounding. The arrangement of the steering angles was (-10°, -8°, -6°, -4°, 4°, 6°, 8°, 10°). The University of Leeds Ultrasound Array Research Platform II (UARP II) equipped with a phased array transducer P4-2v (Verasonics, Inc., WA, USA) was used for *in vivo* measurements with a MI of 0.12 and a PRF of 4 kHz.

B. Motion Estimation and Compensation

The proposed motion estimation algorithm used the correlation between angled diverging waves. A two-stage method was developed to find the correlation and subpixel displacement between angled low-resolution images (LRIs) in the polar coordinate system. The first stage used rigid block matching with correlation correction, achieved by multiplying all available correlation maps from the successive LRI pairs in the set for coherent summation. The second stage used an iterative scheme to improve the resolution and accuracy of the motion estimation by recursively decreasing the kernel size and deforming the kernel based on the results in the previous iteration. The number of iterations was set to two in this study, with different kernel sizes in each stage. The resultant motion estimation in each pixel was then obtained by linearly interpolating the motion estimation results from the last iteration of motion estimation. Based on these estimated displacements, motion compensation was then performed by aligning image pixels of all LRIs prior to coherent compounding. All LRIs with motion were heuristically registered to the first LRI within the set that is used for coherent compounding. For comparison, the image registration model [2, 3] was also applied to the LRIs in the polar grid before coherent summation. During image registration, the default parameters for 2-D images [4] were used.

Results

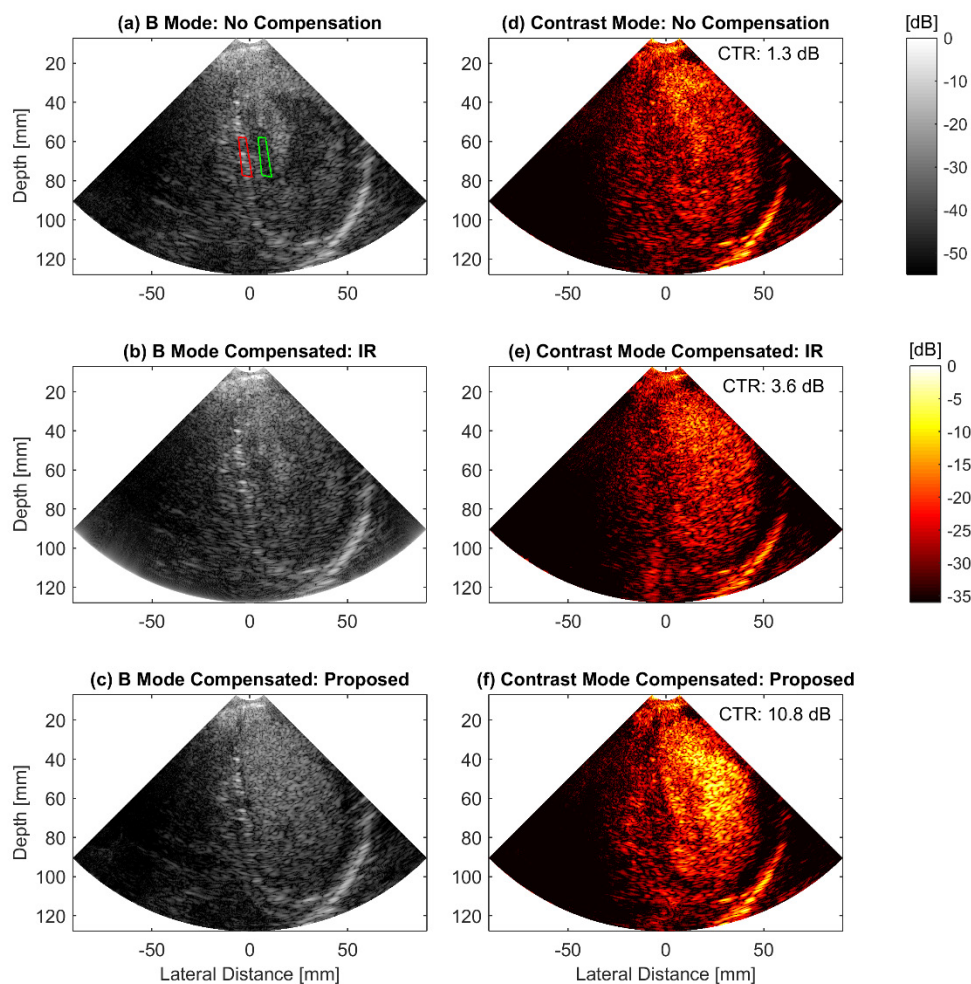


Fig. 1. Typical B-mode and AM contrast-mode compound images. (a) and (d): no motion compensation. (b) and (e): motion compensated using image registration (IR) techniques. (c) and (f): motion compensated using the proposed method.

The quality of the *in vivo* cardiac images was improved when integrated with motion compensation (Fig. 1). The effect of motion compensation was first manifest on B-mode images. For example, without

the use of motion compensation, the microbubbles appeared to be unevenly distributed in the LV, resulting in a total dark region in the vicinity of the septum (Fig. 1a). However, when using motion compensation it is clear that the microbubbles were present throughout the LV (Fig. 1c). With motion correction using the image registration technique, coherent diverging wave compounding was partially improved, with the dark region reduced as shown in Fig. 1b. Whist with the proposed method, the artifacts from the original B-mode image were totally removed without any smearing of the image as shown in Fig. 1(c). The contrast-to-tissue ratio (CTR) between the LV (green box in Fig. 1a) and the surrounding tissue region (red box in Fig. 1a) was calculated for Fig. 1(d), (e) and (f). The proposed method in this study outperforms the image registration technique, with the enhanced delineation of the endocardial border thanks to the improvement of the CTR in Fig. 1(f) (10.8 dB compared to 3.6 dB in Fig. 1e).

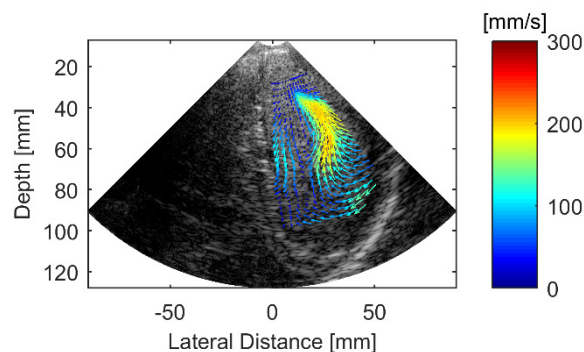


Fig. 2. Composite image of the LV by superimposing flow vectors onto its corresponding B-mode image.

The motion estimation field used for motion compensation in Fig. 1 (f) was encoded to interpret 2-D blood flow vectors in Fig. 2. It demonstrates that the blood flow achieves its maximum at the regions corresponding to the dark regions in Fig. 1 (a) and (c), highlighting the necessity of development of methods for motion compensation in HFR CEE when using diverging waves.

Conclusions

The present study described the implementation of a correlation-based method for correcting motion artifacts in HFR CEE using diverging waves. Motion estimation was performed between angled LRIs prior to compounding and the estimated displacement field was used to counter-shift the motion to achieve coherent summation. Compared against the image registration method, the improved image quality in terms of CTR for AM contrast-mode compound images was quantitatively demonstrated. The combination of the encoded 2-D motion field enabled a multi-modality cardiac imaging tool by providing B-mode, contrast-mode and vector flow mapping simultaneously with a HFR of 250 Hz. Deciphering the interconnection between the simultaneous information (e.g., wall motion, vortex dynamics and myocardial perfusion) obtained from these three imaging modes could be of clinical relevance for early diagnosis of cardiac dysfunction.

References

- [1]. Porée, Jonathan, et al. "High-frame-rate echocardiography using coherent compounding with Doppler-based motion-compensation." *IEEE transactions on Medical Imaging* 35.7 (2016): 1647-1657.
- [2]. Toulemonde, Matthieu, et al. "Effects of motion on high frame rate contrast enhanced echocardiography and its correction." *Ultrasonics Symposium (IUS), 2017 IEEE International*. IEEE, 2017.
- [3]. Rueckert, Daniel, et al. "Nonrigid registration using free-form deformations: application to breast MR images." *IEEE transactions on Medical Imaging* 18.8 (1999): 712-721.
- [4]. <https://uk.mathworks.com/matlabcentral/fileexchange/20057-b-spline-grid-image-and-point-based-registration>.

3D Super-Resolution Ultrasound Imaging *In Vitro* using a 2D Sparse Array

Sevan Harput¹, Kirsten Christensen-Jeffries², Jemma Brown², Jiaqi Zhu¹, Ge Zhang¹,
Chee Hau Leow¹, Matthieu Toulemonde¹, Alessandro Ramalli^{3,4}, Enrico Boni³,
Piero Tortoli³, Robert J. Eckersley^{2*}, Christopher Dunsby^{5*} and Meng-Xing Tang^{1*}

¹Dept. of Bioengineering, Imperial College London, UK

²Dept. of Biomedical Eng., School of Biomedical Eng. & Imaging Sciences, King's College London, UK

³Department of Information Engineering, University of Florence, 50139 Florence, IT

⁴Lab. on Cardiovascular Imaging & Dynamics, Dept. of Cardiovascular Sciences, KU Leuven, Belgium

⁵Dept. of Physics and Centre for Pathology, Imperial College London, London, UK

*These authors contributed equally to this work

Email: S.Harput@imperial.ac.uk, Mengxing.Tang@imperial.ac.uk

Introduction

The development of high speed programmable ultrasound systems and 2D arrays created new opportunities for 3D ultrasound imaging with high spatio-temporal resolution. Several research groups has adapted these developments to super resolution ultrasound (SR US) imaging and achieved 3D imaging by mechanically scanning a volume with a linear probe, by co-aligning multiple linear probes, by using multiplexed 3D clinical US systems, or by using 3D US research systems [1-5]. With the implementation of 3D SR US imaging using a 2D, existing limitations of 2D super-resolution imaging such as elevational resolution and 3D motion compensation can be overcome [6-8]. In this work, a 2D sparse array at a lower frequency closer to microbubble resonance was used to achieve SR in 3D [9,10]. Volumetric US imaging with plane waves was performed and experimental results of 3D SR US imaging are demonstrated.

Methods

The 2D sparse array was specifically fabricated for 3D SR US with an element size of 300 x 300 μm , center frequency of 3.7 MHz and a bandwidth of 60%. The sparse array was designed by selecting 512 elements from a 32 x 35 gridded layout of a 2D matrix array (Vermon S.A., Tours, France) shown in Figure (left) below. Two ULA-OP256 systems were synchronized to transmit 9 plane waves steered within a range of ± 10 degrees in the lateral and elevational directions from the 512 selected elements. Each compounded volume consisted of 9 volumetric datasets acquired in 3.6 ms at 2500 Hz PRF. A 1:1000 diluted Sonovue (Bracco S.p.A, Milan, Italy) solution was flowed through two 200 μm tubes arranged in a double helix shape. A total of 3000 volumetric US frames were acquired in 120 seconds and 3D localization of microbubbles were performed on every frame to generate the 3D super-resolved volumes. Singular value decomposition was used to separate the microbubble signals from the echoes originating from the tube.

Results

Figure (right) shows the volumetric B-mode and 3D SR US image of the sub-wavelength structures, where the imaging wavelength is 404 μm in water. A total of 2319 microbubbles were localized within the 3000 volumes after compounding. 3D SR US images are plotted with depth information color-coded in the image. The FWHM of a single tube appeared as 234 μm at the widest point and 117 μm at the thinnest point. When rotated to the best viewing angle, 81% of the super-localizations were within a diameter of 200 μm .

Conclusions

The main limitation of localization-based SR US imaging performed in 2D is the lack of super-resolution in the elevation direction. In this study, this issue was addressed by using a bespoke 2D sparse array, which achieved super-resolution in the elevational direction and sufficient SNR for 3D SR US

imaging. Two 200 μm , smaller than half wavelength, tubes were resolved in 3D using the 2D spiral array probe.

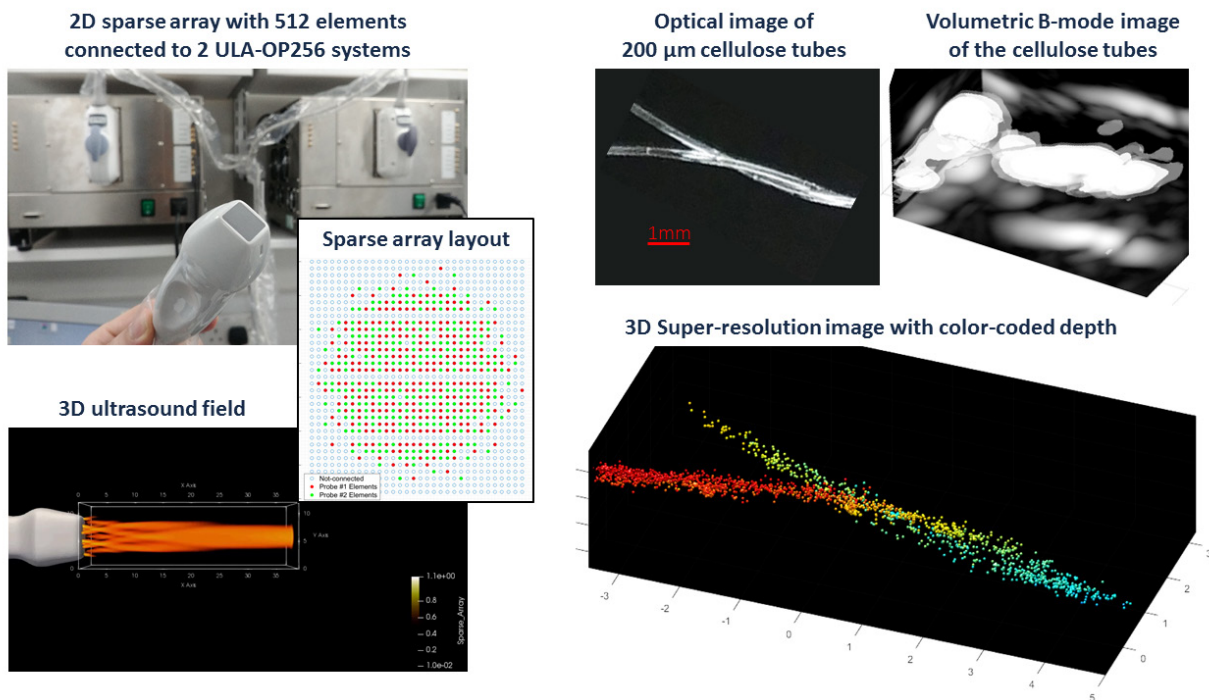


Figure (Left) shows the 2D sparse array with 512 elements and the radiated 3D ultrasound field from the sparse array while plane wave imaging. The sparse array layout is shown in the inset. (Right) shows the optical image of the 200 μm tubes, the corresponding volumetric B-mode image and the 3D super-resolution image. The super-resolution image is color coded with the depth information and zoomed in 200%.

References

- [1]. M. A. O'Reilly and K. Hynynen, "A super-resolution ultrasound method for brain vascular mapping," *Medical Physics*, vol. 40, no. 110701, 2013.
- [2]. Y. Desailly, O. Couture, M. Fink, and M. Tanter, "Sono-activated ultrasound localization microscopy," *Applied Physics Letters*, vol. 103, no. 174107, 2013.
- [3]. C. Errico, J. Pierre, S. Pezet, Y. Desailly, Z. Lenkei, O. Couture, and M. Tanter, "Ultrafast ultrasound localization microscopy for deep superresolution vascular imaging," *Nature*, vol. 527, pp. 499–507, 2015.
- [4]. F. Lin, S. E. Shelton, D. Espindola, J. D. Rojas, G. Pinton, and P. A. Dayton, "3-d ultrasound localization microscopy for identifying microvascular morphology features of tumor angiogenesis at a resolution beyond the diffraction limit of conventional ultrasound," *Theranostics*, vol. 7, no. 1, pp. 196–204, 2017.
- [5]. K. Christensen-Jeffries, J. Brown, P. Aljabar, M.-X. Tang, C. Dunsby, and R. J. Eckersley, "3-d in vitro acoustic super-resolution and superresolved velocity mapping using microbubbles," *IEEE Trans. Ultrason., Ferroelectr., Freq. Control*, vol. 64, no. 10, pp. 1478–1486, 2017.
- [6]. S. Harput, K. Christensen-Jeffries, Y. Li, J. Brown, R. J. Eckersley, C. Dunsby, and M.-X. Tang, "Two stage sub-wavelength motion correction in human microvasculature for ceus imaging," in *IEEE International Ultrasonics Symposium (IUS)*, 2017, pp. 1–4.
- [7]. S. Harput, K. Christensen-Jeffries, J. Brown, Y. Li, K. J. Williams, A. H. Davies, R. J. Eckersley, C. Dunsby, and M. Tang, "Two-stage motion correction for super-resolution ultrasound imaging in human lower limb," *IEEE Trans. Ultrason., Ferroelectr., Freq. Control*, vol. 65, no. 5, pp. 803–814, 2018.
- [8]. O. Couture, V. Hingot, B. Heiles, P. Muleki-Seya, and M. Tanter, "Ultrasound localization microscopy and super-resolution: A state of the art," *IEEE Trans. Ultrason., Ferroelectr., Freq. Control*, vol. 65, no. 8, pp. 1304–1320, 2018.
- [9]. A. Ramalli, E. Boni, A. S. Savoia, and P. Tortoli, "Density-tapered spiral arrays for ultrasound 3-d imaging," *IEEE Trans. Ultrason., Ferroelectr., Freq. Control*, vol. 62, no. 8, pp. 1580–1588, 2015.
- [10]. S. Harput, K. Christensen-Jeffries, J. Brown, J. Zhu, G. Zhang, C. H. Leow, M. Toulemonde, A. Ramalli, E. Boni, P. Tortoli, R. J. Eckersley, C. Dunsby, and M.-X. Tang, "3-d super-resolution ultrasound imaging using a 2-d sparse array with high volumetric imaging rate," in *IEEE International Ultrasonics Symposium (IUS)*, 2018, pp. 1–4.

Development of a long-circulating ultrasound contrast agent

*Ryo Suzuki¹, Johan Unga¹, Daiki Omata¹, Lisa Munakata, Tadamitsu Shima¹
Saori Kageyama¹, Yuno Suzuki¹, Emma Ydamar Marin Essis^{1,2}, Kazuo Maruyama¹*

¹Laboratory of Drug and Gene Delivery System, Faculty of Pharma-Science
Teikyo University, Tokyo, Japan

²School of Pharmacy, Utrecht University, Utrecht, Netherland
Corresponding author: r-suzuki@pharm.teikyo-u.ac.jp

Introduction

Ultrasound (US) imaging is comparatively inexpensive, minimally invasive and provide real-time visualization. It is important to understand the vascular structure of tumor tissue. However, it is difficult to take the US imaging of blood flow in small vessel of tumor tissue. To solve this, microbubbles as US contrast agents have been developed. In Japan, the contrast agent Sonazoid is approved. It is applied for diagnostics of liver cancer as negative staining by being uptaken by kupffer cells in the liver, but not in tumor. However, because the blood clearance of Sonazoid is fast due to the liver accumulation, it would not be suitable for other tumors and disorders. In this study, we tried to develop novel microbubbles for long circulation to observe dynamics of blood flow.

Methods

Preparation of Lipid Bubbles (LB): Bubbles were prepared from liposomes of distearoyl phosphocholine (DSPC), distearoyl phosphatidylglycerol (DSPG) and 1,2 - distearoyl - sn- glycerol - 3-phosphoethanolamine - N - [methoxy (polyethylene glycol) - 2000] (DSPE-MPEG(2k)), which were homogenized together with perfluoropropane (C₃F₈) gas. Then, the bubbles were freeze-dried and rehydrated before use.

Assessment of stability of LB in blood Mice: (ddY, female, 6 weeks), anesthetized with isoflurane, were intravenously administrated LB or Sonazoid (1×10^7 particles / 20 μ L). Then the stability in blood was assessed by comparing intensity of US imaging in kidney. The intensity of US imaging was analyzed with ImageJ software. Then, the time until half of maximum intensity ($T_{1/2}$) was calculated.

Results

$T_{1/2}$ increased with increasing DSPG content. The longest $T_{1/2}$ was achieved with LB containing 60 mol% DSPG, $T_{1/2}$ of LB containing 90% DSPG was shorter compared to LB containing 60% DSPG. In addition, we compared $T_{1/2}$ in kidney between LB containing 60% DSPG and Sonazoid. $T_{1/2}$ of LB containing 60% DSPG was longer than that of Sonazoid. From these results, it was thought that LB containing 60% DSPG could escape from the reticuloendothelial system such as liver.

Conclusions

We succeeded to develop the long circulating microbubble by adding DSPG to the shell of LB. There was optimal ratio of DSPG content of 60 mol%. We expect that our long circulating LB could be a useful for US diagnostics for various types of tumors where Sonazoid is not applicable.

Acknowledgements

This research was partially supported by the MEXT-Supported Program for the Strategic Research Foundation at Private Universities and the Strategic Research Program for Brain Sciences from Japan Agency for Medical Research and Development.

Investigation of PCDA-PFB nanodroplets for multimodal imaging and *in vivo* dosimetry of radiation therapy

Sophie V. Heymans¹, ***Yosra Toumia***², ***Bram Carlier***³, ***Andrea Giammanco***⁴, ***Gonzalo Collado***⁵, ***Heiko Lange***², ***Uwe Himmelreich***⁶, ***Edmond Sterpin***³, ***Nico de Jong***⁵, ***Emiliano d'Agostino***⁷, ***Gaio Paradossi***², ***Jan D'hooge***⁸, ***Koen Van Den Abeele***¹

¹*Department of Physics, KU Leuven Campus KULAK, Kortrijk, Belgium*

²*Department of Chemical Science and Technologies, University of Rome Tor Vergata, Rome, Italy*

³*Department of Oncology, KU Leuven, Leuven, Belgium*

⁴*Department of Energy, Politecnico di Milano, Milan, Italy*

⁵*Department of Biomedical Engineering, Erasmus Medical Center, Rotterdam, The Netherlands*

⁶*Department of Imaging & Pathology, KU Leuven, Leuven, Belgium*

⁷*DoseVue, Philips Open Manufacturing Campus, Turnhout, Belgium*

⁸*Department of Cardiovascular Sciences, KU Leuven, Leuven, Belgium*

Corresponding author: koen.vandenabeele@kuleuven.be

Introduction

Recent advances in radiotherapy aim at rising the therapeutic index by maximizing the tumor dose while keeping the healthy tissue exposure to a minimum. This leads to increasingly complex treatment plans and beam delivery techniques. However, current dose verification methods remain rudimentary and generally consist of offline measurements or point verifications on the patient's skin. Uncertainties in patient positioning, patient anatomy, and machine output may lead to dose inhomogeneities, secondary malignancies, lack of tumor control, and organ failure. The objective of the AMPHORA project is to develop an *in situ* radiation dosimeter based on functionalized, radiosensitive ultrasound contrast agents (UCAs).

Phase change contrast agents, or perfluorocarbon (PFC) nanodroplets (NDs), have been increasingly investigated over the past years because of their capability to extravasate owing to their sub-micron size, and to vaporize into a microbubble contrast agent when triggered by energy sources such as ultrasound (Acoustic Droplet Vaporization, or ADV) [1] or laser light (Optical Droplet Vaporization, or ODV) [2]. These two processes can be considered a suitable *in situ* method to generate microbubbles as a theranostic and multimodal imaging device for cancer diagnosis and therapy. Moreover, several studies have shown that PFC NDs can be detected by ¹⁹F magnetic resonance imaging (MRI) [3].

The vaporization of superheated droplets, suspended in a gel or polymer matrix, induced by high energy ionizing radiation has been extensively used in the field of neutron detection for the last decades, and dosimetry of photon and proton beams has also proven to be feasible. The vaporization threshold is mainly determined by the radiation energy deposited per unit length (LET) and the degree of superheat of the droplet liquid core [4]. To our knowledge, the feasibility of radiation dosimetry based on droplet vaporization has never been assessed for shell-coated, nanometer-sized droplets diluted in fluids mimicking *in vivo* conditions. To this aim, polymerized lipid nanodroplets (PLND), mainly bearing diacetylene moieties, offer some advantages over nonpolymerized ones: enhanced chemical, structural and thermal stability as well as easiness of handling.

In this contribution, we first report an acoustic study of the vaporization signals emitted by nanodroplets of low boiling point perfluorobutane (PFB), b.p. -2°C, when the phase change is triggered by ultrasound (ADV). This is followed by a proof-of-concept experiment testing the capability of these nanodroplets to vaporize when exposed to ionizing radiation. We also report on their *in vitro* detection by ¹⁹F MRI.

Methods

The NDs employed in our experiments are made of liquefied PFB encapsulated in a fatty acid monolayer of 10,12-pentacosadiynoic acid (PCDA), subsequently polymerized by UV exposure. Structural characterization of the poly(PCDA)/PFB droplets' shell was carried out by gel permeation chromatography (GPC) (Shimadzu, IT) and MALDI ToF mass spectrometry equipped with a nitrogen laser (337 nm) (Applied Biosystems, USA). The acoustic droplet vaporization signals were studied with an ultrasonic setup consisting of a water tank in which two focused transducers were immersed and positioned at 90°. One of the transducers (Panametrics V320, 7.5 MHz center frequency) was employed to generate the ADV pulse (4 cycles sine wave, 8 MHz, 477 kPa) and the other transducer (Panametrics V306, 2.25 MHz center frequency) monitored the acoustic signals emitted by vaporizing droplets, in a “pulse high”, “listen low” scheme [1]. The transducers were confocally aligned at the center of a 130 ml sample holder enclosing a fifty-fold dilution of NDs in cell culture medium. The arbitrary waveform generator and acquisition card were computer-controlled using LabVIEW. The received signals were corrected to account for the transducer's receive transfer function and the electronics, yielding acoustic pressure values of the detected events.

For the irradiation experiment, the acoustic setup was brought to the radiotherapy room and aligned with the sample holder located at isocenter. The water temperature was raised to 32°C. Two focused transducers, positioned at 0° and 180°, measured the transmission of broadband pulses through the sample holder, as well as the backscattered signal. A flat transducer was added at 90° for passive detection of radiation-induced droplet vaporization signals. Postprocessing involved filtering the signals with a Butterworth bandpass filter to remove artefacts generated by the linear accelerator and isolate the droplet vaporization signals [1]. The radiation beam was delivered by a 6 MV Varian TrueBeam system, in steps of 4 Gy, up to a total dose of 16 Gy (dose rate of 4.8 Gy/min). The field size was 5 x 6 cm² and the gantry angle was 0°. Acoustic attenuation and scattering of the droplet suspension was measured in between each irradiation, while the passive detection of droplet vaporization was carried out during beam delivery.

Additionally, *in vitro* ¹⁹F MRI axial and coronal scans of the nanodroplets embedded on a gelatin phantom were performed using a 9.4 T MRI scanner equipped with ¹⁹F and ¹H transmit- receive coils.

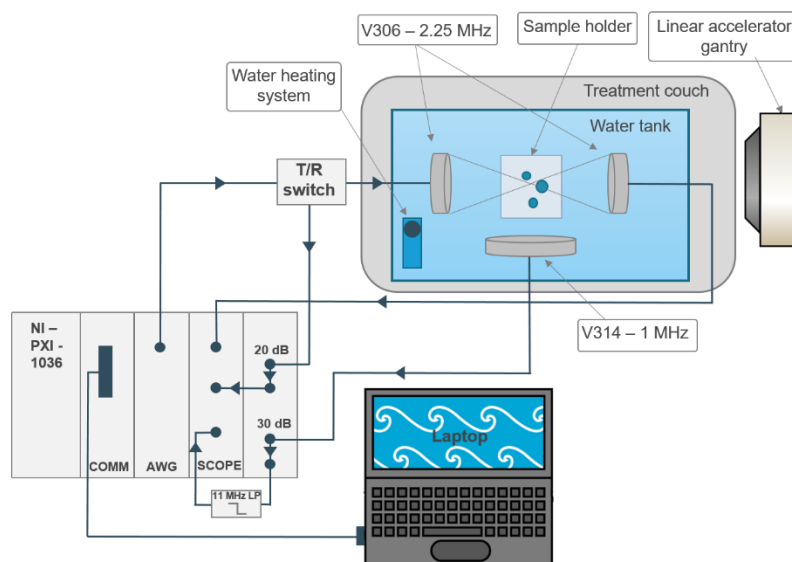


Figure 1: Schematics of the setup for the acoustic detection of PCDA-PFB NDs vaporized by radiation.

Results

The polymerization of the PCDA shell encapsulating PFB nanodroplets leads to the appearance of an intense blue colour as an evidence of the photocrosslinking. The length distribution of the poly(PCDA)

chains, determined by gel permeation chromatography and MALDI ToF spectroscopy, is bimodal and characterized by two populations with degrees of polymerization (DP) of 14 and 22, respectively.

The ADV study revealed that at 8 MHz, pressures above 240 kPa were sufficient to trigger the vaporization process. The detected vaporization signals lay in the range 0.4 – 1 MHz, indicating that the system is detecting the vaporization of large droplets, oscillating around their natural resonance frequency in an exponentially decaying trend, similarly to the results of Sheeran *et al* [1] (Fig. 2). The narrow bandwidth of the ADV pulse and the low center frequency of the receiving transducer allow to discriminate between droplet vaporization events and microbubble scattering signals, whose acoustic signatures differ both in the time and in the frequency domain.

The irradiation experiment showed that it was possible to detect vaporization signals triggered by other means than ultrasound, although it is not clear yet whether those vaporization signals were due to exposure to ionizing radiation or to spontaneous vaporization, as droplet vaporization signals were both detected in the control measurement, prior to beam delivery, and in the recording during irradiation (Fig. 3). The signals possess the same exponentially decaying trend and frequency content as vaporization signals triggered by ADV. The number of vaporization signals decreases with time which coincides with the build-up of large air bubbles on the inner walls of the sample holder, probably shielding the transducer from any vaporization signals arising within the sample holder.

In vitro ¹⁹F MRI scans allowed for clear detection of the poly(PCDA)/PFB nanodroplets. The intensity of the MRI signals is proportional to the PFB concentration with a detection limit of about 20 mM (Fig.4).

Conclusions

Poly(PCDA)/PFB is a promising system which can behave as US contrast agents supporting a dual imaging modality as the PFB core allows for MRI detection. The acoustic signals emitted by nanodroplets during their vaporization have been examined, both for vaporization events triggered by ADV and potentially by ionizing radiation, and it was shown that they have similar temporal and spectral characteristics. While it is too early to draw conclusions on the capability of these poly(PCDA)/PFB droplets to vaporize due to radiation, our study demonstrated that the system can detect droplet vaporization signals caused by other sources than ADV. Improvements of the acoustic setup by replacing the sample holder by a vessel-mimicking tube and the passive detection transducer by a larger, focused transducer will drastically improve the sensitivity and limit of detection. Additionally, with a better control of the experimental conditions (temperature, absence of gas in the dilution liquid), future studies will elucidate whether the observed vaporization signals are induced by ionizing radiation or by spontaneous vaporization. As the degree of superheat of decafluorobutane might not be sufficient for photon detection at body temperature, octafluoropropane nanodroplets, which have a significantly higher degree of superheat, will be tested in photon beams. Besides, the droplet vaporization behaviour will be investigated under a variety of radiation sources, such as clinical proton beams, neutrons, or alpha radiation, to which decafluorobutane droplets are expected to be responsive.

References

- [1]. Sheeran PS, Matsunaga TO, Dayton PA, Phase change events of volatile liquid perfluorocarbon contrast agents produce unique acoustic signatures, *Physics in Medicine and Biology*, 59(2): 379-401, 2014.
- [2]. Dove JD, Mountford PA, Murray TW, Borden MA, Engineering optically triggered droplets for photoacoustic imaging and therapy, *Biomedical Optics Express*, 5(12): 4417- 4427, 2014.
- [3]. Astafyeva K, Somaglino L, Desranges S, Berti R, Patinote C, Langevin D, Lazeyras F, Salomir R, Polidori A, Pépin CC, Urbach W, Taulier N, J. Mater. Chem B, 3: 2892-2907, 2015.
- [4]. D'Errico F, Radiation dosimetry and spectrometry with superheated emulsions, *Nuclear Instruments and Methods in Physics Research B*, 184: 229-254, 2001.

Acknowledgment

This project has received funding from the European Union's Horizon 2020 research and innovation Programme under grant agreement 766456 (AMPHORA).

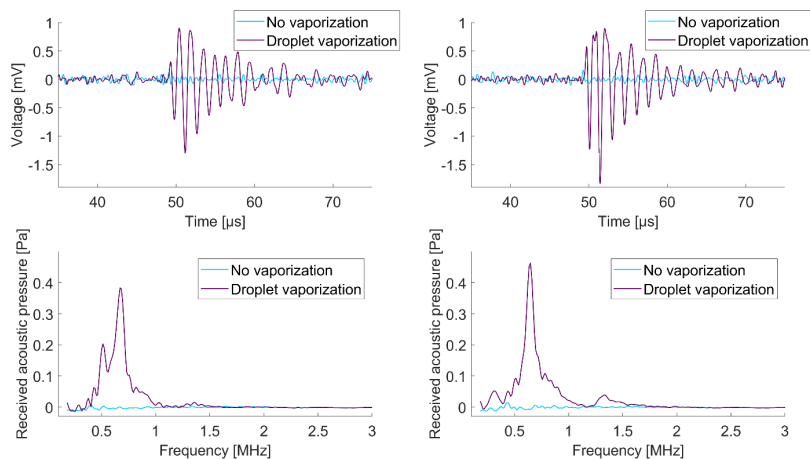


Figure 2: (Top) - time domain signals of vaporization events. (Bottom) - associated spectrums in the frequency domain, for droplet vaporization triggered by ADV.

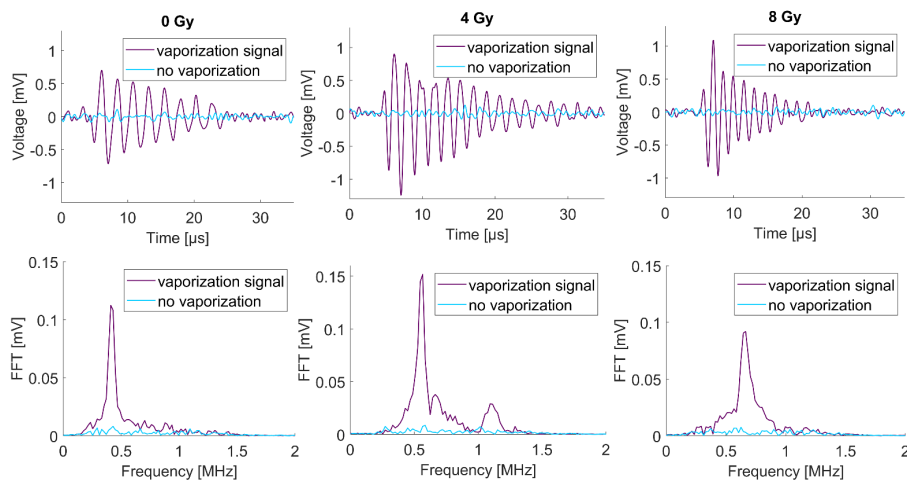


Figure 3: (Top) - time domain signals of vaporization events. (Bottom) - associated spectrums in the frequency domain. The droplet vaporization signals were detected before (0 Gy) and during beam delivery (4 and 8 Gy).

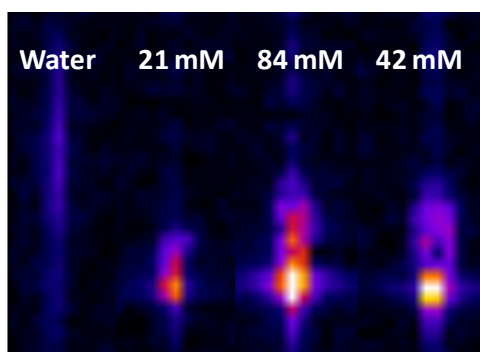


Figure 4: *In vitro* MRI image of poly(PCDA)/PFB nanodroplets in gelatin phantom (coronal scan).

Microfluidic production of fibrin-targeted polymerized shell microbubbles

Catherine A. Gormley¹, Benjamin J. Keenan¹, Jo Ann Buczek-Thomas¹, Amanda C. S. N. Pessoa^{2,3}, Jiang Xu³, Fabrice Monti³, Patrick Tabeling³, R. Glynn Holt⁴, Jon O. Nagy⁵, Joyce Y. Wong¹

¹Department of Biomedical Engineering, Boston University, USA

²School of Chemical Engineering, University of Campinas, Brazil

³Laboratoire de Microfluidique, MEMS et Nanostructures, ESPCI Paris, France

⁴Department of Mechanical Engineering, Boston University, USA

⁵NanoValent Pharmaceuticals Inc., Bozeman, USA

Corresponding author: amanda.pessoa@espci.fr

Introduction

Microbubbles have been widely explored in medical applications such as therapeutic delivery and diagnostic imaging. These small gas bubbles, ranging from 1 μm to 7 μm in size, are highly compressible and can expand and contract when exposed to an acoustic pulse [1]. Depending on an appropriate frequency and sufficient pressure, ultrasound can also be used to fragment or destroy microbubbles within the region being imaged. The microbubbles destruction during ultrasonic excitation leads to an increase in cell membrane permeability, enabling the use of microbubbles as therapeutic agents [2].

The use of thin lipid shells to stabilize the microbubbles gas-liquid interface make these applications possible, and offer different possibilities of tailoring the bubbles surface by using targeting ligands for specific tissue attachment and a local increase in ultrasound imaging signal [3].

In this context, microfluidic devices provide further opportunity for tuning the interfacial coverage of individual bubbles. Benefiting from microscale, microfluidics explores the manipulation of small amounts of fluids along with the development of particular hydrodynamic properties, such as laminar flow regime and minimized heat and mass transfer resistances. These features allow the synthesis of microbubbles with controlled physicochemical characteristics, such as precise size and monodispersity [4]. Moreover, compared to the commonly applied microbubbles production techniques, microfluidic devices enable the decrease of bubbles size to less than 10 μm by simple variations of gas pressure, liquid flow rate and microchannel design, enabling as well a precise control over the shell thickness and composition [1].

In this work, we present a targeted lipid shell microbubble as an ultrasound contrast reagent (UCR) that can be used to detect and treat adhesion-like fibrin formations using clinical diagnostic ultrasound scanners. Adhesions are post-surgical bands of fibrous scar tissue ligating apposing tissues/organs, which can cause different clinical complications, significant morbidity and mortality [5]. Herein, we describe the microfluidic synthesis of gas-core polymerized shell microbubbles (PSMs) that display the fibrin binding peptide CREKA [6] and include an UV cross-linkable lipid to enhance bubble stability. We assessed the bubbles final physicochemical characteristics, including size and stability over 48h. The bubbles showed the potential to identify adhesion-like fibrin formations, and may hold promise in blocking or breaking up fibrin formations *in vivo*.

Methods

Microfluidic chips fabrication

The chips were fabricated with polydimethylsiloxane (PDMS) and glass, by applying standard soft lithography techniques. The molding silicon wafer was prepared with SU-8 photoresist by a two-step UV-exposure procedure to obtain channels with a rectangular cross-section with heights of 1 μm and 20 μm (Fig. 1a), including a microfluidic array of 5 μm wide channels (Fig. 1b). The mold was replicated using

PDMS (Sylgard 184 elastomer kit, Dow Corning, Germany), and further cured inside an oven at 65°C for 4 hr. Oxygen plasma treatment was used to irreversibly bond the PDMS layer with a microscope glass slide.

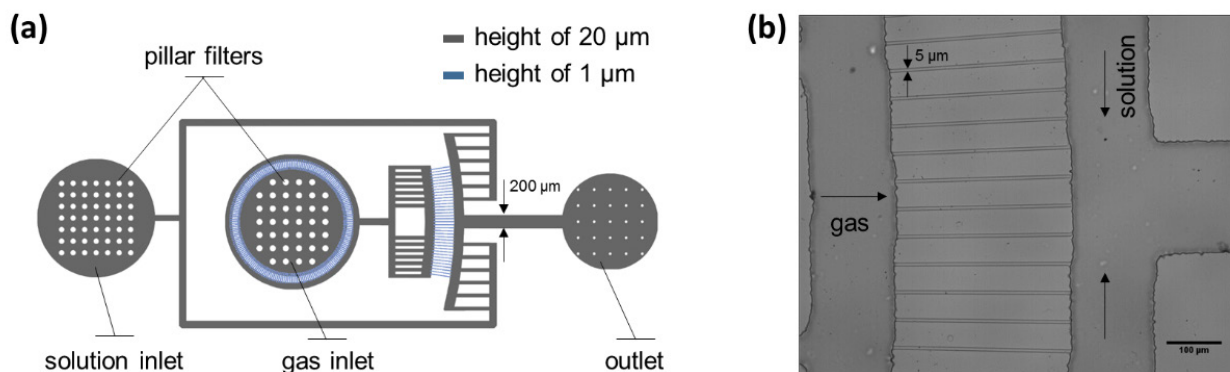


Fig. 1. (a) Schematic drawing of the microfluidic step-emulsification geometry used to produce microbubbles. The chip has channels with heights of 1 μm (blue) and 20 μm (grey). (b) Optical image of the microchannel array at the end of the microfluidic chip, containing channels of 5 μm wide for bubble production (scale bar: 100 μm). (Adapted from [9])

Microbubbles synthesis

The microbubbles were composed by L- α -phosphatidylcholine hydrogenated soy, (hydrogenated soy PC), 1,2-distearoyl-sn-glycerol-3-phosphoethanolamine-N-[methoxy(polyethylene glycol)-2000] (m-PEG2000-DSPE), (5-hydroxy-3-oxypentyl)-10-12-pentacosadiynamide (h-PEG1-PCDA), and 1,2-distearoyl-sn-glycerol-3-phosphoethanolamine-N[amino(polyethylene glycol)-2000]-CREKA (CREKA-PEG2000-DSPE).

The lipid solution was added to the solution inlet and nitrogen gas to the air inlet of the microfluidic device (Fig. 1a). The gas pressure was increased to 18 psi with a solution flow rate of 0.25 mL/min. The microbubble solution was collected and polymerized with a Spectrolinker XL-1000 UV Crosslinker at 253 nm and 5000 x 100 $\mu\text{J}/\text{cm}^2$ to form polymerized shell microbubbles (PSM). Non-targeted microbubbles were produced in the same manner except CREKA-PEG2000-DSPE was substituted with m-PEG-2000-DSPE.

Physicochemical characterization

Microbubble size was measured under brightfield imaging using an inverted microscope. Images were recorded at 20x magnification with 200 ms of exposure time and were analyzed using the ImageJ particle sizer function to determine the diameter of the microbubbles. Microbubble stability was determined in phosphate buffered saline (PBS) and in LP-9 medium (containing Fetal Bovine Serum (FBS), Epidermal Growth Factor (EGF), and hydrocortisone) at a final concentration of 10^5 PSM/mL. The microbubble solutions were stored at 37°C. Size and concentration measurements were determined as described above at 2, 24 and 48 hr.

Ultrasound cytotoxicity

LP-9 human mesothelial cells were cultured on collagen-coated plates and were exposed to 10^5 PSMs (targeted or non-targeted) per mL of growth media. Cells were allowed to acclimate to the presence of the PSMs for 30 min in a 37°C, 5% CO₂ incubator. Cells in all conditions were treated with ultrasound generated by a Terason Ultrasound System equipped with a 7L3 probe for 1 min. Cells cultured in the absence of bubbles and the absence of ultrasound treatment served as controls. Following ultrasound exposure, all cells were washed with sterile PBS and stained with the Invitrogen LIVE/DEAD® Viability/Cytotoxicity Kit. Cellular viability was calculated from analyses of three images from each plate

in each experiment. The resulting fluorescent images were analyzed using Metamorph, ImageJ, Matlab, and Excel.

Results

The chips employed for microbubbles synthesis were based on step-emulsification. By applying this design, the bubbles are formed when the dispersed phase flows through an abrupt transition in the form of a step between the inlet channel and the reservoir [7]. The throughput of the microfluidic device was 2.5×10^6 microbubbles/min on average and the microbubbles were UV cross-linked immediately after production, to yield PSMs. With a single device, this rapid rate of PSM production enables sufficient microbubbles for use in pre-clinical studies, which typically use $\sim 10^8$ microbubbles/mL. Moreover, the microfluidic chip generated microbubbles with tighter, more controlled, size distributions, which have been shown to improve US contrast intensity *in vivo* [8].

In order to evaluate their stability, non-targeted and fibrin-targeted PSMs were incubated in both PBS and media at 37°C. Sizes of each PSM sample were measured at 2, 24 and 48 hr, as shown in Fig. 2a. The mean diameter and the standard deviation of all PSM formulations increased over time, specifically at 24 and 48 hr; however, the mean diameter of the PSMs did not vary with statistical significance. In all the conditions, PSM populations demonstrate a consistent mean diameter of approximately 3 μm .

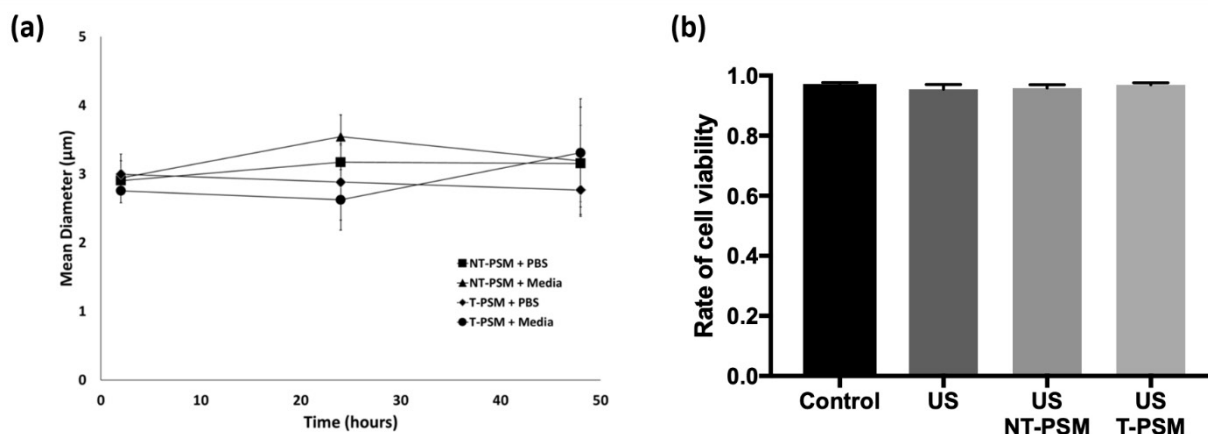


Fig. 2. (a) Diameter and Stability of non-targeted (NT-PSM) and fibrin-targeted (T-PSM) polymerized shell microbubbles (PSMs). The PSMs were incubated in PBS or media at 37°C for 48h. The data are expressed as the mean \pm standard deviation. (b) LP-9 cellular viability after treatment with PSM and ultrasound. LP-9 cells were exposed to either 10^5 targeted and non-targeted PSM (T-PSM and NT-PSM, respectively) in the absence and presence of ultrasound treatment. Cellular viability was assessed in triplicate experiments using the LIVE/DEAD assay. Data is expressed as the mean \pm S.E.M. (Adapted from ref. [9]).

Our results reveal that the PSMs likely remain stable for even longer than 48 hr (Fig. 2a) [9]. Our group performed *in vivo* pilot studies that showed that 48 hr is the minimum amount of time for unbound PSMs to be cleared in the peritoneum, leaving only bound PSMs for accurate imaging and treatment (data not shown). Taking into account the importance of detecting and treating adhesions during the brief time frame in which they are still in their nascent, fibrinous state and most vulnerable, we can infer 48 hr as the time point that is most relevant to the potential clinical applications with these PSMs, such as ultrasound-triggered treatment to break up fibrinous adhesions.

In this context, we evaluated the effect of ultrasound in the presence of PSMs on the viability of cultured mesothelial cells. As the vibration of the PSMs in response to an ultrasound beam can disrupt the fibrin to which they are bound to treat the existing adhesions, we aimed to investigate whether the proposed treatment method could possibly damage the surrounding living mesothelial cells, resulting in the formation of further adhesions. Hence, we compared untreated cells to cells treated with ultrasound in

the presence of fibrin-targeted on non-targeted PSMs (no fibrin is externally added for all conditions) or no PSMs (Fig. 2b).

As presented in Fig. 2b, in all conditions cell viability remained high, over 90%, and is similar to the untreated controls [9]. While further *in vivo* results over a longer time course are required to confirm whether ultrasound treatment in the presence of PSMs is not harmful to cells in the mesothelium and do not result in further inflammation and adhesion formation, these results show that our PSMs are promising alternatives to be applied as ultrasound contrast agents and ultrasound-triggered treatment for breaking up fibrinous adhesions.

Conclusions

In this work, we present CREKA-targeted polymerized shell microbubbles (PSMs) designed to allow ultrasound imaging of early adhesions for diagnostic and treatment purposes. By applying a microfluidic device based on step-emulsification, we were able to continuously produce microbubbles with controlled size, high throughput and stability for long periods of time (for approximately 4 days). These PSMs can be employed for evaluating success of potential treatments in clinical trials, while acting as a possible treatment themselves. This strategy represents a noninvasive technique to breakup early stage adhesions coupled with a reliable detection method aiming to provide an ideal solution to address adhesion-related complications.

References

- [1]. Lin H, Chen J, Chen C, A novel technology: microfluidic devices for microbubble ultrasound contrast agent generation, *Medical and Biological Engineering and Computing*, 54: 1317–1330, 2016.
- [2]. Ferrara K, Pollard R, Borden M, Ultrasound Microbubble Contrast Agents: Fundamentals and Application to Gene and Drug Delivery, *Annual Review of Biomedical Engineering*, 9: 415–447, 2007.
- [3]. Willmann JK et al. Targeted Contrast-Enhanced Ultrasound Imaging of Tumor Angiogenesis with Contrast Microbubbles Conjugated to Integrin-Binding Knottin Peptides, *Journal of Nuclear Medicine*, 51: 433–440, 2010.
- [4]. Anna SL, Droplets and Bubbles in Microfluidic Devices, *Annual Review of Fluid Mechanics*, 48: 285–309, 2016.
- [5]. Schnüriger B, Barmparas G, Branco BC, Lustenberger T, Inaba K, Demetriades D, Prevention of Postoperative Peritoneal Adhesions: A Review of the Literature, *Am. J. Surg.* 201: 111–121, 2011.
- [6]. Zhou Z, Wu X, Kresak A, Griswold M, Lu ZR, Peptide Targeted Tripod Macrocyclic Gd(III) Chelates for Cancer Molecular MRI, *Biomaterials*, 34: 7683–7693, 2013.
- [7]. Li Z, Leshansky AM, Pismen LM, Tabeling P, Step-emulsification in a microfluidic device, *Lab Chip*, 15: 1023–1031, 2015.
- [8]. Streeter JE, Gessner R, Miles I, Dayton PA, Improving Sensitivity in Ultrasound Molecular Imaging by Tailoring Contrast Agent Size Distribution: In Vivo Studies, *Mol. Imaging*, 9:87-95, 2010.
- [9]. Gormley CA, Keenan BJ, Buczek-Thomas JA, Pessoa ACSN, Xu J, Monti F, Tabeling P, Holt RG, Nagy JO, Wong JY, Fibrin-Targeted Polymerized Shell Microbubbles as Potential Theranostic Agents for Surgical Adhesions, [Paper under peer-review].

Graphene Hybrid Contrast Agents for Ultrasound and Multiplexed Photoacoustic Imaging

Yosra Toumia¹, Philippe Trochet², Jithin Jose², Fabio Domenici, Savino Lacerenza², Gaio Paradossi¹

¹Department of Chemical Science and Technologies, University of Rome Tor Vergata, Rome, Italy

²FUJIFILM VisualSonics, Amsterdam, The Netherlands

Corresponding author: Yosra.Toumia@uniroma2.it

Introduction

Photoacoustic Imaging (PAI) is a new preclinical modality based on the photoacoustic effect and combining the high resolution of ultrasound imaging (US) with optical contrast in the near infrared (NIR) spectral region. Therefore PAI allows for a more expanded diagnostic range, i.e. anatomy and functional assessment and molecular imaging. However, developing exogenous NIR contrast enhancers is key towards translating PAI from preclinical to clinics.[1] Herein, we report on hybrid US contrast agents (UCAs), i.e. microbubbles (MBs) and phase change nanodroplets (NDs), decorated with pristine graphene (Gr). Among others, graphene is a material with superior characteristics for PAI as it strongly absorbs light in the NIR almost independently from the wavelength.[2] The acoustic and PA performances of the graphene UCAs were investigated. This work also shows how the biodistribution of graphene hybrid microbubbles can be assessed *in vivo*, and in real-time, with multiplexed PAI.

Methods

Pristine graphene aqueous dispersions were prepared via surfactant mediated ultrasonication of graphite powder (Sigma Aldrich, Italy). Gr was then tethered to two efficient UCAs: (i) poly(vinyl-alcohol) (PVA) air filled MBs, whose surface was functionalized with poly(ethyleneglycol) (PEG) diamine spacer and (ii) photopolymerized fatty acid, i.e. 10,12 pentacosadynoic acid, phase-change perfluoropentane NDs (poly(PCDA)/PFP). This was achieved via a strong covalent coupling using the functional groups of the adequate surfactant stabilizing graphene to the shell of either PEGylated PVA MBs or to poly(PCDA)/PFP NDs.

The acoustic attenuation properties of both Gr PVA MBs and Gr/poly(PCDA)/PFP NDs after acoustic droplet vaporization (1MHz, 3.6W/cm², 30s) were studied with an in-house made setup equipped with two flat 10 MHz transducers and a waveform generator producing sinusoidal bursts generating pressures below 60 kPa.

The *in vitro* study of the photoacoustic performances of both Gr hybrid UCAs was carried out using Vevo LAZR X imaging system (Fujifilm VisualSonics, Amsterdam) equipped with a 15 MHz ultrasound transducer (central frequency) that has an axial resolution of 100 μ m (MX 201). The transducer was modified in such a way that an optical fiber array of 36 mm arranged on both sides of the transducer to perform the multimodal imaging of ultrasound and photoacoustic. A commercially available phantom (Vevo Phantom, VisualSonics, Amsterdam) consisting of transparent plastic capillary tubes mounted in an acrylic dish and immersed in distilled water is used to image and characterize samples of MBs/NDs being injected at the desired concentrations into the tubes. The PA spectra were recorded from 680 to 970 nm, and saved by the VevoLab software for the subsequent spectral unmixing and deconvolution.

An *in vivo* investigation on Gr PVA MBs was conducted on balb female mice under the animal license approved by The Netherlands (protocol number DVS06). The experiments were carried out using the same Vevo LAZR-X multimodal imaging system with the 15 MHz transducer and an array of narrow fiber (16 mm). The animals were injected with 80 μ L of MBs (4×10^7 MBs) via the tail vein. This experiment was performed using a PA gain of 34 dB and a frequency of 15 MHz. The images were acquired by unmixing the spectra of the components, i.e., oxygenated haemoglobin, deoxygenated

haemoglobin, and Gr PVA MBs at selected wavelengths, 682, 710, 734, 924, and 944 nm. 3D full body scan was performed to investigate the biodistribution of the MBs within the range of 36.4 mm at a step size of 0.5 mm, after 20 min from injection. To demonstrate the hybrid contrast functionality of the Gr PVA MBs, we also imaged the same region with a nonlinear contrast mode of ultrasound imaging.

Results

A stable anchoring of pristine graphene can be easily achieved to almost any UCAs platforms, for which a suitable choice of the surfactant stabilizing graphene is key. The main advantages of the approach of coupling graphene to UCAs are: (i) the unique optical and mechanical properties of intact graphene as a strong NIR absorber, and therefore an efficient enhancement of the PA signal in a wide NIR spectral range, (ii) the echogenicity and biocompatibility as a consequence of the robust anchoring of pristine graphene to the bioinert MBs/NDs shell. The Gr PVA MBs maintained their echogenicity as compared to the plain ones. However, a shift from 10 to 11 MHz and a slight decrease in the resonance attenuation was observed when PEG spacers were introduced as bridging moieties between graphene and the surface of PVA MBs. Also, the Gr poly(PCDA)/PFP NDs could efficiently undergo an acoustic droplet vaporization triggered by US. Their acoustic attenuation resonance is similar to lipidic MBs, i.e between 1-2 MHz, and no shift was observed as compared to plain poly(PCDA)/PFP NDs. Both hybrid contrast agents showed strong PA signals *in vitro* and their PA spectra exhibited a separable profile from endogenous species such as haemoglobins (see Figure 1).

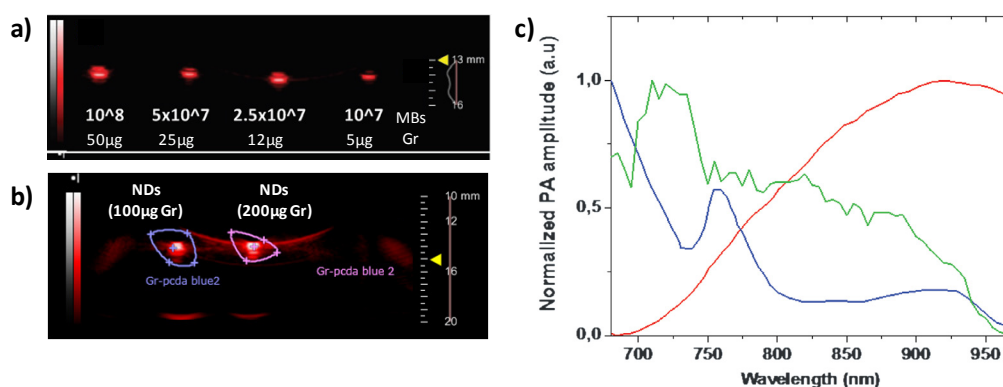


Figure 1. a) and b) *In vitro* phantom PAI of Gr PVA MBs (with PEG spacer of 2000 Da) and Gr poly(PCDA)/PFP NDs, respectively (gain 24 dB); c) PA spectra of Gr PVA MBs (green), oxy haemoglobin (red), and deoxy haemoglobin (blue).

Moreover, Gr PVA MBs demonstrated their efficiency *in vivo* by enhancing significantly contrast signals in both PA and US modes and without any adverse toxicological response, as preliminarily tested in mice (see Figure 2a-b). The interesting PA spectral features of this graphene hybrid construct allowed, for the first time, real-time track monitoring and assessment of its whole body biodistribution in mice by 3D multiplexed PAI scan (See Figure 2a), as well as its quantification in specific organs such as kidneys and liver. The kinetics of perfusion to the kidney was followed in real-time and showed a significant enhancement of the PA signals within 50 s from injection which then decreased due to diffusion to the other organs. The Gr PVA MBs mainly accumulated in liver, spleen and lungs.[3]

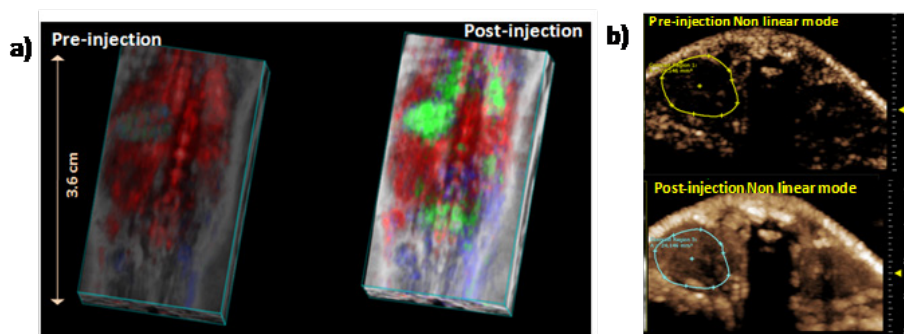


Figure 2. a) *In vivo* biodistribution assessment of Gr PVA MBs by 3D multiplex scan PAI before and after IV injection in mouse. The components are: oxy hemoglobin (red), deoxy haemoglobin (blue) and Gr PVA MBs (green); b) 2D kidneys view: non-linear contrast US imaging before and after intravenous injection (frequency 12.5 MHz, contrast gain 2dB) of Gr PVA MBs.

Conclusions

Graphene hybrid contrast agents are promising systems for PA molecular imaging. As far as we know, this is the first study showing the whole body biodistribution of a pristine graphene hybrid medical contrast agent using a photoacoustic commercial setup. Developing and optimizing these Gr UCAs, as they represent a great potential in PAI, are keen to engineer their surface with bioactive molecules. Future studies are planned to determine the targeting, drug loading, and delivery capabilities of this devices for applications in cancer therapy.

Acknowledgment

Funding from the European Union's Horizon 2020 research and innovation Programme under grant agreement 766456" (AMPHORA).

References

- [1]. Santiesteban, DY, Dumani, DS, Profili D, Emelianov SY, Copper Sulfide Perfluorocarbon Nanodroplets as Clinically Relevant Photoacoustic/Ultrasound Imaging Agents, *Nano Lett*, 17: 5984-5989, 2017.
- [2]. Toumia Y, Domenici F, Orlanducci S, Mura F, Grishenkov D, Trochet P, Lacerenza S, Bordi F, Paradossi G. Graphene Meets Microbubbles: A Superior Contrast Agent for PAI, *ACS Appl. Mater. Interfaces*, 8: 16465-16475, 2016.
- [3]. Toumia Y, Cerroni B, Trochet P, Lacerenza S, Oddo L, Domenici F, Paradossi G, Performances of a Pristine Graphene-Microbubble Hybrid Construct as Dual Imaging Contrast Agent and Assessment of its Biodistribution by Photoacoustic Imaging, *Part. Part. Syst. Charact.*, 35: 1800066, 2018.

Development of new polymeric contrast platforms

F. Domenici, S. Cerra, D. Palmieri, F. Brasili, L. Oddo, Y. Toumia, E. Chiessi, G. Paradossi

Dipartimento di Scienze e Tecnologie Chimiche, Università degli Studi di Roma "Tor Vergata"

Via della Ricerca Scientifica, 00133 Rome, Italy

Corresponding author: fabio.domenici@uniroma2.it

Introduction

The recent physico-chemical advances of polymer ultrasound (US) contrast agents (CAs) are transforming the concept of microbubbles (MBs) into invaluable new multi-responsive platforms of theranostic relevance, combining early diagnosis and therapeutics. On this line, we focused our attention on two case systems: i) crosslinked polyvinyl alcohol (PVA) MBs [1] and ii) "phase change" hybrid shelled microdoplets (MDs) [2] as intriguing proof of concepts to realize drug delivery and multimodal imaging tools for personalized medicine.

i) PVA MBs are the proof of concept for promising theranostic CAs [1]. It has been demonstrated that the crosslinked PVA chains of the shell behave as a biocompatible elastomeric three-dimensional network, providing high stability and relevant echogenicity [1,3]. It is also noteworthy that the easy PVA derivatization allows for tunable strategies to realize environmental responsivity, as a controlled drug release. Despite this, up to now these intriguing peculiarities have not been focused in a unified vision of a theranostic platform, that could not be designed using other types of CAs. Herein, we will discuss the appealing hypothesis to immobilize and concentrate PVA MBs at high densities onto a suitable substrate. The aim of this approach is to develop a two-dimensional macroscopic checkpoint scaffold, where every single MB element maintains its stable and echogenic conformation together with the chemical reactivity. The MBs device would be thus customized for chemical release and molecular sensing. It could even be considered as an "echoserver" for extravascular ultrasound imaging identification.

ii) The main asset of MDs is the possibility to conjugate their drugs and nanoparticles (Nps) cargo capability with the dramatically increased US echogenicity after their transition to MBs, mediated by the acoustic and/or optothermal core vaporization (named ADV and ODV, respectively) [4,5]. The introduction of MDs in the vast theranostics scenario mainly passes through the improvement of their shells to confer greater stability, versatility and higher vaporization efficiency, whilst keeping them to the smallest possible size. In this framework, some of us recently proposed novel double-shelled MDs composed of a perfluorocarbon (decafluoropentane, DFP) liquid core, and an internal surfactant shell coated with a crosslinked polymer (dextran methacrylate, DexMa) [2]. The polymer layer provides higher stability as compared to the surfactant shelled MDs, also upon their transition to MBs. However, many efforts were still required for improving composition and stability of such double-shelled MDs, leading to realize an efficient multi-stimulated phase change MDs.

Both case studies presented herein are schematically summarized in Figures 1 and Figure 2. Despite obvious chemical differences, the polymer network of the two micro-systems allowed for stably hosting photothermal Nps at the water interface, displaying dramatically enhanced responsiveness.

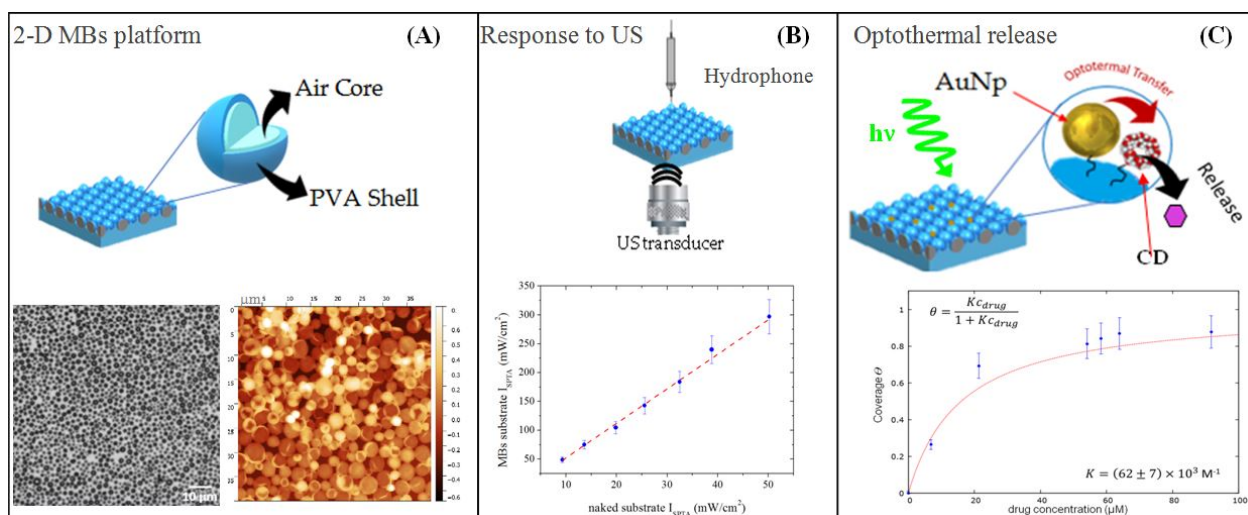


Figure 1. (A) optical microscopy (left) and AFM image (right) together with the sketch of the two-dimensional (2-D) MBs platform. (B) the acoustic response of the MBs substrate, given by the spatial peak temporal average Intensity (I_{SPTA}), plotted vs the control substrate in water. (C) release of drug model (phenolphthalein) from the MBs substrate derivatized with CDs and photothermal Nps; the equilibrium binding affinity, K , of drug-CD interaction was obtained according to Langmuir isotherm fit.

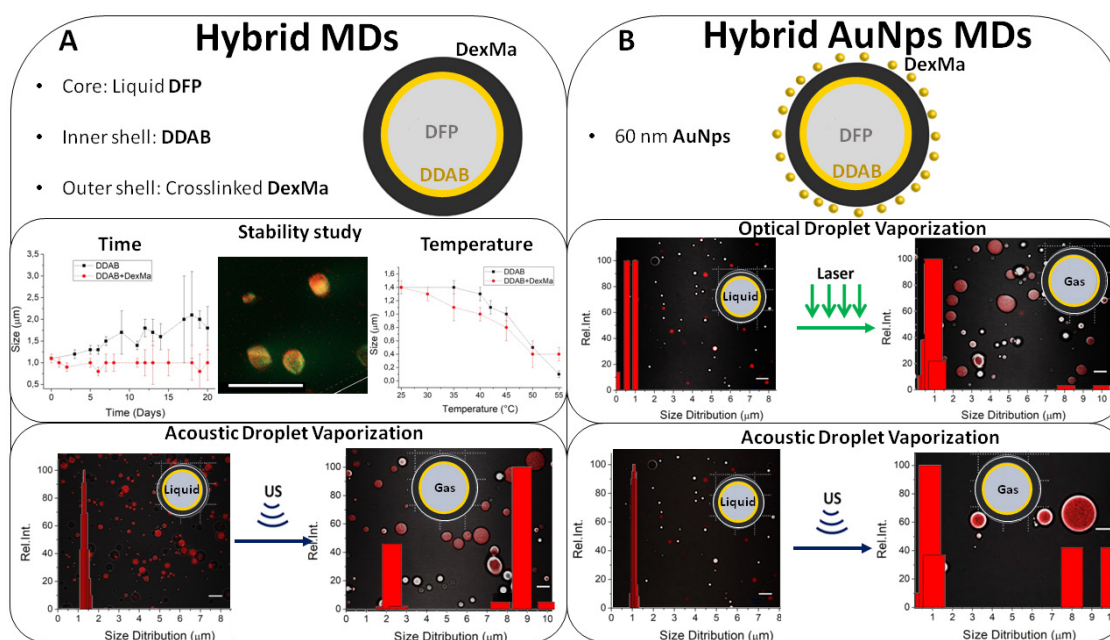


Figure 2. (A) From top to bottom: sketch of the hybrid MD composition; study of the system stability in time (left) and in temperature (right), with a CLSM z stack image; size distributions obtained before and after ADV by DLS; (B) From top to bottom: sketch of a MD conjugated with 60 nm AuNPs; size distributions superimposed to the corresponding CLSM images acquired before and after ODV; size distributions superimposed to the corresponding CLSM images acquired before and after ADV. Scale bars are 10 μ m.

Methods

i) Stable air-filled PVA MBs were obtained by crosslinking telechelic PVA via acetalization reaction at the water/air interface under high shear conditions [6]. Spherical shaped MBs with a narrow size distribution centered at 2 μ m were obtained as measured by confocal laser scanning microscopy (CLSM), dynamic light scattering (DLS) and AFM (Figure 1A). To build the two-dimensional MBs substrate, a monolayer of PVA MBs was deposited by dip-coating onto a borosilicate cover glass, previously functionalized with aminosilanes. The acoustic behavior of the system was investigated with an US

exposure device composed by a signal generator, a piezo-ceramic transducer tuned at 1 MHz, and a needle hydrophone (Figure 1B). Loading and release of low and high molecular weight drugs were obtained by tuning the surface chemistry of the MBs with covalent binding to β -cyclodextrins (CDs). The amphiphilic nature of CDs was exploited to form an inclusion compound with a drug simulated herein by phenolphthalein, absorbing at $\lambda_{\max} = 552$ nm when released in solution. The release of the included molecules was followed as a function of temperature by an optical fiber microplate absorbance reader. An alternative near field photothermal strategy of release was conceived by co-loading of CDs and gold (Au) Nps on the MBs substrate surface. Laser irradiation (Power = 46 mW, $\lambda_{\max} = 532$ nm) was performed at the plasmon resonance absorbance peak of Nps (Figure 1C) and constant temperature.

ii) The MDs were prepared by emulsification under controlled stirring of a premixed amount of ethanol, DFP and the surfactant dioctadecyldimethylammonium bromide (DDAB) in water solvent. Then the DexMa with a substitution degree of 50% (mole percentage of methacrylated units over total repeating units) was added. Both velocity and stirring time were tuned to optimize the yield of MDs in the few micrometer size range. The external DexMa shell of the MBs was subjected to photopolymerization, exposing the colloidal dispersion to ultraviolet source ($\lambda = 365$ nm) for 4 minutes under gentle stirring in the presence of a photoinitiator. The resulting MDs dispersion was centrifuged to further optimize the size at ~ 1 μm . The stability of the MDs was followed over time and temperature by DLS and CLSM measurements (Figure 2A). The thermodynamic features of the DDAB were analysed through differential scanning calorimetry (DSC) measurements. The AuNps conjugation process was followed by UV-Vis absorption spectroscopy, by monitoring the plasmon resonance absorbance peak. For the ADV experiments (Figure 2A), MDs were exposed at 1MHz US varying the intensity (0.5-3.6 mW/cm^2) and the exposition time (30-900 s). The ODV experiments (Figure 2B) were performed by exploiting a green laser light centred at the AuNPs plasmonic resonance wavelength of 532 nm, thus allowing the photothermal process to be activated. The phenomenon was studied varying the laser power (5-50 mW) and the irradiation time (60-300 s). Both ADV and ODV phenomena were monitored by CLSM and DLS.

Results

We will detailly describe the development of two versatile contrast platforms: a two-dimensional echogenic device based on PVA MBs (Figure 1) and hybrid shelled MDs (Figure 2), both suitable for controlled molecular release. Experiments aimed to evaluate either acoustic responsiveness and capability to release molecules through thermal and photothermal stimuli were performed successfully.

i) Specifically for the PVA MBs platform, the optical and near-field microscopy measurements clearly show the formation of two-dimensional highly dense PVA MBs assemblies tightly bonded onto glass substrates. Even if immobilized in such a configuration, the PVA MBs remain stable and maintain their spherical shape, in both air and in aqueous physiological environments (Figure 1A). Preliminary measurements show that our MBs substrates preserve the echogenic properties typical of MBs (Figure 1B), also producing an amplified acoustic wavefront whose gain factor (the maximum value was 6.0 ± 0.2) depends on the MBs surface density. The platform has been modified to accommodate CDs as molecular inclusion systems for thermally-tuned capture and release of a hydrophobic drug molecule model. The properties of this microplate system were characterized by absorption spectroscopy measurements, pointing out the thermodynamic features of the immobilized CDs interacting with the drug model, and showing a favorable binding affinity as compared to that measured in bulk solution. More interesting, we further improved the PVA MBs platform to accommodate photothermal Nps and CDs (Figure 1C). In this way we have shown that it is possible to provide a localized photothermal release of drugs optically tunable (at the plasmonic absorption frequency of the Nps), while keeping constant the temperature of the environment.

ii) Concerning the second case system, the hybrid MDs, we optimized the fabrication protocol of such a novel class of double-shelled phase change contrast agents, recently developed by our group [2], with the aim to improve the droplet stability and better control their size. As a surfactant monomolecular layer

at the interface between DexMA and DFP core we introduced the DDAB, a cationic synthetic "lipid" characterized by a very small cationic head and a long apolar tail, showing a gel-liquid crystalline transition at $T_c \sim 45^\circ\text{C}$. Using this charged amphiphilic layer coated with DexMa, a sharp size distribution of spherical shaped colloidal MDs, centred at $\sim 1\mu\text{m}$, was obtained at physiological temperature. The stability of MDs was evaluated over 15 days, when the surfactant is fully composed by DDAB (Figure 2A). The resulting positive charge of the MDs not only improves the colloidal stability but allowed us to incorporate negatively charged AuNPs onto the MDs surface for several localized optothermal applications. We integrated the MDs shell with AuNPs demonstrating that it is possible to induce the perfluorocarbon core vaporization (Figure 2B), efficiently, by near-field photothermal energy [4]. Both ADV and ODV of the AuNP-MDs hybrid system were optimized depending on the acoustic/photon dose of stimulation. Noteworthy, focusing on DDAB shelled MDs decorated with AuNPs only (without DexMa), we will show that it is easy to overcome the transition point of DDAB assembly optothermally (as T_c of DDAB is not very far from the physiological temperature). In this way we destabilized the MD shell to allow for the release of the nanoparticles and of drugs trapped in the liquid core, while maintaining the environmental temperature fixed at 37°C .

Conclusions

Two pivotal multifunctional MBs contrast platforms have been designed.

i) The density of the PVA MBs units composing the two-dimensional system can be easily quantified and controlled. The stability of the system was tested in different stress conditions, such as US irradiation, temperature and different biomedical relevant environments. Moving towards imaging, our echodevice behaves as a secondary US emitter, strengthening the US wavefront produced by the source. The high resonance frequency (from 10 MHz to 20 MHz, depending on the size of the MB units) could be relevant for high spatial resolution US analysis. Moreover, the control of the MBs immobilization could be improved by lithography to design patterns able to generate interference contrast profiles. In this respect our results could provide novel insights to fabricate an advanced checkpoint tool useful for extravascular and ex-vivo diagnostic imaging, and, more generally, for non-destructive material control. We demonstrated that the PVA MBs substrates can be easily derivatized and transformed into a reliable system to trigger, optically and thermally, *in situ* molecular release.

ii) The upgrade of our double-shelled MDs to a dual optothermal and acoustic phase change CAs was successfully undertaken. We optimized the MDs fabrication protocol (namely the emulsification process and the composition of the surfactant layer) to obtain a sharp size distribution, tunable in the few micrometer range, and suitable to be integrated with AuNPs. The decoration of AuNPs onto the MDs shell was achieved, enlightening a dramatic enhancement in the droplets vaporization efficiency upon excitation with proper US and laser light excitation.

In the perspective view of realizing multifunctional echodevices using MBs and MDs, the possibility to control the drug loading and release capacity by employing US will be considered. In both the case studies the well-known ability of AuNPs to release near-field photothermal energy could also be exploited to promote the photoacoustic effect for multimodal imaging.

References

- [1]. Oddo L, Cerroni B, Domenici F, Bedini A, Bordi F, Chiessi E, Gerbes S, Paradossi G, Next generation ultrasound platforms for theranostics, *Journal of Colloid and Interface Science*, 491: 151-160, 2017.
- [2]. Capece S, Domenici F, Brasili F, Oddo L, Cerroni B, Bedini A, Bordi F, Chiessi E, Paradossi G, Complex interfaces in "phase-change" contrast agents, *Physical Chemistry Chemical Physics*, 18: 8378-8388, 2016.
- [3]. Domenici F, Brasili F, Oddo L, Cerroni B, Bedini A, Bordi F, Paradossi G, Long term physical evolution of an elastomeric ultrasound contrast microbubble, *Journal of Colloid and Interface Science*, under review.
- [4]. Chen Q, Yu J, Kim K, Review: optically-triggered phase-transition droplets for photoacoustic imaging, *Biomedical Engineering Letters*, 8: 223-229, 2018.
- [5]. Lajoinie G, Gelderblom E, Chlon C, Böhmer M, Steenbergen W, de Jong N, Manohar S, Versluis M, Ultrafast vaporization dynamics of laser-activated polymeric microcapsules, *Nature Communications*, 5(3671): 1-8, 2014.
- [6]. Paradossi G, Cavalieri F, Chiessi E, Ponassi V, Martorana V, Tailoring of Physical and Chemical Properties of Macro- and Microhydrogels Based on Telechelic PVA, *Biomacromolecules*, 3(6): 1255-1262, 2002.

Targeting of vascular cell adhesion molecule 1 with an ultrasound contrast agent bearing Designed Ankyrin Repeat Proteins as targeting ligands

A.Kosareva¹, M.Punjabi¹, A. Ochoa-Espinosa¹, L.Xu¹, J.V. Schaefer³, B.Dreier³,
A. Plückthun³, B.A. Kaufmann^{1,2}

¹Department of Biomedicine, University Hospital of Basel, Switzerland

²Department of Cardiology, University Hospital of Basel, Switzerland

³Department of Biochemistry, University of Zurich, Switzerland

Corresponding author: Alexandra.kosareva@unibas.ch

Introduction

Atherosclerosis is an inflammatory disease of the large arteries [1] that progresses silently over decades until it causes stroke and myocardial infarction. In order to prevent such late complications, an early and reliable diagnosis of atherosclerosis is clinically needed. Vascular cell adhesion molecule 1 (VCAM-1) is expressed throughout the pathogenesis of atherosclerosis and promotes recruitment of monocytes to the vessel wall [2]. For this reason, non-invasive imaging of the expression of VCAM-1 could be used for early detection and risk stratification. Contrast enhanced ultrasound molecular imaging (CEUMI) of VCAM-1 has been shown to be feasible in mouse models of atherosclerosis [3]. However, the ultrasound contrast agents that have been used so far have relied on biotin-streptavidin conjugation chemistry and full-size antibodies as targeting agents, which are expensive, potentially immunogenic and may have low targeting efficiency. For clinical translation there is thus a need for the development of ultrasound contrast agents that use smaller, easy to produce and highly specific ligands. Designed Ankyrin Repeat Proteins (DARPin) are multipurpose affinity reagents that have not just proven to recognize targets with exceptional specificity and selectivity, but that also may overcome the aforementioned limitations [4]. Therefore, our aim was to develop and characterize an ultrasound contrast agent carrying a DARPin ligand targeted to VCAM-1.

Methods

Selection: Ribosome display was used to select DARPin binders targeted against murine VCAM-1 [5]. Homogeneous time resolved fluorescence (HTRF) assays were performed to characterize the target binding properties of candidates [6]. To identify high-affinity binders, endothelial cells expressing VCAM-1 after TNF-alpha stimulation were incubated with crude DARPin extracts. Flow cytometry was employed to quantify attachment of individual DARPins to endothelial cells and the best candidates were purified and sequenced.

Characterization: The monomeric state of the high affinity DARPins was verified by size exclusion chromatography (SEC). Microbubble (MB) ultrasound contrast agents were produced by sonication of a decafluorobutane-saturated aqueous solution containing 1,2-distearoyl-sn-glycero-3-phosphocholine (DSPC), polyoxyethylene (40) stearate (PEG40S) and 1,2-distearoyl-sn-glycero-3-phosphoethanolamine-maleimide (DSPE-maleimide). DARPins were conjugated site-specifically via an engineered, unique Cysteine to the maleimide on the microbubble surface. Fluorescein-labeled DARPin was used to determine the amount of DARPin necessary to saturate the maleimide binding sites and to quantify the ligand density on the microbubble surface. The experiments were carried out in triplicates.

Validation: Parallel plate flow chamber studies were conducted to examine the binding efficiency of microbubbles carrying the top DARPin candidates as determined on flow cytometry. Cell culture dishes with bEnd.3 mouse endothelial cells expressing VCAM-1 after TNF-alpha induction were placed in an inverted position on a microscope for video recording. Suspensions of fluorescently labeled MBDARPin and MBcontrol (3x10⁶/ml) were drawn through the flow chamber at a flow rate resulting in calculated shear stress of 2 and 4 dynes/cm². The number of microbubbles attached to the cells was counted for 20 optical fields after five minutes of continuous flow. For in vivo assessment of attachment efficiency of microbubbles bearing DARPins targeted to VCAM-1, a mouse model of murine hind limb inflammation was used (n = 13). CEUMI of the hind limb was performed 4 h after intramuscular injection of tumor necrosis factor (TNF)-α (250 ng) [7] using power modulation and pulse inversion imaging at a centerline frequency of 7 MHz and mechanical index of 0.87.

Results

Ribosome display yielded a large number of binders for VCAM-1 that were selected for further characterization. HTRF and flow cytometry on VCAM-1 expressing endothelial cells allowed to narrow down the number of candidate binders to six high affinity DARPins. All of the selected candidates were monomeric on SEC as well as monoclonal and unique as confirmed by DNA sequencing. Incubation of microbubbles with increasing concentrations of fluorescein labeled DARPIn showed a saturation concentration of 120 μg per 1×10^8 microbubbles. The number of DARPins per microbubble was determined as $1.4 \times 10^6 \pm 7.9 \times 10^5$ and the number of DARPIn molecules per μm^2 as $1.5 \times 10^5 \pm 9.2 \times 10^4$. Flow chamber studies demonstrated selective retention of microbubbles carrying 1730-E12 DARPins compared to microbubbles carrying a non-specific control DARPIn (2 dynes: 18 ± 7 vs. 6 ± 2 microbubbles per optical field, $p < 0.01$, 4 dynes: 25 ± 12 vs. 1 ± 0.5), whereas the five remaining candidate binders tended to show increased retention, which was not significantly different from MBcontrol (Figure 1). In contrast to flow chamber studies, CEUMI of inflamed hind limb showed significant signal enhancement above control for 1732-F8 and 1730-C7 DARPIn binders (Figure 2).

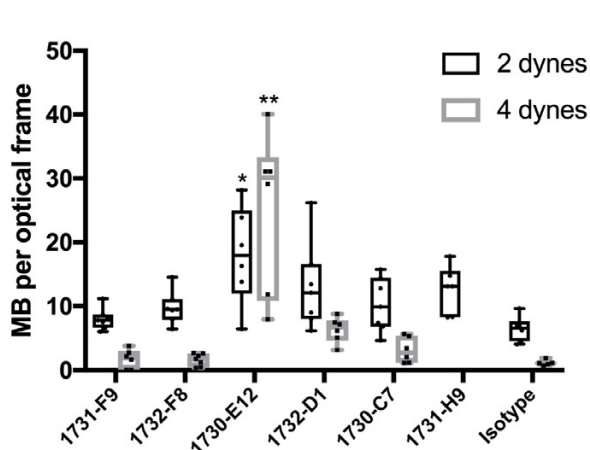


Figure 1: Flow chamber validation: Retention of the microbubbles carrying a DARPIn binder compared to control microbubbles (* $p < 0.05$, ** $p < 0.005$, $n = 5-6$ for each).

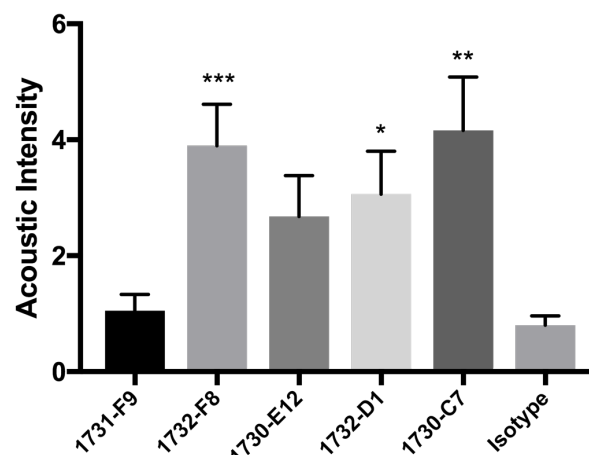


Figure 2: CEUMI acoustic intensity of inflamed hind limb after injection of $\text{MB}_{\text{DARPIn}}$ and $\text{MB}_{\text{control}}$ (* $p < 0.05$, ** $p < 0.005$, *** $p < 0.0005$, $n = 13$).

Conclusions

We have developed and characterized six MB contrast agents, each carrying a different DARPIn ligand for VCAM-1 using maleimide conjugation to the MB surface. While 1730-E12 showed selective adhesion to VCAM-1 *in vitro* on endothelial cells under flow conditions, this did not predict *in vivo* results. 1732-F8 and 1730-C7 showed increased retention *in vivo* and thus detection of VCAM-1 expression in a hind limb inflammation model is possible using microbubbles carrying DARPIn ligands.

References

- [1]. Lusis, A.J., Atherosclerosis. Nature, 2000. 407(6801): p. 233-41.
- [2]. Marui, N., et al., Vascular cell adhesion molecule-1 (VCAM-1) gene transcription and expression are regulated through an antioxidant-sensitive mechanism in human vascular endothelial cells. J Clin Invest, 1993. 92(4): p. 1866-74.
- [3]. Kaufmann, B.A., et al., Molecular imaging of inflammation in atherosclerosis with targeted ultrasound detection of vascular cell adhesion.
- [4]. Plückthun, A., Designed ankyrin repeat proteins (DARPins): binding proteins for research, diagnostics, and therapy. Annu Rev Pharmacol Toxicol, 2015. 55: p. 489-511.
- [5]. Dreier, B. and A. Plückthun, Rapid selection of high-affinity binders using ribosome display. Methods Mol Biol, 2012. 805: p. 261-286.
- [6]. Degorce, F., et al., HTRF: A technology tailored for drug discovery - a review of theoretical aspects and recent applications. Curr Chem Genomics, 2009. 3: p. 22-32.
- [7]. Khanicheh, E., et al., Factors affecting the endothelial retention of targeted microbubbles: influence of microbubble shell design and cell surface projection of the endothelial target molecule. J Am Soc Echocardiogr, 2012. 25(4): p. 460-6.

Formulation and Stability of Chemically-Crosslinked Microbubble Clusters: Novel Applications in Imaging and Therapy

Ronald L. Hall¹, Zachary Juan-Sing Dennis¹, Kenneth Hoyt^{1,2}, Shashank R. Sirsi^{1,2}

¹University of Texas at Dallas, Richardson, TX, USA, 75080

²University of Texas Southwestern, Dallas, TX, USA, 75390

Corresponding author: Shashank.Sirsi@utdallas.edu

Introduction

Currently, ultrasound contrast agents (UCAs – also known as “microbubbles”) are thought of as single gas bubbles stabilized by a biocompatible shell with sizes ranging from 1-10 μm . We propose that the versatility of UCAs in contrast agent imaging and therapy can be improved through judicious design of the hierarchical structure. This study introduces a novel concept of physically cross-linking UCAs forming microbubble (MB) “clusters”. In contrast to traditional UCAs, microbubble clustering offers several unique advantages including more control over size, shell, and gas compositions that can be used to fine-tune the acoustic response and generate novel responses in an ultrasound field. One of the most important challenges in developing cross-linked UCA clusters is controlling the aggregation process to produce cluster sizes viable for *in vivo* circulation and maintaining the stability of cluster after formulation. In this study, we demonstrate that controlled aggregation of chemically cross-linked microbubble clusters

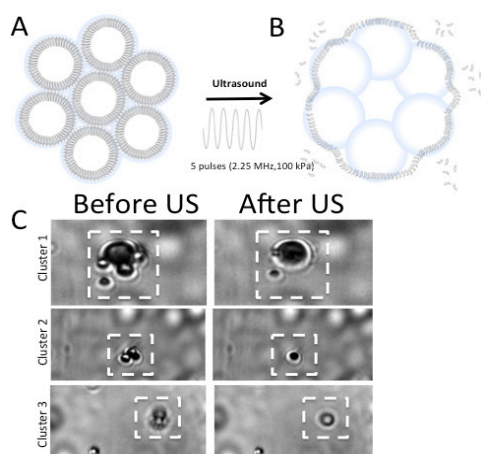


Figure 1. Microbubble Cluster Stability during US application. Immediate microbubble fusion can be driven with low-intensity pulsed ultrasound application. C) Avidin cross-linked clusters are placed in a 200 μm diameter capillary tube and imaged at 100 frames per second to capture cluster formation before and immediately after a single low-intensity ultrasound pulse train is applied (100 kPa, 2.25 MHz, 5 pulses). Examples of 3 individual clusters fusing during ultrasound application is shown.

(CCMCs) is feasible and can produce quasi-stable complexes that slowly fuse into bubbles with individual gas cores. Furthermore, we demonstrate that this process can be driven with low-intensity ultrasound pulses, enabling a rapid fusion of clusters in microseconds which could potentially be used to develop novel ultrasound contrast imaging and drug delivery strategies in future studies. The development of novel microbubble clusters here presents a simple yet robust process for generating novel UCA's with a design that will allow for more versatility in contrast-enhanced ultrasound (CEUS), molecular imaging, and drug delivery applications.

Method

In this study, we optimized the development of lipid-based microbubble clusters by mixing avidin-coated UCAs with a molar excess of biotinylated UCAs while varying injection speeds and molar ratios. Flow cytometry and microscopy were used to demonstrate highly efficient cluster formation using fluorescently labelled microbubbles. High speed ultrasound imaging in a custom flow through testing chamber was used to characterize the cluster response following application of 2.25 MHz focused transducer (Olympus V303-FU, Waltham, MA) and broadband hydrophone (Sonic Concepts Y109, Seattle, WA).

Results and Discussion

In this study we demonstrate a rapid and facile means of increasing UCA sizes through chemical crosslinking. By judiciously controlling the ratios of mixing of reactive bubbles, we demonstrate that CCMBs with median diameters of 3.4 μm (~2 fold increase in median diameter from unconjugated bubbles) can be generated, still small enough to be capable of circulating *in vivo* (<10 μm in diameter). While the procedure in this study was optimized to minimize cluster sizes by over saturation of core

microbubbles that comprise the cluster, we expect that altering mixing ratios can be used to generate larger size clusters if desired.

After formation, CCMBs will coalesce into individual bubbles in solution. Our results indicate this phenomenon is due to Ostwald Ripening, wherein gas from smaller bubbles in the cluster will dissolve and redeposit into larger bubbles to lower the overall surface energy. The kinetics of ripening are highly dependent on bubble concentration and sample polydispersity, however we are able to show almost complete fusion of CCMBs into individual bubbles at 72 hours using the mixing procedure outlined in the methodology. Low-intensity ultrasound pulse trains applied to microbubble cluster (100 kPa, 2.25 MHz, 5 pulses) showed rapid fusion into individual bubbles (Figure 1). This rapid change in the hierarchical structure can potentially be exploited to develop novel contrast imaging and drug delivery strategies.

Conclusion

The goal of this project was to develop a simple method of controlled aggregation to produce stable microbubble clusters with size below 10 μm in diameter (sufficient to circulate in the body), which can be utilized for further studies. In this study, optimize the formulation of microbubble “clusters” for biomedical applications using a controlled aggregation through avidin-biotin linkage interactions. Stoichiometric ratios of avidinated core MBs to biotinylated peripheral MBs were altered in order to maximize loading on core bubbles and minimize the size of the overall clusters. Flow cytometry and microscopy analysis were used to verify cluster formation and loading. The stability of clusters was evaluated over time, demonstrating a quasi-stability nature where clusters would preferentially fuse into larger single UCAs in 1-2 days. Fusion of CCMCs could be accelerated using low-intensity application as well, a unique phenomenon that can be exploited to develop novel imaging and drug delivery strategies.

Lipid coating structure and acoustic response of ultrasound contrast agents containing cholesterol

Simone A.G. Langeveld¹, Inés Beekers¹, Antonius F.W. van der Steen^{1,2}, Nico de Jong^{1,2}, Klazina Kooiman¹

¹Department of Biomedical Engineering, Erasmus MC, Rotterdam, the Netherlands

²Acoustical Wavefield Imaging, Delft University of Technology, Delft, the Netherlands

Corresponding author: s.a.g.langeveld@erasmusmc.nl

Introduction

Microbubbles can be used for many applications such as contrast-enhanced ultrasound imaging, molecular imaging and enhanced drug delivery [1]. Single microbubble behavior is crucial and can for example make the difference between drug uptake or no effect at all. Previous work showed variability of the microbubble behavior in response to ultrasound of equal-sized lipid-coated microbubbles [2,3,4], challenging safe and controlled microbubble-mediated drug delivery. We hypothesize that this variability is caused by a heterogeneous lipid phase distribution of the microbubble coating. To test this, we aim to develop a new microbubble coating with miscible phospholipid components that are all in the same phase. Research on phospholipid monolayers has shown that cholesterol affects the lipid phase distribution [5]. Therefore we produced microbubbles with a cholesterol-containing phospholipid shell and studied the lipid phase distribution and ligand distribution using confocal microscopy. In addition we studied the microbubble response to ultrasound.

Methods

Phospholipid-coated microbubbles with a C₄F₁₀ gas core were made by sonication. The standard composition in mol% was: DSPC 59.4; PEG-40 stearate 35.7; DSPE-PEG(2000) 4.1; DSPE-PEG(2000)-biotin 0.8. The ratio of these compounds was kept the same while different amounts of cholesterol were added (5-15 mol%). The effect of cholesterol on size distribution was studied using a Coulter Counter. The lipid phase distribution of the phospholipid-coating was studied using fluorescent dye Rhodamine-DHPE (0.01-0.02 mol%) and the DSPE-PEG(2000)-biotin distribution (i.e. ligand distribution) was studied using fluorescent streptavidin-Oregon Green 488. High-axial-resolution 3D images were obtained with a 4Pi microscope. Finally, the Brandaris 128 ultra-high-speed camera was used to perform microbubble spectroscopy to assess the individual microbubble response to ultrasound (50 kPa, 1-4 MHz in steps of 200 kHz, single 8-cycle burst) [6]. Analyses of the Brandaris recordings including determination of resonance curves and eigenfrequencies (f_0) were performed as described by van Rooij et al. [2] using MATLAB software and 3D visualisation was performed using AMIRA software.

Results

The mean size of the microbubbles decreased when more cholesterol was added to the coating (mean diameter 4.5 μ m without cholesterol and 1.7 μ m with 15% cholesterol). With 4Pi microscopy we observed a characteristic honeycomb structure in the lipid phase distribution of microbubbles without cholesterol (Fig. 1A). In microbubbles with 8% cholesterol the fluorescent dye Rhodamine-DHPE was distributed homogeneously over the coating, indicating that all components were miscible and in the same phase (Fig. 1B). The ligand on the outside of the coating was distributed homogeneously for both the microbubbles with and without cholesterol. Microbubbles without (n=10) and with cholesterol (n=10, with 8% cholesterol) oscillated and showed resonance behavior. From these resonance curves we determined the eigenfrequency f_0 (Fig. 1C). We found a characteristic response to ultrasound for microbubbles with 8% cholesterol, comparable to the microbubbles without cholesterol.

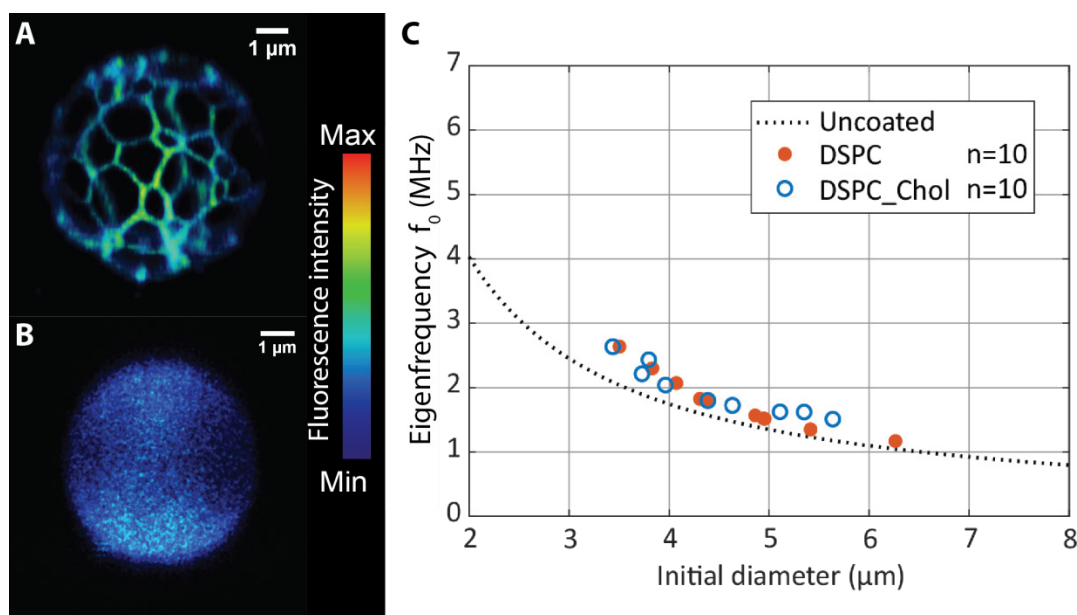


Fig.1A+B) Lipid phase distribution in the coating of a DSPC-based microbubble (A) and DSPC-cholesterol (8%) microbubble (B). Views extracted from a 3D acquisition using Rhodamine-DHPE as fluorescent dye. **C)** Eigenfrequencies (f_0) as a function of initial diameter at 50 kPa peak negative pressure of DSPC-based and DSPC-cholesterol (8%) microbubbles. The eigenfrequency of an uncoated microbubble is shown by a dotted line.

Conclusions

We were able to produce DSPC-based microbubbles containing cholesterol. The lipids were phase separated in the coating of microbubbles without cholesterol, evident by a honeycomb pattern. Addition of cholesterol to the coating composition resulted in a decreased microbubble size and more homogenous lipid phase distribution in the coating. Cholesterol had no effect on the ligand distribution. DSPC-based microbubbles with 8% cholesterol responded to ultrasound in a similar way as our standard DSPC-based microbubbles without cholesterol. These new DSPC-based microbubbles with cholesterol are therefore a promising theranostic agent for molecular imaging and drug delivery.

Acknowledgements – This project is funded by the Phospholipid Research Center in Heidelberg, Germany.

References

- [1]. Kooiman K, Vos HJ, Versluis M, de Jong N, Acoustic behaviour of microbubbles and implications for drug delivery 2014, *Advanced Drug Delivery Reviews*, 72: 28-48, 2014.
- [2]. Rooij T, Luan Y, Renaud G, van der Steen AFW, Versluis M, de Jong N, Kooiman K, Non-linear response and viscoelastic properties of lipid-coated microbubbles: DSPC versus DPPC 2014, *Ultrasound in Medicine & Biology*, 41: 1432-1445, 2015.
- [3]. Kooiman K, Foppen-Harteveld M, van der Steen AFW, de Jong N, Sonoporation of endothelial cells by vibrating targeted microbubbles 2011, *Journal of Controlled Release*, 154: 35-41, 2011.
- [4]. Helfield BL, Cherin E, Foster FS, Goertz DE, Investigating the subharmonic response of individual phospholipid encapsulated microbubbles at high frequencies: a comparative study of five agents 2012, *Ultrasound in Medicine & Biology*, 38: 846-863, 2012.
- [5]. Yuan C, Johnston J, Phase evolution in cholesterol/DPPC monolayers: atomic force microscopy and near field scanning optical microscopy studies 2001, *Journal of Microscopy*, 205:136-146, 2002.
- [6]. Van der Meer SM, Dollet B, Voormolen MM, Chin CT, Bouakaz A, de Jong N, Versluis M, Lohse D, Microbubble spectroscopy of ultrasound contrast agents 2006, *Journal of Acoustical Society of America*, 121: 648-656, 2007.

Acoustically-stimulated nanodroplets for bone fracture repair

S. Ferri^{1,2}, N.D. Evans², D. Carugo¹

¹*MiNaTher, Faculty of Engineering and Physical Sciences, University of Southampton, Southampton, UK*

²*Bone&Joint, Faculty of Medicine, University of Southampton, Southampton, UK*

Corresponding author: S.Ferri@soton.ac.uk

Introduction

Five-to-ten percent of bone fractures result in costly and debilitating conditions such as delayed or non-union, where the bone fails to heal properly [1]. Common therapeutic options include physical stimulation therapies (i.e. mechanical fixation, plaster casts and prostheses), and biological treatments (i.e. autograft, allograft and administration of hormones or protein) [2]. Common treatments are invasive and rely on the immobilisation of the fracture site and, notably, immobilisation leads to a decrease in patients' quality of life. Currently there is no clinically approved systemic therapy for their treatment. Systemic drugs may require high doses for therapeutic efficacy which could lead to possible off-target side-effects [3]. And therefore targeted delivery systems, such as ultrasound-responsive perfluorocarbon nanodroplets (NDs), may be of benefit in stimulation of bone formation in a non-invasive fashion.

NDs can be loaded with drugs and release them upon exposure to ultrasound (US) waves. NDs are sufficiently small to extravasate and accumulate in a target tissue [4]. The MBs formed by ND vapourisation are highly echogenic; when stimulated with US they undergo volumetric oscillations, which can simultaneously release bioactive molecules and mechanically stimulate cells [5].

The therapeutic efficacy of NDs is likely to be influenced by their dimensional properties and acoustic responsiveness at the fracture site. In this study, we tested the hypotheses that (i) different production methods and storage conditions can affect ND dimension, and (ii) NDs with different size display different acoustic behaviour in a fracture model.

Methods

Phospholipid-shelled NDs with a perfluoro-n-pentane (PFP) core stabilised by a layer of DSPC:PEG40S (9:1 molar ratio) were produced in phosphate buffered saline (PBS) by sonication, and their size was subsequently measured with a dynamic light scattering technique (DLS, Zetasizer Nano, Malvern Panalytical Ltd, Malvern, UK). The following parameters were varied to test the influence of production and storage conditions on ND size: PFP:PBS volume ratio (in the range 0.05:1 - 0.15:1, corresponding to concentrations of 50-150 $\mu\text{L}/\text{mL}$), intensity of sonication (in the range 24-72 W), sonication length (from 20 to 60 seconds), and storage temperature (either 4°C or 37°C). The effect of incorporating a lipophilic fluorophore (DiI, 1,1'-dioctadecyl-3,3,3',3'-tetra-methylindocarbocyanine perchlorate) was also investigated. Molar ratios of DSPC:PEG40S:DiI in the range 8.9:1.01:0.0025 - 8.9:1.01:0.025 were tested.

Two different experimental systems were developed to study the acoustic behaviour of NDs: (i) a microfluidic-based acoustic resonator (or acoustofluidic device), and (ii) a microscope-compatible water-tank incorporating a passive cavitation detector (PCD). The acoustofluidic device acts as a resonant cavity, where an ultrasonic standing wave is established within its fluid layer; the device was used to assess whether NDs can phase-transition into microbubbles (MBs). It consists of a glass microcapillary with an elliptical cross-section (0.3 x 6 x 50 mm, thickness 0.3 mm, VitroCom, West Yorkshire, United Kingdom) coupled to a piezoelectric transducer with diameter of 10 mm and thickness of 1 mm (PZT26, Meggitt, Christchurch, Dorset, UK) and it can be primed with 100 μL of ND suspension. The water tank was designed to quantify cavitation activity of NDs upon US stimulation [6]. Both devices were designed using COMSOL Multiphysics (COMSOL Inc., Burlington, MA, USA) and tested *in-vitro*. Moreover, the water-tank apparatus allows investigating ND behaviour within physical models of bone fractures with different geometry. The bone was simulated using a material with comparable acoustic impedance ($z =$

5.41×10^6 kg/m²s, Sawbones, Washington, USA). Different fracture gaps (3.5-5.5 mm), thicknesses (2 and 4 mm), and inclinations (45° and 90°) were evaluated.

Results

In a first series of experiments, the effect of changing the production conditions on ND size was evaluated. The size and size dispersity of NDs are important parameters, since they influence both their ability to extravasate and the response to US stimulation. A narrow size distribution is preferable, as it leads to a predictable and uniform acoustic behaviour [7]. By increasing the volume of PFP from 50 to 150 μ L/mL, ND diameter increased from 162.87 ± 49.42 to 308.17 ± 76.01 nm, as shown in Fig. 1A. An increase in sonication intensity from 48 to 72 W resulted in a decrease of ND diameter from 354.65 ± 127.21 to 315.01 ± 100.56 nm. A sonication of 60 seconds considerably reduced ND size dispersity (diameter: 249.74 ± 9.67 nm). Finally, the addition of DiI at different molar ratios did not affect ND size. Importantly, NDs were stable at both 4°C (up to 6 days) and at 37°C (up to 110 minutes), as shown in Fig. 1B; however, some evidence of ND-to-MB phase transition was observed after 40 minutes at 37°C.

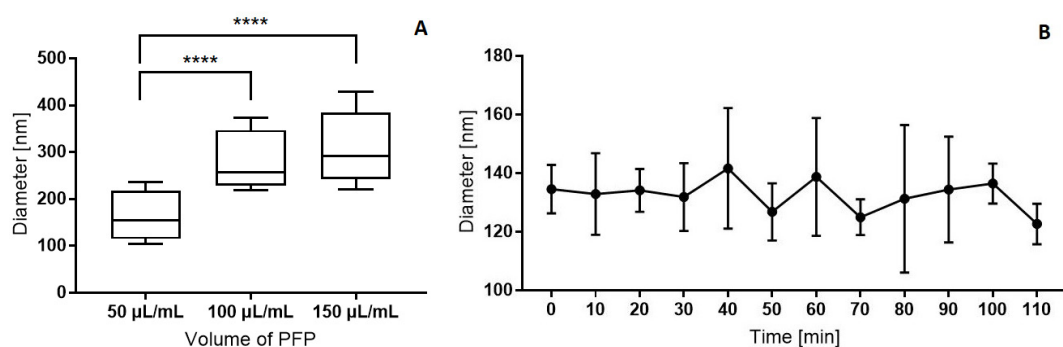


Figure 1: A) Diameter of NDs produced with different volumes of PFP in the range 50-150 μ L/mL. By increasing the quantity of PFP, ND diameter increased from 162.87 ± 49.42 to 308.17 ± 76.01 nm ($p < 0.0001$). B) The graph shows that NDs are stable at 37°C. ND diameter was measured every 10 minutes for 110 minutes.

Using the acoustofluidic device, it was demonstrated that DSPC:PEG40s NDs transitioned into MBs upon acoustic stimulation (frequency = 1.75 MHz, driving voltage = 15 V), as shown in Fig. 2A and Fig. 2B. Numerical simulations showed that it was possible to generate a uniform acoustic field at a target plane, within a compact apparatus designed to evaluate ND cavitation activity, as illustrated in Fig. 2C and Fig. 2D. The presence of a fracture model caused spatial perturbations to the acoustic pressure field, which depended on the geometrical characteristics of the fracture. Ongoing studies are investigating how these perturbations affect ND response.

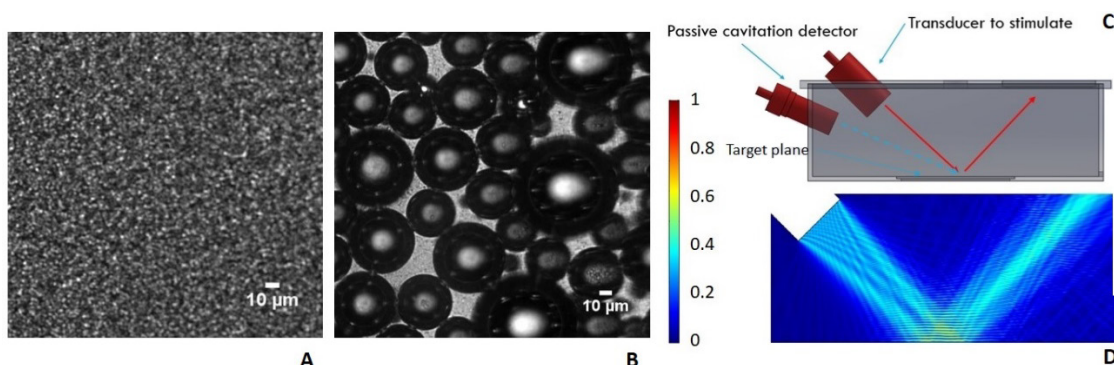


Figure 2: A,B) Microscope images showing phase transition of NDs to MBs, induced by an US stimulation of 10 seconds (frequency = 1.75 MHz, driving voltage = 15 V, continuous wave). C) Schematic of the microscope-compatible water-tank for stimulating NDs. D) Acoustic pressure field determined from numerical simulations. The setup allows the generation of relatively homogeneous US stimulation conditions at the target plane, and is designed to accommodate physical models of bone fractures.

Conclusions

A protocol was established to produce DSPC:PEG40s NDs with clinically acceptable diameter and size dispersity. It involved the use of 100 $\mu\text{L}/\text{mL}$ PFP, which was sonicated for 60 seconds with an intensity of 72 W. Moreover, experimental systems were developed to characterise NDs phase transition in-vitro, under well-defined acoustic stimulation regimes.

Future work will focus on characterising the acoustic response of NDs within physical models of bone fractures. Further studies will also investigate the relationship between ND acoustic response and the release of biologically active compounds.

References

- [1]. Corrarino JE. Fracture repair: Mechanisms and management. *The Journal for Nurse Practitioners*, vol. 11, no. 10, pp. 960-967, 2015.
- [2]. Haffner-Luntzer M, Liedert A and Ignatius A. *Mechanobiology of bone remodelling and fracture healing in the aged organism*. 2016.
- [3]. Lavrador P, Gaspar VM and Mano JF. Stimuli-responsive nanocarriers for delivery of bone therapeutics - barriers and progresses. *Journal of Controlled Release*, vol. 273, pp. 51-67, 2018.
- [4]. Paproski RJ and Zemp RJ. Comparing nanodroplets and microbubbles for enhancing ultrasound-mediated gene transfection. *2013 IEEE International Ultrasonics Symposium (IUS)*, 2013.
- [5]. Lee YJ, Carugo D, Crake C, Owen J, de Saint Victor M, Seth A, Coussios C and Stride E. Nanoparticle-Loaded Protein-Polymer Nanodroplets for Improved Stability and Conversion Efficiency in Ultrasound Imaging and Drug Delivery. *Advanced Materials*, vol 2, no. 37, pp. 5484-5492.
- [6]. King DA, Malloy MJ, Roberts AC, Haak A, Yoder CC and O'Brien WD. Determination of postexcitation thresholds for single ultrasound contrast agent microbubbles using double passive cavitation detection. *The Journal of the Acoustical Society of America*, vol. 127, no. 6, pp. 3449-3455, 2010.
- [7]. Sheeran PS and Dayton PA. Improving the performance of phase-change perfluorocarbon droplets for medical ultrasonography: Current progress, challenges, and prospects. *Scientifica*, vol. 2014, p. 579684, 2014.

Level-set based numerical simulation of acoustic droplet vaporization

Sukwon Park¹, Gihun Son¹

*¹Department of Mechanical Engineering, Sogang University, Seoul, South Korea
Corresponding author: gihun@sogang.ac.kr*

Introduction

Acoustic droplet vaporization (ADV) is a phenomenon in which volatile microdroplets are phase-changed into vapor bubbles by acoustic pulses. The ADV process receives increasing attention as a promising technique for medical diagnosis and therapy. For its practical applications, a fundamental understanding and prediction of the ADV process is essentially important. Despite a number of studies [1], a general predictive model for the ADV process has not yet been developed due to the difficulties in tracking the phase-change bubble interface motion occurring in a few microseconds.

Methods

In this work, we used the level-set (LS) interface tracking method which was modified to treat the droplet and bubble surfaces and to implement the matching conditions of velocity, stress and temperature at the interfaces by incorporating the ghost fluid and semi-implicit pressure correction methods [2].

Results

Computations were performed for the ADV process of a dodecafluoropentane (DDFP) droplet of 1 μ m radius immersed in liquid water at the human body temperature of 37°C. Initially, a spherical DDFP bubble of 0.1 μ m radius is assumed to form at the center of the droplet. If acoustic pulsing is not applied, the initial bubble having a temperature of 53°C, which is the saturation temperature corresponding to a pressure of 0.275Mpa evaluated from the Young-Laplace equation, shrinks due to the condensation heat transfer to the ambient. We use the sine pulses of 0.5-4 MPa amplitudes and 1-12 MHz frequencies for acoustic initiation of droplet vaporization. The computations demonstrated the whole process of bubble growth including complete droplet vaporization and subsequent bubble expansion and shrink.

The numerical results for the bubble growth near a wall showed that the oscillation amplitudes of the bubble pressure and radius as well as the droplet lifetime are little dependent on the existence of the wall, but the oscillation period greatly increases with the wall.

Computations were also conducted for the ADV process in a tube. The numerical results showed that the bubble growth rate decreases as the tube radius decreases. The effects of acoustic parameters and flow velocity on the bubble growth in tubes with different radii were quantified.

Conclusions

The acoustic-driven vaporization of DDFP droplets near a wall was numerically investigated by employing the level-set method which was modified to track the multiple interfaces and to include the effects of liquid-vapor phase change and bubble compressibility. The numerical method was proved to be applicable to investigate the effects of acoustic parameters and tube conditions on the bubble growth in ADV.

References

- [1]. Shpak O, Kokhuis TJA, Luan Y, Lohse D, de Jong N, Fowlkes B, Fabiilli M, Versluis M, Ultrafast dynamics of the acoustic vaporization of phase change microdroplets,” *Acoust. Soc. Am*, 134: 1610-1621, 2013.
- [2]. Lee J, Son G, A Sharp-interface level-set method for compressible bubble growth with phase change,” *Int. Commun. Heat Mass Trasf*, 86: 1-11, 2017.

Ultrasound precise vaporization threshold microdroplets

*E. Teston, S. Décombas-Deschamps, V. Hingot, M. Tanter, O. Couture**

*Physics for Medicine Paris, ESPCI Paristech, Inserm U979, PSL University
Corresponding author: Olivier.couture@espci.fr*

Introduction

Acoustic droplet vaporization (ADV) encounter more and more potential biomedical applications. Perfluorocarbon – composite or not – microdroplets are interesting candidates for such experimentations as these chemicals have low boiling points. Hingot et al. have recently shown that ADV could be achieved in a sub-wavelength region, [1] and that two release zones closer than the fourth of the wavelength can be separated with fluorescence imaging or using ultrafast ultrasound localization microscopy. In this study, the vaporization threshold of microdroplets is well defined *in vitro*. We thus wondered whether these droplets could be used as *in vivo* local pressure probes, which could be useful to determine reached pressure when realizing ultrasound therapy through a complex medium such as the skull. We therefore wondered whether the presence of absorbers would modify vaporization thresholds of previously described composite microdroplets [2] and we also realized early investigations about the influence of frequency on release pressure threshold.

Methods

Water in perfluorohexane in water micro-emulsions were prepared as previously described. [2] Paraffin-gels were made out of medium-density type paraffin-gel wax, and candle wax introduced in a range from 0% to 16% w/w. Approximately 10^7 composite droplets are injected in a cellular culture plate placed horizontally in a water-bath for acoustical coupling (Figure 1). The plate is observed through a macroscope (Leica, MZ10F) with an 8x magnification, and pictures are taken with a Single-Lens Reflex (SLR) camera (Canon EOS70D). This plate is also placed at the focal distance of a 128-elements linear array used at 5 MHz pulse frequency. The array is piloted by a programmable ultrasound scanner capable of ultrafast imaging, able to emit arbitrary pulses over the 128 channels and record echoes to achieve frame rates of several thousand per second. It is used to generate $2 \mu\text{s}$ focused pulses between 0.5 and 6 MPa peak-negative pressure (PnP). Acoustic monitoring was achieved by emitting 10 and 200 plane-wave images (13 kHz frame rate) before and after pulses, which were then subtracted. For each paraffin gels added between droplets and transducer, the focused pulses intensity was incrementally increased until the droplet release was observed acoustically or optically.

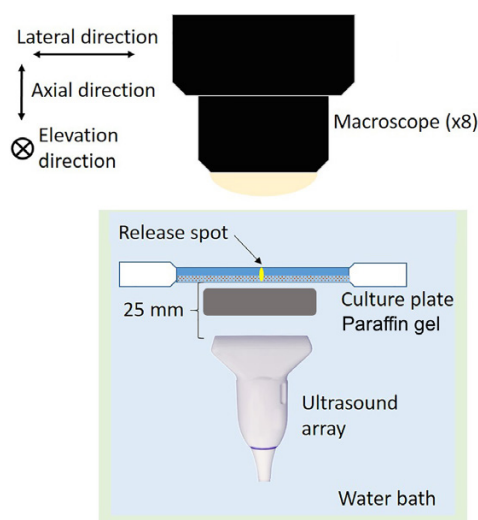


Figure1. Experimental set-up used for *in vitro* acoustic vaporization.

A hemispheric transducer (Imasonics) connected to an amplified function generator was also used to assess the influence of pulses frequency on vaporization threshold. The set-up remained the same, while the focused pulse properties were changed to 2.25 MHz. In this case, ADV was only observed through fluorescence microscopy, as ultrafast monitoring is not possible with this transducer.

Peak negative pressure (PnP) at focal spot were evaluated in water using an interferometer described by C. Barrière et al.^[3] It uses the phase modulation of a laser beam reflected on an 5 μm -thick optically reflective mylar membrane materializing moving particles.

Results

We measured the PnP obtained behind all gels using the interferometer (Figure 2 left), which allowed us to determine their attenuation coefficients (Figure 2 right). Conversely to what is expected, the fact that lower frequencies do not seem to be those for which we observe lowest attenuations is an artifact due to the inefficiency of the linear probe to emit pulses at 2.5 or 3 MHz. Similar measurements were realized with the hemispheric transducer at 2.25 MHz.

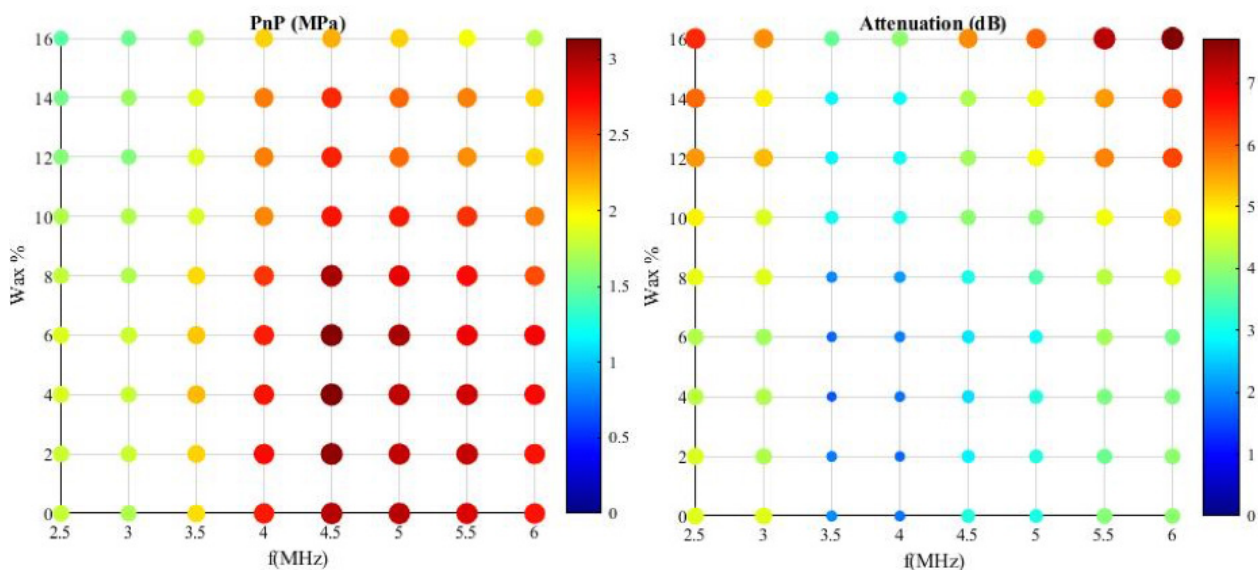


Figure 2. Left: PnP values at focal spot of linear transducer depending on wax percentage and pulse frequency. Right: attenuation coefficient of gels calculated from measured PnP.

Knowing the attenuation coefficients of our gels, we were then able to accurately determine the PnP vaporization threshold or composite microdroplets for all gels and for both linear array at 5 MHz and hemispheric transducer at 2.25 MHz (Figure 3).

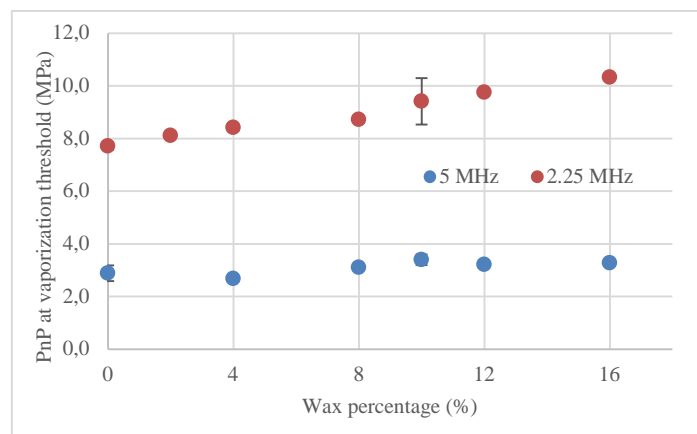


Figure 3. PnP absolute values at vaporization threshold

Conclusions

These results show that vaporization threshold does not depend on the presence of an absorbing medium between transducer and droplets. However, there is an important shift between both transducer, which may be explained by the strong influence of frequency on vaporization threshold.^[4-6] The slight increase observed for 2.25 MHz experiments is the consequence of the non-linearity of the amplifier we used at highest voltages. Yet, potential aberration is not taken into account here, and may have a significative influence. Experiments with mice skull were also realized and we were able to compare its attenuation to formulated gels, as well as observe droplet vaporization through it. All these data suggest that ADV is a reliable phenomenon in well-defined situations. However, some conditions such as pulse frequency, droplet environment (e.g. blood vessel diameter), droplet composition or size may strongly impact ADV and it is important to decipher their influence prior to use them as therapeutic agents or pressure probes.

References

- [1]. Hingot V, Bézagu M, Errico C, Desailly Y, Bocheux R, Tanter M, Couture O, *Appl. Phys. Lett.* 109:194102, 2016.
- [2]. Teston E, Hingot V, Faugeras V, Errico C, Bézagu M, Tanter M, Couture O, *Biomedical Microdevices*, 20:94, 2018.
- [3]. Barrière C, Montaldo G, Jacob X, Royer D, Fink M, Quantitative measurements of ultrasonic shock waves using a standard optical interferometer.
- [4]. Kripfgans OD, Fowlkes JB, Miller DL, Eldevik OP, Carson PL, *Ultrasound Med. Biol.* 26(7):1177-1189, 2000.
- [5]. Kripfgans OD, Fowlkes JB, Woydt M, Eldevik OP, Carson PL, *IEEE Trans. Ultrason. Ferroelectr. Freq. Control*, 49(6):726–738, 2002.
- [6]. Lacour T, PhD manuscript « Modélisation de la vaporisation acoustique de gouttelettes micro- ou nano-métriques encapsulées par des coques hyperélastiques ou des tensio-actifs », 2018.

Pharmacokinetic analysis of targeted nanobubbles for quantitative assessment of PSMA expression in prostate cancer

Simona Turco¹, Reshani Perera², Hessel Wijkstra^{1,3}, Agata A. Exner², M. Misch¹

¹*Biomedical diagnostics lab, Eindhoven University of Technology, Eindhoven, the Netherlands*

²*Departement of Radiology, Case Western Reserve University, Cleveland OH, United States*

³*Departement of Urology, Amsterdam University Medical Center, Amsterdam, the Netherlands*

Corresponding author: s.turco@tue.nl

Introduction

Despite showing promise, the sensitivity of contrast enhanced ultrasound (CEUS) for prostate cancer diagnosis is still limited [1]. The introduction of novel microbubbles (MBs) targeted to the vascular endothelial growth receptor factor 2 has opened new possibilities for molecular imaging of prostate cancer [2, 3]. However, the detection rate in a phase-0 clinical trial was still limited to 65% [2]. More effective contrast agents are needed to improve diagnostic accuracy. Recently, ultrasound nanobubbles (NBs) are emerging as promising agents for improved cancer diagnostics and therapy [4]. Thanks to their reduced diameter, which is about 10 times smaller than MBs, they can cross the vascular endothelium, providing greater possibilities for targeted imaging and therapy, including targets no longer limited to the vessel wall. In this context, a long-circulating NB targeted to the prostate-specific membrane antigen (PSMA) was recently developed, showing promise for selective accumulation in tumors expressing PSMA [5]. In this work, we propose pharmacokinetic modeling of the kinetics of PSMA-targeted NBs by the simplified reference tissue model [6, 7]. While this model has been originally developed for receptor kinetic studies in nuclear medicine, it is here adapted for CEUS, enabling quantitative assessment of PSMA expression by estimation of the binding potential BP. The model is validated by comparing the estimated binding parameter obtained for three different US contrast agents (conventional MBs, non-targeted NBs, and PSMA-targeted NBs) in a dual tumor mouse model, carrying a PSMA-positive tumor in one flank, and a PSMA-negative tumor in the other flank.

Methods

Pharmacokinetic modeling

PSMA-targeted NBs can cross the vascular endothelium and distribute into tissue, especially in case of enhanced vascular permeability (e.g., angiogenic tumor vasculature). Moreover, they may also attach to the membrane of cells expressing PSMA. The kinetics of PSMA-targeted NBs may thus be described by a pharmacokinetic model with three compartments: the plasma compartment, the “free” tissue compartment, where no specific NB binding occurs, and the “bound” tissue compartment, where specific NB binding may occur. When a reference tissue is also considered, i.e., a tissue without specific binding, the kinetics of targeted-NB can be described by the following differential equations

$$\left\{ \begin{array}{l} \frac{dC_r(t)}{dt} = K_1 C_p(t) - k_2 C_r(t) \\ \frac{dC_f(t)}{dt} = K_1 C_p(t) - k_2 C_r(t) - k_3 C_f(t) + k_4 C_b(t), \\ \frac{dC_b(t)}{dt} = k_3 C_f(t) - k_4 C_b(t) \end{array} \right. \quad (1)$$

where $C_p(t)$, $C_f(t)$, $C_b(t)$, and $C_r(t)$ are the concentrations of NBs in the plasma, free, bound, and reference tissue compartments, respectively; K_1 ($\text{ml} \cdot \text{ml}^{-1} \cdot \text{min}^{-1}$) is the rate constant for transfer from plasma to free compartment; k_2 is the rate constant for transfer from free to plasma compartment (min^{-1}); k_3 is the rate constant for transfer from free to bound compartment (min^{-1}); k_4 is the rate constant for transfer from bound to free compartment; K'_1 is the rate constant for transfer from plasma to reference compartment ($\text{ml} \cdot \text{ml}^{-1} \cdot \text{min}^{-1}$); k'_2 is the rate constant for transfer from reference to plasma compartment (min^{-1}). When the kinetics in the target region are difficult to distinguish between the free and bound compartments, the system of equation in (1) can be simplified by replacing the second and third equations by

$$\frac{dC_t(t)}{dt} = K_1 C_p(t) - k_{2a} C_t(t), \quad (2)$$

where $C_t(t)$ is the NB concentration in the target tissue, and k_{2a} (min^{-1}) is the apparent (overall) rate constant for transfer from target compartment to plasma, for which the following relationship should hold

$$\frac{K_1}{k_{2a}} = \frac{K_1}{k_2} (1 + \text{BP}), \quad (3)$$

with BP being the binding potential defined as $\text{BP} = k_3/k_4$. If the NB concentration in the target and reference tissues can be measured, defining the ratio $R_1 = K_1/K'_1$, the solution of the simplified reference tissue model can be obtained as

$$I_t(t) = R_1 I_r(t) + \left(k_2 - \frac{R_1 k_2}{1 + \text{BP}} \right) I_r(t) * e^{-\frac{k_2}{1 + \text{BP}} t}, \quad (4)$$

where $I_t(t) = G \cdot C_t(t)$ and $I_r(t) = G \cdot C_r(t)$ are the linearized acoustic intensity over time in the target and reference tissues, respectively, and G is a multiplicative constant. In fact, although in practice the concentrations $C_t(t)$ and $C_r(t)$ are not available, a linear relationship between the acoustic intensity and the contrast concentration can be assumed, provided that time-intensity curves (TICs) obtained from CEUS loops are properly linearized [7].

Contrast ultrasound imaging on tumor models

A dual tumor mouse model was obtained by subcutaneous implantation of PSMA-positive PC3pip cells in one flank of a mouse, and PSMA-negative PC3flu cells in the other flank. The animal was handled according to a protocol approved by the Institutional Animal Care and Use Committee (IACUC) at Case Western Reserve University. Once the tumor diameter reached ~ 0.8 cm, the animal underwent a CEUS exam by injection of a 200- μL bolus of either non-targeted NBs or PSMA-targeted NBs, which were prepared according to [5]. Imaging was performed with a Toshiba US scanner (AplioXG SSA-790A, Toshiba Medical Imaging Systems, Otawara-Shi, Japan) equipped with a PLT-1204BT probe working at 12 MHz (MI, 0.1; dynamic range, 65dB; gain, 70dB; imaging frame rate, 0.2 frames/s), which was placed so as to visualize both tumors in the same field of view. After 30 min, repeated high-intensity flashes were applied to destroy any residual NB, and the other agent (non-targeted NBs or PSMA-targeted NBs) was administered with the same protocol. Finally, the mouse received a 200- μL bolus of Lumason (Bracco Diagnostics Inc, Plan-les-Ouates, Switzerland) and scanning was repeated as above.

Regions of interest (ROIs) were drawn on both PSMA-positive and PSMA-negative tumors, and TICs for each ROI were collected and linearized. For each contrast agent, the binding potential BP was estimated by fitting the linearized TIC from the target tissue (PSMA-positive ROI) by equation (4), using for the reference tissue the TIC obtained from the PSMA-negative ROI. Non-linear curve fitting was performed by the Trust-region reflective algorithm, constraining the parameters between 10^{-5} and 5, and repeated 50 times. For each repetition, 100 random initializations of the fitting parameters were tried, and the estimated parameters providing the minimum squared error were selected.

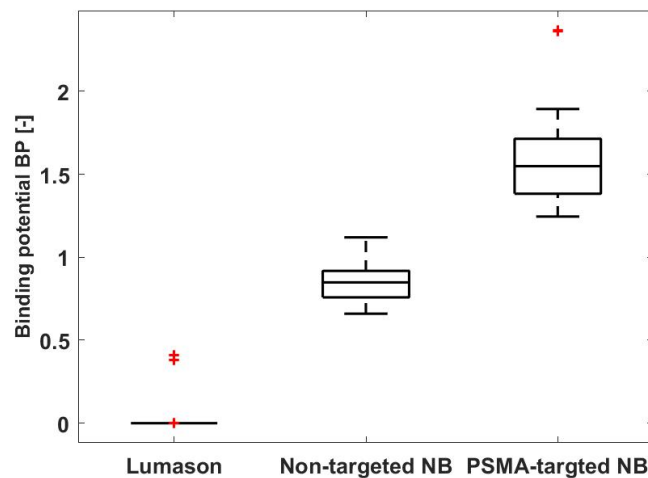


Fig. 1 Estimated BP for Lumason, Non-targeted NB, and PSMA-targeted NB in a PSMA-positive tumor.

Results

The boxplot in Fig.1 shows the estimated BP for the three different US contrast agents over 50 repetitions of the fitting procedure. The estimated BP was nearly zero for conventional MBs, while the highest value was obtained for PMSA-targeted NBs. Examples of TICs obtained for the three different contrast agents in the reference and target tissues, together with corresponding model fits are shown in Fig. 2.

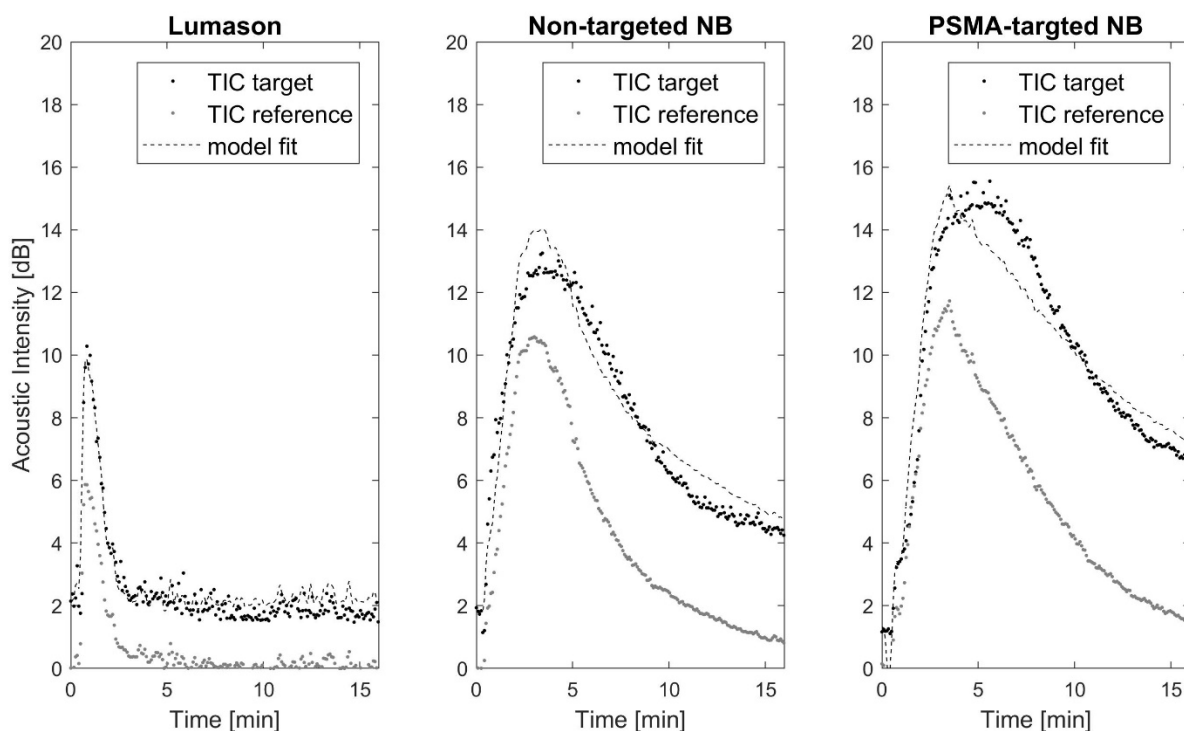


Fig. 2 Examples of TICs extracted from the reference tissue (PSMA-negative ROI) and target tissue (PSMA-positive ROI), together with corresponding model fit of the target TIC.

Conclusions

In this work, pharmacokinetic analysis of targeted-NBs was performed by the simplified reference tissue model. The binding potential BP was estimated for quantitative assessment of PSMA expression in a PSMA-positive tumor model. As expected, the estimated BP was nearly zero for conventional MBs, which cannot cross the vascular endothelium and thus cannot reach the binding target (cell membrane). The highest BP was obtained for PSMA-targeted NBs, suggesting that these NBs are able to reach and bind to the target. Although a non-zero BP value was also obtained for non-targeted NBs, it should be noted that $BP=k_3/k_4$, and thus reflects both binding (k_3) and unbinding (k_4). This suggests that non-specific binding may still occur for non-targeted NBs. To conclude, pharmacokinetic analysis of the kinetics of PSMA-targeted NBs by the simplified reference tissue model is feasible. The binding potential BP may represent a promising parameter for quantitative assessment of PSMA expression in prostate tumors. However, the proposed method requires the presence of a reference tissue in the field of view. In the future, alternative pharmacokinetic models could be investigated that include modeling of the contrast plasma concentration, similar to [3], permitting additional assessment of the vascular compartment, and avoiding the need to measure the concentration in the reference tissue.

References

- [1]. Wink, Margot, et al. "Contrast-enhanced ultrasound and prostate cancer; a multicentre European research coordination project." *European urology* 54.5 (2008): 982-993.
- [2]. Smeenge, Martijn, et al. "First-in-human ultrasound molecular imaging with a VEGFR2-specific ultrasound molecular contrast agent (BR55) in prostate cancer: a safety and feasibility pilot study." *Investigative radiology* 52.7 (2017): 419-427.
- [3]. Turco, Simona, et al. "Quantitative ultrasound molecular imaging by modeling the binding kinetics of targeted contrast agent." *Physics in Medicine & Biology* 62.6 (2017): 2449.
- [4]. Perera, Reshani H., et al. "Ultrasound imaging beyond the vasculature with new generation contrast agents." *Wiley Interdisciplinary Reviews: Nanomedicine and Nanobiotechnology* 7.4 (2015): 593-608.
- [5]. Perera, Reshani H., et al. "Nanobubble Extravasation in Prostate Tumors Imaged with Ultrasound: Role of Active versus Passive Targeting." *IEEE International Ultrasonic Symposium 2018, Kobe, Japan*.
- [6]. Lammertsma, Adriaan A., and Susan P. Hume. "Simplified reference tissue model for PET receptor studies." *Neuroimage* 4.3 (1996): 153-158.
- [7]. Mischi et al. "Quantification of Contrast Kinetics in Clinical Imaging", Springer Nature, 2018.

Multi-Source Passive Acoustic Source Localisation for Diagnostic and Therapeutic Applications

Catherine M. Paverd¹, Erasmia Lyka¹, Constantin-C. Coussios¹

*¹Institute of Biomedical Engineering, University of Oxford, Oxford, United Kingdom
Corresponding author: catherine.paverd@eng.ox.ac.uk*

Introduction

Many *in vitro* and *in vivo* ultrasound applications rely on cavitation effects. Thus the localisation of cavitation activity can provide significant benefit in assessing treated versus untreated regions. In addition, accurate localisation of cavitation could provide information on nuclei distribution within an area, which may prove useful for diagnostic applications such as tumour vessel imaging. Presently, the most advanced method of monitoring cavitation during therapy is Passive Acoustic Mapping (PAM), which relies on conventional or adaptive beamforming, and aims to display the total cavitation energy in a spatial region [1,2]. For a single linear ultrasound array at a typical distance of 70 mm from a target, the spatial resolution of a real-time adaptive PAM algorithm is approximately 0.5 x 5 mm. Although PAM provides a useful indication of cavitation activity, some *in vitro* and *in vivo* applications have smaller length scales and require precise localisation of cavitation events rather than assessment of total cavitation energy in a large region. Recently, super-resolution imaging techniques for both active and passive source mapping have been developed for use in these situations, however these approaches assume the presence of a single acoustic source within the Point Spread Function of the system [3,4]. In reality, multiple sources may be present, for example, when high concentrations of cavitation nuclei are used.

Methods

Here we present a two-step approach to separate and localise multiple simultaneous cavitation events, and we verify the technique through simulation and experiment. In the proposed algorithm, we first use a method known as Independent Component Analysis (ICA) to reconstruct the signals generated by individual cavitation events using higher-order statistical methods [5]. ICA treats each element in the central part of the array as an individual receiver that records a linear mix of signals generated from separate cavitation sources, called Independent Components (ICs). The second part of the algorithm estimates source location for each IC using a Time-Difference-of-Arrival method of Acoustic Source Localisation (ASL). Time delays for each IC on every element of the array are determined using a generalised cross-correlation approach, and ASL is performed by fitting a polynomial to the delays.

We evaluate the new IC-ASL cavitation localization algorithm for a variety of situations using both simulated and experimental data. For experiments, either a 3% agarose gel phantom, or flow channels containing Sonovue® (Bracco) microbubbles, were placed at the focus of a single HIFU transducer. Short pulses of 5 to 100 cycles at 0.5 MHz with peak rarefactional pressures in the range 0 – 3 MPa were used to cause cavitation in the phantom or flow channels. For cavitation monitoring, received signal data was passively recorded on two perpendicular linear arrays which, when combined, enable high-resolution PAM imaging of cavitation with a resolution of 0.4 mm at a distance of 70 mm from the array. These high resolution PAM images were used to verify the cavitation source locations predicted by the novel cavitation localization method.

Results

In a clinical context, it is typically only possible to use a single array for cavitation monitoring due to limited acoustic access. An example result from experimental data, using an agarose gel phantom excited by 0.5 MHz ultrasound at approximately 72 mm from the array is shown in Figure 1. PAM reconstruction

of the broadband acoustic emissions detected by only one of the two arrays often produced a single, elongated region of cavitation activity. By contrast, the IC-ASL cavitation localization method was able to distinguish multiple cavitation events within the central 1.5 x 1.5 mm area of the PAM cavitation map produced using a single array. These distinct cavitation events were typically less than 1 mm apart, and coincided to within 0.5 mm of the location of cavitation events seen on PAM maps produced using two orthogonal arrays.

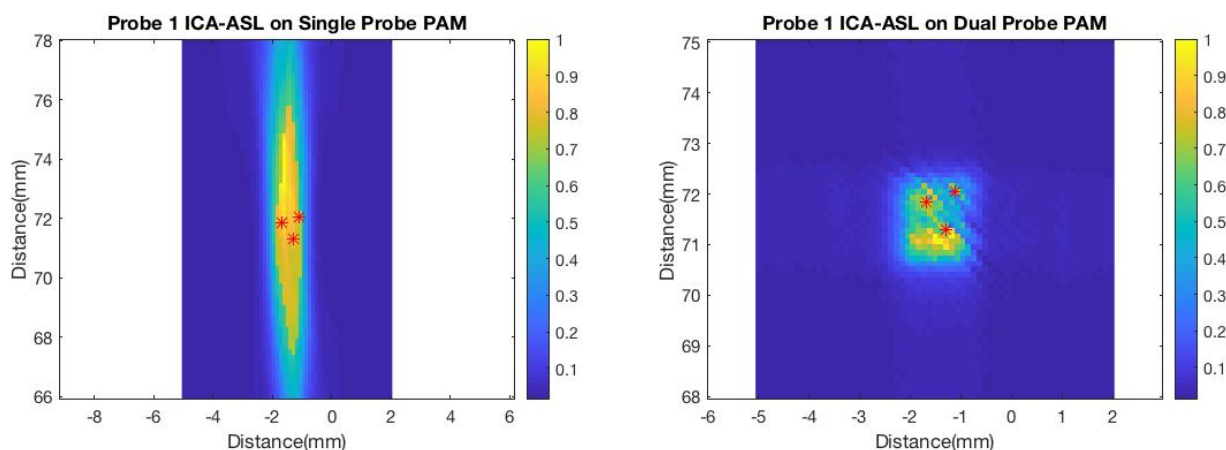


Figure 1: Normalised PAM images created with data from a single probe (left), and dual probes (right). Red stars indicate the output of the BSS-ASL algorithm created using data from a single probe (Probe 1).

Conclusions

The proposed method combining Independent Component Analysis with Acoustic Source Localization has significant potential to improve the accuracy of cavitation localisation for *in vitro* and *in vivo* work, especially in the clinically relevant case where it is only possible to use a single array for cavitation mapping. Further work is necessary to assess system performance limits and to validate the proposed technique *in vivo*.

References

- [1]. Gyöngy, Miklos, et al. Use of passive arrays for characterization and mapping of cavitation activity during HIFU exposure. Ultrasonics Symposium, 2008. IUS 2008. IEEE. IEEE, 2008.
- [2]. Coviello, Christian, et al. Passive acoustic mapping utilizing optimal beamforming in ultrasound therapy monitoring. The Journal of the Acoustical Society of America 137.5 (2015): 2573-2585.
- [3]. Errico, C. et al. Acoustic super-resolution with ultrasound and microbubbles, Nature, vol 527
- [4]. O'Reilly, M. & Hynynen, K., A super-resolution ultrasound method for brain vasculature mapping. Med. Phys, vol 40
- [5]. Hyvärinen, A. Fast and Robust Fixed-Point Algorithms for Independent Component Analysis. IEEE Tran. Neural Networks 10(3)

Spatiotemporal assessment of the cellular safety of cavitation-based therapies by passive acoustic mapping

Cameron A. B. Smith, Constantin C. Coussios

*Institute of Biomedical Engineering, University of Oxford, Oxford, UK
Corresponding author: cameron.smith@eng.ox.ac.uk*

Introduction

Ultrasound-induced cavitation can significantly enhance drug delivery for brain, cardiovascular, oncological, transdermal, and intracellular applications, but can also generate potentially adverse bioeffects that need to be monitored to ensure treatment safety. Previous work using passive cavitation detectors has shown correlations between the cavitation dose and cellular and vascular damage, including haemolysis [1,2]. However, this monitoring is limited to the confocal region between the single-element passive cavitation detector and the therapeutic ultrasound field. More recently, Passive Acoustic Mapping (PAM) using multi-element arrays has proven to be effective at determining the location and extent of cavitation activity both in vitro [3] and in vivo [4,5]. However, while PAM is capable of producing an estimate of the cavitation energy produced by an acoustic source [6], the relationships between the source strength predicted by PAM and cellular bioeffects have not been previously investigated. In this work, the unique opportunity provided by PAM to quantify cavitation dose across an entire volume of interest during therapy is utilised to provide set-up independent measures of spatially localised cavitation dose. This spatiotemporally quantifiable cavitation dose is then related to the level of cellular damage occurring within an ultrasound field under a range of exposure and cavitation nucleation conditions.

Methods

A summary of the experimental set-up is provided in figure 1. Eppendorf tubes containing samples of 0.5 ml of freshly harvested horse blood of physiological haematocrit were mixed with one of two different types of cavitation agent (SonoVue® microbubbles or gas-stabilizing sub-micron solid particles [7]) and placed at the focus of a 0.5 MHz therapeutic transducer. Two perpendicular and co-planar L7-4 linear arrays were used to simultaneously and passively capture acoustic emissions from cavitation to achieve a PAM resolution of 0.4 mm in both the lateral and axial directions. The samples were then exposed to peak rarefactional pressures in the range of 0-2 MPa, using pulse durations in the range of 50-50,000 cycles with duty cycles in the range 1-5% duty cycle which have been previously shown to be effective for drug delivery [8]. Due to the different combinations of cavitation nucleation agent, exposure parameters and location within the therapeutic ultrasound field, different levels of cavitation are generated within each Eppendorf tube, which can be spatio-temporally monitored in real time using PAM. The cumulative cavitation dose observed within each sample over the duration of the exposure can subsequently be correlated to the level of haemolysis, characterized by 541 nm light absorption in plasma-free haemoglobin following sample centrifugation.

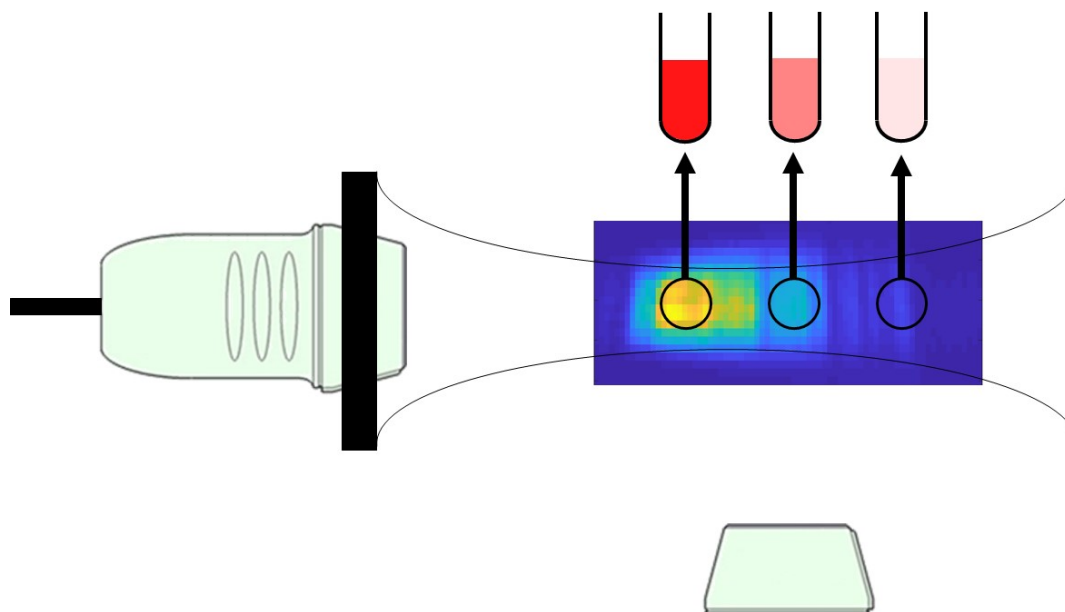


Figure 1: Experimental methods

Results

In the absence of PAM information, with increasing pressure and duty cycle, increasing levels of haemolysis in the range 0-45% were observed, but the level of haemolysis differs for a given set of exposure conditions across cavitation nucleation agents. PAM maps could also be used in the absence of haemolysis information to quantify the cavitation dose within each sample, demonstrating increasing levels of cavitation with increasing pressure and duty cycle. The PAM-derived cavitation dose was found to correlate strongly with the level of haemolysis, irrespective of the exposure conditions or cavitation nucleation agent used.

Conclusions

Initial evidence in anuclear erythrocytes suggests that the cavitation dose predicted by PAM provides a good predictor of cellular damage irrespective of the ultrasound parameters or the cavitation nucleation agent being used. Subject to future work validating this finding in both nuclear cell lines and cells embedded within a viscoelastic media, PAM could become an essential tool for ascertaining the safety of cavitation-enhanced treatments in real time.

References

- [1]. Chen, W. S. et al. Inertial cavitation dose and hemolysis produced in vitro with or without Optison, *Ultrasound in Medicine and Biology*, 29: 725-737, 2003.
- [2]. Hwang, J. H. et al. Correlation between inertial cavitation dose and endothelial cell damage in vivo, *Ultrasound in Medicine and Biology*, 32: 1611-1619, 2006.
- [3]. Coviello, C. et al. Passive acoustic mapping utilizing optimal beamforming in ultrasound therapy monitoring. *The Journal of the Acoustical Society of America*, 137.5, 2573-2585, 2015.
- [4]. Choi J. J. et al. Non-invasive and real-time passive acoustic mapping of ultrasound-mediated drug delivery *Physics in Medicine and Biology*, 59.17: 4861-4877, 2014.
- [5]. Crake, C. et al. Enhancement and passive acoustic mapping of cavitation from fluorescently tagged magnetic resonance-visible magnetic microbubbles in vivo, *Ultrasound in Medicine and Biology*, 42.5: 1302-1306, 2016.
- [6]. Gray, M. D. et al. Diffraction Effects and Compensation in Passive Acoustic Mapping, *IEEE transactions on ultrasonics, ferroelectrics, and frequency control*, 65.2: 258-268 2018.
- [7]. Kwan, J. J. et al. Ultrasound-propelled nanocups for drug delivery, *Small*, 11.39: 5305-5314 2015.
- [8]. Myers, R. et al. Polymeric cups for cavitation-mediated delivery of oncolytic vaccinia virus, *Molecular Therapy*, 24.9: 1627-1633 2016.

Microbubble – microvessel interactions and their influence on UmTDD: Simulation study

R. Domingo-Roca¹, J.C. Jackson², H. Mulvana¹

¹Medical and Industrial Ultrasonics/School of Engineering, University of Glasgow, Glasgow, UK

²Centre for Ultrasonic Engineering/EEE Department, University of Strathclyde, Glasgow, UK

Corresponding author: roger.domingo-roca@glasgow.ac.uk

Introduction

Ultrasound-mediated Targeted Drug Delivery (UmTDD) is a rapidly advancing field with great potential for localised treatment of many diseases. Microbubbles (μ Bs) are used as the target objects and are ensonified to oscillate and produce bioeffects. Even though physics of μ B oscillations have been thoroughly studied [1-3], the impact of confinement within microvessels on their behaviour is non-trivial [2,3].

The size of gas-filled micro-bubble contrast agents has both an impact on bubble distributions within the body and dictates the resonance frequency when driven acoustically. Upon exposure to low-amplitude acoustic fields, μ Bs are known to spherically oscillate at small amplitudes. As oscillations increase in amplitude, approximation of expansion as being symmetric becomes increasingly inaccurate, eventually leading to μ B rupture at sufficiently large peak negative pressures. This ability to selectively direct or amplify acoustic energy through μ B oscillation is the basis for their use in localised therapeutic applications.

Understanding the existence and extent of μ B-cell interaction becomes a determining factor within the complex microvasculature-fluid system. Thus, it becomes essential to better understand the influence of small blood vessels on μ B flow and oscillation under a driving acoustic field in order to exploit UmTDD as a clinically applicable technology.

It is well known that real physical systems at equilibrium become nonlinear when driven at large amplitudes, which has consequences on the effective resonance frequency of the system. Changes in external acoustic pressure will create μ B resonance frequency shifts, having a direct effect on their oscillation amplitude. Hence, these effects must be taken into account experimentally when studying UmTDD applicability. Furthermore, μ Bs enclosed within capillary networks suffer an extra degree of hydrostatic and mechanical damping due to confinement and vessel-wall effects respectively which lead to a shift in their resonance frequency, invalidating the assumption of using the Minnaert frequency during these treatments. In addition, the continuous interaction with the capillary wall will produce a further shift of the resonance frequency, as high- and low-pressure regions are created around the μ B.

In this work, we study how the resonance frequency of contrast agent μ Bs is modified as a function of two key parameters: relative radius between capillary and μ B, and μ B proximity to the vessel wall. We use acoustic-pressure amplitude values relevant for UmTDD treatments, which have been reported to be from hundreds of kPa to a few MPa [4,5], to ensure we are operating in a regime of maximised μ B oscillation. The obtained results help us to better understand the key parameters influencing UmTDD efficiency and allow us to develop a platform in which we can directly study key parameters related to its efficacy and potential.

Methods

Micro-bubble oscillation is modelled using two-phase flow in the finite element analysis (FEA) software COMSOL Multiphysics©. We theoretically assess the resonance frequency shift μ Bs undergo within blood capillaries and how it is influenced by μ B position and size relative to blood capillary diameter. These studies included μ B radii from 0.5 to 4 μ m within 5 μ m radius capillaries. Before

studying the influence of μB relative size and position, μB behaviour in an infinite fluid domain was studied and validated against Rayleigh-Plesset behaviour.

Results

FEA COMSOL simulation has proven to be a good tool to obtain an approximate behaviour of μBs when confined within blood vessels. Prior to the study, the μBs were checked to follow the ideal gas law, as well as the Rayleigh-Plesset behaviour when acoustically driven in an infinite volume of fluid. These two previous studies were run to ensure data reliability (Fig. 1) and validated the use of a 2D system to optimize computation time while keeping data accuracy.

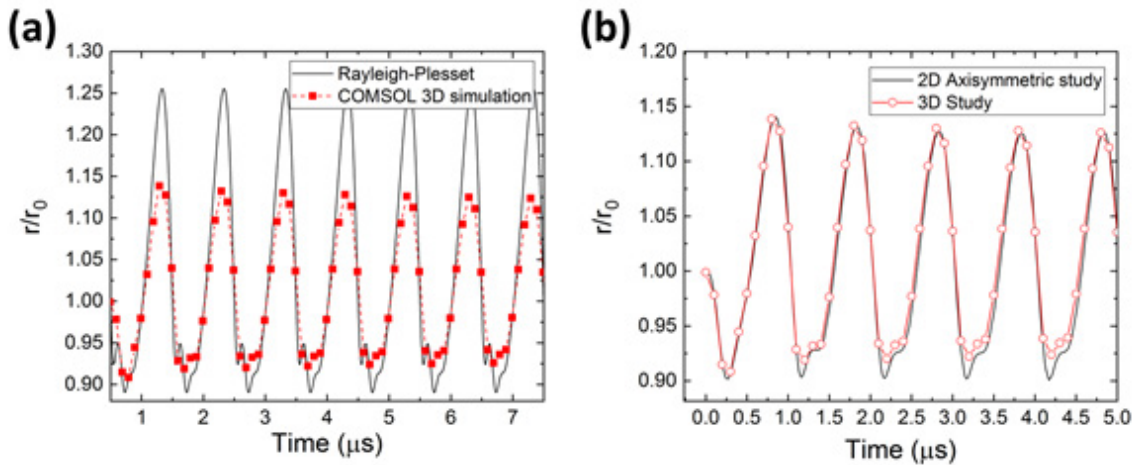


Fig. 1: Data validation. (a) shows the comparison between COMSOL results obtained from 3D geometries and the results obtained from solving the Rayleigh-Plesset equation. (b) Shows a comparison between COMSOL results obtained from simulations using 3D and 2D-axisymmetric geometries.

Confined μBs suffer a non-negligible decrease of their resonance frequency when compared with their corresponding Minnaert frequencies (Fig. 2). However, when the confinement effects are insignificant, μBs re-gain their Minnaert frequency. This resonance frequency shift is due to an increase in the damping of the system, as both the surrounding fluid and the solid vessel wall contribute to it. This result could be hugely beneficial for the development of UmTDD technology for medical applications, as resonance frequency shifts up to 44.2%, suggest that a greater response of the μBs would occur at its confined resonance frequency than at their Minnaert frequency.

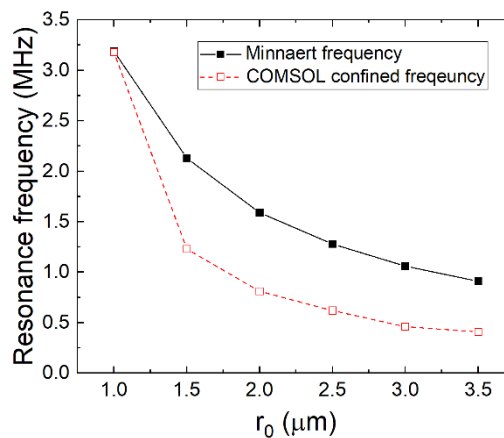


Fig. 2: Comparison between the resonance frequency of micro-bubbles when surrounded by an infinite volume of liquid (Minnaert frequency, as shown by the empty squares connected with a red-dashed line) and when confined within a blood vessel. When a $1 \mu\text{m}$ radius bubble is confined within a large enough vessel, the Minnaert frequency is recovered. As the bubble becomes highly confined, deviation from the Minnaert frequency becomes larger.

Proximity of the μ Bs to the vessel wall was studied in COMSOL to see how the different positions can influence the resonance frequency of the system (Fig. 3, where 0 represents the centre of the vessel). From Fig. 3 it can be observed that as μ B size increases, the resonance frequency shift decreases. Our resonance frequency study is limited to μ B oscillations no larger than the internal diameter of the vessel, which was observed to take place from 2.5 μ m radius bubbles upward. Hence, for radii above this value, a proper study of the resonance frequency of the system cannot be performed as oscillation amplitude exceeds the confinement of the vessel. It can be further observed from Fig. 3 that the maximum frequency shift as a function of μ B position is of 120 kHz.

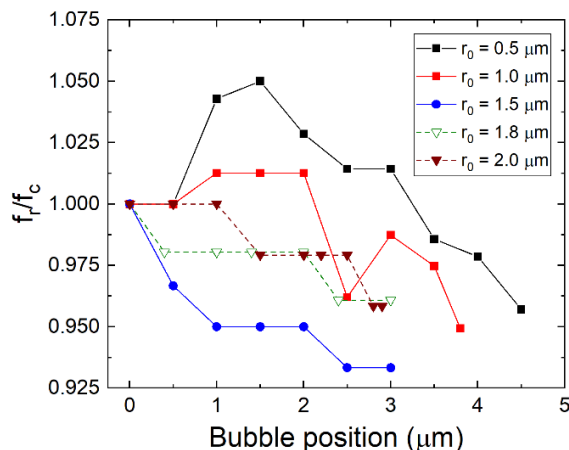


Fig. 3: Resonance frequency shift for different micro-bubble sizes as they approach the vessel wall. Their resonance frequency has been normalised to their resonance frequency when placed at the centre of the vessel (f_c).

Conclusions

In this work, we show that μ B confinement and proximity to vessel wall are key factors to take into consideration to develop UmTDD protocols, as they have both been observed have an effect on the resonance frequency of the system. We have proved that simulation using COMSOL is an appropriate tool as it provides good agreement between theoretical and simulated results. Whereas confinement effects have been observed to produce a dramatic shift of the resonance frequency of the system (44% shift with respect to Minnaert frequency), proximity to vessel wall was observed to produce maximum frequency shifts of 120 kHz (representing maximum shifts of an 8.22%), becoming unimportant for UmTDD given the wide bandwidth of the used transducers.

The next step is to experimentally validate these results by using 3D-printed micro-channels using tissue-mimicking materials. These will be filled with blood-mimicking fluid altogether with 2-8 μ m μ Bs, and the full system will be acoustically stimulated using several ultrasonic frequencies that will allow determining the resonance frequency of the system by recording the μ Bs oscillation using high-speed camera technology and by adequately treating the obtained data.

References

- [1]. Lauterborn W, Kurz T, Physics of bubble oscillations, Reports on Progress in Physics, 73: 106501, 2010.
- [2]. Leighton TG, The inertial terms in equations of motion for bubbles in tubular vessels or between plates, Journal of the Acoustical Society of America, 730: 3333-3338, 2011
- [3]. Vincent O, Marmottant P, On the statics and dynamics of fully confined bubbles, Journal of Fluid Mechanics, 827: 194-224, 2017.
- [4]. Baseri B, Choi JJ, Tung Y-S, Konofagou EE, Multi-modality safety assessment of blood-brain barrier opening using focused ultrasound and definity microbubbles: A short-term study, Ultrasound in Medicine & Biology, 36: 1445-1459, 2010.
- [5]. Sutton JT, Haworth KJ, Pyne-Geithman G, Holland CK, Ultrasound-mediated drug delivery for cardiovascular disease, Expert opinion on drug delivery, 10: 573-5592, 2013.

Real-time Cavitation Therapy Monitoring with a Clinical Scanner

Sara B. Keller, Michalakis Averkiou

*Department of Bioengineering, University of Washington, Seattle, USA
Corresponding author: sbkeller@uw.edu*

Introduction

Ultrasound-mediated drug delivery using microbubbles is a promising drug delivery technique that can lead to enhanced local therapeutic effect or macromolecule transport. The therapeutic mechanism is thought to be a result of cavitation events in the site of interest [1]. Depending on the desired therapeutic outcome, different types of cavitation activity, stable or inertial, may be preferred [2]. Therefore, there is a need for real-time monitoring of cavitation activity during therapy. Currently, most passive cavitation detection schemes are done with single element transducers [3,4], which do not have the ability to spatially localize the source of cavitation events, or with research scanners [5,6] that do not have the computational efficiency to perform cavitation detection in real time. Our hypothesis is that we can manipulate clinical systems to monitor microbubble cavitation activity during therapeutic pulse sequences in real-time.

Methods

Experimental Setup

A single element focused transducer (diameter = 50 mm, focal distance = 50 mm, frequency = 1.1 MHz) was used as the source of cavitation excitation. A Philips EpiQ (C5-1 transducer) was modified to listen to cavitation activity. Microbubbles were supplied with a peristaltic pump through silicon tubing (outer diameter = 9.5 mm). The center of the tube was placed at the focus of the transducer, such that microbubbles flowed left to right. The curvilinear array was placed 3.5 cm away and 90 degrees from the length of the tubing such that the cross section of the tube appeared as a circle when using standard B-mode imaging. This is shown more clearly in Fig. 1.

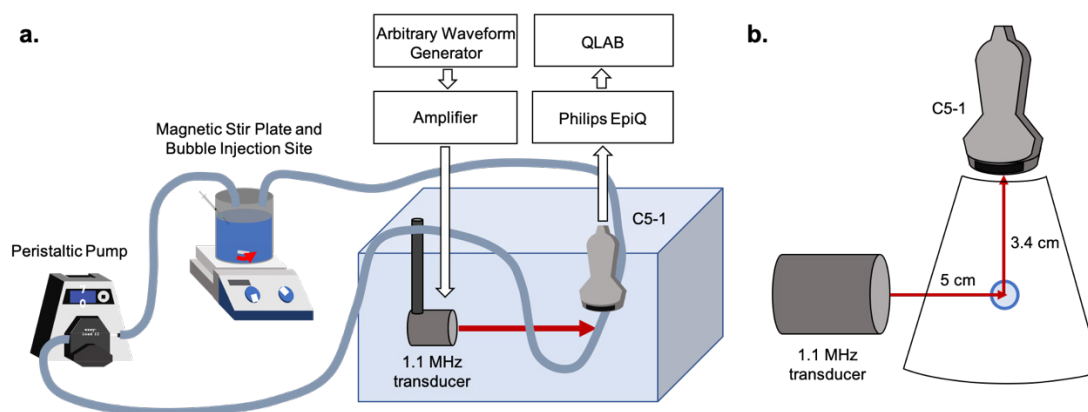


Figure 1: (a) Experimental setup for imaging cavitation activity. (b) Schematic of setup with defined distances and sector width.

Triggering and Synchronization

Transmission from the single element transducer was synchronized with the imaging system such that a single pulse would be sent for each frame. The imaging system was reduced to a sector width of 45 lines, each with an average PRF of 9.1 kHz (or 110 μ s per line). The frame rate was 201 Hz, meaning that it took 5 ms to create each frame. Image formation was internally triggered once per second, meaning that while each frame took only 5 ms to make, the system paused for 1 second before continuing to make another

frame. Pulses were delayed so that they arrived in the center of the sector width. This was done according to Equation 1, where FR is the frame rate of the imaging system (201 Hz), N_{cyc} is the number of cycles per pulse, and $freq$ is the driving frequency of the single element transducer (1.1 MHz). This process is shown in Fig. 2a.

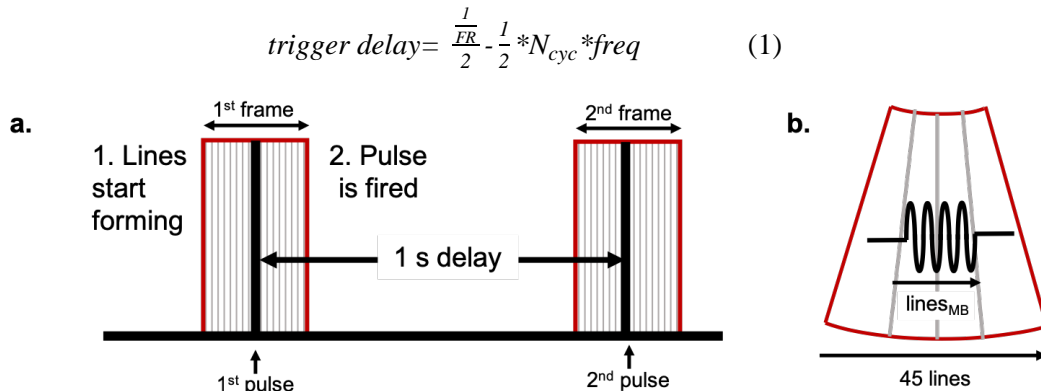


Figure 2: (a) Frame and pulse synchronization. The pulse is sent such that it appears in the center of the frame as described in Equation 1. (b) Schematic of how pulse cycle length compares with the number of lines that microbubble activity appears in. This sector width is further described in Equation 2.

Transmit and Receive Parameters

Transmit parameters for the transducer inducing cavitation were: pressure (0.4 and 4 MPa) and cycles (10, 100, 1000, 2500). Image settings for the clinical scanner were: frame rate (201 Hz), conventional (fundamental) imaging at 3.7 MHz (Gen), line PRF was 9.1 kHz. The scanner was set to 0 volts transmit and was thus operated as a “true” passive cavitation detector (PCD) but it still performed signal acquisition line-by-line. We will refer to this mode as cavitation imaging.

Image Collection

Image loops were acquired for all tested parameters. Image loops were analyzed in QLAB (Philips Medical Systems, Bothell, WA). The first frame that sound appeared was isolated. Gain was appropriately thresholded and remained consistent between all conditions.

Results

Figure 3a shows the position of the tube with and without microbubbles in relation to the sector width with conventional low MI imaging. Figure 3b shows the frames taken from a 4 MPa pulse with 10, 100, 1000, and 2500 cycles, with cavitation imaging (C5-1 only receiving sound).

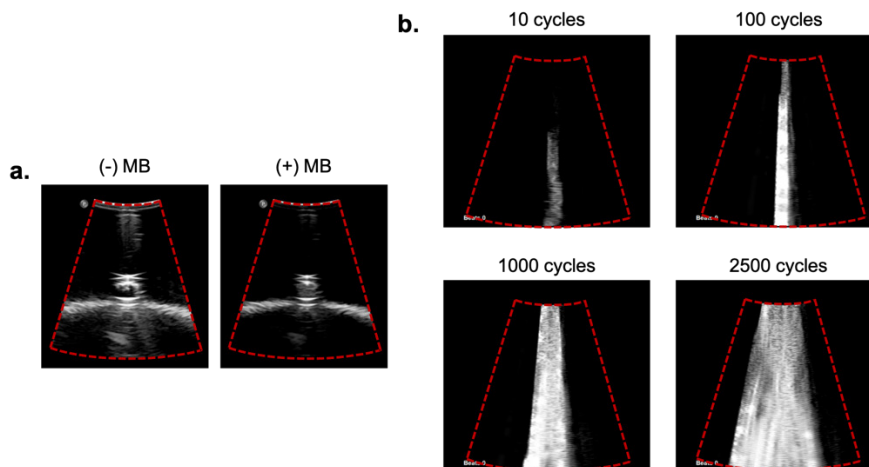


Figure 3: (a) Image of tube using conventional B-mode low MI fundamental imaging with and without microbubbles. (b) Isolated frames from 4 MPa transmit pulses with 10, 100, 1000, and 2500 cycles, recorded with cavitation imaging. As seen, the sector width increases with increasing numbers of cycles.

Increasing the number of cycles increases the number of lines that see bubble activity. This is related to both the imaging frame rate and the pulse duration. This is further justified in Equation 2, where $lines_{MB}$ is the number of lines that receive microbubble signal, pulse duration is the time duration of the pulse (equal to N_{cyc} divided by $freq$), and line duration is the time per line (equal to 1 over the PRF , or 110 us).

$$lines_{MB} = \text{roundup}\left(\frac{\text{pulse duration}}{\text{line duration}}\right) \quad (2)$$

From eq. (2) we calculate the number of lines that see bubble signal for 10, 100, and 1000, and 2500 cycles to be 1, 1, 9, and 21, respectively as seen in Fig. 2b.

When comparing the cavitation images produced with 0.4 and 4 MPa we can identify the type of cavitation: inertial versus stable by the image intensity. A more elegant way to classify cavitation is by frequency analysis of the collected RF data. We are currently changing the receive algorithm of the scanner in order to display cavitation classification easily.

Conclusions

We have developed a way to use a clinical scanner to passively receive ultrasound scattering from microbubbles by using synchronized frame-triggering techniques. This allows for real-time observation of bubble activity during a treatment that produces cavitation. The frequency bandwidth of imaging systems can be tuned to allow for direct observation of specific harmonic components, such as sub- and ultra-harmonics, or broadband frequencies in order to classify cavitation. Real-time qualitative classification of cavitation activity can easily be implemented in the clinic.

References

- [1]. Ferrara K, Pollard R, Borden M. Ultrasound Microbubble Contrast Agents: Fundamentals and Application to Gene and Drug Delivery. *Annu Rev Biomed Eng* 2007;9:415–47.
- [2]. Lentacker I, De Cock I, Deckers R, De Smedt SC, Moonen CTW. Understanding ultrasound induced sonoporation: Definitions and underlying mechanisms. *Adv Drug Deliv Rev Elsevier B.V.*, 2014;72:49–64.
- [3]. Qiu Y, Luo Y, Zhang Y, Cui W, Zhang D, Wu J, Zhang J, Tu J. The correlation between acoustic cavitation and sonoporation involved in ultrasound-mediated DNA transfection with polyethylenimine (PEI) in vitro. *J Control Release* 2010;145:40–48.
- [4]. Goertz DE, Todorova M, Mortazavi O, Agache V, Chen B, Karshafian R, Hynynen K. Antitumor Effects of Combining Docetaxel (Taxotere) with the Antivascular Action of Ultrasound Stimulated Microbubbles. Woloschak GE, ed. *PLoS One Public Library of Science*, 2012;7:e52307.
- [5]. Haworth KJ, Bader KB, Rich KT, Holland CK, Mast TD. Quantitative Frequency-Domain Passive Cavitation Imaging. *IEEE Trans Ultrason Ferroelectr Freq Control* 2017;64:177–191.
- [6]. Lyka E, Coviello CM, Paverd C, Gray MD, Coussios C-C. Passive Acoustic Mapping using Data-Adaptive Beamforming Based on Higher-Order Statistics. *IEEE Trans Med Imaging* 2018;1–1.

Single-bubble-induced elastic deformation of capillary-mimicking hydrogel channels

James H Bezer¹, Hasan Koruk², Akaki Jamburidze³, Valeria Garbin³, James J Choi¹

¹Department of Bioengineering, Imperial College London, London SW7 2AZ, United Kingdom

²Mechanical Engineering Department, MEF University, Istanbul 34396, Turkey

³Department of Chemical Engineering, Imperial College London, London SW7 2AZ, United Kingdom

Corresponding author: j.choi@imperial.ac.uk

Introduction

Microbubbles experience a translational force in the direction of propagation of an ultrasound wave. It has previously been demonstrated that this can be used to induce measurable deformations of soft hydrogels using large, dilute bubble populations in large diameter channels [1][2]. This study aims to investigate whether significant, reversible displacements can be induced by a single microbubble in capillary-like microenvironments under safe ultrasound parameters. Being able to precisely and controllably deform blood vessels using individual bubbles may allow us to improve microbubble therapies by better understanding microbubble-tissue interactions. This technique may also have other applications, such as deriving tissue elasticity values at super-resolution, and precise stimulation of mechanotransduction pathways [3].

Methods

We made $10\pm 5\mu\text{m}$ and $25\pm 10\mu\text{m}$ diameter wall-less channels in soft polyacrylamide gels with Young's modulus measured at $1.2\pm 0.5\text{kPa}$ (rheometer: 1Hz and shear strains of 0.1-10%). The gels were formed around thin metal wires threaded between two hypodermic needles, which were then removed after the gel had set. These channels are comparable in size to typical capillaries, which have a diameter around $5\text{-}10\mu\text{m}$ [3][4], and have comparable elasticity to soft tissue [6]. In-house manufactured microbubbles [1] were then introduced to the channel. Bubble dynamics were observed using a high-speed camera (Photron SA5, connected to an Olympus microscope) at up to 30,000fps, and 40x magnification. A 1MHz focused transducer (Olympus) was used at Peak Rarefactional Pressure (PRP) between 25 and 400kPa. Pulse lengths tested were between 1000 and 50000 cycles.

Results

Several bubbles were observed to reversibly deform the gel by up to $11\mu\text{m}$ (examples in Fig. 1&2). The largest deformations were observed with bubbles of diameter around $3\text{-}5\mu\text{m}$. Bubbles returned to their initial positions after sonication, indicating elastic gel deformation. These deformations were observed at pressures as low as 170kPa, and always less than 400kPa ($MI < 0.4$), which are deemed to be safe for imaging[7].

Conclusions

We have shown that single microbubbles are capable of generating reversible deformations of up to $11\mu\text{m}$ in soft tissue-mimicking hydrogels under safe ultrasound parameters. Further data will be acquired to better understand the relationship between induced deformations and parameters such as bubble size, gel stiffness, and ultrasound frequency. Ongoing work involving *in vitro* live rat brain slices will investigate whether similar results can be obtained in real tissue, and to investigate several biological effects, such as stimulation of astrocyte mechanotransduction pathways.

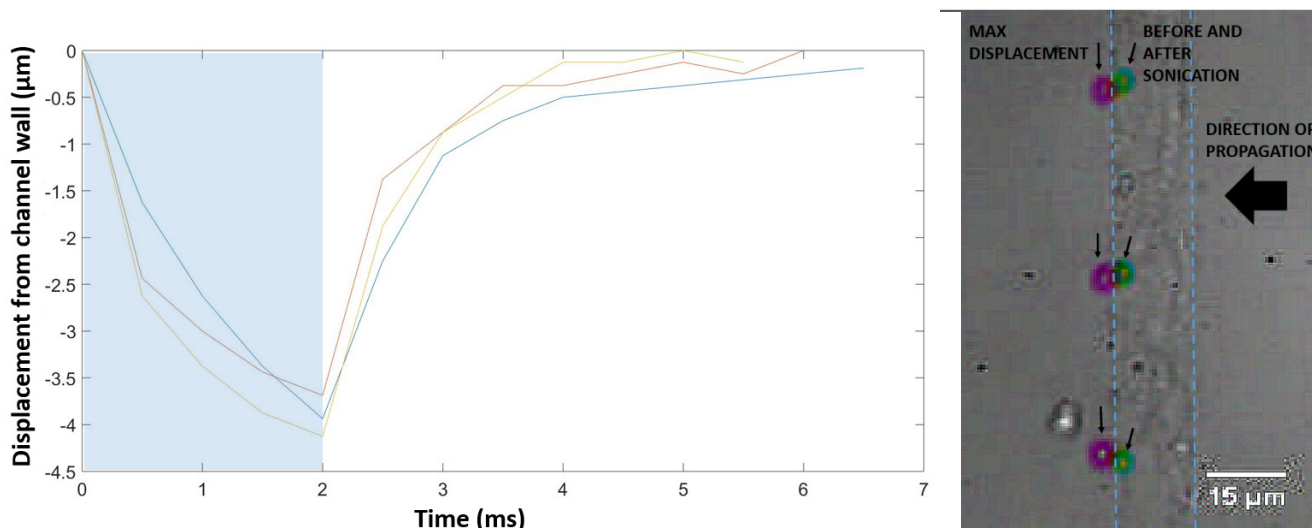


Figure 1: Microbubbles deforming a material from within a 15µm diameter channel. Microbubbles were administered into a wall-less 15-µm-in-diameter channel and then sonicated with a 2-ms pulse (PRP=270kPa, $f_0=1$ MHz). The microbubbles moved from their original position (green, $t=0$ ms), against the issue wall (red, $t=2$ ms), and back to its original position. The bubbles' diameters (small arrows, top to bottom) were 4.0, 4.6, and 3.7 ± 0.5 µm. Dotted lines indicate the channel edges. Graph shows displacement of each bubble from its initial position during and after sonication, showing a return to its initial position. Blue line on graph = top bubble on image; Red = middle; Yellow = bottom. Shaded region indicates period of sonication

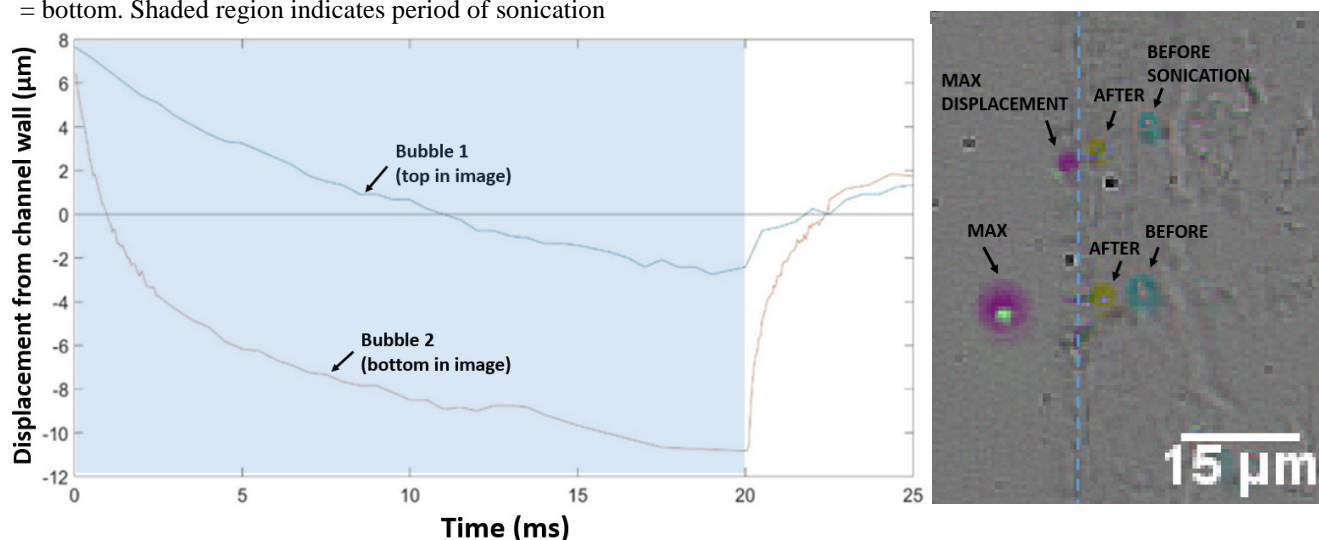


Figure 2: Microbubble displacement. Image: Blue (before) = 0ms; Red (Max): 20ms; Yellow (after) = 25ms. Parameters: 20ms pulse; 1MHz; PRP = 170kPa; Channel size: 33 ± 4 µm; bubble diameters: 2.3 ± 1 µm (top bubble in image, blue line on graph), 3.2 ± 1 µm (bottom in image, red line on graph).

References

- [1]. H. Koruk, A. El Ghamrawy, A. N. Pouliopoulos, and J. J. Choi, "Acoustic particle palpation for measuring tissue elasticity," *Appl. Phys. Lett.*, vol. 107, no. 22, 2015.
- [2]. N. Saharkhiz, H. Koruk, and J. J. Choi, "The effects of ultrasound parameters and microbubble concentration on acoustic particle palpation," *JASA*, 2018.
- [3]. A. S. Kozlov, M. C. Angulo, E. Audinat, and S. Charpak, "Target cell-specific modulation of neuronal activity by astrocytes," *PNAS*, vol. 103, no. 43, 2006.
- [4]. R. F. Potter and A. C. Groom, "Capillary diameter and geometry in cardiac and skeletal muscle studied by means of corrosion casts," *Microvasc. Res.*, vol. 25, no. 1, pp. 68–84, 1983.
- [5]. L. H. Smaje, P. A. Fraser, and G. Clough, "The distensibility of single capillaries and venules in the cat mesentery," *Microvasc. Res.*, vol. 20, no. 3, pp. 358–370, 1980.
- [6]. C. T. McKee, J. A. Last, P. Russell, and C. J. Murphy, "Indentation Versus Tensile Measurements of Young's Modulus for Soft Biological Tissues," *Tissue Eng. Part B Rev.*, 2011.
- [7]. G. ter Haar, "Safety and bio-effects of ultrasound contrast agents," *Med. Biol. Eng. Comput.*, vol. 47, no. 8, pp. 893–900, 2009.

A novel model for an encapsulated microbubble based on transient network theory

Bashir M. Alnajar¹, Michael L. Calvisi¹

¹*Department of Mechanical and Aerospace Engineering, University of Colorado, Colorado Springs, USA
Corresponding author: mcalvisi@uccs.edu*

Introduction

Encapsulated microbubbles (EMBs) are widely used to enhance contrast in ultrasound sonography and are finding increasing use in biomedical therapies such as drug/gene delivery and tissue ablation. EMBs consist of a gas core surrounded by a stabilizing shell made of various materials, including polymers, lipids and proteins. We propose a novel model for a spherical EMB that utilizes a statistically-based continuum theory based on transient networks to simulate the encapsulating material. The use of transient network theory provides a general framework that allows a variety of viscoelastic shell materials to be modeled, including purely elastic solids or viscous fluids. This approach permits macroscopic continuum quantities – such as stress, elastic energy and entropy – to be calculated locally based on the network configuration at a given location. The model requires a minimum number of parameters that include the concentration of network elements, and the rates of attachment and detachment of the elements to and from the network. Using measured properties for a phospholipid bilayer, the model closely reproduces the experimentally-measured radial response of an ultrasonically-driven, lipid-coated microbubble. The model can be readily extended to large nonspherical EMB deformations, which are important in many biomedical applications.

Methods

We consider a spherical, encapsulated gas bubble of instantaneous radius, R , which is suspended in an infinite, incompressible, Newtonian liquid. Due to the encapsulation, we neglect the presence of vapor in the interior and treat it as adiabatic. We assume spherical symmetry and use spherical polar coordinates (r, θ, ϕ) to denote position. If we further assume the shell thickness, d_s , is small compared to the bubble radius (i.e., $d_s \ll R$), the gas density is negligible, and that the shell density and liquid density are comparable, then conservation of momentum in the radial direction yields [1],

$$R\ddot{R} + \frac{3}{2}\dot{R}^2 = \frac{1}{\rho_l} \left[\left(p_0 + \frac{2\sigma}{R} \right) \left(\frac{R_0}{R} \right)^{3\kappa} - p_0 - p_{ac}(t) - \frac{2\gamma}{R} - 4\mu_l \frac{\dot{R}}{R} + \frac{3d_s}{R} \sigma_{rr}(R, t) \right], \quad (1)$$

where ρ_l is the liquid density, μ_l is the liquid viscosity, γ is the surface tension, κ is the ratio of specific heats, R_0 is the initial radius, \dot{R} is the radial velocity, \ddot{R} is the radial acceleration, t is time, p_0 is the hydrostatic pressure of the surrounding liquid, $p_{ac}(t)$ is the applied acoustic pressure, and σ_{rr} is the radial component of the stress tensor in the shell.

In this study, we present a new approach to model the viscoelastic mechanical properties of the bubble encapsulation by utilizing transient network theory (TNT) based on the work of Vernerey et al. [2]. The theory considers the shell material as an active network of interconnected elements that attach and detach at nodes with rates k_a and k_d , respectively, depending on the force applied. The approach here applies to any viscoelastic material and the individual elements could represent, for example, polymer chains, individual lipids, lipid domains or proteins, depending on the encapsulating material. The concentration of elements (or chains) that are attached to the network (moles per unit current volume) is represented by $c(t)$. To estimate the mechanical behavior, the density of the elements (or chains) and the average distance between elements (or chain length) are required. The TNT provides evolution equations

to describe how these quantities vary in time in response to deformation and temperature fluctuations [2]. In the case of a permanent network, in which the rates of attachment and detachment are zero and the concentration is steady, the model reduces to that of an elastic solid. For the case where the kinetics of attachment and detachment are much faster than the rate of loading, a model for a viscous, incompressible fluid is recovered.

In this analysis, we make several simplifying assumptions about the EMB encapsulating material: 1) the dissociation rate coefficient, k_d , is constant; 2) the shell is incompressible; 3) the concentration of attached network elements, c , is steady; 4) the shell temperature is steady and uniform; and 5) mechanical energy dissipation is neglected. The first three assumptions yield the following constant concentration,

$$c = \frac{k_a}{k_a + k_d} c_{tot}, \quad (2)$$

where c_{tot} is the total concentration of elements, including those that are not connected to the network. Equation (2) also implies that the association rate constant, k_a , is constant due to assumptions 1) and 3). Given all of the assumptions above, it can be shown that the radial component of stress in the shell, σ_{rr} , is given by the following equation,

$$\sigma_{rr}(t) = \frac{2}{3} ck_B T \left\{ e^{-k_d t} \left[\left(\frac{R_0}{R(t)} \right)^4 - \left(\frac{R(t)}{R_0} \right)^2 \right] + \int_0^t k_d \left[\left(\frac{R(\tau)}{R(t)} \right)^4 - \left(\frac{R(t)}{R(\tau)} \right)^2 \right] e^{-k_d(t-\tau)} d\tau \right\}, \quad (3)$$

where k_B is the Boltzmann constant and T is the temperature, which is assumed here to be uniform throughout the entire domain. The last term in (3) involves an integral from the initial time $t = 0$ to the current time t , which demonstrates that the instantaneous stress in the shell depends on prior values of the radius, i.e., the shell behavior is history-dependent.

The EMB model using the TNT is represented in simplified form by equations (1)-(3) above. These include three independent parameters for the shell that may be specified as k_a , k_d and c_{tot} , in addition to the temperature, T . However, if temperature is assumed constant, as in the present work, then we can reduce the number of shell parameters to two, $ck_B T$ and k_d , which have physical meaning as discussed below. To solve this model, we apply a 4th-order Runge-Kutta method using MATLAB to numerically solve the nonlinear ordinary differential equation (1) for the radius, $R(t)$, using the values of c and σ_{rr} given by (2) and (3), respectively. The history integral in (3) is solved via the trapezoidal method.

Results

To validate our EMB model using the TNT, we compare the results of simulations to the experimental data of van der Meer et al. [3], as presented in Tu et al. [4]. In the experiment, a lipid-shelled microububle (BR-14, Bracco Diagnostics) with an initial radius of $R_0 = 1.7 \mu\text{m}$ was excited in water with an 8-cycle Gaussian-tapered acoustic pulse with a 2.5 MHz center frequency and 40 kPa maximum pressure amplitude, as shown in the left figure of Fig. 1. The experimental measurements of radius vs. time are shown as circles in the right figure of Fig. 1. To determine appropriate parameters for the TNT model, we derive estimates based on measured properties of lipid bilayers. The experimental data in Fig. 1 shows that the variation in radius – and, thus, the shell strain – is on the order of 10%. For small deformations and constant values of c and k_d , the TNT model degenerates to the well-known Maxwell model of viscoelasticity in which the shear modulus is given by $ck_b T$ and the relaxation time by $1/k_d$ [2]. Based on the results of measurements of shear moduli and relaxation times for solvent-free glycerol mooleate bilayer lipid membranes by Crawford and Earshaw [5], we set $ck_B T = 0.771 \text{ mN/m}^2$ and $k_d = 2.94 \times 10^4 \text{ s}^{-1}$. The liquid parameters in equation (1) are set equal to those for water at standard conditions. Using

these parameter values and the acoustic forcing shown in Fig. 1, the radial response predicted by the TNT model is plotted as a solid line in the right figure of Fig. 1. The fit between the simulation data and the experimental data is quite good over most of the pulse cycle, except near the end of the pulse where there is noticeable discrepancy. This discrepancy suggests there may be damping mechanisms in the EMB that are not accounted for in our model.

In Tu et al. [4], the experimental radius vs. time data shown in Fig. 1 is compared with the simulation results of three spherical EMB models by Marmottant et al. [6], Chatterjee and Sarkar [7] and Hoff [8]. The best-fit shell parameters for each model were determined iteratively by minimizing the standard deviation (STD) between the experimental and calculated radii data. The agreement between the experimental results and these three models based on the best-fit parameters are not shown here, but are similar to the results shown with the TNT model in Fig. 1. In particular, the radius computed by the Marmottant, Sarkar and Hoff models closely match the experimental data in the middle of the pulse cycle, but show noticeable deviations during the beginning and ending transient periods. Thus, the TNT model provides comparable matching to the observed radius vs. time data as the Marmottant, Sarkar and Hoff models. Similar to these models, the TNT model requires the specification of two shell parameters, which in this case are $ck_B T$ and k_d . An important distinction, however, is that the radial response predicted by the TNT model is based on the use of experimental measurements to estimate the shell parameters, whereas the other models use iterative fitting to determine parameter values that provide a good match to the observed data. It is important to note that the use of data from [5] for a lipid bilayer is not ideal as the actual EMB is coated with a lipid monolayer. However, the close fit to the observed radius vs. time data provided by TNT through the use of measured properties, rather than fitted parameters, is encouraging.

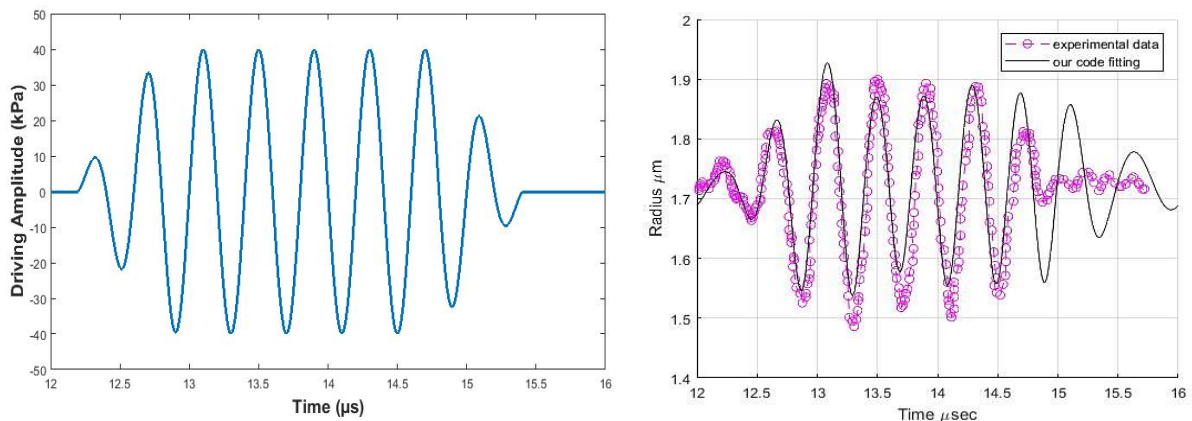


Figure 1: (Left) Gaussian-tapered acoustic pulse with 8 cycles, a 2.5 MHz center frequency and 40 kPa maximum pressure used as input forcing. (Right) Radial response of EMB for $R_0 = 1.7 \mu\text{m}$ based on the transient network shell model (solid line) plotted against the experimental data (circles) of van der Meer et al. [3]. The parameters used in the model are $ck_B T = 0.771 \text{ mN/m}^2$ and $k_d = 2.94 \times 10^4 \text{ s}^{-1}$.

Conclusions

We have presented a novel model for a spherical encapsulated microbubble (EMB) by using a statistically-based continuum theory known as transient network theory (TNT) to account for the shell mechanics. The TNT framework is based on a network of elements that dynamically attach and detach to each other based on specified kinetic rates. The model requires a minimum number of parameters to represent the shell behavior. By using measured values for lipid bilayers to determine these shell parameters, the model accurately simulates the experimental data of a lipid-coated EMB driven by an acoustic pulse. The use of TNT to model the encapsulation has several advantages over current approaches to modeling EMBs. For example, the TNT has the potential to model any viscoelastic material – lipids, polymers or proteins – as well as purely elastic solids or viscous fluids. In addition, microscale physics

that may be important for understanding the dynamic behavior of EMBs can be incorporated into the TNT model in a natural way, unlike present continuum-level models. Furthermore, the TNT provides a means to compute shell stresses locally and account for large amplitude deformations, which allows the theory to be readily adopted into more complex models of nonspherical EMB oscillation.

References

- [1]. Doinikov AA, Haac JF, Dayton PA, Modeling of nonlinear viscous stress in encapsulating shells of lipid-coated contrast agent microbubbles, *Ultrasonics*, 49: 269-275, 2009.
- [2]. Vernerey FJ, Long R, Brighenti R, A statistically-based continuum theory for polymers with transient networks, *Journal of the Mechanics and Physics of Solid*, 107: 1-20, 2017.
- [3]. van der Meer SM, Dollet B, Voormolen MM, Chin CT, Bouakaz A, de Jong N, Versluis M, Lohse D, Microbubble spectroscopy of ultrasound contrast agents, *Journal of the Acoustical Society of America*, 121: 648-656, 2007.
- [4]. Tu J, Guan J, Qiu Y, Matula TJ, Estimating the shell parameters of SonoVue microbubbles using light scattering, *Journal of the Acoustical Society of America*, 126: 2954-2962, 2009.
- [5]. Crawford GE, Earnshaw JC, Viscoelastic relaxation of bilayer lipid membranes. Frequency-dependent tension and membrane viscosity, *Biophysical Journal*, 52: 87-94, 1987.
- [6]. Marmottant P, van der Meer S, Emmer M, Versluis M, de Jong N, Hilgenfeldt S, Lohse D, A model for large amplitude oscillations of coated bubbles accounting for buckling and rupture, *Journal of the Acoustical Society of America*, 118: 3499-3505, 2005.
- [7]. Chatterjee D, Sarkar K, A Newtonian rheological model for the interface of microbubble contrast agents, *Ultrasound in Medicine and Biology*, 29: 1749-1757, 2003.
- [8]. Hoff L, *Acoustic Characterization of Contrast Agents for Medical Ultrasound Imaging*, (Kluwer, Dordrecht), 2001.

The screenshot shows the LiveMedia website interface. At the top left is the 'LIVE MEDIA' logo. A search bar contains the text 'Search videos, photos and events...'. Below the search bar are five navigation buttons: 'CONGRESSES' (red), 'COURSES' (blue), 'EVENTS' (green), 'NEWS' (dark blue), and 'WEBTV' (purple). The main content area features a dark header with the text 'Congresses | The 24th European symposium on Ultrasound Contrast Imaging'. Below this is a light grey banner with the event title 'The 24th European symposium on Ultrasound Contrast Imaging' and the dates '17-18 January 2019 - Hilton Hotel Rotterdam, The Netherlands'. It also mentions 'An ICUS Conference'. The banner includes a collage of images: a diagram of a cell, a B-mode ultrasound image, a color Doppler image, and a grid of small circular images with a handwritten note. Below the banner, the organizers and scientific board members are listed.

Organised by: Nico de Jong, Folkert ten Cate, Rik Vos, Klazina Kooiman, Annemien van den Bosch, and Arend Schinkel
Scientific board: Mike Averkiou, Mark Borden, Paolo Colonna, Olivier Couture, Beat Kaufmann, and Eleanor Stride

WEBCASTING

Introducing exciting news for our friends who are not able to join the 24rd European symposium on Ultrasound Contrast Imaging in Rotterdam! To learn from the best in the world even if travel is not an option, you can join the Symposium through worldwide live streaming by the WEB CONFERENCE CHANNEL, through Livemedia www.livemedia.com/24symposium. For info of the the previous symposium check www.livemedia.com/23symposium.

Videos will remain hosted on Livemedia indefinitely and available for on demand viewing. Once registered, remote participants will receive log in credentials that will allow them access and will monitor the viewing time. GAIN ONLINE ACCESS to the well known 24th European symposium on Ultrasound Contrast Imaging.

Please register here: www.livemedia.com/24symposium. For any inquiries please contact Irene Syraki irene@livemedia.gr or the symposium secretariat.



The 24th European Symposium on Ultrasound Contrast Imaging Rotterdam is sponsored by:

Bracco Suisse SA

Marco Graf, Senior
Communication Events Manager
Manno, Switzerland

KNAW

Marja van der Putten
Director Academy Science Funds
Het Trippenhuus
Amsterdam, the Netherlands

Philips Healthcare

John MacQuarrie
Senior Product Manager
Ultrasound
Bothell, U.S.A.

Siemens Healthineers

Helen Cleminson
SHS US IN ADGI
United Kingdom

GE Healthcare

Julie Hillsdon
Marketing & Compliance Co-
Ordinator
United Kingdom

Samsung

Electronics Benelux

Luc van Dalen, Business
Development Manager
Health Medical Equipment
The Netherlands

Oldelft Ultrasound

Stefan Roggeveen
Commercial Manager
Delft, the Netherlands

Visualsonics Fujifilms

Adrie Gubbels
Amsterdam, the Netherlands

TIDE Microfluidics

Wim van Hoeve
Enschede, the Netherlands

Coeur

Eric Boersma
Erasmus MC - Thoraxcenter
Rotterdam, the Netherlands

Mindray Medical

Germany GmbH

Hongbo Zhu
Marketing Ultrasound Europe
Darmstadt, Germany

AMB Labs

Jameel Feshitan,
Boulder, USA

Nederlandse

Hartstichting

Mrs. E. Buitenhuis
Manager Research Dept.
Den Haag, the Netherlands

FIRST ANNOUNCEMENT 2020

**25th EUROPEAN SYMPOSIUM ON
ULTRASOUND CONTRAST IMAGING**

16-17 JANUARY 2020

ROTTERDAM, THE NETHERLANDS

Information on the 25th EUROPEAN SYMPOSIUM ON ULTRASOUND CONTRAST
IMAGING: Mieke Pruijsten, m.pruijsten@erasmusmc.nl

sponsors:

Golden sponsor



GE Healthcare



PHILIPS

SAMSUNG

SIEMENS
Healthineers



Silver sponsor



mindray
healthcare within reach



The 24th European Symposium of Ultrasound Contrast Imaging, Rotterdam is sponsored by:



GE Healthcare



SIEMENS
Healthineers

PHILIPS



KNAW

SAMSUNG



mindray
healthcare within reach

